CORRELATION OF THE MECHANICAL PROPERTIES AND WEAR BEHAVIOUR WITH THE MICROSTRUCTURAL CHARACTERISTICS OF TOOL STEELS

Božo Skela

Doctoral Dissertation
Jožef Stefan International Postgraduate School
Ljubljana, Slovenia

Supervisor: Prof. Dr. Bojan Podgornik, Institute of Metals and Technology, Lepi pot 11, Ljubljana, Slovenia
Co-Supervisor: Dr. Marko Sedlaček, Institute of Metals and Technology, Lepi pot 11, Ljubljana, Slovenia

Evaluation Board:
Prof. Dr. Miha Čekada, Chair, Jožef Stefan International Postgraduate School (IPS) and Jožef Stefan Institute (IJS), Ljubljana, Slovenia
Prof. Dr. Vojteh Leskovšek, Member, Jožef Stefan International Postgraduate School (IPS) and Institute of Metals and Technology (IMT), Ljubljana, Slovenia
Dr. Manel Rodriguez Ripoll, Member, AC2T Research GmbH, Wiener Neustadt, Austria

MEDNARODNA PODIPLOMSKA ŠOLA JOŽEFA STEFANA
JOŽEF STEFAN INTERNATIONAL POSTGRADUATE SCHOOL

Božo Skela

CORRELATION OF THE MECHANICAL PROPERTIES AND WEAR BEHAVIOUR WITH THE MICROSTRUCTURAL CHARACTERISTICS OF TOOL STEELS

Doctoral Dissertation

POVEZAVA MEHANSKIH LASTNOSTI IN OBNAŠANJA OBRABE Z MIKROSTUKTURNIMI KARAKTERISTIKAMI ORODNIH JEKEL

Doktorska disertacija

Supervisor: Prof. Dr. Bojan Podgornik

Co-Supervisor: Dr. Marko Sedlaček

Ljubljana, Slovenia, April 2021

To my family, that supported me and endured my crankiness. To my special Lady, that was always by my side, offering unselfish help and support, and always knew how to put a smile on my face.

Acknowledgments

This research was conducted at the Institute of Metals and Technology in the frame of the research program P2-0050, financed by the Slovenian Research Agency. This work was partly funded by the project COMET InTribology, FFG No. 872176 (project coordinator: AC2T research GmbH, Austria).

Firstly, I would like to express my thanks to my co-supervisor dr. Marko Sedlaček for his guidance and availability when I needed him. He is largely responsible for my introduction to research work at IMT. Our discussions and his valuable comments were very much appreciated. Furthermore, his guidance during conference travels was of great help and something I greatly enjoyed.

Secondly, the same gratitude goes to the supervisor and head of the Department of Metallic Materials and Technology, Prof. Dr. Bojan Podgornik, for giving me the opportunity to work there. His guidance, suggestions and valuable comments were indispensable for improvement to my thesis.

Furthermore, this thesis would not have been completed without the contributions, help and support of other co-workers. I would like to express special thanks to:

- Dr. Fevzi Kafexhiu for assistance with SEM investigations and constructive discussions about the results,
- Dr. Ana Kračun, for constructive discussions, unselfish help, guidance around IMT and help with data processing,
- Branko Zvonar for assistance with the vacuum heat treatment and preparation of specimens,
- Uni. Dipl. Inž. Kem. Inž. Martin Topole for his immediate technical help when needed,
- Dr. Borut Žužek, dr. Agnieszka Zuzanna Guštin, Rok Rezar, Gašper Puš for mechanical properties testing,
- Dr. Črtomir Donik and Barbara Šetina-Batič for SEM (EBSD) and XRD measurements and assistance with microstructural examinations,
- Nataša Lipovšek for discussions and preparations of the metallographic specimens for microstructure observations,
- Zdenko Majer, Robert Lampe, Luka Snoj for helping with specimen preparations,
- Jelka Kovač for chemical analysis of the specimens,
- Dr. Franci Vode for assistance with the preparations of thermocouples for temperature measurements during heat treatments.
- Dr. Petra Močnik from the Slovenian National Building and Civil Engineering institute (ZAG) for assistance when using their tribotester for unidirectional sliding wear testing.
- Dr. Manel Rodriguez Ripoll and his team from the AC2T Research GmbH, Wiener Neustadt, Austria, for their assistance regarding elevated temperatures wear testing.

Finally, I would like to thank my girlfriend, friends and family for constantly encouraging and supporting me.

Abstract

Wear is one of the key problems with many types of engineering components as it can limit their life expectancy. The same is true for tools and tool steels, which are the focus of this doctoral thesis. Tool-wear response and behaviour are closely related to a material's final microstructure and properties. Most of the existing literature is focused on the commercially available steels where the heat-treatment regimes are selected in a manner to achieve the highest hardness so as to improve the wear resistance. However, the consideration of a specific microstructure at different hardness levels and understanding the influence of the microstructure constituents on the tribological properties are not yet properly clarified. Furthermore, it is of great interest to tribologically evaluate conventional tool steels to their full potential, as more specialised materials are much more expensive. The aim of this doctoral dissertation was to investigate and describe the influence of the different microstructures of conventional tool steels (different carbide morphology, orientation, fraction, size, type) and the corresponding matrix hardness on a tool steel's wear properties and its behaviour during wear.

The variation in chemical composition results in a different volume fraction, type and the size of the hard particles in the matrix microstructure, i.e., carbides. In addition, the microstructure is influenced by altering the heat treatment. The results show that the best wear properties are provided by a fine-grain matrix with a grain size ASTM 5 or finer, achieved by the proper selection of the austenitization temperature. On the other hand, improper austenitization can result in an increased matrix grain size or the presence of residual carbides, which consequently deteriorate the mechanical properties and the wear resistance. The presence of different carbides in terms of fraction, type and size (morphology) in the martensitic matrix has different effects on the wear, being matrix-hardness dependent. At high hardness levels a high fraction of large eutectic carbides (M_7C_3 type) provides an improved abrasive wear resistance. However, when the bulk hardness drops below a certain value (<54 HRC) a larger amount and a homogeneous distribution of smaller secondary carbides ($M_{23}C_6$ and MC type) combined with a very small amount of larger ones provides the best results. Matrix hardness is important for preventing carbide removal from the matrix, especially in the case of an abrasive wear mechanism. In this case the wear is intensified due to the plastic deformation of the tempered martensite matrix, followed by carbide cracking and their removal from the matrix. In the case of adhesive wear, the wear resistance is in general improved by an increased fraction of carbides, especially large ones. However, as the contact conditions become milder those carbides can start to act as cutting edges, traps for wear debris and areas of transferred material build-up, thus leading to high overall wear rates.

Thermal loading of the tool steel results in a significant decrease in its tensile and yield strength. However, the wear response at elevated temperatures is not solely governed by a change in the mechanical properties and a drop in the hardness caused by the decomposition of the tempered martensitic matrix, but also by the formation of an oxide glazed layer. A softer matrix promotes its formation, so leading to reduced wear rates.

Povzetek

Obraba je ena ključnih težav v mnogih vrstah inženirskih komponent, ki določa njihovo življenjsko dobo. Enako velja za orodja in orodna jekla, ki so osrednja tema te doktorske disertacije. Odziv in obrabno obnašanje orodja v različnih proizvodnih procesih in delovnih pogojih je v veliki meri povezano z njihovo končno mikrostrukturo in lastnostmi. Večina obstoječe literature je osredotočena na komercialno dostopna jekla, kjer so režimi toplotne obdelave izbrani tako, da se doseže največja trdota materiala za zmanjšanje obrabe. Vendar upoštevanje specifične mikrostrukture pri različnih trdotah in razumevanje vpliva na tribološke lastnosti še ni ustrezno razjasnjeno. Zraven tega je pomembno, da se tribološko ovrednoti konvencialna orodna jekla do potankosti, saj so bolj specialni materiali veliko dražji. Zato je bil cilj te doktorske disertacije raziskati in opisati vpliv različnih mikrostruktur konvencionalnih orodnih jekel (različna morfologija karbida, usmerjenost, delež, velikost, tip) in trdote martenzitne matrice na obrabne lastnosti in obnašanje med obrabo. Razlika v volumskih deležih, tipu in velikosti trdih delcev v matrici, tj. karbidov je posledica različnih kemijskih sestav jekel. Poleg tega smo na mikrostrukturo vplivali s spremembo toplotne obdelave.

Rezultati so pokazali, da ima najboljše obrabne lastnosti fino zrnata matrica z velikostjo zrn ASTM 5 ali manjše, doseženo s primerno temperaturo avstenitizacije. Po drugi strani pa lahko nepravilna avstentizacija materiala vodi do rasti avstenitnih zrn ali prisotnosti neraztopljenih karbidov, kar posledično poslabšala mehanske lastnosti in odpornost proti obrabi.

Prisotnost karbidov različnega tipa, deleža in velikosti (morfologije) v martenzitni matrici ima različne učinke na obrabo, kar pa je tudi odvisno od trdote matrice. Pri višjih trdotah matrice večji delež velikih evtektičnih karbidov (tipa M_7C_3) pripomore k izboljšani obrabni odpornosti. Po drugi strani pa, kadar trdota pade pod določeno vrednost (<54 HRC), večji delež in bolj homogena distribucija manjših karbidov ($M_{23}C_6$ in MC tipa) v kombinaciji z manjšim deležem večjih, da najboljše lastnosti. Trdota matrice je pomembna za preprečevanje odstranjevanja karbida iz matrice, zlasti pri mehanizmu abrazivne obrabe. Obraba se poveča zaradi plastične deformacije popuščene martenzitne matrice, kar vodi v pokanje velikih karbidov in njihove odstranitve iz matrice.

Pri adhezijski obrabi se odpornost proti obrabi na splošno izboljša s povečanim deležem karbidov, zlasti velikih. Kadar pa so kontaktni pogoji milejši, lahko ti karbidi delujejo kot rezalni robovi, pasti za obrabne delce in območja kopičenja prenesenega materiala, kar vodi do visoke stopnje adhezijske obrabe.

Toplotna obremenitev jekla za delo v vročem znatno zmanjša natezno trdnost in mejo tečenja pri določeni trdoti. Mehanizem obrabe pri povišanih temperaturah ni odvisen le od sprememb mehanskih lastnosti, temveč tudi od oksidacije površine, ki se obrablja. Mehkejša matrica pospeši oksidacijo površine, kar zavre abrazijsko obrabo.

Contents

List of Figures

List of Tables

Abbreviations

AFM	. . . atomic force microscope
ASTM	. . . American Society for Testing and Materials
AISI	. . . American Iron and Steel Institute
BSE	. . . backscattered secondary electron
BCC	. . . body-centred cubic structure(α – and/or δ– ferrite)
COF	. . . coefficient of friction
EDS	. . . energy-dispersive X-ray spectroscopy
EBSD	. . . electron backscattered diffraction
FCC	. . . face-centred cubic structure(austenite)
FEG	. . . field-emission gun
FIB	. . . focused ion beam
HV	. . . Vickers hardness
HRC	. . . Rockwell hardness
HT-CAT	. . . high-temperature continuous abrasion test
HTCIAT	. . . high-temperature cyclic impact/abrasion test
HSS	. . . high-speed steels
IIT	. . . instrumented indentation testing
LFM	. . . lateral force microscope
LM	. . . light microscopy
MIM	. . . metal injection moulding
M_3C	. . . carbide type with M standing for metal (usually Fe-rich)
M_6C	. . . carbide type with M standing for metal (usually Mo-rich)
M_7C_3	. . . carbide type with M standing for metal (usually Cr-rich)
$M_{23}C_6$	. . . carbide type with M standing for metal (usually Cr-rich)
Mat. No.	. . . material Numbers (Werkstoff Nummers) designation for steel types
PM	. . . powder metallurgy
SEI	. . . secondary Electron Image
SEM	. . . scanning electron microscopy
SD	. . . sliding direction
SiC	. . . silicon carbide
TEM	. . . transmission electron microscope
XRF	. . . X-ray fluorescence
XRD	. . . X-ray diffraction

Symbols

A	. . . elongation
A_p	. . . projected contact area
D	. . . diameter of the specimen in the unnotched area of test region
d	. . . mean diagonal of indentation (mm)
E	. . . modulus of elasticity
F_N	. . . normal load
F	. . . applied load
F_f	. . . frictional force
h_c	. . . contact depth of the indenter with the sample at Fmax
H	. . . indentation hardness
K	. . . wear constant
K_{IC} or K_C	. . . fracture toughness
L	. . . load when presenting Hertzian contact pressure
N	. . . normal force between the surfaces
N (*)	. . . number of particles each carrying load
P	. . . Holloman-Jaffe parameter linked to the tempering process
P (*)	. . . load at fracture
p_H	. . . Hertzian contact pressure
R_m	. . . tensile strength
R_{p02}	. . . yield strength
R	. . . radius
s	. . . sliding distance
t	. . . time
T	. . . temperature
V	. . . sliding speed
W_s	. . . wear volume
W_e	. . . element equivalent
Z	. . . reduction area of tensile test specimens after testing
α	. . . ferrite
ε	. . . strain
Φ	. . . diameter of the counter-body ball
σ	. . . stress
Q	. . . total volume removed per unit sliding
μ	. . . coefficient of friction
α_3	. . . material independent-constat
α_4	. . . constant

(*) Due to variations in the literature and the same symbols used in different equations, some of the symbols may be doubled. Their meaning is further described in the text at the appropriate places of the thesis.

Chapter 1

Introduction

The wear of surfaces is present in a variety of engineering applications and has both economic and technical consequences. From an economic perspective, the cost resulting from friction and wear is estimated to be in the range of 1 to 4% of the gross national product of industrialized countries. The effect of abrasion wear is particularly evident in industrial fields such as agriculture, mining, mineral processing and earthmoving work. Wear is also one of the key problems in many types of engineering components as well as being a very important factor in determining the life expectancy of certain components. This is particularly important for tools and dies in the metal processing and forming industry.

The influence of a material's microstructure on the mechanical properties is directly related to the kinetics of the phase transformation. Change in microstructure has a strong influence on properties and is directly related to the resistance of the material to wear.
Wear is the progressive loss of material from contacting surfaces in relative motion. Almost all machines lose their durability and reliability due to wear and the possibilities of new, advanced machines are restricted by wear problems. Therefore, wear control has become an important requirement for advanced and reliable technology of the future. A wear mechanism can be quickly changed because it is influenced by many factors, like operating conditions and material selections. All this requires that the tool material has very good mechanical properties and anti-wear properties. Mechanical and thermal loadings lead to damages on the tool surface, which can further result in tool failure [1, 2].

Most of the existing literature is focused on the commercially available steels where heat-treatment regimens are selected in a manner to achieve the highest hardness of the material without much consideration of the changes that are happening in the microstructure. Material strength (hardness) and toughness are the main properties that have been observed to increase the wear resistance of the material [3]. In general, the abrasive wear rate is proportional to the hardness of the material, which is especially true for pure metals. However, in certain cases the material toughness has been found to have a major influence in terms of wear resistance [3]. From the viewpoint of the microstructure, understanding the tribological properties in terms of microstructure and microstructural changes is not yet properly clarified. The development of high-hardness, wear-resistant steels is mostly focused on ensuring high hardness on the basis of a martensitic matrix. This is based on the assumption that the wear resistance is proportional to the hardness of the material. Different experimental findings show that just the high hardness of the martensite matrix does not guarantee a high wear resistance. The brittleness of the martensite may cause a lower wear resistance, even though the hardness of the material is very high.

In this doctoral research we were focused on the wear behaviour of cold- and hot-work tool steels. We pursued wear mechanism and behaviour on the surface and in the subsurface of the material and how the wear affects the contacting microstructure of the tool steel during sliding against differen counter body. The research work was focused on different microstructures and hardness values of different tool-steel compositions. The variations in the chemical compositions result in different volume fractions, types and sizes of hard

particles in the matrix microstructure, i.e., carbides/carbo-nitrides. The aim was to thoroughly investigate and describe the effect of their type, size and density of distribution in the matrix on the tribological properties. For a more detailed knowledge of the behaviour of carbides in the matrix, experiments were designed in such a way as to monitor their movements at the initial stages of wear and after longer exposure to a counter-body during relative motion. In order to investigate the influence of different microstructures, the heat-treatment regimens were planned in such a manner as to obtain tool steels with the same hardness level. This enabled us to exclude the parameter of bulk hardness and focus on the microstructure's influence on the tribological behaviour. In order to investigate the volume fraction and type of carbides in the matrix, different tool steels with different chemical compositions were used. The microstructure constituents were tribologically described and also correlated with other mechanical properties, especially fracture toughness. The influence of the formation and wear debris removal from the contacting surfaces was also addressed.

The main idea behind the doctoral dissertation is that the mere hardness of tool steel, used in practice to select the heat-treatment procedure, is not sufficient to determine the wear resistance of the steel. With knowledge of the influence of individual microstructure components on the wear behaviour of tool steel, microstructure optimization for the best tribological performance of the contact surfaces can be performed.

Chapter 2

State of the Art

2.1 Fe-Fe_3C

The most widely used engineering material today is steel. Steel is an alloy of iron and carbon, according to the Fe-C binary diagram (Figure 1), containing up to 2.11 wt. % carbon. Since many steel grades nowadays are alloyed with different alloying elements, this definition has been revised so that the steel must contain at least 50 wt. % of iron and must contain one or more alloying elements (carbon, manganese, silicon, nickel, chromium, molybdenum, vanadium, titanium, niobium, aluminium). However, the binary phase diagram of iron and carbon (Figure 1) is still the basis of steel production and heat treatment. Iron exists in two crystal forms below its melting temperature: ferrite and austenite. Ferrite has a body-centred cubic crystal structure, which is stable from room temperature up to 912 °C and from 1394 °C to the melting point of 1530 °C. The low-temperature form is called α-ferrite and the high-temperature form is δ-ferrite. Austenite has a face-centred cubic (fcc) structure and is also known as γ-iron. It exists in the temperature range between 912 °C and 1394 °C [3]. If the carbon content is low, two phases can exist: solid solutions of ferrite and austenite. Carbon atoms are placed on the interstitial sites of the crystal structure of austenite or ferrite. At higher carbon contents, cementite is formed in the steel, a compound with chemical formula Fe_3C. Cementite has an orthorhombic structure. The stability of those three phases depends on the temperature, and the composition is represented in the phase diagram in Figure 1. Steels are commonly classified as hypoeutectic or hypereutectoid based on the carbon level, less or more than the eutectoid point (0.77 % wt.). The basis of the heat treatment lies in the transformation of austenite during cooling to room temperature to other microstructure constituents (ferrite, pearlite, bainite, martensite).

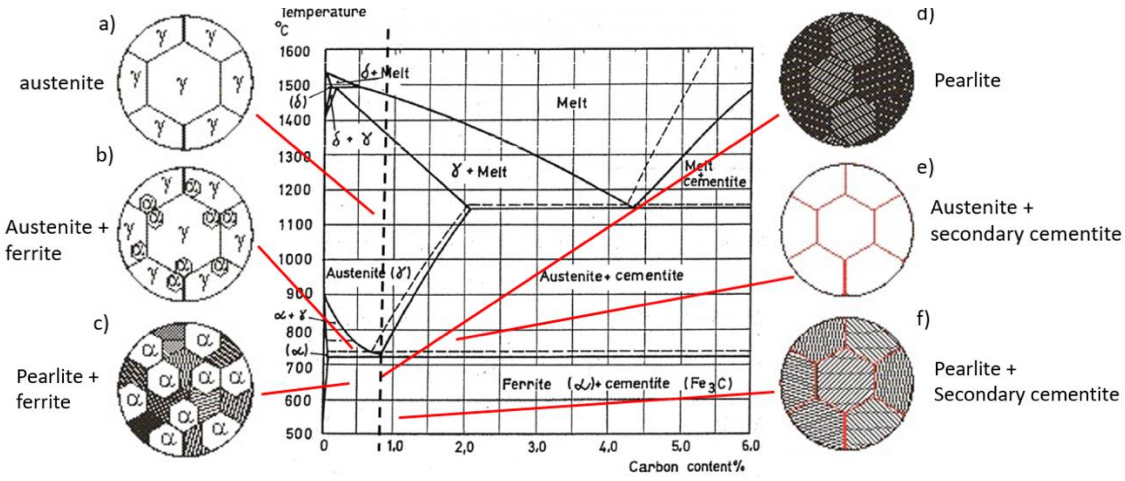

Figure 1: Fe-C binary phase diagram [4]

Critical temperatures as a function of carbon content marking the boundaries between the various phase fields are labelled on the iron-carbon phase diagram. These are the processing temperatures for the formation and transformation of austenite. They have a given designation "A" [5]. The alloying elements commonly used in tool steels shift the boundaries of the iron-carbon phase diagram. Each element, depending on its atomic size and electronic structure, as related to its atomic number or position in the periodic table, may stabilize either the ferrite crystal structure or the austenite crystal structure. Manganese, nickel, cobalt and nitrogen stabilize the austenite region and decrease the critical temperatures. On the other hand, silicon, chromium, molybdenum and aluminium are ferrite stabilizers and raise the critical temperatures, thus shrinking the austenite phase field. Some elements may form dispersions of nitrides, carbides, or carbonitrides in the austenite [5].

2.2 Tool Steels

Tool steels are used as a material for tools to shape other metals or materials. They are usually highly stressed during service. They are used in processing routes like cutting, forming, machining, battering, die casting or to shape and cut wood, paper, rock, or concrete.

They are used in applications where they have to withstand severe service conditions and thus they have to have high hardness and durability. In order to achieve high hardness, steel needs to have a martensitic microstructure, which is significantly harder than other microstructure constituents like ferrite and pearlite (Figure 2).

A mixed classification system for tool steels is based on prominent characteristics such as alloying elements, special mechanical properties, heat treatment or application.

Tool steels with higher amount of alloying elements have a comparatively narrow carbon range. On the other hand, carbon tool steels and low-alloy tool steels have a wide range of carbon contents [6, 7].

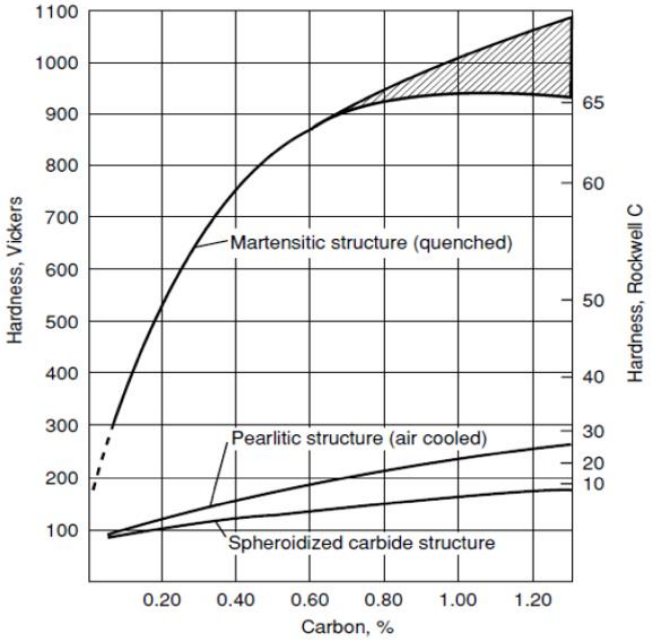

Figure 2: Hardness of different types of steel microstructures [1].

The American Iron and Steel Institute (AISI) classifies tool steels into different groups [6]:

- Molybdenum high-speed steels,
- Tungsten high-speed steels,
- Intermediate high-speed steels,
- Chromium hot-work steels,
- Tungsten hot-work steels,
- Molybdenum hot-work steels,
- Air-hardening, medium-alloy, cold-work steels,
- High-carbon, high-chromium, cold-work steels,
- Oil-hardening cold-work steels,
- Shock-resisting steels,
- Low-alloy special-purpose tool steels,
- Low-carbon mould steels,
- Water-hardening tool steels.

2.2.1 Microstructure and alloy element carbides in tool steels

The microstructure of steel consists of a spatial arrangement of crystalline aggregates of different phases. The size, shape, distribution, composition, and crystal structure of these phases control the final properties of any given steel, including hardness, strength, ductility, impact toughness, and creep strength [6]. Tool steels are usually delivered in the soft-annealed condition. In this condition the material has a microstructure with very low hardness ready to be machined into the desired shape. The microstructure in this state consists of spherical carbides in a matrix of ferrite grains. In a high-carbon steel with the presence of other alloying elements (e.g., AISI D2 steel), are larger eutectic M_7C_3 type carbides in a ferrite matrix among uniformly sized spheroidized carbides [6]. This type of microstructure is also referred to as spheroidized pearlite (globular cementite (carbides) in a ferrite matrix).

The basis of heat treatment lies in the transformation of austenite during cooling to room temperature to other microstructure constituents. To achieve a good combination of the needed properties, tool steels commonly used in applications with severe service conditions or at elevated temperatures have microstructures of tempered martensite with alloying-element carbide precipitates [1, 8]. For this reason, two main mechanisms are pursued for strengthening: solid-solution hardening and precipitation hardening (carbides precipitated during tempering reinforce the martensite matrix).

Martensite is a hard micro-constituent that is obtained when steels are rapidly cooled (quenched) to room temperature from the austenite region. As the transformation itself is non-diffusive, there is a negligible migration of carbon. The lack of space for carbon atoms when transforming from austenite to α-ferrite distorts the lattice by expanding in one direction, and so creating a tetragonal structure (Figure 3) [9].

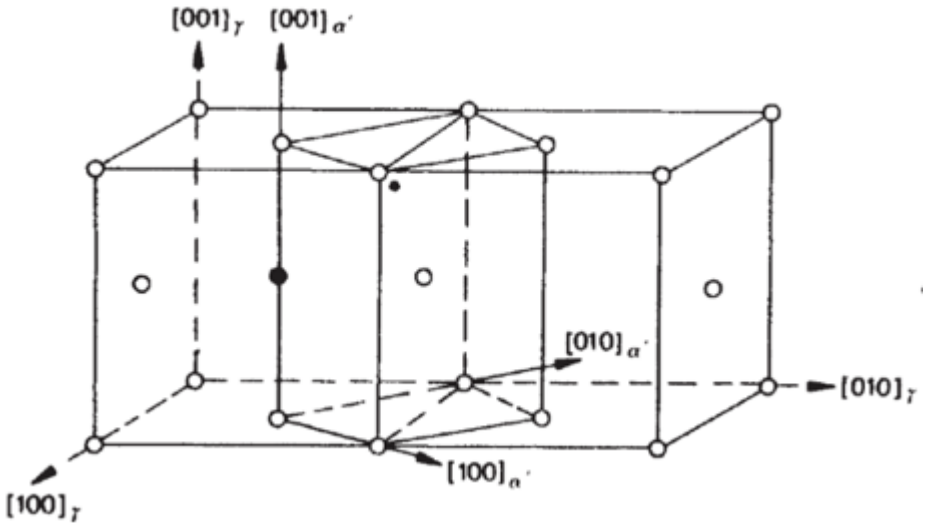

Figure 3: Martensite transformation during rapid cooling from austenite region; tetragonal unit cell outlined in austenite [9].

Martensite is a supersaturated solid solution of carbon in ferrite. The hardening of steel with martensite formation comes from the hardening of the martensite crystals with alloying carbon content in the solid solution. Deformations caused by shear movements during the transformation increase the density of the dislocations. Due to the fine microstructure development the sliding distances of the dislocations are shortened [10, 11]. Because the martensite transformation occurs through a shear mechanism and without diffusion, the morphology of martensite is mostly lath-, lenticular-, or plate-like. The martensite that forms in low-carbon steel (<0.5 wt. % C) is lath like and shows mainly dislocations, whereas martensite that forms from high-carbon steels is plate-like and shows twins. In principle, various physical processes that lead to the tempering of martensite start as soon as the martensite is heated to above room temperature. These physical processes are associated with different temperature ranges. In the first stage of tempering (100 to 200 °C), ε-carbide forms from martensite. In the case of alloyed steels, the iron atoms can be replaced by other elements. After the precipitation of ε-carbide in stage I, the martensite is still supersaturated with carbon to a certain extent and would undergo further decomposition on heating to higher temperatures. In the temperature range of 200 to 350 °C, the retained austenite in the carbon and low-alloy steels decomposes into ferrite and cementite. In highly alloyed tool steels, the retained austenite is much more stable, resulting in the higher tempering temperatures needed for transformation to occur. The formation of stable carbides that is typical for the third stage of tempering may overlap with the second stage of tempering. In the temperature range of 250 to 750 °C, cementite precipitates within the martensite. The composition of the cementite is Fe_3C. In alloyed steels, it is denoted as M_3C, where M corresponds to substitutional alloying additions (e.g., Cr, Mn) in addition to Fe. The nucleation of cementite may occur at ε-carbides and may grow by dissolution of the ε-carbide. In high-carbon steels, the cementite precipitates along the twin boundaries of martensite. Other sites for the nucleation of cementite are the prior austenite grain boundaries or interlath boundaries. With the formation of cementite, most of the carbon in the martensite is removed from the solid solution. Tempering at higher temperatures leads to the precipitation of more equilibrium alloy carbides such as M_7C_3 and $M_{23}C_6$. In steels containing Cr, Mo, V, and Ti, these carbides are associated with hardening of the steel, which is called secondary hardening. The precipitation of these carbides also leads to the dissolution of cementite. During secondary hardening precipitated

alloy-element carbides precipitated during tempering contribute to the high yield strength by impeding the mobility of the matrix dislocations [6].

Alloying to produce large volume fractions of alloy carbides is a major difference in the design of tool steels compared to the design of low-alloy steels [1]. Relatively large alloy carbides distributed in the martensite matrix (1–6 µm and up to 25 µm) are in general significantly harder than the matrix. Large volume fractions of carbides provide the high hardness and wear resistance required to shape other materials. They provide an improved resistance to abrasive wear. The alloy carbides may be produced during solidification, during hot work or austenitizing for hardening, and during tempering of the martensitic microstructures [1]. Figure 4 presents a comparison of hardnesses between different types of carbides that appear in tool steels. The M_7C_3 carbide type with a hexagonal crystal structure are in general Cr-rich carbides. M stands for metal element in the phase, where in this case M means chromium; however, traces of elements like Mo and V can be present. They are very effective against abrasive wear as eutectic carbides in many high-chromium, high-carbon-containing tool steels. Large carbides of this type are present in steels where carbide-forming elements are added in such amounts that exceeds their solubility. This will lead to carbides that are not dissolved during hardening and are mainly formed directly during solidification [12]. Due to alloying-elements segregation, clusters of segregated carbides are present in the as-cast material. Hot work breaks up the segregated solidification structures, but because the alloy carbides are stable during high-temperature hot working, they are elongated by the hot work [1]. They are also found as a product of tempering in high-speed steels; however, their size is much smaller. The hardness of M_7C_3 carbides ranges roughly from 15 to 20 GPa (1500 to 2000 HV) [13]. Similar elements as for the M_7C_3 carbide type form $M_{23}C_6$ carbide, where M again mainly stands for Cr. The $M_{23}C_6$ carbide type has a cubic crystal structure. Such carbides are usually formed during annealing, depending on the chromium content in the steel. They start to dissolve during austenitization at temperatures exceeding ≈ 900 °C [7]. They are present in high-Cr steels and all high-speed steels. Cr can be replaced with Fe to yield carbides with W and Mo [1]. Their hardness is in general somewhat lower than the hardness of the M_7C_3 carbide type (1300 HV). Another carbide type usually containing an increased amount of chromium is M_3C, known as cementite. However, here the main M element is Fe. It typically forms between iron and carbon. Cementite does not exhibit hardness high enough to promote abrasive-wear resistance in tooling conditions [14]. Very effective abrasive-wear inhibitors often found in tool steels are MC-type carbides, the hardness of which is very high (Figure 4) compared to other carbide types and microstructure constituents. They have a face-centred cubic structure. They mainly dissolve V, with the incorporation of W and small amounts of Cr and Fe. It has been reported that MC is the carbide phase with the greatest composition variability [13]. They are thermally stable type carbides usually formed as isolated particles. These carbides provide very good cutting performance. Vanadium carbides have very limited solubility in the matrix [13, 15]. M_6C type carbides formation is encouraged by tungsten [16]. M is either W, Fe and Mo or a combination commonly denoted as $(Fe,Mo,W)_6C$ or h-carbide. In some cases, depending on the steel composition, it can also consist of moderate amounts of Cr and V. The chemical composition of M_6C is quite stable. These carbides dissolve in the austenite matrix at temperatures ranging from ≈ 1150 °C to the solidus temperature; however in practice they do not dissolve completely [15, 16]. M_6C has a face-centred cubic structure and exhibits a hardness of around 1500 HV. M_6C carbides are extremely abrasion resistant and are present in all high-speed steels. Molybdenum promotes the formation of M_2C-type carbides. These carbides have a hexagonal crystal structure. At elevated temperatures they become unstable. At around ≈ 750 °C they transform to M_6C-type carbides in a reaction with Fe [17]. They usually

precipitate during tempering of high-speed steels as a metastable or transition carbide, associated with secondary hardening. M_2C carbides have the second-highest hardness, following MC-type carbides (Figure 4).

After a hardening heat treatment, the microstructure of tool steels can also contain some retained austenite. This is the austenite phase that was not transformed upon quenching from the austenitizing temperature. Its amount in the microstructure is strongly dependent on carbon content as well other alloying elements that strongly influence the Ms temperature (temperature at which transformation from austenite to martensite occurs – martensite start). Carbon and almost all alloying elements commonly used in tool steels lower the Ms temperature. As a result, the higher the amounts of alloying elements dissolved in the austenite, the lower the Ms temperature, and the greater the amount of retained austenite at room temperature. This is way with increased austenitizing temperature increases the amount of retained austenite as the austenite composition is enriched with carbon and other alloying elements as carbides dissolve. Due to that less martensite will be formed upon cooling to room temperature [1]. The amount of retained austenite can be reduced or transformed to mixtures of ferrite and cementite in the second stage of tempering as discussed earlier. Similar to hardened carbon and low-alloy steels, the more highly alloyed austenite can transform to bainitic mixtures of carbides and ferrite. The bainitic microstructure consists of ferrite plates called sheaves (subunits). They are separated by thin films of austenite, martensite, or cementite. In general, plate-shaped subunits under certain conditions may exhibit a lath structure. The bainitic microstructure can occur in two different forms: upper bainite and lower bainite. Typically, lower bainite forms in high-carbon steels below the temperature at which upper bainite forms and above the Ms temperature. The lower bainite microstructure is similar to that of tempered martensite [6].

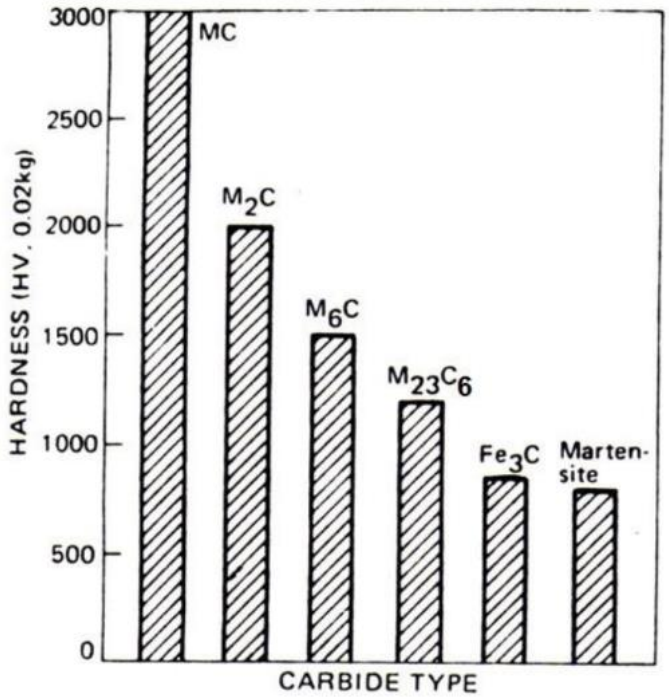

Figure 4: HV hardness of different types of carbides in tool steels [1].

As mentioned above, different alloying elements in steel have a different effect on the properties of the material. The general influences of alloying elements are: formation of solid solutions and different phases, changing the temperature of phase transformations,

changing the solubility of carbon in ferrite or austenite and influencing the rate of transformations [18].

Table 1 summarizes the general alloying elements that are present in tool steels and their effects.

Table 1: Alloying elements in tool steels [7].

Element	**Effect**	**Stoichiometry of carbides**
C	hardening, formation of carbides, promotes formation of MC type carbides	...
Mn	increases depth of hardening	/
Si	raises the solubility of carbon in the matrix and as-quenched hardness	/
Cr	hardenability, corrosion resistance, formation of important wear resistant carbides	M_3C, M_7C_3, $M_{23}C_6$
Mo	hardenability, formation of different types of wear-resistant carbides, lowers tempering brittleness in low-alloyed steels	M_2C, M_6C
V	hardenability, hot hardness, formation of carbides and nitrides, VC important for abrasive wear resistance, much harder than Fe, Cr or Mo carbides	MC
W	hot hardness, formation of hard tungsten carbides	M_6C
Co	increases thermal stability and secondary hardness, reduces toughness and wear resistance	/
Ni	increases toughness and hardenability, reduces lattice distortion and cracking during quenching	/

2.2.2 Hot-work tool steels

Today, there are numerous types of hot-work tool steels that can be divided into three larger subgroups by the AISI. They are characterized by the highest amount of alloying element to impart the high hot hardness: chromium, tungsten and molybdenum (Table 2) [1]. Hardness is used to quantify the material's resistance to plastic deformation, and thus against wear mechanisms such as abrasion, scratching and erosion. The typical carbon content in hot-work tool steels is relatively low (0.30–0.40 wt.% C) [7].

Table 2: Classification of hot-work tool steels by the AISI [5, 7].

Chromium hot-work tool steels	**Tungsten hot-work tool steels**	**Molybdenum hot-work tool steels**
H10, H11, H12, H13, H14, H19	H21,H22, H23, H24,H25, H26	H42, H43
3–5 wt. % Cr, working hardness of 40–55 HRC	work hardness of 40–55 HRC, enhanced thermal stability, more prone to brittleness relative to chromium hot-work steels	molybdenum and tungsten hot-work steels show similar properties for the same value of W_{eq}*, lower initial costs, greater care in heat treatment must be given

*W_{eq}– element (tungsten) equivalent

The steel for hot-work applications must be resistant to softening at elevated temperatures. Hot-work tool-steel grades are commonly alloyed with strong carbide-forming elements such as chromium, vanadium and molybdenum. Carbides of those metals precipitated during tempering in the temperature range of secondary hardening retard the softening and can also increase the hardness (secondary hardening). The changes of the alloy-element carbides and the recovery of the dislocation-rich martensitic structure that occurs at elevated temperatures determine the resistance to softening. In general, the hardness of steels decreases with the increasing temperature [8]. Thus, the hardness stability at elevated temperature is very important. The high-temperature hardness of several steels, among which are also the hot-work tool-steel grades Mat. No. 1.2343 (AISI H11) and Mat. No. 1.2367 (AISI H10), was investigated by Torres et al. [18]. These grades belong to the chromium hot-work tool steels. The grades were not among the hardest martensitic alloys tested, but showed the best stability up to 600 °C. As high strength and toughness are key to the resistance to mechanical and thermal shocks, one of the direct ways of improving it is a change in the chemical composition. Delanges et al. studied the precipitation and the effect of silicon on the stability of the carbides precipitated during secondary hardening at elevated temperatures in the hot-work tool steel AISI H11 [19]. It was shown that silicon shifts the secondary hardening peak to a lower tempering temperature [7, 19].

Hot-work tool steels are used in different applications including the die casting of light metals and alloys, extrusion, die forging, etc. Their surface is sometimes continuously exposed to temperatures that are in their tempering temperature range. Because of that, the so-called tempering effect of the tool surface can take place. Eventually, the tempering effect will result in a decrease of the mechanical and wear properties of the tool's surface [20–23]. For example, a forging tool's surface can often exceed 500 °C, even if only temporally. Die-casting process temperatures in the case of the die casting of brass alloy were reported to lead to die-tool surface temperatures of around 750 °C, detected at a depth of 0.25 mm, although only for a very short period of time (0.35 s), when the 980 °C brass alloy contacts the die surface [10].

2.2.3 Cold-work tool steels

Cold-work tool-steel applications are restricted to, as their name indicates, lower working temperatures (200-260 °C). In general, cold-work tool steels are high-carbon steels that contain a relatively low amount of alloying elements (tungsten, manganese, chromium and molybdenum). The total alloying contents are too small to provide high-temperature

resistance to softening. In general, they are classified into three groups. The classification of cold-work tool steels by the AISI is given in Table 3.

- Group A are air-hardening, medium-alloy tool steels. Because of their reasonably good abrasion resistance, improved toughness and virtually homogeneous carbide distribution they are used for forming, blanking, and drawing dies. This group of steels is suitable for high-precision tools, as they show very good stability with respect to dimensional changes.
- Group D cold-work tool steels have high carbon and chromium contents. The high chromium content provides a high red hardness (at high temperatures). They possess an excellent wear resistance and non-deforming properties and are used in applications like blanking and cold-forming dies, drawing and lamination dies, thread-rolling dies, shear and slitter blades, and forming rolls. The most popular of this group of steels is the D2 steel grade.
- Group O are oil-hardening steels and can be through-hardened upon quenching in oil. O series tool steels are used for blanking, coining, drawing, and forming dies and punches, shear blades, gauges, and chuck jaws after oil quenching and tempering. They are used for short-run applications [6, 7].

Table 3: Classification of cold-work tool steels by AISI association [7].

Air-hardening, medium-alloy, cold-work steels	**High-carbon, high-chromium, cold-work steels**	**Oil-hardening cold-work steels**
A2, A3, A4, A6, A7, A8, A9, A10	D2, D3, D4, D5, D7	O1, O2, O6, O7
principal alloying elements: C, Mo, Cr, Mn, high degree stability of shape upon quenching	principal alloying elements: C (1.5-2.35 wt-%), Cr (12 wt-%), excellent resistance against wear, susceptible to distortion, edge brittleness, cracking during hardening	high-carbon content, relatively low content of principal alloying elements, the wear resistance is not as good as for group A and group D, low initial costs

2.3 Hardening Heat Treatment

There are various types of tool steels on the market, which differ in terms of chemical composition and properties. The final application of the tool steel determines what mechanical and wear properties the material requires. The heat-treatment procedure for the chosen tool-steel grade has a major influence and is one of the most important procedures in tool steels' production. In general, the hardening heat treatment of steel grades consists of heating the material to the austenitizing temperature, quenching and tempering. This is schematically shown in Figure 5. The temperature and time of those processes differ for different steel grades and the final properties that need to be achieved.

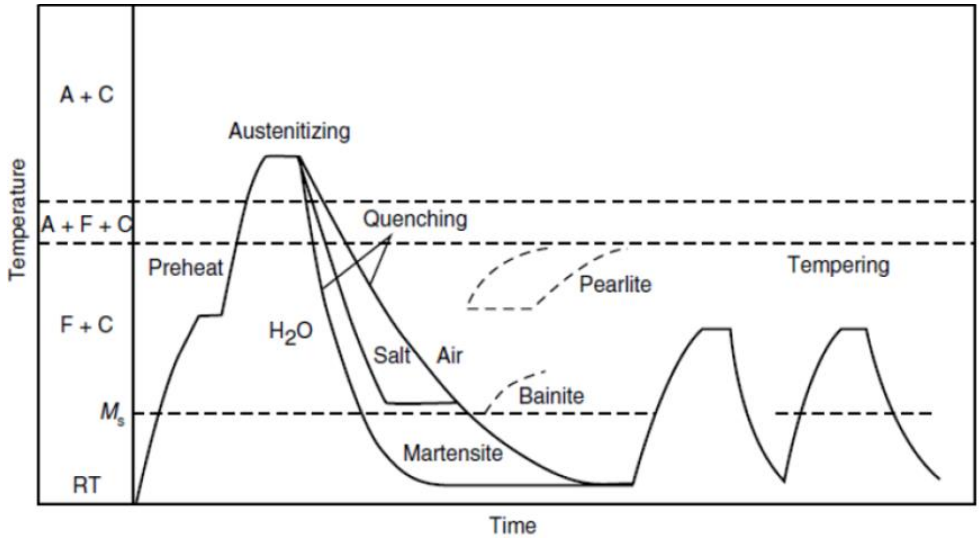

Figure 5: General heat-treatment regime of tool steels [1].

2.3.1 Heating to the hardening temperature

Some steels require faster and some slower heating rates to a chosen austenitizing temperature. Temperatures and heating rates are usually recommended by the steel manufacturers and should be followed when heat treating steels. When heating tool steels to the desired austenitizing temperature at least two preheating stops should be made, especially for larger samples. The goal of step heating is to avoid a temperature gradient between the surface and the core of the heated work piece. The thermal expansion of the microstructure constituents and the dimensional changes that occur at different times lead to internal stresses that can, if high enough, result in cracking of the material [1]. Many factors influence the heating and later soaking time of the components that are heat treated (Figure 6).

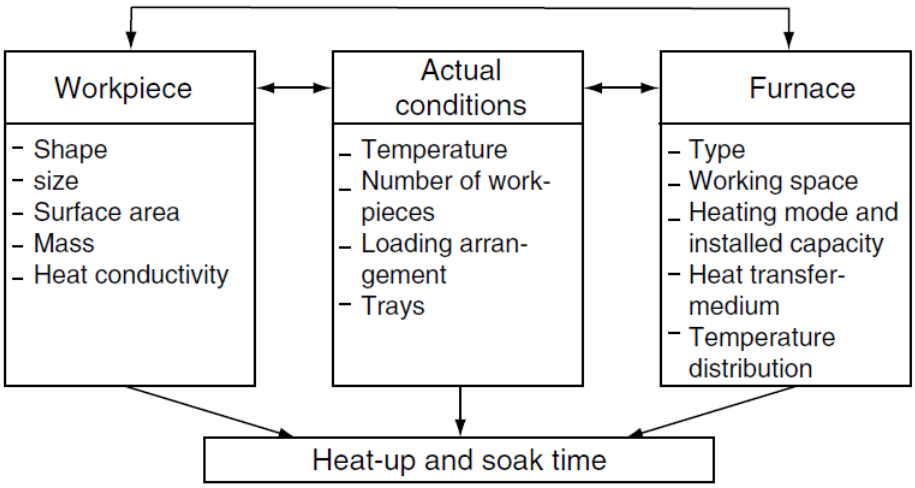

Figure 6: Influencing factors of the heating-up and soaking times [12].

2.3.2 Holding time at the austenitization temperature and quenching

The austenitizing temperature for tool steels differs for different tool-steel grades. Higher austenitizing temperatures are needed for the dissolution of primarily formed metal carbides into the solution of austenite.

The purpose of austenitization is to adjust the chemistry of the austenite to provide the required "martensite start" (Ms) temperature. With austenitization we achieve the required hardenability by maximizing the amount of martensite after quenching. Austenitization is the dissolution of alloying elements that form the supersaturated solid solution after quenching. This later precipitates in the process of the secondary hardening effect during tempering by forming carbide precipitates and additionally hardens the material [1].

Austenitization is determined by the proper austenitizing temperature and soaking time. If these two parameters are too low and too short, the material results in incomplete quenching and the metal does not reach the desired hardness. If the temperatures are too high and the soaking time is too long, enlargement of the austenite grains occurs (large martensite needles), which leads to a high brittleness of the quenched products, which often occurs at the initial grain boundaries of the austenite grains.

Quenching is the rapid cooling of steel from the austenitization temperature. This is done in different cooling media like gas, water, oil or air, depending on the required cooling rate.

Steels which have high stabilities of austenite are subjected to step quenching, in order to lower the input of stresses. The maximum hardness of a product is impossible to achieve, because there is always some retained austenite left during quenching [6].
Sometimes, to transform the retained austenite that is stable at room temperature, a sub-zero treatment is applied. Quenching continues by immersing the steel in liquid air or quenching mixtures (temperatures below room temperature), thus passing the austenite to the martensite transformation [6].

2.3.3 Tempering

Tempering, the final heat-treatment step applied to tool steels, produces the final structure and mechanical properties of the hardened steel [1]. It is usually performed after quenching to decrease the residual stresses caused by the rapid cooling. During tempering the martensitic structure goes into quasi-equilibrium, where the ferrites and carbides are formed by nucleation and growth. The tempering must be applied because the as-quenched martensitic microstructure is too brittle to use. The tempering temperature varies for different types of tool steels. Tool steels that contain a smaller amount of alloying elements are tempered at lower temperatures. On the other hand, steels with higher amounts of alloying elements are tempered in the temperature range 500–600 °C, two or three times. Sometimes the mechanism of austenite transformation during tempering consists of an austenite transformation to martensite upon cooling after tempering, and not the complete transformation to mixtures of ferrite and cementite, as discussed earlier [1]. At these temperatures, substitutional quantities of dissolved elements are mobile, and alloying-element carbides can form (except for plain carbon and low-alloyed tool steels) [7]. Figure 7 presents the general tempering diagram for four classes of tool steel. Those are carbon and low-alloys steels (class 1), medium-to-high-alloy cold-work steels (class 2), highly alloyed high-speed steels (class 3) and medium-to-high-alloy hot-work die steels (class 4). In classes 2 and 4, and especially 3, increases in hardness occur. This is called the secondary hardening effect, as the precipitation of alloy-element carbides occurs (disperse precipitates

of special carbides depending on the composition of the tool steel: TiC, VC, Mo_2C, W_2C), which additionally strengthens the steel. The M_6C are rather coarse and do not add to the strengthening. Because of the rapid coagulation of the Cr_7C_3 carbide at 550 °C, in contrast to Mo_2C and especially W_2C carbides, chromium has a small effect on the secondary hardening [6].

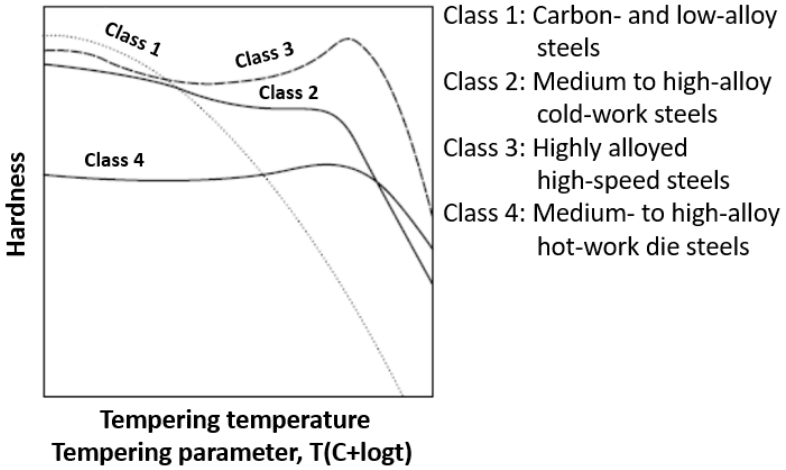

Figure 7: General appearance of the tempering diagram as a function of hardness for tool steels [7].

Hardness, temperature and time of tempering are mathematically interconnected by the expression formulated by Holloman and Jaffe:

$$P = T(k + \log t) \tag{1}$$

P is a Holloman-Jaffe parameter linked to the tempering process, T is the temperature in Kelvin, k is a constant and t is the time in hours. P corresponds to a hardness value that can be read from the diagram (master parameter curve). For the majority of alloy steels the constant k is 20 [10].

2.4 Tribology

Tribology is the field of science that focuses on the contact surfaces of parts that are in relative motion (rolling, sliding). It embraces all subjects involved when surfaces in contact move in relation to each other. Surface interactions practically dictate the functioning of every device. The surfaces of solids consist of the characteristic features that influence friction, wear and lubrication. Two fundamental types of features of special relevance to wear and friction are atomic scale defects and surface roughness. Improving the wear properties of materials can benefit in considerable production and energy savings [24, 25]. Wear has been defined as the material removal from solid surfaces due to the interaction with a mating surface, which may cause failure of the component [26, 27]. The regimes of wear, mechanisms and wear rate depend on the load level, chemical composition, microstructure and surface properties of the material [26]. Wear resistance is one of the most important properties, especially in tool steels. In most cases, wear is a key cause of component failure or the need for their replacement. It also leads to the formation of transfer films, either from the machined material or from the oxide residues and wear debris. Reducing the wear of the tool steels, therefore, prolongs the material's surface properties and prolongs the tool's life. It also reduces the possibility for crack initiations

that can lead to further tool failures. Obtaining the desired surface roughness and the properties of the tools also increases the quality of the products, their surface quality and dimensions.

2.4.1 Wear mechanisms

There are four general wear mechanisms: abrasive wear, adhesive wear, fatigue wear and corrosion wear.

Abrasive wear generally occurs when hard and relatively soft materials are in plastic contact. During sliding, hard and sharp asperities of the harder material penetrate the softer one (Figure 8) [27].

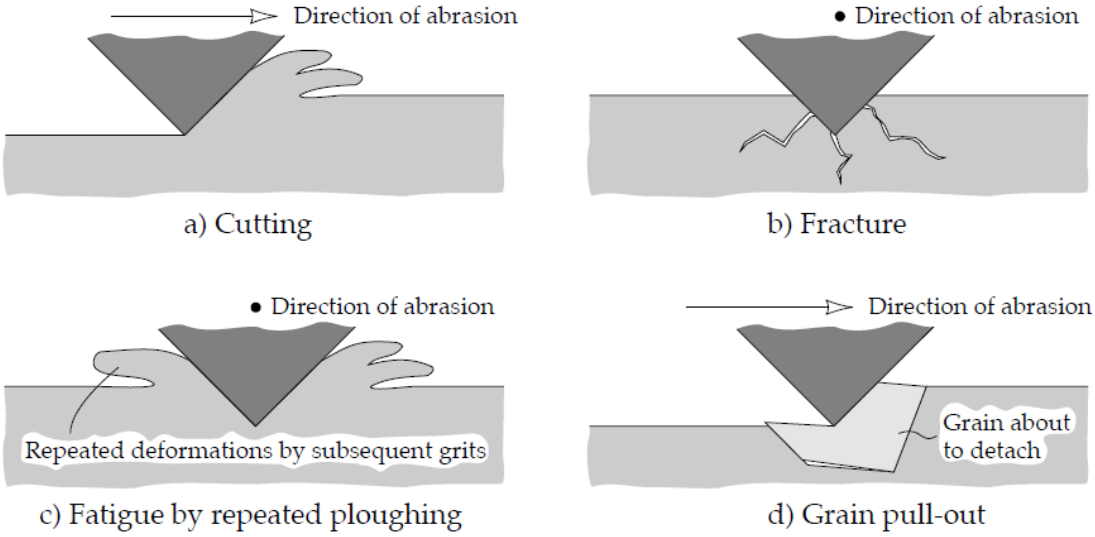

Figure 8: Mechanisms of abrasive wear: micro-cutting, fracture, fatigue and grain pull-out [25].

Adhesive wear generally occurs when two similar materials are in contact and strong adhesive bonds are formed in the contact interface. Localized bonding between the contacting surfaces occurs, which leads to material transfer between those surfaces (Figure 9) [27].

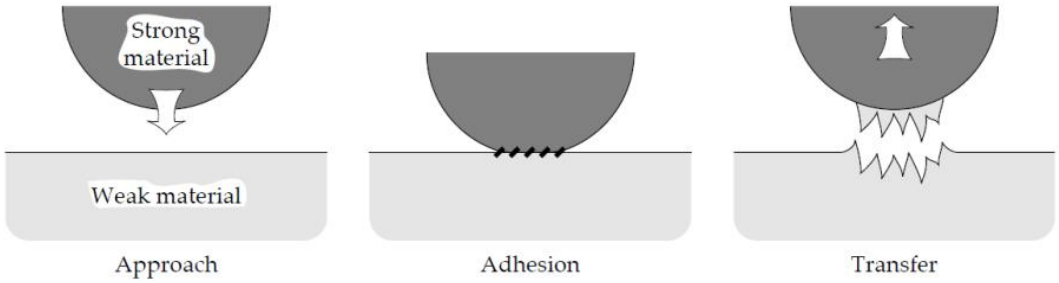

Figure 9: Process of metal transfer due to adhesion [25].

Fatigue wear is generally caused by a cyclic loading during friction. During sliding and rolling, the material in contact is subjected to very high local stresses. This repeatedly stresses the surface and leads to micro-crack formation and propagation. Wear particles are generated by a certain number of repeated contacts [25, 27].

Corrosion wear generally occurs when sliding/rolling takes place in a corrosive environment. Tribochemical reactions produce a reaction layer on the surface. At the same time, such a layer is removed by sliding. The wear rate is determined by the relative growth rate and the removal of the reaction layers [27].

2.4.2 Methods for wear investigations

There are countless influencing parameters when determining the wear properties or wear resistance, which makes the evaluation of wear a demanding task [28]. Scientists investigating wear properties use different approaches and testing rigs, depending on the goal of the investigation; unidirectional ball-on-disk test, twin disc test-rigs, reciprocating ball-on-disk test, high-temperature continuous abrasion test (HT-CAT), high-temperature cyclic impact/abrasion test (HTCIAT)…[29–34]. Emphasis in tribotesting must be given to the mechanical properties and contact area of the two tested solids. In model testing (i.e., pin (ball)-on-plate) the applied load is related to the so-called Hertzian contact pressure. The German physicist Heinrich Hertz described elastic deformation when a spherically shaped body with a load L comes in a contact with a flat surface, which is deformed to create a contact zone of radius a (Figure 10) [35]. Also, at the microscopic level, the contacting surfaces are not completely flat, but show ridges and valleys, asperities, and depressions. The real contact area between two solids consists of touching the top of the asperities and hence it is typically a small fraction of the apparent contact area [36].

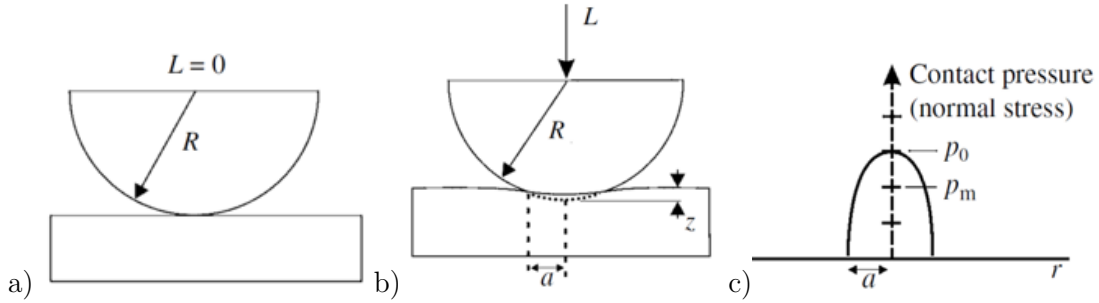

Figure 10: Sphere on flat contact geometry; a) no load, b) load = L and c) distribution of contact pressure across the contact zone [35].

The characterization and determination of wear after the test can be most easily done by measuring the wear by the weight loss. The sample is weighted before and after the test and the volume loss can be calculated. However, more reliable and one of the most widely used methods for the measurement of material loss is a measurement of the wear volume using a 3D confocal microscope. Based on the wear-volume measurement the wear rate is obtained by dividing the volume loss by the sliding distance:

$$\text{wear rate} = \frac{W_s}{s}\ [\text{mm}^3/\text{m}] \tag{2}$$

Wear is also often expressed in terms of specific wear rate, dividing the upper equation by the load applied:

$$\text{specific wear rate} = \frac{W_s}{F_n\, s}\ [\text{mm}^3/\text{Nm}] \tag{3}$$

where W_s is the wear volume, F_n is the applied load and s is the sliding distance.

Phases that are present on worn surfaces can be identified from X-ray diffraction (XRD) measurements. For the investigation of the microstructure below the worn surfaces, scanning electron microscopes (SEM) with electron X-ray dispersive spectroscopy (EDS) and electron backscattered diffraction (EBSD) techniques are used. To obtain a good insight into the wear behaviour and wear mechanism, the microstructures within the wear tracks are analysed from different view points, including top and cross-sectional views of the wear track. Focused ion beam (FIB) techniques are also applied for SEM and transmission electron microscope (TEM) analyses of the worn surfaces [37–40]. SEM, EBSD and FIB/SEM analyses were found to give a consistent view of the subsurface deformation and behaviour taking place during wear, as reported by [37]. However, in this particular case, the tribo-corrosion behaviour of a 304 L stainless steel/alumina contact was the main focus of the investigation.

Sliding wear damage to the subsurface layer, which undergoes severe plastic deformation, leading to nanograin formation with a distinct crystallographic orientation was studied by Cai et al. [41]. In this study the technique of orientation-imaging microscopy was employed using an SEM equipped with a HKL Technology EBSD system. The sliding wear tests conducted on bronze and Ni showed that the microstructure beneath the wear scar consists of a deformed bulk zone and a severely plastically deformed layer of nanograins, as presented in Figure 11 [41]. The local crystallographic directions of the sliding direction (SD) are colour-coded according to the inset. There have also been studies focused on the cross-sectional observation of the wear tracks for wear tests performed on different types of steel [21, 29].

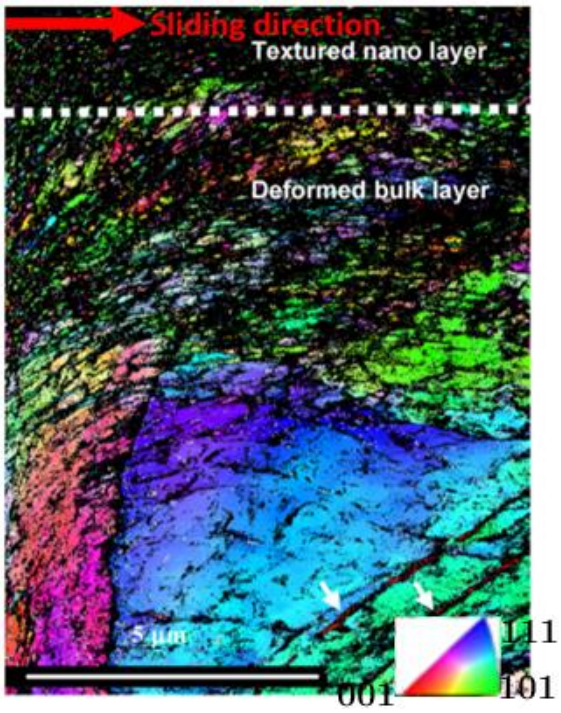

Figure 11: Orientation imaging map for spinodally hardened bronze, worn at room temperature [41].

2.4.3 Friction

Friction is defined as the resistance to movement of one body over another. It is the dissipation of energy between sliding bodies. It depends on the contact conditions, the surface roughness, the presence or absence of oxides or adsorbed films, etc. The tangential friction force is proportional to the normal force in sliding. The proportionality between the friction force and the normal load has led to the definition of "kinetic" and "static" coefficients of friction (COFs). In the literature, COFs are very simplistically quoted as "properties" of certain combinations of materials. However, COFs are dependent on many parameters such as temperature and sliding speed and in some instances, there is no exact proportionality between the friction force and the normal load. Much of the characteristics of friction are a result of the properties of rough surfaces in contact. A basic feature of a sliding contact is that it is distributed over a lesser number of larger contact areas rather than a large number of contact points. It appears that the contact between dry-sliding surfaces, e.g., during oxidative wear or fretting, is controlled by a series of lamellar bodies (compacted wear particles) that are formed from material from both sliding surfaces. These areas do not have a fixed location inside the contact but instead move slowly across the surface as sliding progresses. The frictional interaction appears to be controlled by mechanical inter-locking between "lumps" on opposing surfaces [25]. In general, the contribution to the friction force comes from two mechanisms. Junctions of the tips of the asperities on a very local scale between the two materials in relative contact (cold welding) and ploughing of the broken asperities and wear particles trapped between the sliding surfaces [36]. The frictional force can be expressed as:

$$F_f = \mu N \ [\mathrm{N}] \tag{4}$$

where F_f is the frictional force, μ is the static (μ_s) or kinetic (μ_k) frictional coefficient and N is the normal force between the surfaces [N].

2.5 Wear of Tooling Materials

In many industrial applications of tool steels, the main reason for tool failure is considered to be wear of the tool. Wear is affected by different kinds of loadings the tools are exposed to during operation. Tool-steel wear is greatly dependent on the content of the alloying elements determining the microstructure of the tool steel and the fraction of wear-resistant carbides in the matrix. It has been shown that for steels, pearlite and bainite do not exhibit such good wear resistance as a martensitic microstructure with carbides [2]. As hard particles in the microstructure, carbides dictate the wear resistance [13]. Additionally, a greater influence on the abrasive wear comes from the hardness of the martensite rather than its volume fraction [42, 43].

Furthermore, the wear behaviour and wear resistance of the tooling material, i.e., tool steel, is largely related to the tempering conditions as well as to the prevailing wear mechanism [2]. Several papers can be found on the effect of heat-treatment regimes on the hardness and wear behaviour of tool steels, which will be discussed in the following chapters regarding cold- or hot-work tool steels [2, 26, 44, 45].

The properties of the material, like hardness and toughness, are the two main parameters that have already been correlated with the wear of the material. In this way, abrasive wear can be minimized substantially. The Archard model for adhesive and abrasive wear has for decades been the widely accepted equation, which for instance, combines hardness and applied external load during the wear testing:

$$Q = \frac{KF_n}{H} \tag{5}$$

Q is a total volume removed per unit sliding, F_n is total applied normal load, H is the indentation hardness of wearing material and K wear constant.

There are, however, modified models that more precisely define the abrasive wear of the specific material of interest (for brittle materials, composite materials, etc.), also taking into account other material properties, such as fracture toughness, carbide size, carbide volume fraction, etc. [28]. Materials' abrasive wear that exhibits more brittle behaviour, has been described in more detail, taking fracture toughness and elastic modulus into consideration. The abrasive wear model based on lateral cracking and describing the volume wear rate per unit sliding distance Q due to all the particles involved is

$$Q = \alpha_3 \mathrm{N} \frac{(E/H)F^{9/8}}{K_c^{1/2}H^{5/8}} \tag{6}$$

where α_3 is a material-independent constant, N is the number of particles each carrying load F and E is the elastic (Young's) modulus. K_C is the fracture toughness of the material. In another approach, the volume wear rate per unit sliding distance is

$$Q = \alpha_4 \mathrm{N} \frac{F^{5/4}}{K_c^{3/4}H^{1/2}} \tag{7}$$

where α_4 is a constant [46].

The hardness of tool steels is mainly affected by two mechanisms: solid-solution hardening of the martensite (elements dissolved that in general contribute to a hardness increase are carbon, chromium and molybdenum) and by carbides present in the martensite matrix (undissolved and precipitated carbides during tempering) [47]. However, the hardness, fracture toughness and especially the wear resistance of carbides in Fe-based alloys are not well defined yet and described in the literature. Same types of carbides can be found in different Fe-based alloys, but the composition, shape and properties can differ significantly from carbides found in different steel types.

Traditionally, the wear of tool steel is altered and overcome with increasing tool hardness, which leads to a decrease in toughness of the material. However, in some cases of the combined action of abrasion and impact, the brittle nature of the martensite microstructure can often lead to less performance compared to a lower relative hardness, but better ductility [48]. This issue is being addressed by optimizing the hardness-toughness relationship through accurate microstructure design [13].

Studies were made on different tool steels (cold- and hot-work steels) investigating their wear behaviour in various heat-treated conditions. Wear processes and mechanisms that are taking place on the tool surfaces are being quite extensively investigated. Observations of wear tracks created on different types of tool steels subjected to different heat-treatment conditions using various testing equipment and tribological test parameters were performed, aiming at an insight into the microstructure behaviour in the wear-track area [2, 21, 26, 29, 37, 40, 44, 49–56]. Studies were made on the influence of carbide particles on the wear behaviour in different tool steels. The decreasing effect on wear and the

superior wear resistance contribution of the alloy carbides, especially from MC-type carbides, in comparison to iron carbides were observed by Kasak and Neuymeyer [49].

In the industrial processing of aluminium and its alloys, the tools exhibit a strong work material adhesion and material transfer. This mainly occurs on the tool's surface irregularities, like scratches and protruding carbides, which additionally leads to material build-up [57].

A schematic representation of the wear mechanism for a microstructure with a different distribution and size of carbides is shown in Figure 12. Small carbides with a fine distribution are not as abrasion resistant as larger carbides with a non-uniform distribution. The proper size and homogenous distribution show the best abrasion resistance [47].

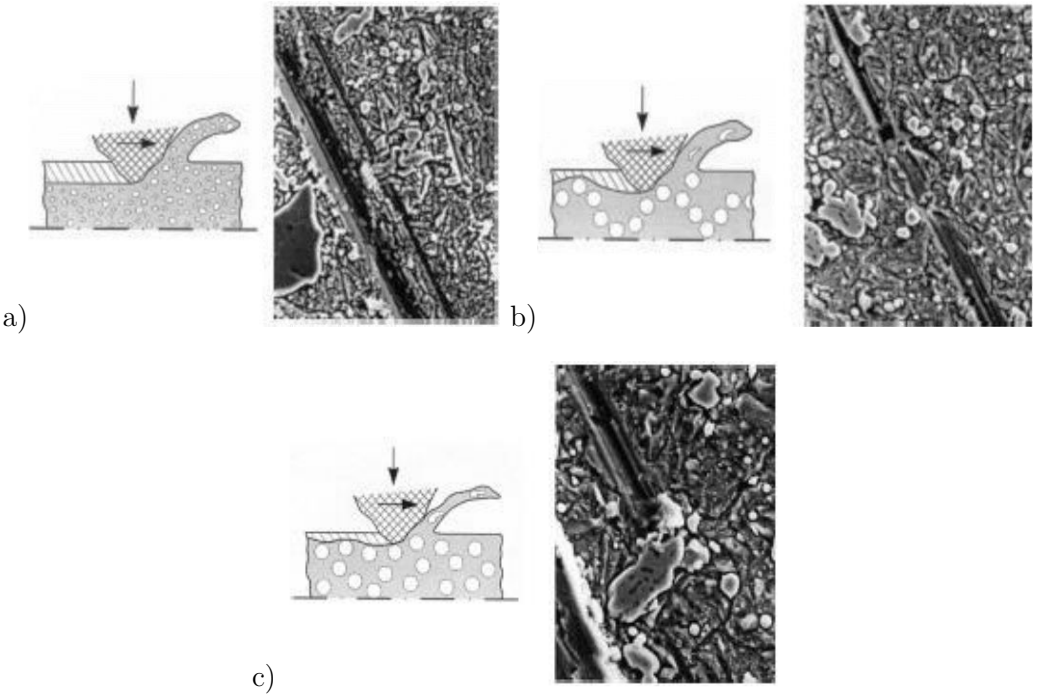

Figure 12: Wear behaviour influenced by the carbide size and distribution; a) fine homogeneous distributed carbides, b) network of bigger carbides and c) homogenous dispersion of bigger carbides [47].

The carbides present in the matrix play an important role in the mechanical response of the tool steel [13]. Furthermore, as a micro constituent of the microstructure, carbide wear and fracture resistance influence the tool's performance. The mechanical performance of carbides, i.e., the hardness and fracture toughness, were studied by some authors regarding tool steels [13, 58].

The tribological properties can be influenced by many factors that affect the wear behaviour of the material. For example, wear can be qualitatively correlated by the hardness of the material at room temperature, meaning that the softer the material, the higher the wear losses [46]. On the other hand, various experimental observations suggest that hardness is not always the key factor that affects the wear resistance. The brittle nature of the martensite microstructure can often lead to less performance compared to a lower relative hardness, but better ductility. This is especially the case under the combined action of the abrasion and impact [48].

When dealing with hot-work tool steels and high-temperature operations, the formation of oxide tribolayers controls the overall wear behaviour by preventing the metal-to-metal contact [29].

2.5.1 Hot-work tool-steel wear

Hot-work tool-steel wear is, among other stresses, also usually greatly influenced by thermal loading. During operations, such tools are exposed to different loads and stresses like heat, pressure, corrosion and the sliding of work material, which result in thermal, mechanical and tribological loadings. In the highly loaded tool-steel applications like hot forging and extrusion, the abrasive wear is the dominant wear mechanism responsible for about 70 % of the tool breakdowns. However, adhesive wear and galling are also two very important mechanisms that have to be considered [55]. The predominant wear mechanism determines the wear behaviour under a given condition [26].

Another thermally and mechanically loaded application of hot-work tool steels is the hot-stamping process, where the wear of the tool is likely to occur [59]. In the study of Schwingenschlögl et al. [60] where the basic friction and wear mechanisms within hot stamping were investigated, they were comparing commonly used hot-work tool steel Mat. No. 1.2367 and the newly developed special hot-work tool steel Mat. No. 1.2383, with increased thermal conductivity. The difference was in the alloying elements, as among the wear resistance in hot stamping an important parameter of the tool is also its thermal conductivity. Therefore, in order to balance the wear resistance, hardenability and thermal conductivity, the composition of the Mat. No. 1.2383 was altered, reducing the chromium and molybdenum contents, and increasing some other elements (V, Ni, Mn) [61]. Chemical-composition variation results in microstructural differences and affects the type of precipitated carbides. The investigation showed that a hardness increase improves the tool steel's adhesive wear resistance, obtained by decreasing the elastic deformation of asperities on the tool surface. On the other hand, as the main friction mechanisms in hot-stamping material transfer, ploughing and asperities flattening were identified [60].

In the study of Telasang et al. [50] where laser-surface-engineered (hardening and melting) AISI H13 hot-work tool steel was investigated, pits were observed in the wear tracks that could be caused by the removal of fine carbides during wear. Large carbides can be exposed to partial fragmentation and removal from the surface if contact surfaces are exposed to very high loads. The pits can then be the starting points for the formation of micro-cracks. Also hard and brittle martensite with a large number of defects can be exposed to local tempering if subjected to a high load wear, resulting in high contact temperatures [50].

As stated before, wear can be qualitatively correlated with the hardness of the material at room temperature. However, at elevated temperatures, various experimental observations suggest that hardness is not always the key factor [46, 48]. In high-temperature applications the formation of oxide tribolayers is very common, which are controlling the overall wear behaviour by preventing the metal-to-metal contact [29]. However, high temperatures in combination with high loads can be detrimental. Softening of the substrate leads to insufficient tribolayer support and when combined with high contact stresses breaking up and spalling of the tribolayer may occur [62].

In general, at high temperatures there is a higher oxidation rate and thus an increase in the oxide scale thickness, which directly influences the tribological behaviour of the contact surfaces [63]. When two oxidized surfaces are in sliding contact the thickness, the nature, the adherence to the substrate and hardness of the oxide layers affect the wear rate and the generated coefficient of friction (COF). An abrasion wear mechanism with a high COF will be predominant if the oxide particles are hard and loose. However, if they are compacted in the contact and the formation of a glazed layer takes place, then the adhesion mechanism and a low COF will prevail [30]. Also under high temperature conditions, the wear mechanism is influenced by the sliding speed. At low sliding speeds it leads to an

easier formation of thicker and wear-resistant oxide scales, as compared to higher sliding speeds [64].

In the study by Wei et al. [2] on chromium hot-work tool steel AISI H13 it was found that the material wear mechanism and wear resistance are closely correlated with the tempering conditions. In the dry sliding adhesive wear of AISI H13 steel, the specimens tempered at 600, 200 and 440 °C presented higher wear resistance than the ones tempered at 500, 650 and 700 °C [2]. Wear mechanisms depend on the strength and fracture resistance as well as on the thermal stability, which is especially important for the elevated-temperature wear resistance [2]. The effect of tempering time on the hardness and wear rate of hot-work tool steel H13 was investigated by Bahrami et al. [26]. The worn surfaces of tempered AISI H13 tool steel were found to be covered with oxides, distributed between individual asperities. Furthermore, the work hardening of subsurface layers was observed and the possibility of the in-situ surface tempering phenomena was proposed [26].

Increasing the load in the wear tests conducted by Telasang et al. [50] on a quenched and tempered (46-48 HRC) hot-work tool steel AISI H13 resulted in a significant wear-track increase due to the excessive plastic deformation and the fracture of the edges of the wear track. In the case of the 5 % chromium martensitic hot-work tool steel, plastic deformation parallel to the direction of friction was observed in the microstructure directly below the wear track. The initial orientation of the tempered martensitic laths was found to influence the plastic deformation [21].

2.5.2 Cold-work tool-steel wear

Different investigations have been made regarding one of the most widely used cold-work tool steels, with the designation of AISI D2 or Mat. No. 1.2379.

In the study by Singh et al. [44] they investigated how the microstructure and abrasive wear of D2 steel is affected by multiple tempering heat treatments. With increasing tempering temperature during multiple tempering, coarsening of the carbides occurs, resulting in a lower abrasive wear resistance of the tempered D2 steel. The highest abrasive wear resistance is shown by an as-quenched sample, due to martensitic microstructure with fine carbides.

Some cold-work tool steels are medium or highly alloyed, having increased carbon and chromium content. Their wear resistance is therefore greatly improved with carbide-forming elements present.

Casellas et al. [13] evaluated the hardness and fracture toughness of different types of carbides in different steel types, including AISI D2 cold-work tool steel. In this type of tool steel, only one type of eutectic (primary) carbides is present. Those carbides (M_7C_3) rich in chromium, showed great dependence of fracture toughness values on the carbide orientation. Their fracture resistance is highly anisotropic [13]. The hardness of the eutectic M_7C_3 carbides in AISI D2 tool steel measured with nano-indenter in the study by Casellas et al. [13] was ranging from roughly 15 to 20 GPa.

Wear behaviour of the hardened AISI D2 cold-work tool steel against martensitic carbon steel during dry sliding and increasing sliding speed (in the range 281–409 mm/s) was studied by Gaard et al. [65]. Severe adhesive wear component was found to be increasing with increasing sliding speed.

The impact of the tool steel's microstructure on the friction and initial material transfer was investigated by Karlsson et al. [66]. A slider-on-flat surface tribometer was used. They found that the initial material transfer and coefficient of friction increased at lower loads and was enhanced by the proof strength and ductility of the tool material at higher loads. Such a trend was suggested because of the increase of the surface temperatures caused by a frictional heating [65]. Increased testing temperatures (of the bulk specimens) in the

laboratory wear test are normally used to replicate surface temperatures occurring due to frictional heating. However, differing conclusions have been made regarding wear behaviour when sliding speed and bulk temperatures are increased independently [65, 67]. Okonowo et al. [68] wanted to clarify the different conclusions of other authors and studied the effect of sliding speed on the wear of steel tool-steel pairs in two different scenarios: controlling the testing temperature of a bulk specimen at low-speed sliding conditions and controlling the sliding speed to achieve the same surface temperature as in the first case [68]. In the testing conditions that are relevant for AISI D2 tool steel/mild steel pairs they showed that the dominant wear mechanism is adhesive wear for all sliding speeds used and the largest adhesion was occurring at the slowest sliding speeds. At low sliding speeds and low-temperature conditions, the amount of transfer layer on the tool-steel surface decreases with increasing sliding speed and increasing bulk temperature [68]. However, increasing sliding speed to replicate the bulk temperature conditions may not result in equivalent wear rates or wear mechanisms.

In the automotive industry chromium cold-work tool steels, like AISI A2 and AISI D2, that are alloyed also with molybdenum and vanadium, are used where more demanding operations are performed. It is of great interest to tribologically evaluate conventional tool steels and find its full potential, as more exclusive materials are much more expensive [69]. The study by Kirkhorn et al. [69] was focused on an investigation of different tooling materials that are in use in sheet-metal forming to correlate the frictional outcome with the microstructure. The initial frictional conditions of a tool/sheet system were explored. However, although they conducted tests on eight different cold-work tool-steel materials, having extremely diverse microstructures and amounts of carbides, a direct correlation between the amount of carbides and the coefficient of friction could not be clearly seen [69].

2.5.3 Wear of other materials

The wear of other materials that are used in different applications is also being extensively investigated, with the aim to improve and prolong components' life times. Those are, for example, different high-speed steels (HSS), steels for excavator teeth and agricultural components, steels for cold-work rolls, rail-road steels, composites with a matrix based on HSS, copper materials, etc. Therefore, for a full understanding of tool steels' wear and the effect of the microstructure, literature reviews of other materials are also important.

In the study by Guo et al. [56] an investigation of the micro-mechanical properties and micro-wear behaviour of secondary carbides in Fe-Cr-W-Mo-V-C alloy was presented. The alloy is used for cold-work rolling in the cold rolling mill and is exposed to high forces during application. The highest hardness and elastic modulus for secondary carbides measured by nano-indentation was found for MC-type carbides. A single-pass scratch test also revealed the appearance of parallel trans-granular cracks within the carbides perpendicular to the sliding direction. Cracks propagate through the whole carbide, but do not propagate into the matrix. Micro-cutting is the main wear mechanism of the secondary carbides. The wear mechanism of secondary carbides was proposed and is schematically shown in Figure 13. Due to the cutting force (FT), transverse surface cracks on the carbides within the groove perpendicular to the sliding direction can be formed (upper scheme). Under the action of a normal force FN, internal centre cracks parallel to the surface of the specimen will be generated inside the carbides. When the pulling force is large enough the carbide is detached from matrix. The scheme in Figure 13 shows the mechanism when the carbide is loacted on the edge of the scratch [56].

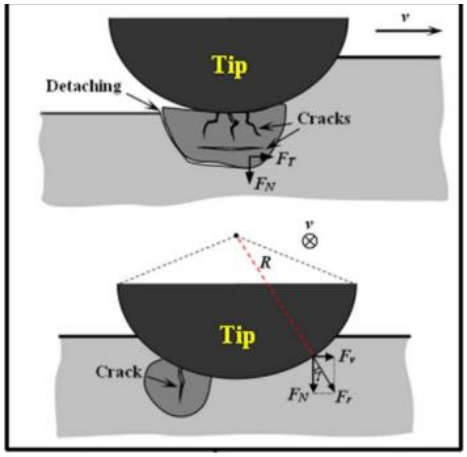

Figure 13: Illustration of wear mechanism of secondary carbides investigated in alloy Fe-Cr-W-Mo-V-C [56].

In another study performed by Badisch and Mitterer [70], the effect of microstructure on the abrasive wear was investigated. The martensitic matrix of high-speed steels with different volume fractions of primary carbides was exposed to different abrasives (SiC, Al_2O_3, ZrO_2). It was shown that the hardness of the abrasive material in relation to primary carbides plays an important role in determining the wear rates. If the abrasive particles are harder than the primary carbides, the mechanical properties of the matrix like hardness and ductility play a dominating role [71]. Carbides in the metal matrix can increase the abrasive wear resistance up to four times compared to the corresponding carbide-free steel. At approximately 30 % volume fraction of carbides, the maximum abrasive wear resistance is achieved. Above that the brittleness appears to cause a reduction in the wear resistance [7].

Fontalvo et al. [72] investigated the adhesive wear behaviour of six model alloys based on HSS AISI M4 steel with the focus on the two requirements for the steels under study: the martensitic matrix after heat treatment should be approximately the same and the carbide content varied from 0 to 25 mol. %, with all the primary carbides being of MC-type. They concluded that adhesive wear is determined by two parameters: carbide content and distance between carbides. Adhesive wear was reduced by increasing the carbide content and decreasing the distance between the carbides. This might be achieved by increasing the number of carbides without changing their size or maintaining the same number of carbides and increasing the size of the carbides [72].

In the study of García et al. [73] the wear behaviour of composites processed by MIM (metal injection moulding) was investigated. Metal-matrix composites based on an AISI M2 high-speed steel matrix reinforced with different proportions of VC were fabricated. Specimens with the same microstructure were produced, once with MIM and other time with powder metallurgy (PM) technique, in order to assess the quality and the performance of the specimens obtained via the MIM method. Unreinforced and reinforced specimens with 3, 6 and 10 wt. % of VC carbides were prepared and compared. In both cases the tendency for better wear resistance was towards composite materials with the addition of carbides. In general, the composites processed by MIM displayed denser and more homogeneous microstructure, which provided better wear behaviour compared to conventional PM production. However, in both cases the minimum wear rates were observed for samples with 6 wt. % of VC carbides, especially when tested under high loads. Deterioration of wear resistance at a higher VC content (specimens with 10 wt. % of VC) was explained by the fact that the addition of a large amount of reinforcement VC carbides creates larger precipitates at the grain boundary with lower adhesion to the matrix. These

sites could be easily fractured and create a third-body effect on the friction and wear, explaining the higher wear rate and the COF [73].

A study conducted by Yin et al. [74] on 20CrNi2Mo steel with a martensite microstructure (material for excavator teeth and agricultural components) was focused on an examination of the microstructure underneath the contact surface after a dry sliding test [74]. Plastic deformation and large strains underneath the surface induced as a result of wear were found to lead to structural evolution events like recrystallization, cold working and grain refinement [74–76]. As shown in Figure 14, non-affected martensite laths are present far away from the wear-induced layer, slightly bent martensite laths in the plastic deformed layer and severe plastic deformed layer, where nano-laminated martensite is elongated and fragmented parallel to the sliding direction [74]. Some of the new technologies like surface mechanical grinding and friction-wear-induced severe plastic deformation are using this to form subsurface nanostructures. Gradient nanograin structures can improve the friction performance and the strength of materials [77].

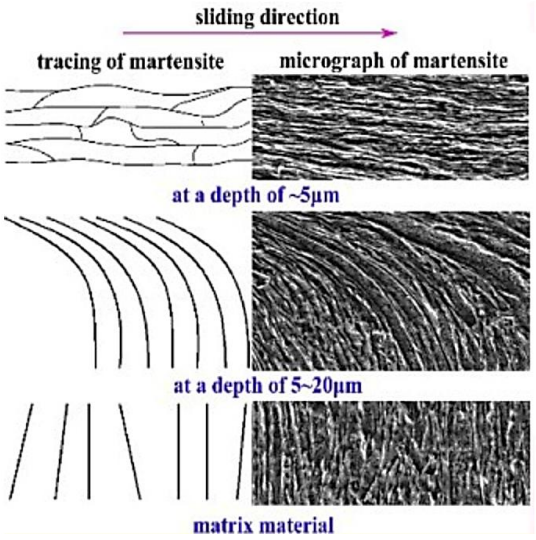

Figure 14: Microstructure evolution and subsurface layer of 20CrNi2Mo steel after dry sliding wear test [74].

The wear behaviour of different steels with the same hardness was compared in the study of Zambrano et al. [78]. The aim was to determine whether the steels of similar hardness, but different microstructures and compositions, exhibit the same sliding-wear behaviour under lubricated conditions. The steels used are meant for a wide range of applications: AISI 5610 (springs and forgings), AISI 1045 (medium carbon steel for forgings) and AISI O1 (high speed steel). The investigated steels had microstructures of pearlite, ferrite and perlite, and a ferrite matrix with globular cementite. The fully pearlitic microstructure showed the best wear resistance, while the worst was displayed by the steel with globular cementite in a ferritic matrix [78]. On the other hand, the affected area under the wear scar was very narrow for the fully perlite structure, as well for the structure of globular cementite in the ferritic matrix, but relatively broad for the ferrite and pearlite structure. In this case microconstituents of the microstructure are oriented in the sliding direction [78]. Great importance is also given to the wear behaviour and correlations with the mechanical properties of pearlitic and bainitic steels, used for rail roads. In a study by Alwahdi et al.[79], the depth of the shear deformation beneath the worn surface of used rail-road steel was examined. As shown in Figure 15, strain hardening is at a maximum at

the surface of the rails and then decreases in a non-linear trend. The surface hardness reaches a value ≈ 1.8 times that of the bulk material (up to 400 HV 0.01) for all pearlitic rail steels examined. The work hardened zone was almost 200 µm thick.

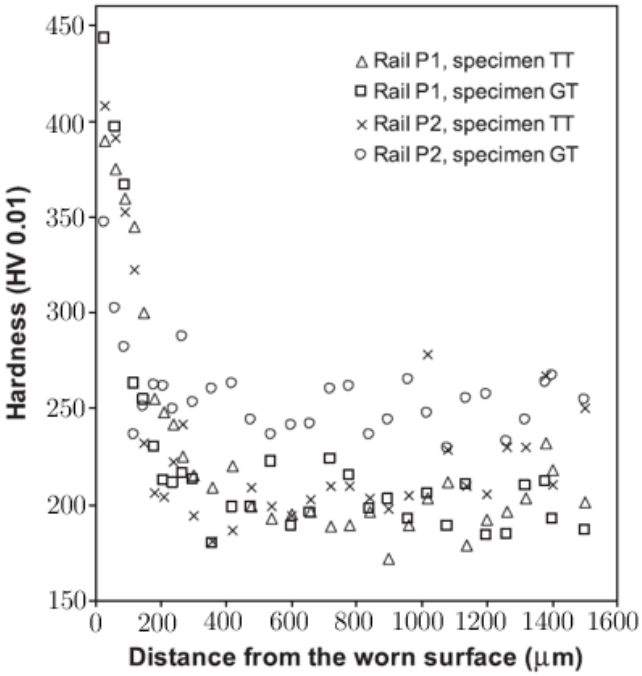

Figure 15: Rails' hardness variation with depth from worn surface [79].

Cai et al. [80] investigated the effect of an annealing treatment and grain size on the dry-sliding wear behaviour of copper. It was confirmed that grain size is an indicator of the material strength and wear resistance [81]. Microstructure observations of sub-surface layers showed dynamic recrystallization and abnormal grain growth when high-load testing was applied. At low loads the grain refinement took place under the contact area [80].

Chapter 3

Aims and Hypothesis

3.1 Aims

The aim of this doctoral study was to find correlations between the tribological behaviour and the microstructural characteristics of tool steel. This doctoral thesis was focused on the wear behaviour of the cold- as well hot-work tool steels at room and elevated temperatures. The mechanisms that are occurring during the wear process on the surface and subsurface of the material and how the wear affects the contacting microstructure of tool steel with the counter body were investigated. The research work was focused on the different microstructures and hardness values of different tool-steel compositions. The variations in the chemical compositions results in different volume fractions, types and sizes of hard particles in the matrix microstructure, i.e., carbides/carbo-nitrides. The aim was to thoroughly investigate and describe the effect of their type, size and density of distribution in the matrix on the tribological properties, as well to find experiments that will describe their movement during the initial stages of wear and after longer exposure to a counter-body during relative motion.

Furthermore, tool steels are used in everyday life in a hardened condition exhibiting high hardness. Therefore, our work also included heat-treatment regimes, to obtain tool steels with the same hardness level. The microstructure constituents were then tribologically described and also correlated with the other very important mechanical property of tool steel, i.e., fracture toughness.

When dealing with tool steels, an important role prior to the tool's application is played by the heat-treatment regime, which affects final mechanical properties of the tool steel. Therefore, one part of this doctoral thesis was also focused on the variations of the heat treatment of one of the investigated tool steel in extreme regimes, where other mechanical properties, like impact toughness and tensile strength, were also tested.

In addition, as hot-work tool steels operate at elevated temperatures, the mechanical and tribological testing was also performed at elevated temperatures.

In order to accomplish the aims, the following goals have been established:

- Choosing appropriate tool steels with different chemical compositions for achieving different volume fractions and types of carbides in the matrix.
- Determination of the microstructure constituents in chosen tool steels using thermodynamic calculations with ThermoCalc software.
- Heat treatment of different tool steels with the aim of achieving similar hardness levels (3–5 groups of different hardness levels).
- Investigation of type, size, distribution and volume fraction of hard carbide particles in the selected tool steels.
- Determination of the mechanical properties in terms of fracture toughness and hardness of the selected tool steels.
- Wear-resistance determination of selected tool steels and defining the appropriate tribological tests for descriptions of the microstructure and carbide phases present during wear.

3.2 Hypothesis

The thesis of the doctoral dissertation is that the mere hardness of the tool steel, used in practice to determine the wear resistance, is not sufficient. With a knowledge of the influence of individual microstructure components on the wear behaviour, an improvement in the tribological properties of the contacting materials can be foreseen and predicted. Systematic planning of the microstructure with improved wear properties is possible with advanced knowledge of the individual components of the microstructure, such as the size, the type, the volume fraction of carbides, the mechanical properties of matrix and how these components influence the wear behaviour. Based on this, the following hypothesis were set:

- Determining correlations between microstructure, mechanical properties and tribological behaviour of tool steels will be a major step forward in understanding the influence of microstructure and its constituents on wear.
- Better wear resistance is achieved with the material with the preferred type and volume fraction of carbides when compared to a material with the same hardness but different volume fraction and type of carbides.
- The orientation of the large carbides' distribution influences the material's wear resistance.
- The initial wear behaviour of the material is influenced by the size and fraction of the microstructure constituents.
- Less wear is observed when wear debris are removed from the wear contact.
- Inappropriate heat treatment of the material, resulting in an improper microstructure, leads to lower wear resistance and worse mechanical properties, regardless of the hardness level obtained.
- Beside hardness, fracture toughness is an important property of the material, determining its wear resistance.

Chapter 4

Materials and Methods

4.1 Material

In order to achieve the set goals, tool steels with different chemical compositions were chosen. This provided us with microstructures having different volume fractions and types of carbides in the matrix. The chosen tool steels fall into the chromium group of cold- or hot-work tool steels. In general, the biggest difference in the materials is in increasing the carbon and chromium contents influencing the fraction and size of large eutectic carbides (M_7C_3) as well the secondary $M_{23}C_6$. Other elements' variation is also present, providing the presence of other carbide types (MC). Typically, the higher the carbide-forming alloy element's content and the higher the carbon content, the higher the alloy-carbide content and the hardness of a tool steel. A description of the tool steels selected with increasing alloying elements is given in the following subchapters.

4.1.1 Hot-work tool steel

Mat. No. 1.2367 mod. or AISI H11 mod. is primarily used as a material for tools in the process of die casting of light metals and alloys. However, because of its good toughness it is also often used for highly stressed hot-work structural parts. It can also be used for die forging and extrusion tool applications. It is a commercially available AISI H11 hot-work tool steel with a modified composition. It has lower content of Si and Mo, and slightly increased V content. It also has added Ni, which increases hardenability and often improves toughness and ductility. These types of steels are usually tempered at temperatures above 500 °C to achieve their optimal mechanical properties in terms of hardness and toughness. Typical working hardness for hot-work applications is 45 to 48 HRC [45]. The amount of carbon content in this steel is more than half lower compared to cold-work tool steels used in this work. This is not sufficient for the formation of large eutectic carbides. It was chosen due to the mainly martensitic microstructure obtained after the hardening heat treatment with a low carbide fraction. The material was delivered in a shape of hot-forged plates in a soft-annealed condition. Its chemical composition is given in Table 4.

Table 4: Chemical composition of investigated hot-work tool steel in wt. %.

Element	%C	%Si	%Mn	%S	%Cr	%Ni	%Mo	%V	Base
Mat. No. 1.2367 mod	0.36	0.30	0.50	<0.005	4.9	1.51	1.7	0.66	Fe

4.1.2 Cold-work tool steels

Mat. No. 1.2363 or AISI A2 cold-work tool steel is used for a broad spectrum of applications, ranging from cold forming, deep drawing, circular, straight and trimmer shears, to even some hot-working tasks like die casting [82]. It is, for the most part, the

most popular grade of tool steel in the United States today. It is a very good, relatively easy machining tool steel. It shows high dimensional stability after heat treatment. It gets wear resistance from increased carbon and chromium content (5%), resulting in the presence of eutectic carbides as well other carbide types in the microstructure after heat-treatment. Typical hardness for applications is between 57–62 HRC. The material was delivered in the shape of hot-forged plates in a soft-annealed condition.

Mat. No. 1.2990 can be used in applications like cutting and punching tools including precision cutting tools, threading dies and rolls, rotary shear blades, cold pilger mandrels, pressure pads and plastic moulds, cold-forming and deep-drawing dies, woodworking tools and cold rolls. It is a ledeburitic cold-work steel with high hardness, good toughness and high tempering resistance combined with high wear resistance.

Due to the development of material that is being processed and shaped using tool steels and increasing its strength, the demands for tool-steel properties are also increasing. Deformation stresses are increasing, with which conventional tool steels performance in terms of toughness more than wear resistance, is the reason for tool failure [83]. Therefore, the development of modified Mat. No. 1.2379 cold-work tool steels is pursued. One of such is the steel type Mat. No. 1.2990 with a decreased volume fraction of eutectic carbides, which however strongly influence the steel's wear resistance. This has been compensated by steel enrichment with strong carbide-forming elements and a complementary contribution of the MC-type carbides in the matrix [83]. The tool steel material was delivered in a soft-annealed condition in the shape of a plate cut from a hot-rolled ingot.

Mat. No. 1.2379 or AISI D2 cold-work tool steel is commonly used for punching tools, cold extrusion, deep drawing, profile rolling, etc. [82]. It is one of the most widely used tool steels. It is an excellent air-hardening, highly wear-resistant tool steel. It is difficult to work and grind due to the high chromium content (12%) combined with the higher carbon amount. It is also a highly stable ledeburitic steel, with an option of tempering on the secondary hardening peak. It is usually tempered at a hardness level ranging from 55 to 62 HRC. Delivered in the shape of hot-forged as well hot-rolled plates in a soft-annealed condition. Chemical compositions of the cold-work tool steels used are presented in Table 5.

Table 5: Chemical composition of investigated cold-work tool steels in wt. %.

Element	%C	%Si	%Mn	%S	%Cr	%Ni	%Mo	%V	Base
Mat. No. 1.2363	1.00	0.25	0.48	0.008	5.00	/	1.0	0.2	Fe
Mat. No. 1.2990	0.95	0.26	0.74	<0.002	7.9	/	1.7	1.8	
Mat. No. 1.2379	1.41	0.35	0.20	0.006	11.1	/	0.76	0.85	

4.2 Heat Treatment

4.2.1 Dilatometry

Dilatometry is a technique that enables the determination of a wide variety of properties like linear thermal expansion, coefficient of thermal expansion, sintering temperature, shrinkage steps, phase transitions, density change, softening point and decomposition temperature, anisotropic behaviour, and glass-transition temperature. The equipment is very sensitive and precise in measuring the dimensional changes of a material as a function of time and can be used for the simulation of different heat-treatment conditions before going on a larger scale. A wide range of materials can be tested using dilatometry such as traditional and advanced ceramics, glasses, metals, and polymers. Dilatometry experiments were first conducted at different austenitizing temperatures for the hot-work tool steel used in this work, in order to see changes in the microstructure (dissolution of residual carbides and grain size increases) and hardness with respect to the austenitizing temperature. The austenitization temperatures were from 950 °C to 1150 °C with increments of 20 °C. The austenitization time was 15 min and the cooling speed was 10 K/s. The experiments on the investigated hot-work tool steel material were conducted with the dilatometer type DIL805 A/D using standard test specimens [84].

4.2.2 Effect of heat-treatment parameters

The heat treatment (HT) of tool-steel test specimens machined from forged or rolled plates was conducted in horizontal vacuum furnace Ipsen VTC – 324-R with high-pressure gas quenching using nitrogen gas. A high vacuum (10^{-3}–10^{-4} mbar) that is created in a vacuum furnace is sufficient to produce bright metallic surfaces on most steels after the heat-treatment process. The use of a vacuum heat treatment also substantially reduces the impact of the environmental pollution [85].

In the first phase, the microstructure represented by mainly tempered martensitic matrix was altered, to see how the matrix properties influence the wear as well other mechanical properties (hardness, tensile properties, impact toughness). For this, a hot-work tool steel was used, exhibiting a low carbide fraction. Furthermore, in this case, residual carbides could be almost completely dissolved at higher austenitization temperatures, which could not have been done for the used cold-work tool steels, having eutectic carbides. For the complete dissolution of such carbides we would have to enter the liquid region, as such carbides form during solidification. Three sets of hot-work tool-steel specimens (1.2367 mod.) were prepared, austenitized at different temperatures, i.e., 950 °C, 1030 °C and 1150 °C. A low austenitization temperature of 950 °C was considered to achieve the retarded dissolution of residual carbides, 1030 °C as the conventional austenitization temperature for this type of hot-work tool steel and 1150 °C, where almost complete dissolution of pro-eutectoid carbides (carbo-nitrides) should take place. This steel, without coarse eutectic carbides, consisting of mainly tempered martensitic microstructure after HT, was a subject of unconventional austenitization to pursue the material's response in terms of mechanical properties and wear.

From the last preheat sequence at 850 °C the specimens were heated to the final austenitization temperature at a heating rate of 14 °C/min. Specimens were held at the austenitization temperature for 15 min and followed by gas quenching at a quenching speed of 3 °C/s using nitrogen gas at a pressure of 1.05 bar. A set of as-quenched specimens were, after the austenitization, taken from the furnace and used for microstructure investigation of the fraction of undissolved carbides left after austenitization. Others were subsequently

double tempered, with the first tempering performed at 500 °C. Second tempering was conducted at different temperatures, ranging from 520 °C to 640 °C with the increments of 30 °C. The tempering time for first and second temperings was 2 h at each temperature. Heat-treatment parameters aimed at determining their effect on the hot-work tool-steel microstructure and properties are listed in Table 6.

Table 6: Parameters of the heat-treatment process for the hot-work tool steel.

Mat. No. 1.2367 mod. (material A)	
T_{aus} = 950°C / 1030 °C / 1150 °C (15 min)	
1st tempering at 500 °C / 2 h	
2nd tempering (different temperatures)	
Time of tempering	Temperature
2 h	520 °C
	550 °C
	580 °C
	610 °C
	640 °C

From the described group of heat-treated hot-work tool-steel specimens those displaying similar hardness at different austenitizing temperatures were selected and labelled as presented in Table 7. This was done to enable a direct comparison and eliminate the influence of hardness on the wear. The letter P stands for tempered specimens having an assigned number, indicating the austenitization temperature (1-full dissolution of residual carbides, 2-conventional heat-treatment, 3-retarded dissolution).

Table 7: Labels of the tested hot-work tool-steel specimens with similar hardnesses achieved after different heat treatments applied.

Label	**Heat-treatment**		
	***T_{aus} /time**	***$T_{1\ temp}$ /time**	***$T_{2\ temp}$/time**
Mat. No. 1.2367 mod. (material A)			
P1	1150 °C/ 15 min	500 °C/ 2h	610 °C / 2h
P2	1030 °C/15 min		580 °C / 2h
P3	950 °C/ 15 min		520 °C / 2h

4.2.3 Recommended heat-treatment regime

The final set of specimens was heat treated according to the producers' recommendations and available tempering diagrams, conducted in the same horizontal vacuum furnace as described in the previous subchapter. These materials, as described before, were chosen to obtain variations in the carbide fraction and type in the martensitic matrix after HT.

After the last preheat (850 °C) the specimens were heated at a speed of approximately 14 °C/min to the austenitizing temperatures given in Table 9, soaked for up to 20 min and gas quenched. Specimens were quenched with nitrogen gas at different pressures of 1.05 bar or 5 bar. After quenching the specimens were immediately tempered after reaching a temperature of 65 °C. Tempering temperatures and regimes were chosen based on the

tempering diagrams provided from the selected steel suppliers (Figure 16) aimed at achieving similar hardness values between the specimens from different tool steels. For each tool steel the target hardness values were 55 HRC, 50 HRC and 45 HRC (Table 8).

Due to the obtained wear results for hardness groups 1, 2 and 3, which will be discussed later and to show the importance of matrix hardness when large eutectic carbides are present in the steel, an additional hardness group was made (Table 8), i.e., labelled w for materials with designation Mat. No. 1.2363 (specimen w-B) and Mat. No. 1.2379 (specimen w-D). This group was also made to verify the literature claims [82] that material Mat. No. 1.2379 (specimens D) shows better wear resistance than Mat. No. 1.2363 (specimens A) at its working hardness.

The specimens were heat treated in such a manner to obtain a high working hardness level (app. 60 HRC after quenching and tempering). At this hardness level the influence of eutectic carbide orientation in the martensitic matrix was also evaluated. At lower hardness levels other wear mechanisms intensify the abrasive wear, thus masking the influence of the carbides' orientation. The heat-treatment procedures for all tool-steel specimens subjected to the recommended regime are listed in Table 9.

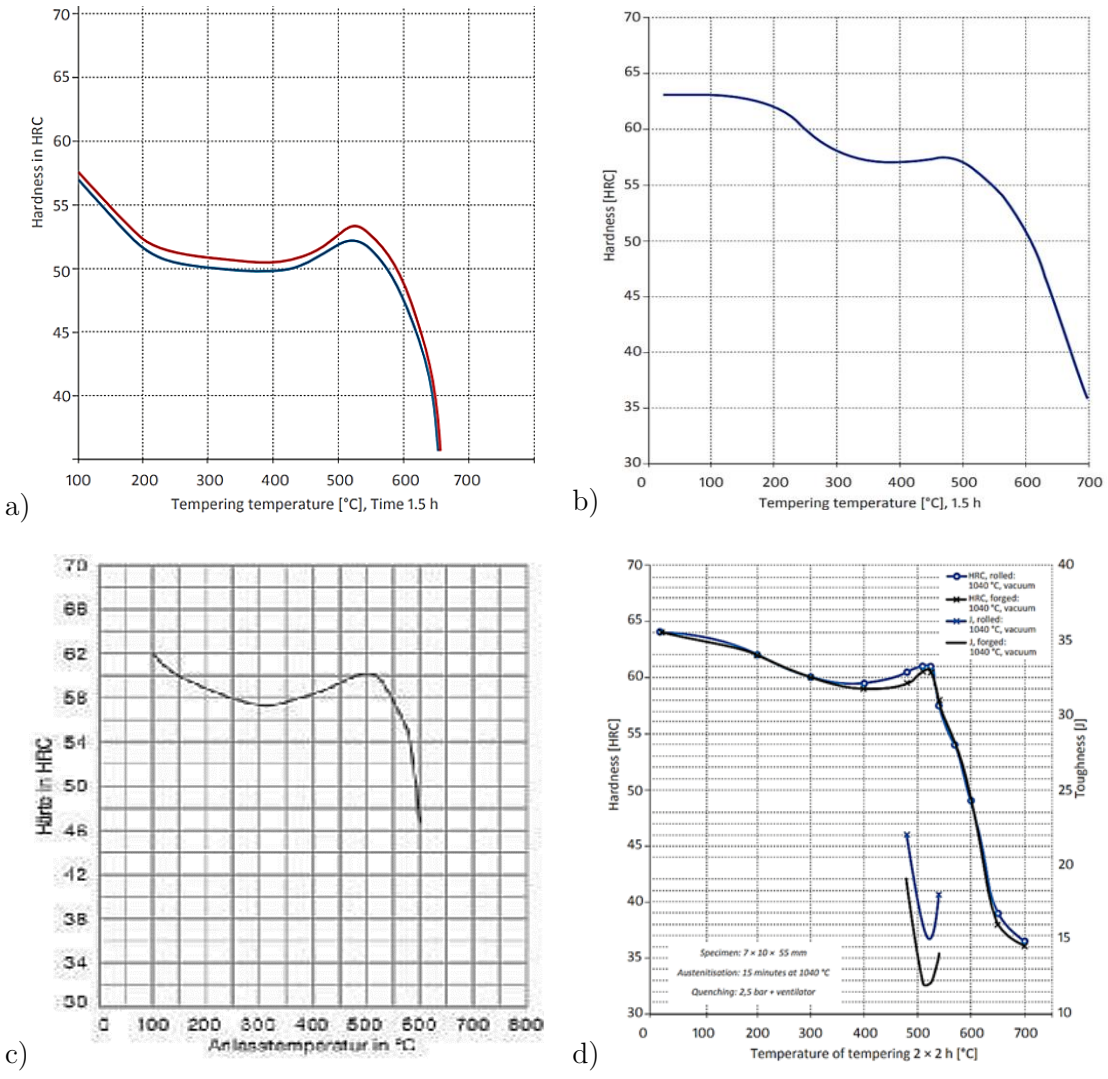

Figure 16: Tempering diagrams from supplier's brochures; a) 1.2367 mod b) Mat. No. 1.2363 c) Mat. No. 1.2990 and d) Mat. No. 1.2379.

Table 8: Targeted hardness levels for defined hardness groups (1, 2, 3 and w).

Group	**Target Hardness**
1	55 HRC
2	50 HRC
3	45 HRC
w	60 HRC

Table 9: Parameters of the heat-treatment process for the selected tool steels.

Label	**Heat-treatment**		
	***T_{aus}/time**	***$T_{1\ temp}$/time**	***$T_{2\ temp}$/time**
Mat. No. 1.2367 mod. (material A)			
1-A	1030 °C / 20 min	500 °C / 2h	510 °C / 2h
2-A			595 °C / 2h
3-A			615 °C / 2h
Mat. No. 1.2363 (material B)			
w-B	950 °C / 20 min	265 °C / 3 h	/
1-B		537°C / 3 h	/
2-B		587 °C / 3h	/
3-B		600 °C / 3 h	615 °C / 2h
Mat. No. 1.2990 (material C)			
1-C	1050 °C / 20 min	592 °C / 2h	/
2-C		611 °C / 2h	/
3-C		622 °C / 2h	/
Mat. No. 1.2379 (material D)			
w-D	1020 °C / 20 min	235 °C / 2 h	/
1-D		530 °C / 2h	558 °C / 2h
2-D		570 °C / 2h	580 °C / 2 h
3-D		590 °C / 2h	600 °C / 2h

4.3 Thermodynamic Calculation with Thermo-Calc Software

In materials engineering, thermodynamic modelling tools like ThermoCalc software are very important in terms of exploring the equilibrium and phase relationships in complex materials. They are also becoming more and more used in scientific investigations as well as in the metal-production and metal-working industry.
However, ThermoCalc software requires thermodynamic databases that have been produced by a systematic evaluation of experimental and theoretical data. The data are listed in different databases for various materials. In our calculations the TEOL5 database was used. The suitable selection of the database can provide the user with predictions of stable and metastable heterogeneous phase equilibria, the designing of phase diagrams (binary, ternary and multicomponent), the calculation of transformation temperatures (liquid, solidus), and determining the thermodynamic properties (enthalpy, thermal capacity and activity) of chemical reactions [86].

4.4 Characterization

4.4.1 Sample preparation

Specimens were sectioned from as-delivered material having dimensions of 20×20×10 mm^3. After heat treatment, a standard metallographic procedure for tool steels was used when preparing metallographic specimens. They were prepared by grinding using SiC papers of different grit size, followed by polishing with a 3-µm and 1-µm diamond suspension. For carbide-type characterization the specimen surface was prepared with final polishing and etching with OP-S suspension (oxide polishing suspension), exposing the hard phases from the matrix. In order to reveal the microstructure of the investigated specimens, chemical etching using Vilella etchant (2 g picric acid, 10 ml HCl, 200 ml alcohol) or Nital (5 ml HNO_3, 95 ml alcohol) was carried out. The samples were placed in a beaker with ethanol and ultrasound cleaned for 1 min. Finally, all the samples were dried in hot air.

4.4.2 Microscopy

4.4.2.1 Light microscopy (LM)

Metallographically prepared specimens were examined by optical microscope Microphot FXA, equipped with Nikon 3CCD video camera Hitachi HV-C20A and analytical Software. With an optical microscope we cannot get information on the chemical composition, crystal structure and orientation of the crystal grains; however, characterization of the microstructure can be made in terms of inclusions distribution, revealing grain and phase boundaries, or evidence of any mechanical deformation.

4.4.2.2 Scanning electron microscopy (SEM)

A FE-SEM JEOL JSM 6500F field-emission scanning electron microscope and a ZEISS Crossbeam 550 FIB-SEM Gemini II scanning electron microscope (SEM) were used for detailed microstructure investigation. The SEM micrographs of etched specimens were taken in the secondary-electron imaging (SEI) mode using an accelerating voltage of 15 kV. SEM is a powerful tool for various investigations at the micron and submicron levels.

To evaluate the size distribution and fraction of the most abundant carbides that are present on the surface (which are exposed to wear) of the materials investigated, feature counting was performed using INCA software at different magnifications (depending on carbide size) and on 10 randomly chosen areas. Based on the difference in contrast between the matrix and carbides in BSE mode, their size distribution and fraction could be evaluated. The technique of using SEM and BSE mode can be used without prior etching of the specimen's surface. Due to the carbide variation in the composition and morphology, the carbides (MC, M_7C_3, $M_{23}C_6$) can be differentiated in the matrix. Carbides of MC-type being rich in vanadium appear dark/black. More difficulties are present with M_7C_3 and $M_{23}C_6$, both having a darker-grey contrast and being rich in chromium (Figure 17). They were mainly selected by their size [87]. Based on their size those carbides were classified as eutectic carbides - EC (> 5 µm) and secondary carbides - SC (≤ 5 µm). Secondary carbides where also further classified as large secondary carbides – LSC ($1 < \text{size} < 5$ µm) and small secondary carbides – SSC ($0.1 < \text{size} < 1$ µm). Such classifications of carbides have been reported in detail and used in previous studies [88, 89]. During automatic feature analysis, also an EDS analysis was performed for every particle detected to confirm their type (chromium or vanadium rich). In order to include different size ranges of carbides and to

fulfil statistical accuracy, size and spatial distribution was performed at different magnifications (500×, 2500×, 4000× for Cr-rich carbides and 500×, 5000× and 10000× for V-rich carbides). For V-rich carbides two size groups (range < 1 µm and ≥ 1 µm) were considered.

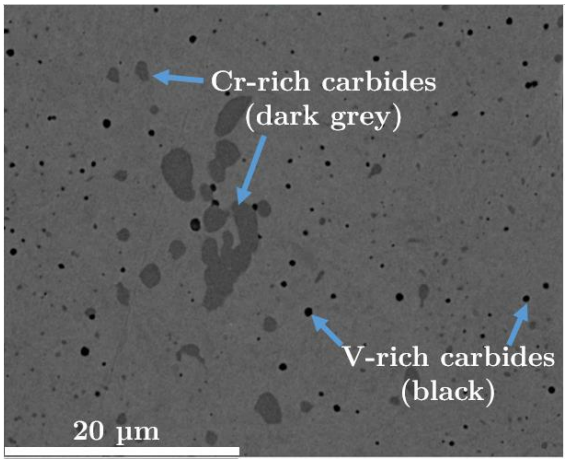

Figure 17: Example of carbide detection in the matrix using INCA software; material C with Cr- and V-rich carbides.

SEM/EBSD (electron back-scatter diffraction) technique was used for microstructural crystallographic investigations and phase determination in the investigated tool steels. A highly polished sample is tilted to typically 70° and electron diffraction occurs when the incident beam reaches the sample surface at an accelerating voltage of 10–30 kV and a current of 1 to 50 nA. With the beam stationary, an EBSD pattern emanates spherically from this point. The diffraction pattern is seen on the phosphor screen placed in the path of the diffracted electrons. SEM electron optics affect the spatial resolution of the technique. [90].

4.4.2.3 Atomic force microscope (AFM)

An atomic force microscope (AFM) Nanoscope IIIa, Digital Instruments was used for the morphology-friction analysis on the microscale. Our goal was to see if there is any difference in the frictional response of carbides and matrix. For this, hardened specimens of Mat. No. 1.2379 steel (material D) in hardness group 2 (app. 49 HRC) were used. Material D contains the highest fraction of large eutectic carbides at the same time being large enough to ensure sufficiently large surface of carbide phase. Specimens were prepared in such a manner that carbides were protruding from the surface, following surface preparation specified for the EBSD characterization technique. Final polishing and etching with OPS suspension are applied after a standard metallographic procedure consisting of grinding and polishing with diamond paste. Measurements were performed with the silicon-based cantilever tip over the scan area of 15.0 µm × 15 µm using scan rate of 1 Hz. The aspect ratio used was 1.00 and the amplitude set point 0.51 mV. For a simple comparison among different specimens it is sufficient to measure the lateral forces by the electrical response [91]. In our case measurements were performed following the rule of subtraction of the lateral force profiles recorded in both directions (trace and retrace).
The AFM is designed to produce imaging of different types of surfaces, including materials with very low or no conductivity (polymers, ceramics, composites, glass, and biological samples). Forces between atoms are used to map the tip-sample interaction and produce the AFM image. An important parameter in AFM microscopy is stiffness of the cantilever,

needed to calculate the interaction forces, which are not measured directly. Most Atomic Force Microscopes use a laser beam deflection system, with a laser beam reflected on the back of the AFM tip equipped cantilever and onto a position-sensitive detector. The laser position on the photodetector is used to track the surface for imaging, when the tip interacts with the surface. Materials for AFM tips and cantilevers are typically Si or Si_3N_4 with a radius of a few nm [92].

In tribology, atomic force microscopy plays an important role in determining the morphology as well as tribological behaviour of materials and surfaces on the microscale [93]. The schematic representation of the friction force measurement with complete surface scanning cycle (subtraction and addition) and tip behaviour for normal and lateral forces is shown in Figure 18. Friction measurements can be conducted using lateral force microscopy (LFM) mode [94].

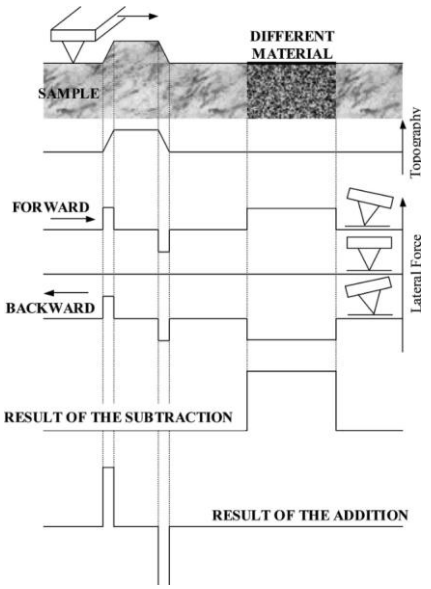

Figure 18: Schematic of the surface scanning cycle [94].

4.4.2.4 Alicona 3D-focus variation optical measurement microscopy

The wear resistance of the tested tool-steel specimens exhibiting variations in microstructure and mechanical properties and influenced by nominal load and sliding speed was evaluated in terms of wear volume, measured using a 3D microscope Alicona Infinite Focus G4. The wear resistance was plotted in terms of the specific wear rate calculated by equation (3) on page 16. High-resolution 3D optical device provides a 3D image with a great contrast. It works on the variation of the focus and operates on the principle of illumination of the selected slice of the sample. The device enables quantitative surface analysis, measurement of roughness and profile. Computer control of the optical system enables extremely fine potentiometric focus control and image digitalization [95].

4.5 Mechanical Properties

4.5.1 Hardness

4.5.1.1 Rockwell technique

The bulk hardness of the investigated specimens subjected to different heat-treatment parameters was measured using the Rockwell-C Wilson-Rockwell B 2000 machine according to the SIST EN 6508-1:2016 standard procedure [96]. Diamond cone (spheroconical shape with a 120 ° cone and rounded peak of 0.2 mm radius) shown in Figure 19 was used as an indenter in the Rockwell hardness testing [97].

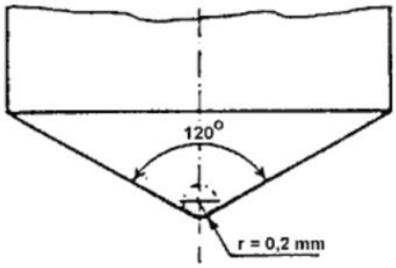

Figure 19: Diamond cone indenter for standard Rockwell-C hardness test [97].

4.5.1.2 Vickers technique

The hardness of the matrix of all the tool steels used was measured according to the standard Vickers hardness testing method using an Instron Tukon 2100B apparatus and load of 5 N (HV0.05). The Vickers test was performed with a highly polished indenter with square-based pyramidal diamond shape and with angles of 136 +/- 5° as presented in Figure 20 [97]. The whole testing procedure and the equipment for hardness testing are standardized according to the standard SIST EN ISO 6507-1:2018 [98].

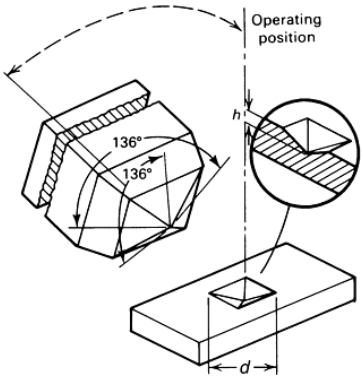

Figure 20: Diamond pyramid indenter used for the Vickers test and resulting indentation in the work piece; d, mean diagonal of the indentation in millimetres [97].

4.5.1.3 Instrumented Indentation Testing (IIT)

Quick Matrix indentation mode was used, resulting in a hardness distribution map throughout the microstructure [97]. The nano-indentation matrix size was 30×30 nano-indents, giving us in total 900 measurements per specimen. The minimum space between

them was 4 µm and maximum load used was 10.00 mN. Loading and unloading rate used was 60 mN/min. Information about indenters shape compensation were obtained from calibration: h_c = 701,8 nm; A_p = 1,21x10^7 nm^2.
The method of nano-indentation (Instrumented Indentation Testing) employs high-resolution instrumentation, with which a good control and monitoring of the load and displacement of an indenter are achieved. Loads small as 1nN can be applied and displacements of 0.1 nm can be measured. Simultaneously, the indentation load-displacement data is obtained and evaluated. It is a technique commonly used to measure the mechanical properties of thin films and coatings, mainly the hardness. For the current investigation an Anton Paar NHT^3 nano-indentation tester, with load range from 0.1 mN to 500 mN was used.

4.5.2 Toughness testing

4.5.2.1 Impact toughness

The impact toughness tests were performed according to SIST EN ISO 148-1:2016 standardized impact toughness testing using the prescribed Charpy V-notch specimens (Figure 21) [99].

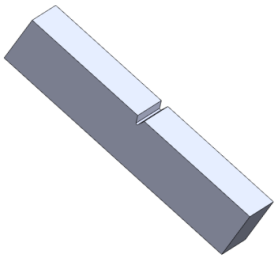

Figure 21: Schematic representation of Charpy V-notch test specimen.

4.5.2.2 Fracture toughness

Fracture toughness is the ability of the material to withstand crack propagation, i.e., fracture in the presence of cracks [97, 100]. Fracture toughness testing was performed using CNPTB - circumferentially notched and fatigue pre-cracked tensile bar specimens (Figure 22) [101]. Fatigue crack as seen under the microscope is shown in Figure 23. The radial symmetry of the test specimen allows an investigation and correlation of the microstructure effects on different material properties, including fracture toughness. Through radial symmetry, a uniform microstructure over the whole cross-section of the specimen is provided. After pre-cracking, performed under rotating-bending loading, specimens were subjected to tensile loading until fracture. This was executed by an Instron 8802 tensile test machine at a cross-head speed of 1.0 mm/min. By measuring the load at fracture and the diameter of the brittle fractured area (Figure 23), fracture toughness can be calculated according to eqn. (8), valid for linear elastic behaviour and as long as the condition $0.5 < d/D < 0.8$ is fulfilled. For each tool-steel material and hardness level, at least four samples were tested and the average fracture toughness calculated.

$$K_{ic} = P3 - D/2 - 1.27 + 1.72 \cdot Dd \ [\mathrm{MPa/m^2}] \quad (8)$$

where P is the load at fracture, d is the fractured area and D is the diameter of the specimen in the unnotched area (10 mm) [102].

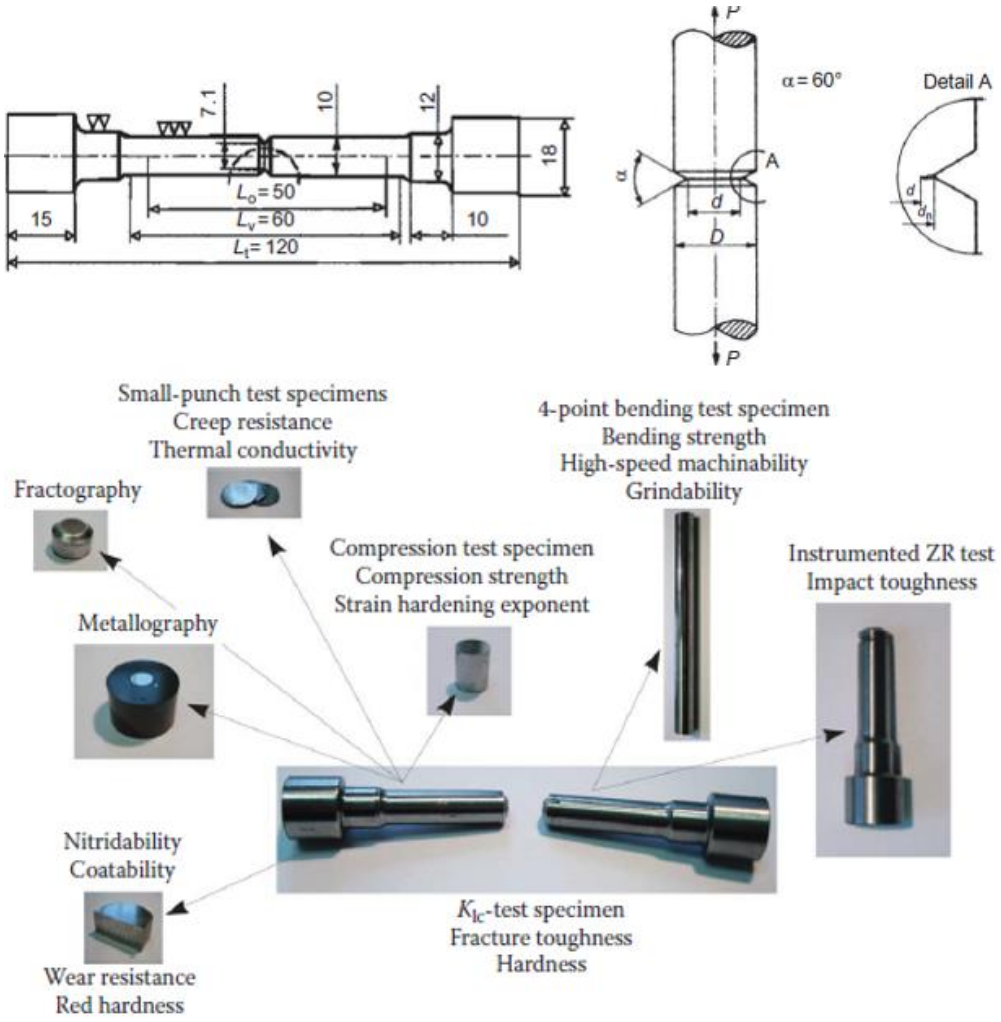

Figure 22: CNPTB-test specimen for fracture-toughness measurement and determination of various additional tests [100].

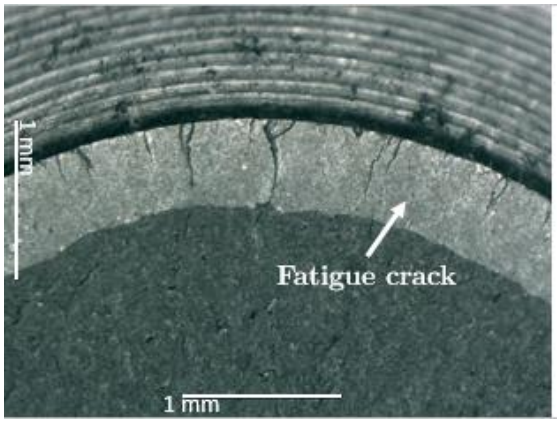

Figure 23: Fracture surface of the test specimen with indicated fatigue crack (bright ring).

Many studies were made on the fracture toughness of tool and high-speed steels by using non standardized CNPTB or K_{ic} test specimens by Leskovšek et al. [45], [100], [103]–[106]. They established that the plain strain conditions are easily obtained. Also, a model for the estimation of the fraction toughness for high-speed and cold-work tool steels on the basis of microstructural parameters and material properties was proposed [100]:

$$K_{ic} = 1.363 * \left(\frac{HRC}{HRC-53}\right) * \left[\sqrt{E * d_p} * (f_c)^{-\frac{1}{6}} * \left(1 - f_{c>a_{crit}}\right) * (1 + f_{aust})\right] [\mathrm{MPa/m^2}] \quad (9)$$

The semi-empirical correlation shown in eqn. 9 is valid for hardness values above 57 HRC and includes the constant 1.363, modulus of elasticity E [MPa], the mean distance between undissolved eutectic carbides d_p[m], the Rockwell hardness [HRC], volume fractions of undissolved eutectic carbides and retained austenite, f_c and f_{aust}, the cumulative fraction of undissolved eutectic carbides $f_{c>a_{crit}}$ and/or carbide clusters larger than the critical defect size a_{crit} [100].

4.5.3 Tensile testing

The standard B-type tensile-test specimens shown in Figure 25 (DIN 50125:2009-07) were used for the tensile tests performed with the INSTRON 1255 and INSTRON 8802 test machine [107]. This test enables an evaluation of the Ultimate tensile strength (R_m), Yield strength ($R_{p0.2}$), elastic deformation properties (Young's modulus and Poisson's ratio), and ductility properties (elongation and reduction area). A quantitative measurement (force-extension data) of how the test sample under an applied tensile force is deformed is being recorded and monitored, as shown in Figure 24. The applied load or force and the elongation relationship for most metallic materials is linear in the initial phase of the test, before reaching the Yield strength. The material reacts plastically after this point is reached [97]. In the linear region, the material follows Hooke's law:

$$E = \frac{\sigma}{\varepsilon} \text{ [Pa]} \quad (10)$$

where σ is stress, ε is strain and E is modulus of elasticity.

The point/value at which the plastic deformation of the material starts in the presence of an applied load is called the yield strength.

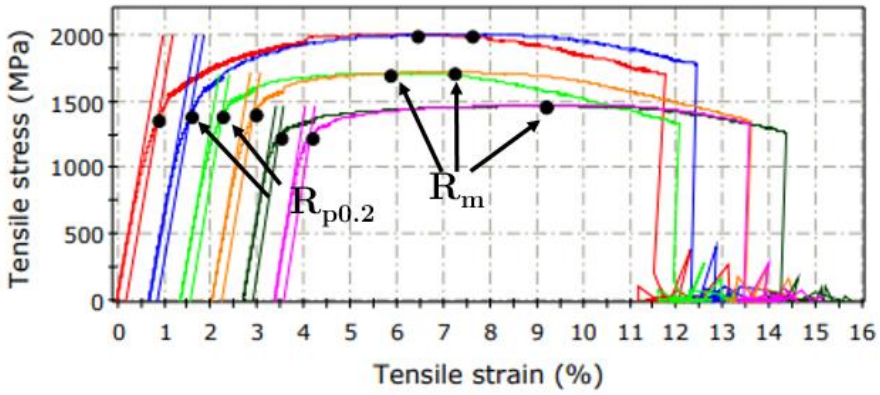

Figure 24: Tensile strain – tensile stress diagram as obtained during tensile testing of materials with indicated $R_{p0.2}$ (yield strength) and R_m (tensile strength) points.

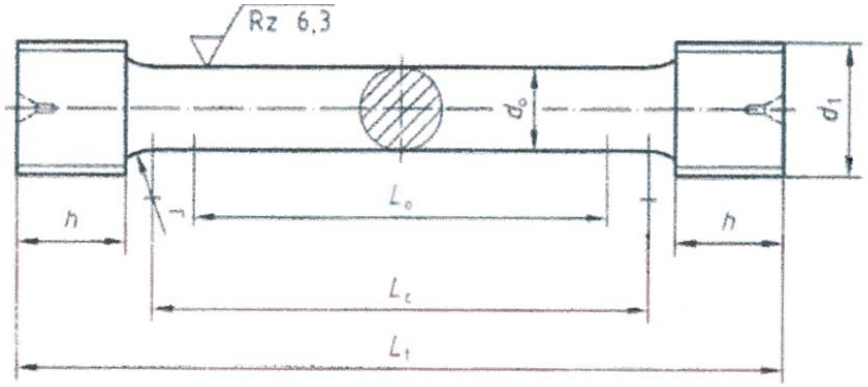

Tolerance d_o [mm]	d_o	L_0	d_1	r min	h min	L_c min	L_t min
0.04	10	50	M16	8	12	60	97

a) *All dimensions in mm

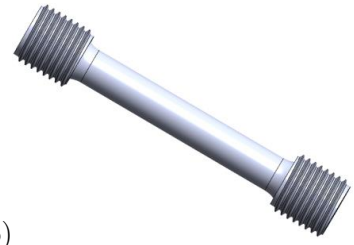

b)

Figure 25: Tensile-test specimen used for a mechanical properties evaluation.

4.6 Tribological Testing

Tribological tests were performed under different configurations and contact conditions in order to simulate different wear mechanisms. For pure abrasive wear conditions, Al_2O_3 (HV 1250–1700) ceramic ball was used as a counter-body. Since its hardness is much higher than the hardness of the investigated tool steels, wear is more or less concentrated on the tested tool-steel specimens. To provoke abrasive-adhesive wear a 100Cr6 steel counter-body ball (~58 HRC) was selected. Although it is harder than the tested tool steels, similarities in hardness and material type result in simultaneous wear of both contact surfaces and material transfer. Furthermore, higher adhesion forces are expected due to the steel-to-steel contact. Finally, to achieve mainly adhesive wear an AISI 304L stainless-steel ball with a significantly lower hardness level (<30 HRC) than the specimens under investigation was used as a counter-body.

4.6.1 Reciprocating sliding ball-on-plate wear testing

Simulative model tests in terms of ball-on-plate reciprocating sliding are not the perfect method for replicating the service conditions of tools. However, it is a good approach for determining a tool's wear resistance. Temperature, contact load, sliding speed and material in contact strongly affect the wear behaviour and the prevailing wear mechanism [108–110].

For the evaluation of the wear resistance and wear behaviour of the investigated tool steels, the in-house made universal tribometer Hitman with reciprocating movement shown in Figure 26a was used. The apparatus enables tribological testing at sliding speeds from 0.0004 to 1.3 m/s and load levels from 15 up to 500 N. The schematic illustration of the ball-on-plate contact configuration between the ball and the investigated material shows Figure 26b.

a)  b) 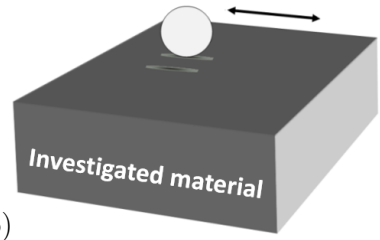

Figure 26: a) Reciprocating sliding wear test apparatus Hitman used and b) schematic of the ball-on-plate contact configuration.

To evaluate the influence of the carbide fraction, the size and type of the abrasive as well the adhesive wear, tool-steel specimens with different bulk hardness levels were subject to oscillations (a = 4 mm) and loaded against different counter balls under different contact conditions. For pure abrasive wear conditions, a 20-mm diameter Al_2O_3 ball and normal loads of 102 N and 30 N (corresponding to a nominal Hertz contact pressure of about 1600 MPa and 1000 MPa) were used. Also, two different sliding speeds were selected (0.12 m/s and 0.01 m/s), simulating high speed and low speed contact conditions. The high sliding speed was obtained by using an oscillation frequency of 15 Hz and a low sliding speed at 1 Hz.

The influence of the hard phase particles in the case of the combined abrasive-adhesive wear (20-mm diameter hardened 100Cr6 bearing steel ball) was investigated at a load of 40 N (corresponding to a nominal Hertz contact pressure of 1000 MPa). The same contact conditions were used when provoking a pure adhesive wear component against a soft 20-mm-diameter 304L stainless-steel ball. When using steel counter balls, sliding conditions with a high sliding speed (0.12 m/s) and a low sliding speed (0.01 m/s) were applied. The sliding distance in the case of an abrasive wear investigation was 100 m under high-speed conditions, and 60 m under low-speed conditions. For adhesive and abrasive-adhesive wear tests, high-speed tests were run for 100 m and low-speed tests for 4 m in order to investigate the initial wear phase. In order to ensure adequate repeatability, at least three repetitions were performed for each specimen group and contact conditions. Wear resistance was compared in terms of the specific wear rate, taking into account sliding distance, wear volume measured and load used. All the test parameters are shown in Table 10.

Table 10: Test parameters for the reciprocating wear testing using the Hitman machine.

Counter body	**(Φ20)-Al_2O_3**		**(Φ20)-100Cr6 / 304L**	
Hertz contact pressure [MPa]	1600 and 1000		1000	
Nominal load [N]	102 and 30		40	
Sliding speed [m/s]	0.12	0.01	0.12	0.01
Amplitude [mm]	4		4	
Frequency[Hz]	15	1	15	1
Test time [s]	833	7500	833	500
Sliding distance [m]	100	60	100	4

For determining the role of carbides and wear debris generated during reciprocating sliding as third bodies, the in-situ removal of generated wear debris was accomplished by the "air blowing" method. The assembly for this kind of tests is presented on Figure 27. The nozzle was placed directly near the wearing region. During the reciprocating sliding "air blowing" was conducted for the whole time period of the test in order to remove wear debris as fast as they are created. "Air-blowing" reciprocating sliding tests were performed under low-load/high-sliding-speed conditions (Al_2O_3 counter-body 30 N, 0.12 m/s) to be compared with the abrasive wear results without the in-situ removal of the wear debris. Tests were performed for different tool steels in hardness group 1 (55–53 HRC). The testing parameters are given in Table 10.

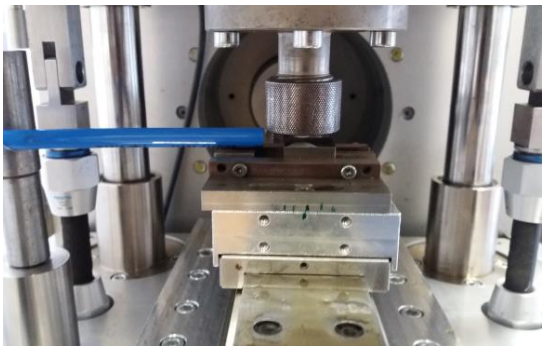

Figure 27: Reciprocating test rig with nozzle for air-blowing method.

The hot-working process of tool steels (hot rolling or forging) creates texturing of large stable eutectic carbides (Figure 28b). When tool steels are cast the melt starts to solidify, where carbides are formed. Because of the long, slow solidification process, an interconnected segregated network of carbides is formed. These create non-uniformity of the microstructure. As hot rolling or forging is done, these segregated areas of carbides are physically elongated, resulting in a directionally oriented microstructure. In the case of the tool steel Mat. No. 1.2379 (specimens labelled w-D, from the hardness group 58–60 HRC) the effect of the carbides' orientation on the abrasive wear resistance was also evaluated. The wear tests were performed perpendicular and parallel to the rolling/carbides orientation under low-load/high-speed conditions (Al_2O_3 counter-body, 30 N, 0.12 m/s). Figure 28c and d have labelled directions in which low-load/high-speed abrasion reciprocating tests were performed.

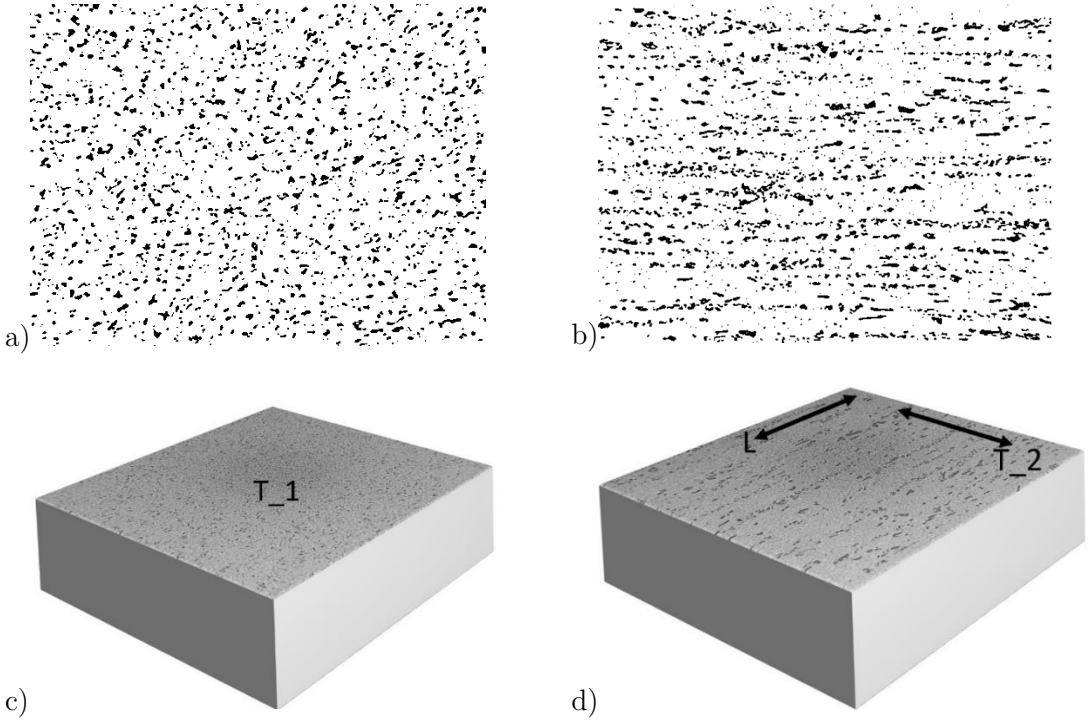

Figure 28: Schematic of large eutectic carbides distribution in D material; a) transverse and b) longitudinal direction of hot rolling, c) T_1 and d) T_2 and L wear testing direction.

Elevated-temperature abrasive wear tests for hot-work tool steel material were performed at temperatures of 250°C and 500 °C and an ambient atmosphere for all three hardness-level groups. Tests were performed in a high-temperature reciprocating sliding test rig (SRV), with an inclinable and air-conditioned test chamber. The elevated-temperature test parameters are listed in Table 11.

Table 11: Elevated-temperature reciprocating sliding test parameters.

Counter body	**(Φ20)-Al_2O_3**
Hertz contact pressure [MPa]	1000
Nominal load (N)	30
Sliding speed [m/s]	0.1
Amplitude [mm]	4
Frequency[Hz]	15
Test time [s]	1666
Sliding distance [m]	200
Temperatures [°C]	RT, 250 °C, 500 °C

4.6.2 Unidirectional sliding ball-on-plate wear testing

The ball-on-disc unidirectional sliding wear tests were carried out to get a better insight into the behaviour of the microstructure, especially of the hard carbide phase on the wear resistance under oriented deformation within the worn area. Tests were performed in air under ambient temperature using a TRIBOtechnic ball-on-plate TRIBOtester shown in Figure 29a. The schematic illustration of the contact between the ball and the investigated material is shown in Figure 29b.

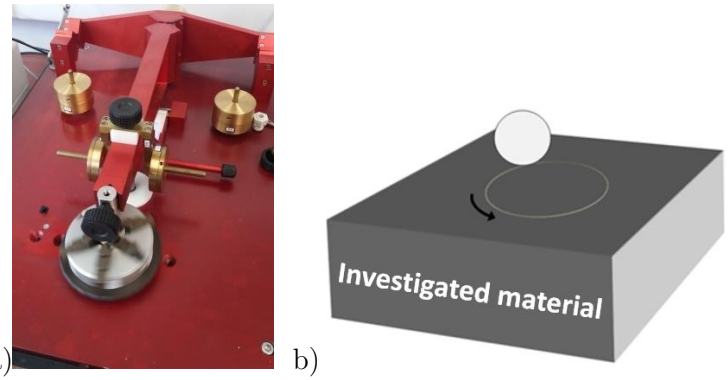

Figure 29: a) TRIBOtechnic unidirectional and oscillating ball-on-plate TRIBOtester and b) schematic of the ball-on-plate contact configuration.

One set of experiments was aimed at analysing the microstructure behaviour (tempered martensite matrix and hard carbides) during running-in, i.e., at the very beginning of the sliding. Tests were performed with 10-mm diameter ceramic Al_2O_3 ball at a load of 6 N (p_H = 1000 MPa) and sliding speed of 0.12 m/s. Parameters are listed in Table 12.

To simulate the running-in behaviour of carbides when protruding from the contact surface, 10 sliding pass tests were conducted on specimens for hardness group 2 (48–50 HRC), prepared according to the EBSD preparation procedure. This includes grinding using SiC papers, followed by polishing with a diamond suspension. Protruding carbides from the matrix were achieved with final polishing and etching with OPS suspension, exposing the hard phases from the matrix.

A second set of unidirectional sliding tests, aimed at analysing the long-term wear behaviour, was performed under the same contact conditions as the first set (Table 12), but for a much longer time and sliding distance. The number of sliding passes was increased to 3500, which corresponds to a total sliding distance of 200 m. Long-term unidirectional sliding tests were performed on hardness-level groups 2 and 3 specimens, with hardness values of 48–50 HRC and 44–46 HRC, respectively. For the top view microstructure observations tests of about 1400 laps (approx. 80 m of sliding distance) were enough to obtain sufficient wear scar width and depth on the specimen surface when pre-polished. However, in some cases tests had to be prolonged up to 3500 laps (200 m of sliding) to obtain sufficient wear-track depth, needed for a cross-sectional analysis.

Table 12: Test parameters for unidirectional ball-on-disc sliding tests.

Counter body	**(Φ10)-Al_2O_3**
Nominal load (N)	6
Hertz contact pressure [MPa]	1000
Sliding speed [m/s]	0.12
Laps	10, 1400, 3500
Sliding distance [mm]	0.6, 80, 200

Chapter 5

Calculations of Phase Stability

Thermodynamic calculations using ThermoCalc software were made to evaluate and predict the stability and type of carbides that exist in the microstructures of the investigated tool steels. In the following subchapters, calculated equilibrium diagrams of phase stability and phase occurrence are described. The calculations were performed using actual chemical compositions of the investigated cold- and hot-work tool steels given in Table 4 and Table 5, which were obtained by prior XRF analysis of all the materials used. Subchapters of steels descriptions with Thermo-Calc software are listed in the order of increasing carbide fraction. The lowest fraction shows hot-work tool steel Mat. No. 1.2367 mod. (in this work labelled A) and the highest cold-work tool steel Mat. No. 1.2379 (in this work labelled D). However, the thermodynamic software calculations of phase stability as performed in our work are limited to the equilibrium state. Therefore, deviations from microstructures achieved in practice are expected. The calculations serve as mere approximations and for which carbide types are to be expected in the used tool steels based on their chemical composition. Furthermore, thermodynamic calculations are useless without an accurate and valid database needed for the desired calculations. Therefore, the results of the thermodynamic calculations are mainly limited by the extent of the thermodynamic data that are gathered in the database used.

5.1 Steel Mat. No. 1.2367 mod. (material A)

In the case of commercially available, modified, hot-work tool steel Mat. No. 1.2367 mod. (material A), that falls in the family of AISI H11-type steels, the most stable are vanadium-rich carbides (red line). These carbides are stable up to approximately 1140 °C (Figure 30). The other carbides predicted to exist in the investigated hot-work tool steel are $M_{23}C_6$ (chromium rich carbides – bright blue line) and M_6C (molybdenum rich carbides – green line). However, they are already dissolving at lower temperatures at approximately 810 °C for $M_{23}C_6$ and at 880 °C for M_6C. $M_{23}C_6$ (chromium rich carbides) are the most abundant in the temperature range between 500 °C and 800 °C. Equilibrium calculations predict about 5 % of $M_{23}C_6$ type carbides at 500 °C, which slowly decrease and completely dissolve at approximately 800 °C. The other microstructure constituents are body-centred ferrite-type phase (yellow line), which in our case is tempered martensite and austenite (dark blue line).

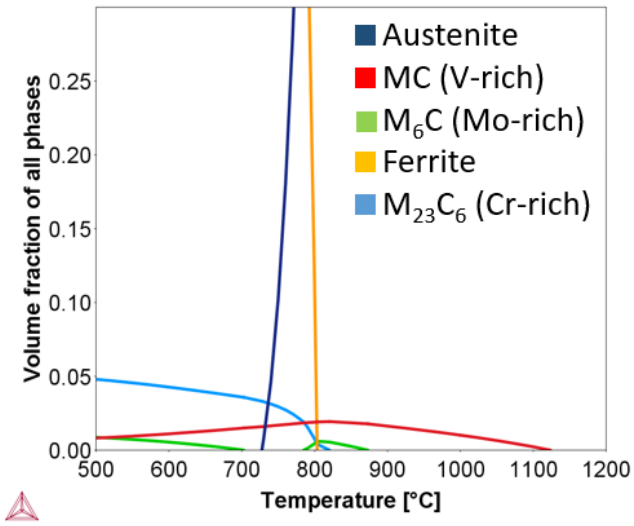

Figure 30: ThermoCalc calculations of phase stability for hot-work tool steel Mat. No. 1.2367 mod. (material A) showing volume fraction of all phases present with 1 being 100%

5.2 Steel Mat. No. 1.2363 (material B)

The equilibrium calculated diagram of phase stability for the cold-work tool steel Mat. No. 1.2363 is presented in Figure 31. The predicted carbide types being present in the microstructure of this steel are mainly M_7C_3 (purple line) as well of a very small amount of vanadium-rich carbides (red line). The other microstructure constituents are body-centred ferrite type phase (yellow line), representing tempered martensite and dark blue line representing austenite phase. However, austenite is a high-temperature phase, as also shown on the graph, existing in temperatures above approximately 760 °C. The type of carbides predicted in this steel are stable to temperatures above ≈1080°C for M_7C_3 type, and ≈1130 °C for vanadium-rich type. The point of highest fraction for M_7C_3 type is predicted at around 750 °C, at slightly above 10 %. At typical tempering temperatures (above 500 °C), from 8 to 10 % of M_7C_3 carbide type phase is predicted. However, this is only true for the equilibrium state of the material.

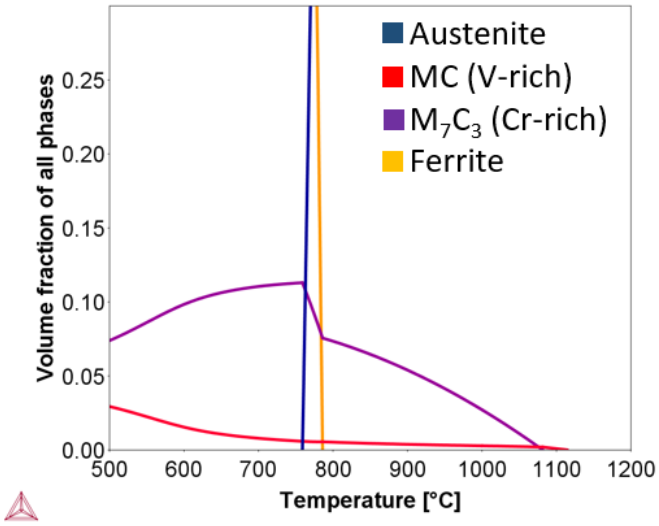

Figure 31: ThermoCalc calculations of phase stability for cold-work tool steel Mat. No. 1.2363 (material B) showing volume fraction of all phases present with 1 being 100%

5.3 Steel Mat. No. 1.2990 (material C)

The equilibrium calculated diagram of phase stability for the tool steel Mat. No. 1.2990 is presented in Figure 32. Three types of carbides are predicted in the case of this cold-work tool steel in the microstructure with tempered martensite matrix (yellow line). Those carbides are M_7C_3 (purple line), $M_{23}C_6$ (bright blue line) and MC type (red line). The highest fraction at the tempering temperatures is predicted for $M_{23}C_6$ type carbides, at around 10 %, with their volume fraction slowly decreasing with increased tempering temperature up to their complete dissolution at about 900°C. This steel also contains the highest fraction of MC-type carbides compared to all the other tool steels used in this study. MC-type carbides also show the highest stability and presence through the whole temperature range, as shown in Figure 32.

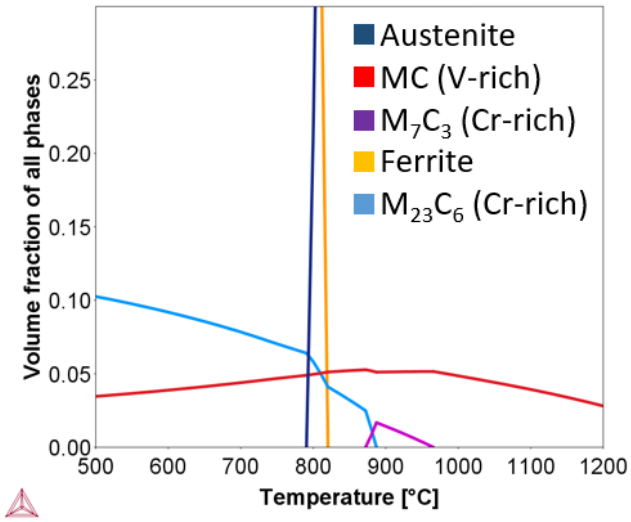

Figure 32: ThermoCalc calculations of phase stability for cold-work tool steel Mat. No. 1.2990 (material C) showing volume fraction of all phases present with 1 being 100%.

5.4 Steel Mat. No. 1.2379 (material D)

The equilibrium calculated diagram of phase stability for one of the most widely used cold-work tool steel AISI D2 or Mat. No. 1.2379 is presented in the Figure 33. This tool steel, compared to others used in the current study, contains the highest fraction of large eutectic carbides of M_7C_3 type (purple line), rich in chromium. A mass fraction above 10 % is present in the high-tempering-temperature range (above 500 °C). Furthermore, other types of chromium-rich carbides of the $M_{23}C_6$ type (bright blue line) are also predicted to exist in the martensite matrix after tempering (yellow line). There are also MC-type carbides (red line) predicted, with their fraction remaining almost constant throughout the entire temperature range.

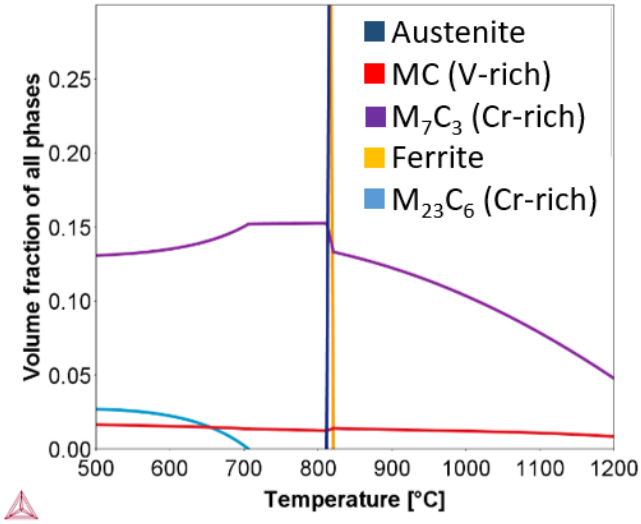

Figure 33: ThermoCalc calculations of phase stability for cold-work tool steel Mat. No. 1.2379 (material D) showing volume fraction of all phases present with 1 being 100 %.

Chapter 6

Experimental Results

The central point of this investigation was a comparison of hot- and cold-work tool-steel wear response at similar hardness levels. This was achieved by performing either unconventional hardening of hot-work tool steel with mainly martensitic microstructure (effect of grain size and dissolution of residual carbides) or by the recommended heat treatment of selected hot- and cold-work tool steels, resulting in different microstructures in terms of phases.

6.1 Microstructure

6.1.1 Carbide types in the investigated tool steels

The type of undissolved particles in the martensite matrix of the hot-work tool steel as a function of austenitizing temperature (specimens P; Table 7) was characterized by EDS analysis using SEM and EBSD. Two types of residual carbides were confirmed in the quenched and tempered microstructure of the investigated hot-work tool steel (Figure 34). One was enriched with vanadium, being the MC type, which was mainly detected for austenitizing temperatures of 950°C and 1030 °C. This is in the agreement with studies by Delagnes et al. and Smith et al. [19, 111], where mainly MC type vanadium carbides were reported, being the most stable ones and remaining undissolved in the matrix even at higher austenitization temperatures. However, at the upper austenitization temperature, only a few MC carbides were left, as will be discussed later. On the other hand, the chromium- and molybdenum-enriched carbides of $M_{23}C_6$ type were only observed at the lowest austenitization temperature of 950 °C. Note, that in the chemical composition analysis of carbides we also see elements from the background (matrix phase) that are present due to the size of the interaction volume of X-rays.

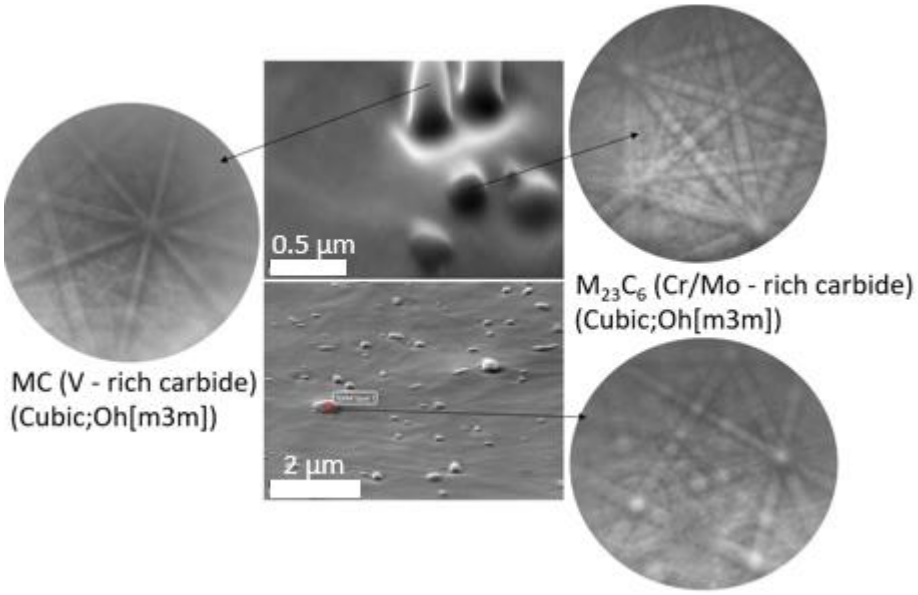

Spectrum (wt. %)	C	Si	V	Cr	Mo	Fe
MC	7.2	0	24.4	4.5	2.5	61.4
$M_{23}C_6$	6.2	0.8	1.9	6.1	18.2	66.7
	6.9	0.3	1.6	20.3	4.8	65.7

Figure 34: Mat. No. 1.2367 mod. (material A) austenitized at 950°C (P3 specimen); EBSD patterns of V- and Cr/Mo-rich carbides and the corresponding EDS analysis in weight %.

Electron backscatter diffraction (EBSD) performed on the investigated tool steels subjected to recommended heat-treatment regime and tempered to a hardness-group level 2 (48–50 HRC) confirmed different carbide types present in the tempered martensite matrix. Due to the predominant influence of the chemical composition on the carbide type only results for one hardness group are presented. The same carbides are present in the tempered specimens of the same steel, regardless of the tempering temperature and final specimen hardness. In the case of all three cold-work tool steels used in this investigation, the larger carbides were confirmed to be M_7C_3 type with a hexagonal structure and enriched in chromium, as shown on Figures 37-39. This is in accordance with the Thermo-Calc calculations.

The distribution and presence of large eutectic carbides remains unchanged during hardening. As shown in Figure 35, large eutectic carbides show an elongated structure along the hot-rolling direction (Figure 35a), but an equiaxed and uniform distribution in the cross-section view (perpendicular to rolling direction; Figure 35b).

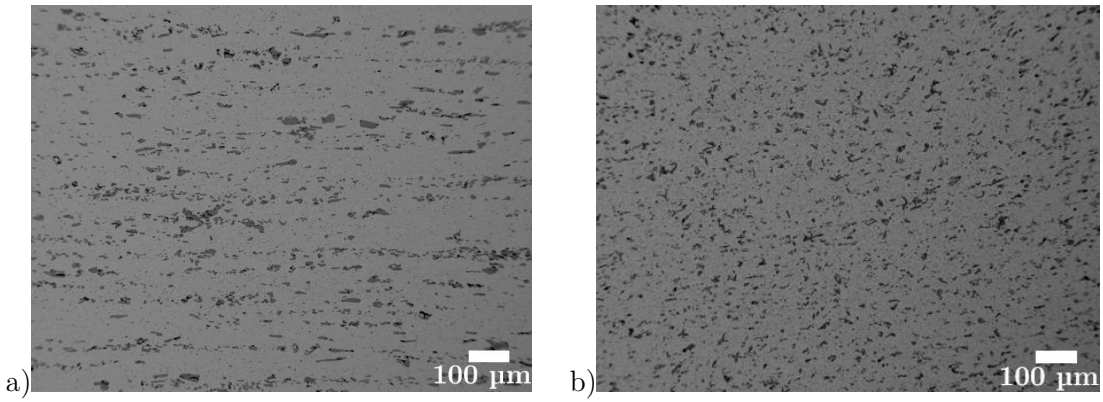

Figure 35: BSE micrograph of polished specimen microstructure of steel D (w-D specimen); a) longitudinal direction and b) cross-section view.

Another type of chromium-rich carbides, being $M_{23}C_6$ type (Figures 37-39), with a cubic structure are also present in all three cold-work tool steels. They are, however, smaller compared to the large M_7C_3 type carbides, but are more evenly distributed through the martensite matrix. The smaller carbides are secondary carbides. With the EBSD technique, another type of carbides of the MC-type could also be detected. Those where mainly found in the cold-work tool steel Mat. No. 1.2990 (material C) and hot-work tool steel Mat. No. 1.2367 mod. (material A). In both cases, the MC-type carbides observed were vanadium rich (Figure 36 and Figure 38).

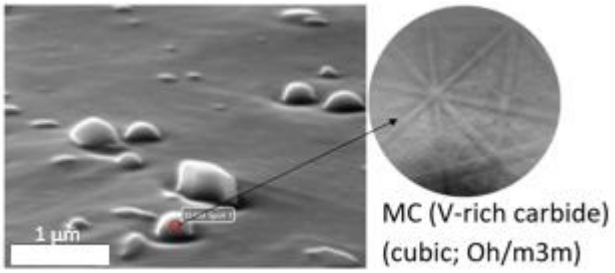

Spectrum (wt. %)	C	Mn	Si	V	Cr	Mo	Fe
MC	10.8	0.6	0.3	40.6	5.8	4	37.9

Figure 36: Mat. No. 1.2367 mod. (2-A) specimen; EBSD patterns of V-rich carbides and b) chemical composition of MC carbide and the corresponding EDS analysis in weight %.

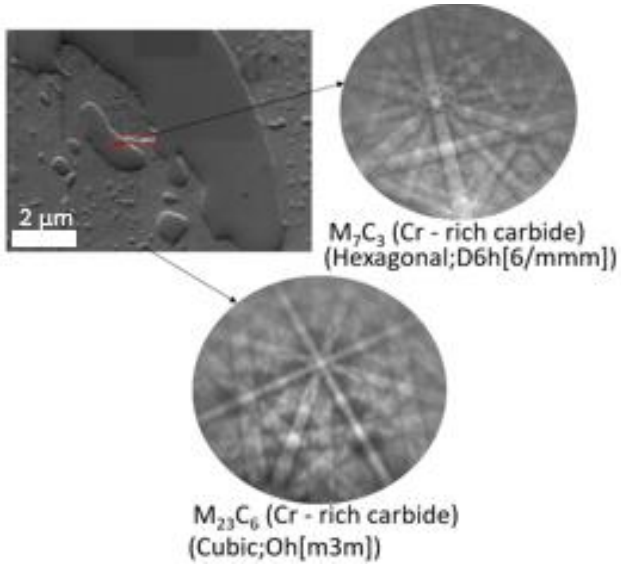

Spectrum (wt. %)	C	Mn	Si	V	Cr	Mo	Fe
M_7C_3	7.5	0.9	0.3	4.2	36.8	6.3	44.3
$M_{23}C_6$	5.2	0.5	0.3	0.7	17.8	4.1	71.7

Figure 37: Mat. No. 1.2363 (2-B) specimen; EBSD patterns of Cr-rich carbides and the corresponding EDS analysis in weight %.

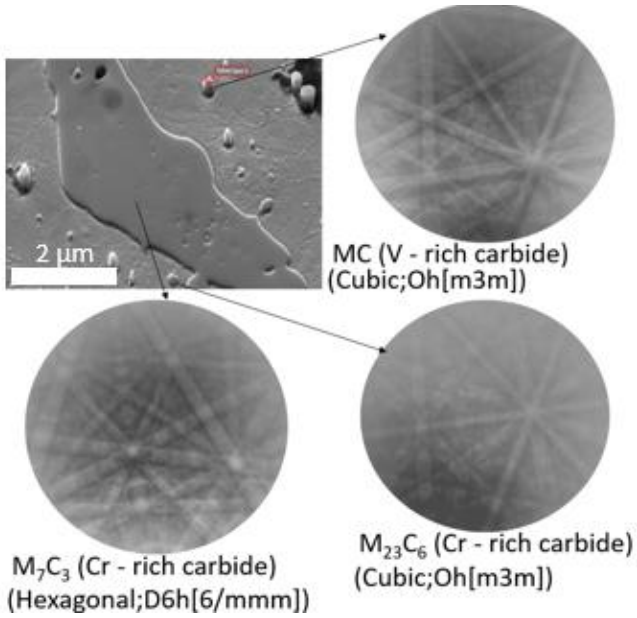

Spectrum (wt. %)	C	O	Mn	V	Cr	Mo	Fe
M_7C_3	7.1	1.9	0.9	11.8	37.5	5.6	35.2
$M_{23}C_6$	5.4	1.2	0.9	3.2	22.7	4.4	62.1
MC	9.8	0	0.6	50.3	8.4	6.2	24.6

Figure 38: Mat. No. 1.2990 (2-C) specimen; EBSD patterns of Cr- and V-rich carbides and the corresponding EDS analysis in weight %.

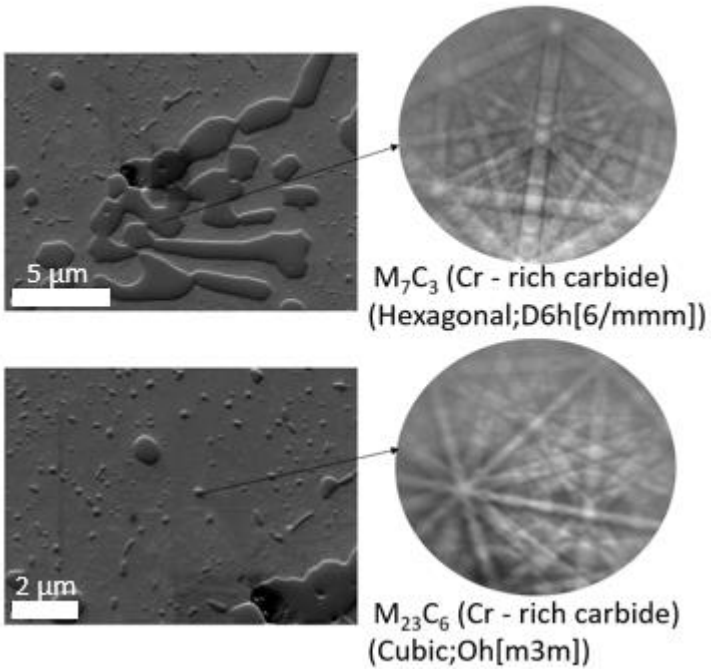

Spectrum (wt. %)	C	Mn	V	Cr	Mo	Fe
M_7C_3	8.6	0	5.1	46.2	1.5	38.6
$M_{23}C_6$	7.9	0.3	1.7	24	1	65.1

Figure 39: Mat. No. 1.2379 (2-D) specimen; EBSD patterns of Cr-rich carbides and the corresponding EDS analysis in weight %.

6.1.2 Effect of austenitization temperature

Different sets of hot-work tool-steel specimens for tribological and mechanical testing were chosen based on the preliminary dilatometry experiments, changing the austenitization temperature. At a low austenitization temperature of 950°C, retarded dissolution of the residual carbides was achieved, while at the upper temperature (1150 °C), almost complete dissolution of the pro-eutectoid carbides (carbo-nitrides) took place. MC-type carbides, found at the two lower austenitization temperatures (950 °C and 1030 °C), are important for obstructing the grains from growing during austenitization. This can be best seen from the optical micrograph in Figure 40a, where a high austenitizing temperature (1150 °C) resulted in excessive grain growth. This has a detrimental effect on the impact toughness and the ductility [112]. Austenite grain size at a chosen austenitization temperature was estimated using the JMatPro software. The software was used, as the primary austenite grain size is very difficult to measure in the case of a fully martensitic microstructure, especially for low austenitization temperatures. The process of revealing grain boundaries depends on the chemical composition of the steel, the heat treatments, etc [113, 114]. However, for the highest temperature (1150 °C), the grain boundaries were well visible (Figure 40a), thus allowing an exact grain size evaluation. In this case, the grain size experimentally determined according to the ASTM E112–13 standard, was close to the calculated value. The average grain size for the austenitization temperature of 1150 °C is 199.7 µm (2.0 ASTM), for 1030 °C, 74.9 µm (4.9 ASTM) and for the 950 °C, 36.9 µm (6.9 ASTM). Dissolution of the vanadium-rich carbides at high austenitizing temperatures also provides more vanadium that is dissolved in the matrix. This results in a higher volume

fraction of the precipitated vanadium-rich carbides during tempering. Those are the most responsible for the secondary hardening effect during tempering and maintaining a high hardness (shown in the next sub-chapter on mechanical properties) [115]. In the case of more conventional intermediate austenitizing temperatures (i.e., 1030 °C) small quantities of M_3C and $M_{23}C_6$ carbides can also be present in the as-quenched microstructure. However, in the present case the presence of those carbides was not observed. On the other hand, the chromium- and molybdenum-enriched $M_{23}C_6$ type carbides were found at the lowest austenitization temperature.

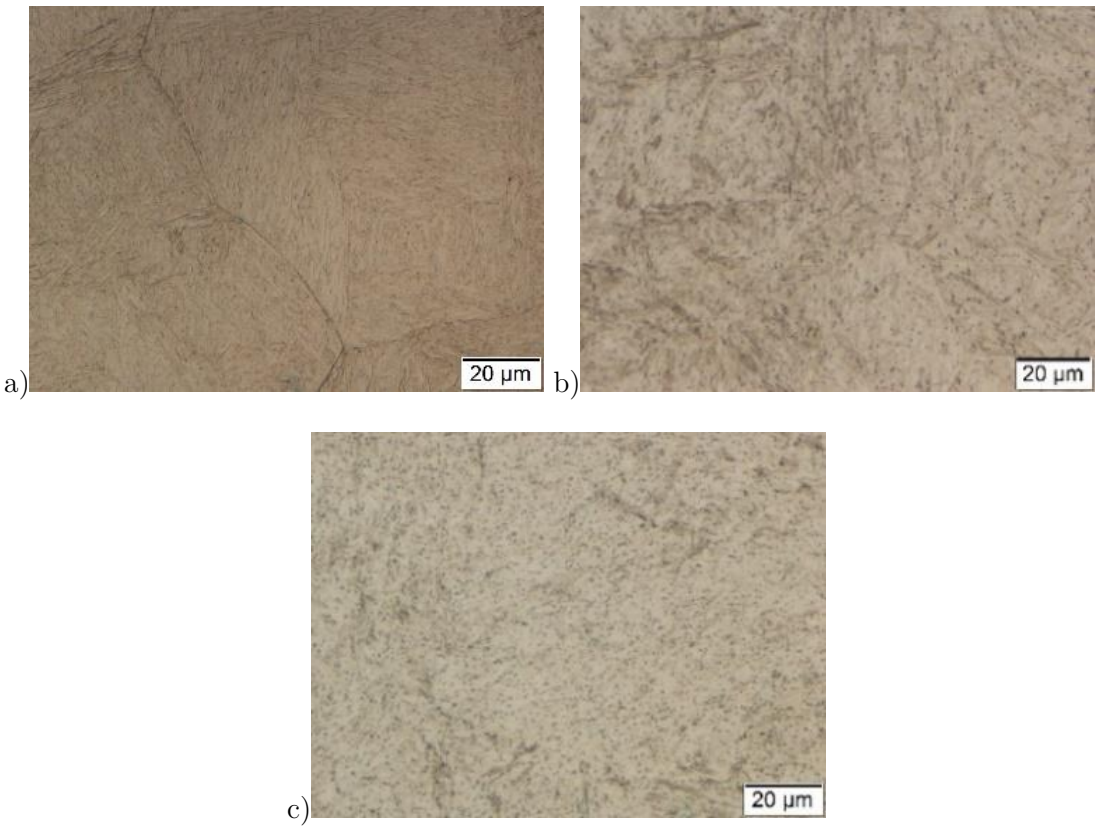

Figure 40: As-quenched microstructure of hot-work tool steel austenitized at different temperatures; a) 1150°C, b) 1030°C and c) 950°C.

After tempering, the microstructure of the hot-work tool steel consists of tempered martensite with the distribution of very finely precipitated, vanadium-rich MC carbides, cementite shown as white thin lamellar structure between martensitic laths, and chromium-based carbides (Figure 41). Typically, the microstructure of tempered martensite, with a fraction of undissolved vanadium-rich carbides, very finely precipitated vanadium-rich carbides, cementite and chromium-based carbides is obtained when following the recommended heat-treatment procedure at the austenitizing temperature of 1030 °C [1]. Such a microstructure was also obtained in our case as seen in Figure 41b. A comparison of tempered microstructures for 1.2367 mod. hot-work tool steel, austenitized from three different temperatures and tempered to a similar hardness level is shown in Figure 41. For the specimen austenitized from high temperature (specimen P1; Figure 41a), extensive decomposition of the martensite can be observed. Furthermore, coarser martensite laths due to larger prior austenite grains and larger amount of soluted carbon, with indistinct boundaries are present. In such a microstructure, practically no residual carbides can be

found, compared to the case of lower austenitization temperatures. However, there are small white precipitated structures present, which seem to start coarsening, as typically found for high tempering conditions. On the other hand, for lower austenitization temperatures (specimen P2 and P3), lower tempering temperatures were applied to achieve comparable hardness. This is due to the larger amount of residual carbides left in the microstructure after austenitization, as shown in Figure 41c. They are visible as white spherical phases in the grey matrix. Furthermore, significantly smaller amounts of plate-like needles are present in such a microstructure, presenting the M_3C phase (Figure 41c).

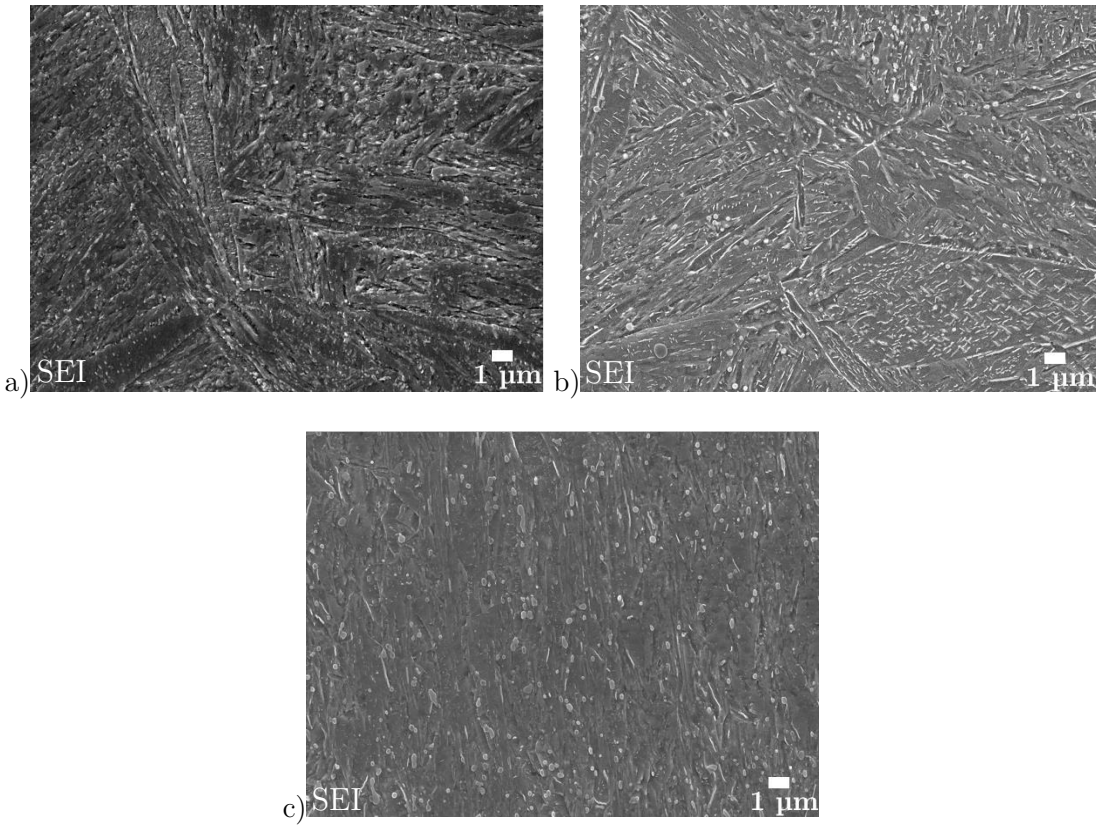

Figure 41: Microstructure of tempered hot-work tool-steel specimens displaying similar hardness (50–52 HRC), but obtained at different austenitizing and tempering temperatures; a) high (specimen P1), b) intermediate (specimen P2) and c) low austenitization and tempering temperatures (specimen P3).

6.1.3 Recommended heat-treatment

6.1.3.1 Mat. No. 1.2367 (material A)

In the case of the modified hot-work tool-steel Mat. No. 1.2367 (material A), fine vanadium-rich MC carbides could be found in the martensite matrix microstructure, as shown in Figure 42. Among the carbon, also nitrogen can be detected in those hard-phase particles, indicating the presence of vanadium-rich carbides and carbo-nitrides [19, 111]. The proeutectoid phase is containing moderate amounts of molybdenum and chromium (Figure 36); however, massive eutectic Cr-rich carbides are not present in this steel, as shown in Figure 42 and Figure 43. Tempering results in a microstructure of tempered martensite with the rearrangement of the carbon in the martensite crystals and the precipitation of alloy carbides. Evolution of the microstructure with increasing the second tempering

temperature is presented in Figure 43. After tempering, the microstructure starts to show tempered martensite with precipitated carbides that precipitate from the supersaturated solid solution of as quenched martensite. The prevailing contribution to achieving high hardness in hot-work tool steels comes from the tetragonal deformation of the cubic crystal cell of austenite during quenching and the non-diffusive transformation to the martensite microstructure by restraining the carbon on interstitial sites of the prior austenite crystal structure. During tempering the martensite matrix goes into the quasi-equilibrium state, the precipitation of the alloy carbides takes place and the rearrangement of carbon in the martensite crystals with a lowering of the tetragonality of martensite occurs, which was already described earlier. Besides the mentioned very fine, face-centred-cubic vanadium-rich MC carbides and cementite, also chromium-based carbides (facetted M_7C_3 type, globular $M_{23}C_6$ type, elongated FeCr-rich M_3C type) can form [1, 51, 112]. However, the size of such carbides in hot-work tool steels is well below 1 µm [19]. Therefore, we can say they do not directly contribute to the abrasive wear resistance. The precipitation sequence of the M_3C and M_7C_3 during the tempering process greatly depends on the Si content and is, for hot-work tool steels, described in [116]. Details of the microstructure on such a scale (nano-scale) using the TEM technique was not pursued in our investigation. There is a lot of research in the literature regarding TEM evaluations of the microstructure of hot-work tool steel [116, 117]. Nevertheless, from the figures below (Figure 43) we can see that at the highest tempering temperature (specimen 3-A) a more blurred microstructure is observed as a higher level of decomposition of the martensite occurs. Moreover, a larger amount of white phases (precipitated carbides) is observed (Figure 43c*)*, however they started to coarsen.

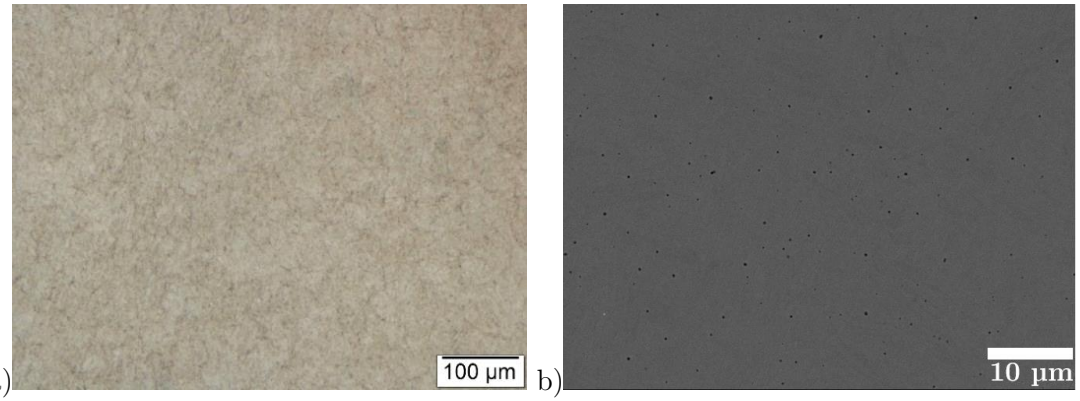

Figure 42: Microstructure of 2-A specimen; etched a) and b) BSE micrograph of polished specimen surface.

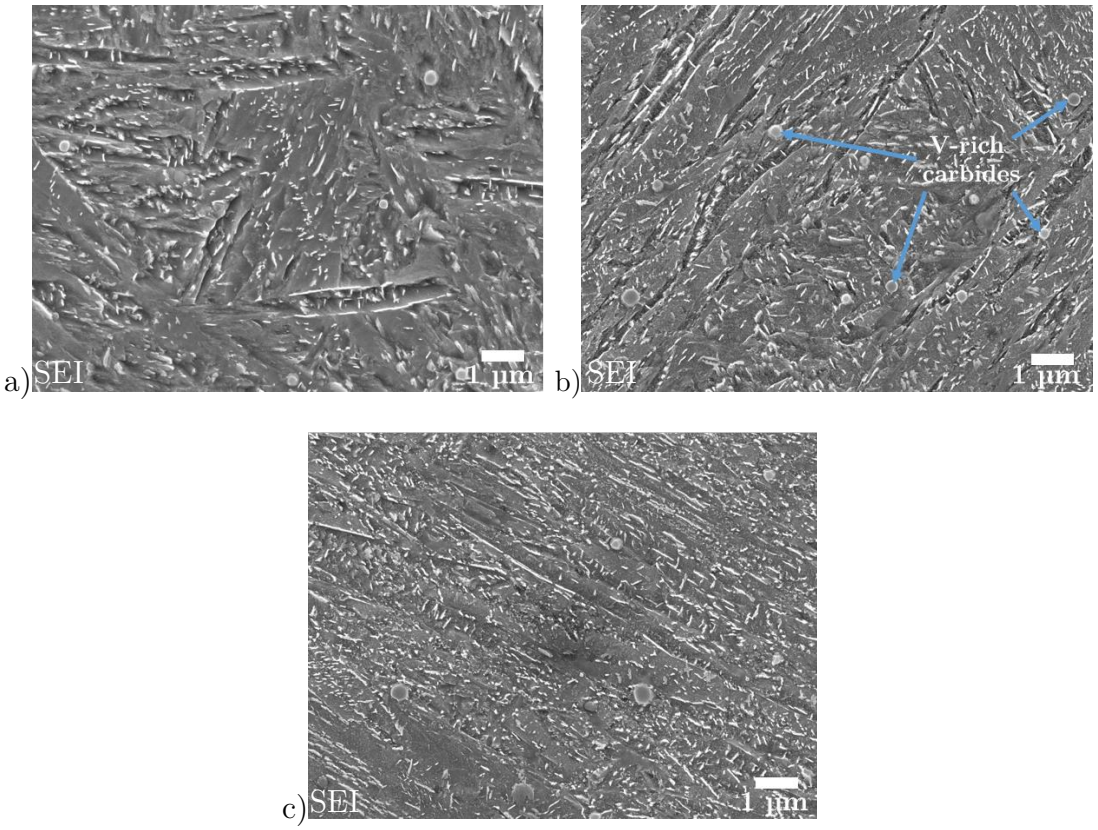

Figure 43: Etched microstructure of tempered hot-work tool-steel specimen at higher magnifications; a) 1-A, b) 2-A and c) 3-A.

6.1.3.2 Mat. No. 1.2363 (material B)

The microstructure of cold-work tool steel Mat. No. 1.2363 (material B) after quenching and tempering is presented in Figure 44 and Figure 45. Similar to the other two cold-work tool steels (material C and D), although in a smaller amount due to the lower concentration of carbon and chromium (1 % C, 5 % Cr), eutectic carbides (white phase) are distributed in the tempered martensite matrix. Eutectic carbides correspond to the chromium-rich carbides of the M_7C_3 type. Besides large eutectic carbides, significant amount of smaller Cr-rich secondary carbides of $M_{23}C_6$ type can also be observed, as shown in Figure 44b and Figure 45. At the recommended austenitization temperature (950 °C) an almost complete transformation into martensite occurred after quenching. Very little retained austenite ($<$ 1.5 %) is left, which is almost completely eliminated after the subsequent tempering [11].

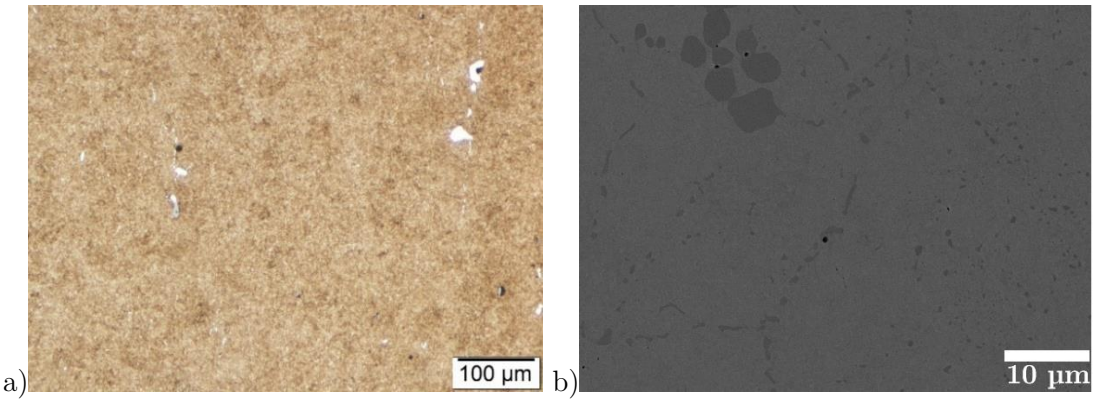

Figure 44: Microstructure of 2-B specimen; etched a) optical and b) BSE micrograph of polished specimen surface.

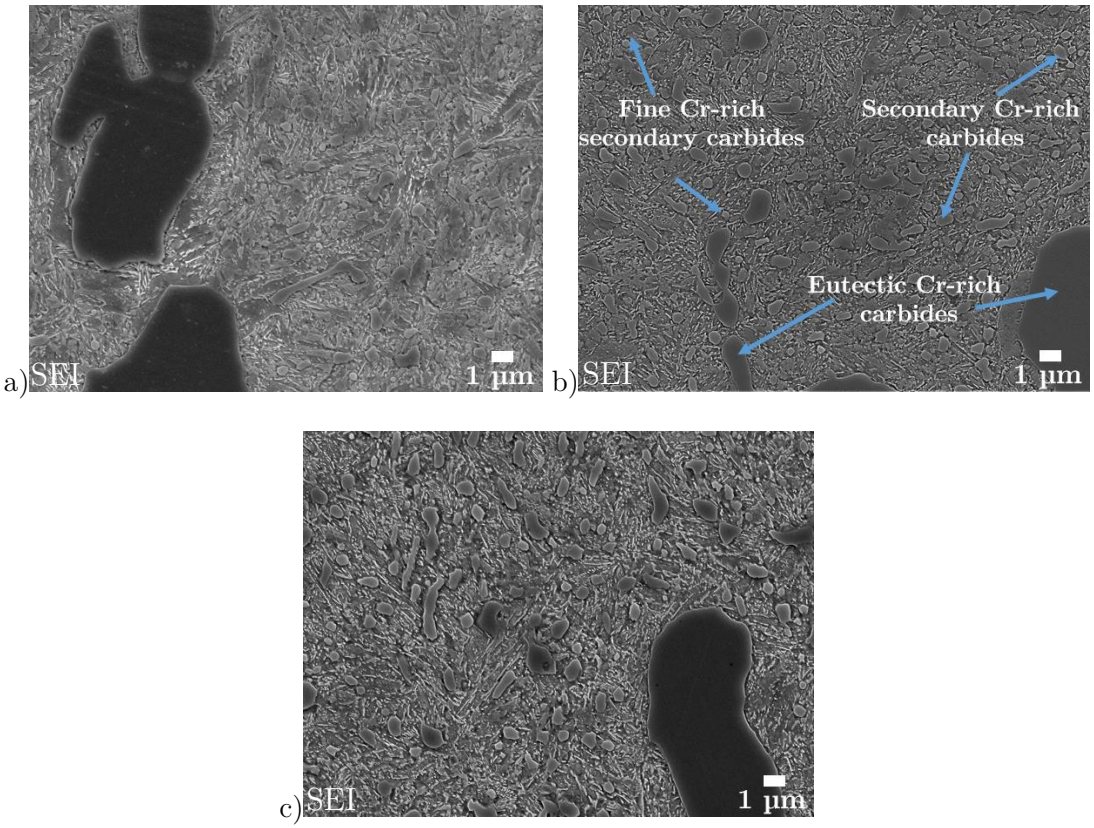

Figure 45: Etched microstructure of tempered cold-work tool-steel specimens at higher magnifications; a) 1-B, b) 2-B and c) 3-B.

6.1.3.3 Mat. No. 1.2990 (material C)

The microstructure of steel Mat. No. 1.2990 (material C) after quenching and tempering to a hardness group 2 (48–50 HRC) is shown in Figure 46 and the evolution of the microstructure with increasing the second tempering temperature is presented in Figure 47. Compared to the D material the average size of the coarse carbides in the steel C is reduced to 5–10 µm. Furthermore, OM micrographs also indicate a lesser amount of such

carbides, as well as a lesser amount and significantly smaller fine carbides (white phases), which is in accordance with the literature [83] and confirmed by the SEM analysis. Besides larger chromium-rich carbides, a significant amount of smaller secondary Cr-rich carbides (grey phase) and V-rich carbides (black phase) could be observed (Figure 46b). Those are evenly distributed through the tempered martensite matrix. Due to the large quantities of vanadium in this steel, coupled with the high carbon content, the volume fraction and the size of fine V-rich carbides are not negligible.

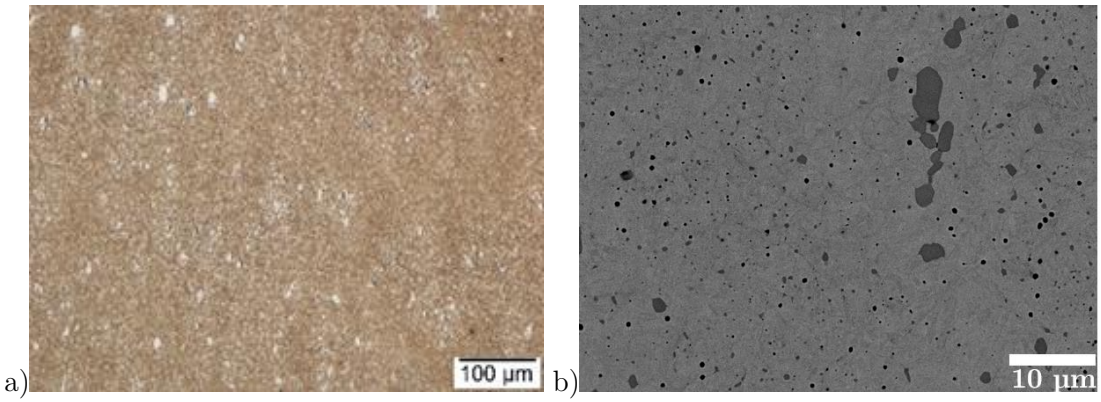

Figure 46: Microstructure of 2-C specimen; etched a) optical and b) BSE micrograph of polished specimen surface.

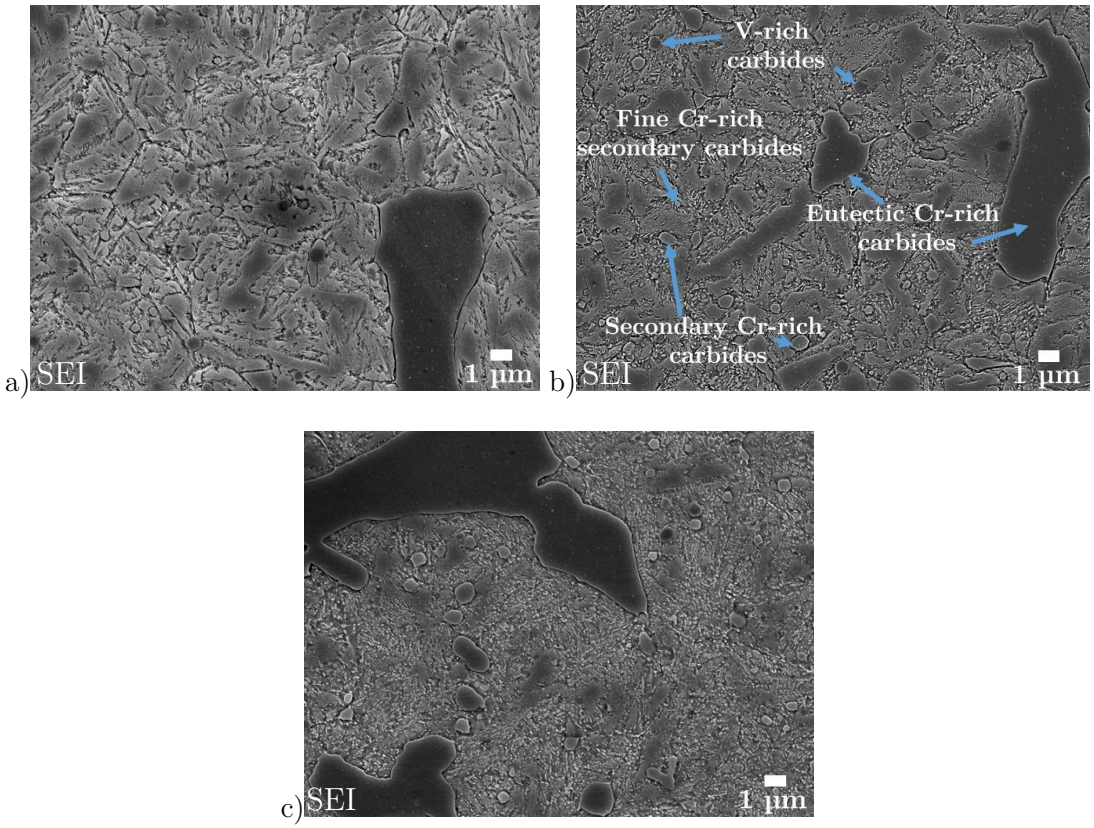

Figure 47: Etched microstructure of tempered cold-work tool-steel specimens at higher magnifications; a) 1-C, b) 2-C and c) 3-C.

6.1.3.4 Mat. No. 1.2379 (material D)

The microstructure of heat-treated cold-work tool steel Mat. No. 1.2379 (material D), following the recommended heat-treatment procedure and the austenitizing temperatures clearly show the presence of a large amount of carbides in the matrix of tempered martensite (Figure 48 and Figure 49). A high density of large eutectic M_7C_3 carbides with a significant amount of smaller secondary $M_{23}C_6$ carbides can be observed (large and small dark-grey phases on the composition-contrast-based BSE image; Figure 48b). Both carbides are typical carbide types in chromium-containing cold-work tool steels. Coarse eutectic M_7C_3 carbides form during the solidification process due to high fraction of carbide-forming elements [1]. Reports state that the fraction of coarse carbides in Mat. No. 1.2379 cold-work tool steel ranges between 7 and 15 % with an average size of 15–20 µm [83, 89]. In the current case, tempering temperatures were above the temperatures commonly used for this type of steel in order to achieve the same hardness level for all the tool steels included in the investigation. Higher tempering temperatures result in an increased amount of fine secondary carbides, as well as in carbide coarsening [44]. Furthermore, higher tempering temperatures also cause enrichment of the eutectic and coarse secondary carbides in the Fe content. The tempering temperature also affects the sequence of carbide precipitation. It has been reported that the precipitation sequence is: $M_3C \rightarrow M_7C_3 \rightarrow M_{23}C_6$, with increasing the tempering temperature [9], as already discussed earlier (Subchapter 2.2.1). The precipitation of Cr carbides occurs at lower and intermediate tempering temperatures and iron-rich carbides enriched with Cr at higher temperatures. This indicates the decomposition of martensite into ferrite and, an as yet unmentioned, but very abundant carbide form, orthorhombic cementite (M_3C) [6]. Another microstructure constituent in high-alloy tool steels is retained austenite. Generally, the higher are the austenitizing temperatures, the more the austenite is enriched with carbide-forming elements, which makes it highly stable with respect to martensite formation [118]. However, in the current case the specimens were austenitized at intermediate temperatures (1020 °C) and immediately double tempered at temperatures above 500 °C, thus reducing the retained austenite fraction to a very low level. This was confirmed by the X-ray diffraction (XRD) measurements. For all the steels investigated and all the three hardness groups the retained austenite fraction of below 1.5 % was identified.

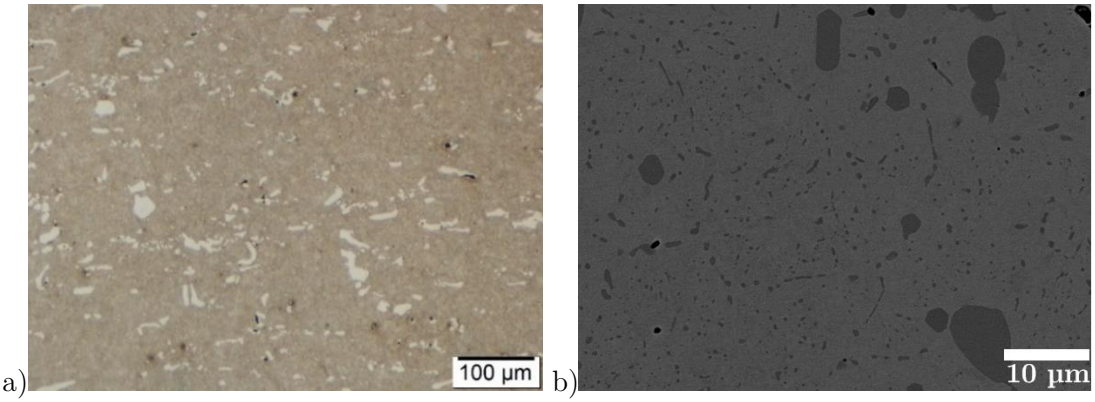

Figure 48: Microstructure of 2-D specimen; etched a) optical and b) BSE micrograph of polished specimen surface.

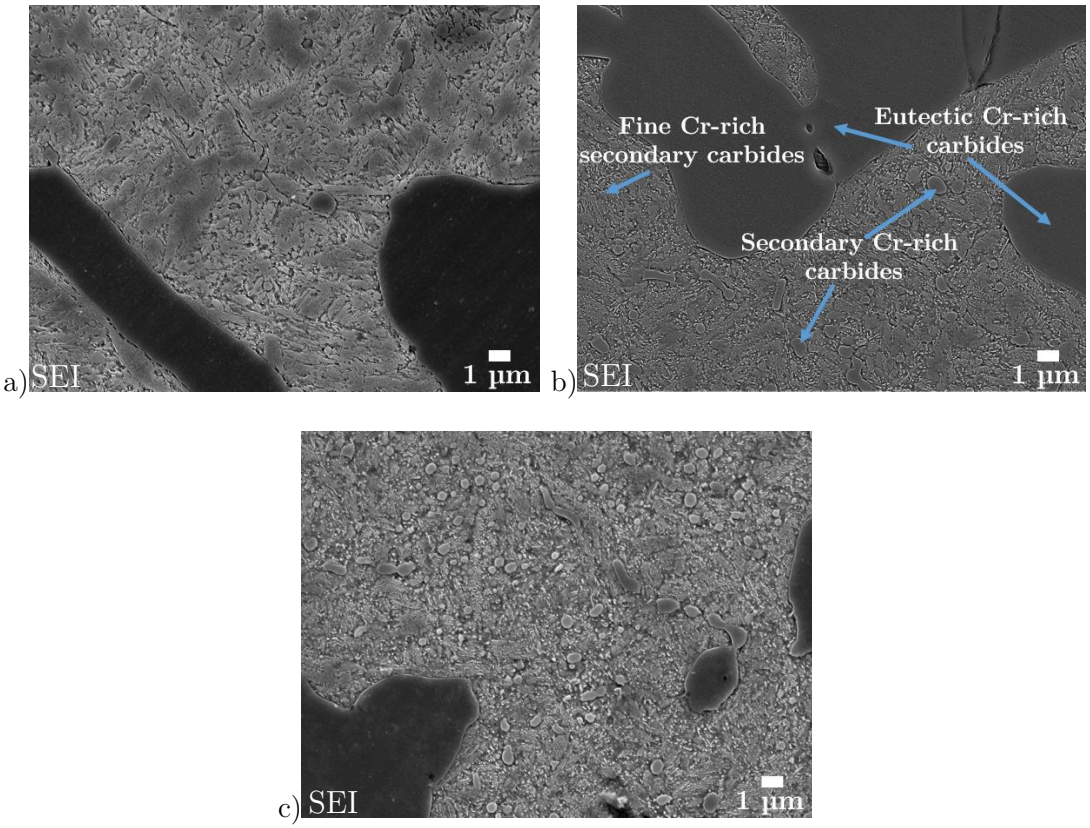

Figure 49: Etched microstructure of tempered cold-work tool-steel specimens at higher magnifications; a) 1-D, b) 2-D and c) 3-D.

6.1.4 Carbide fraction and distribution

The volume fraction of the small (<600 nm) undissolved carbides in hot-work tool-steel specimens subjected to different austenitizing temperatures is shown in Table 13. The highest volume fraction was found for the lowest austenitization temperature of 950 °C, being 0.9 %, including 0.4 % of $M_{23}C_6$ cubic Cr/Mo rich carbides and 0.5 % of small V-rich MC-type carbides. The fraction of vanadium-rich carbides is reduced with an increased austenitization temperature, with their fraction at 1030 °C being 0.3 %. At the highest austenitization temperature of 1150 °C, almost all the V-rich carbides are dissolved into the matrix.

Table 13: Volume fraction (in %) of undissolved Cr/Mo- and V-rich carbides of as-quenched specimens, determined by INCA Feature analysis over 10 randomly selected areas of ≈ 200 × 200 µm^2.

Austenitization temperature	**un-dissolved MC type carbides/carbo-nitrides (V rich) [%]**	**un-dissolved $M_{23}C_6$ type carbides (Cr/Mo rich) [%]**
1150 °C	0.01±0.01	/
1030 °C	0.3±0.1	/
950 °C	0.5±0.1	0.4±0.1

For the tempered specimens P1, P2 and P3, slightly higher values of detected carbides were obtained (Table 14). However, the trend is similar as for the as-quenched specimens. The highest fraction of carbides is shown by the specimen austenitized and tempered at the lowest temperatures (P3), with the overall carbide volume fraction of just over 1.2 %. It is followed by specimen P2 (hardened according to the recommended heat treatment), having 0.4 % of mainly MC vanadium-rich carbides. The specimen hardened at the highest temperatures (P1) again shows a substantially lower carbide fraction of just 0.03 %. The average size of the carbides, being residual and precipitated, present in quenched and tempered specimens of hot-work tool steel, is shown in Figure 50.

Table 14: Volume fraction (in %) of Cr/Mo- and V-rich carbides in quenched and tempered specimens, determined by INCA Feature analysis over 10 randomly selected areas.

Specimen	**MC type carbides/carbo-nitrides (V rich) [%]**	**$M_{23}C_6$ type carbides (Cr/Mo rich) [%]**
P1	0.03±0.03	/
P2	0.4±0.1	/
P3	0.7±0.2	0.5±0.2

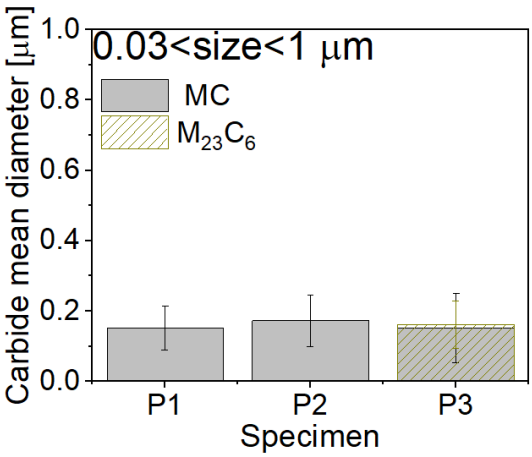

Figure 50: Carbides' mean diameter for MC and $M_{23}C_6$ types present in hot-work tool steel (material A) when subjected to different austenitization and tempering temperatures.

Table 15 shows the volume fraction (in %) of carbides in the investigated cold-work tool steels after tempering. The highest fraction of carbides is found in material D, having up to 12 % of carbides present in the martensite matrix, with a very high fraction of eutectic carbides (up to 7 %). This is expected as the carbide fraction greatly depends on the chemical composition of the steel and is in agreement with other studies [88, 89]. The second-highest carbide fraction is present in tool steel C, (up to 6. 4 %), which also shows up to 1 % of MC-type carbides rich in vanadium. On average, 2 % of eutectic carbides was detected in this steel. Cold-work tool-steel B had the lowest carbide fraction among all the cold-work tool steels investigated, with up to 4.8 %. However, the lowest carbide fraction is shown by the hot-work tool steel (material A; up to 0.5 %). In this case only V-rich carbides were detected with the available techniques. Nevertheless, other Cr-rich carbides (M_7C_3 and $M_{23}C_6$) can also be present, as already described in Chapter 6.1.1.

Table 15: Volume fraction (in %) of detected Cr- and V-rich carbides in the tempered tool-steel specimens determined by INCA Feature analysis over 10 randomly selected areas (≈ 200 × 200 µm² for carbides < 1 µm and 1x1 mm² for carbides > 1 µm²)

Specimen	Cr-rich C [%]			V-rich C [%]	Total [%]
	EC	LSC	SSC		
1-A				0.4±0.1	0.4
2-A				0.4±0.2	0.4
3-A				0.5±0.1	0.5
w-B	0.5 ±0.1	0.9±0.8	2.2±0.7		3.6
1-B		1.3±0.9	1.9±0.3		3.7
2-B		1.9±0.9	2.3±0.7		4.8
3-B		1.1±0.5	1.7±0.3		3.3
1-C	2.0 ±0.3	1.8±0.6	1.6±0.6	0.9±0.1	6.3
2-C		2.0±1.0	1.4±0.4	0.9±0.2	6.4
3-C		2.1±0.8	1.2±0.4	1.0±0.2	6.3
w-D	6.9 ±0.7	2.3±0.9	2.4±0.8		11.6
1-D		2.7±1.3	2.2±0.3		11.8
2-D		3.0±1.0	2.4±0.4		12.2
3-D		3.0±0.5	2.6±0.5		12.5

EC – eutectic carbides; LSC – large secondary carbides; SSC – small secondary carbides

The carbides' distribution in terms of density (relative frequency) and size (equivalent circle diameter – ECD) in the investigated steels after the recommended heat-treatment to a certain hardness group is presented in Figures 51-62. In Figure 51 to Figure 53 for Cr-rich carbides larger than 5 µm, in Figure 54 to Figure 56 for Cr-rich carbides ranging between 1 and 5 µm and in Figure 57 to Figure 59 for Cr-rich carbides smaller than 1 µm. Since no Cr-rich carbides could be detected in the hot-work tool steel (material A) using the INCA feature counting, only the results for cold-work tool steels are presented. The distribution of the V-rich MC-type carbides found in hot-work tool steel (material A) and cold-work tool steel (material C), which are smaller than 1 µm is shown in Figure 60 and for V-rich carbides larger than 1 µm in Figure 61. The majority of carbides (Cr and/or V-rich) found in all four tool steels investigated are smaller than 1 µm. However, the carbides' size distribution among specimens of the same material, but different hardness level, still varies. This is mainly due to the non-uniform distribution of the carbides. Steels that contain large quantities of carbon and carbide-forming elements are prone to segregation during the solidification process. This results in areas of the microstructure with clusters of massive eutectic carbides and thus in their increase in density and greater scattering.
In terms of Cr-rich carbides, the smallest number was found in the size range larger than 5 µm, which is true for all the hardness groups and all three cold-work tool steels investigated. However, the influence of the larger carbides on the surface hardness is higher as they are covering a larger area of the surface, as will be discussed later (Chapter 6.2.2). The highest density of chromium-rich carbides larger than 5 µm, classified as M_7C_3 type eutectic carbides was observed in cold-work tool steel D, having almost up to 30 particles/mm² in the 5–6 µm range. Nevertheless, even for larger carbides the size density of the large carbides remains quite high, as compared to other cold-work tool steels at a similar hardness level (Figures 51-53).

A similar distribution of large Cr-rich carbides was observed for cold-work tool steel C, with the highest density of large Cr-rich carbides found in the 5–6 µm range and followed by a steep decrease. Only a few eutectic carbides larger than 10 µm are present in the matrix of material C (Figure 51b, Figure 52b, Figure 53b). This is due to the lower quantities of carbon (1 %) and carbide-forming elements such as Cr (8 %) as compared to cold-work tool steel D (1.5 % C and 12 % Cr). In the case of cold-work tool steel B, the density of Cr-rich carbides larger than 5 µm is significantly lower compared to the other two cold-work tool steels. The highest density of those carbides is in the 5–6 µm range; however, never reaching more than 10 carbides/mm^2. This is true for specimens in all three hardness groups (Figure 51a, Figure 52a and Figure 53a).

The largest mean diameter of the large Cr-rich eutectic carbides (EC) is shown by cold-work tool steel D (≈ 10 µm), followed by steel B (≈ 8.7 µm) and steel C (≈ 7.5 µm).

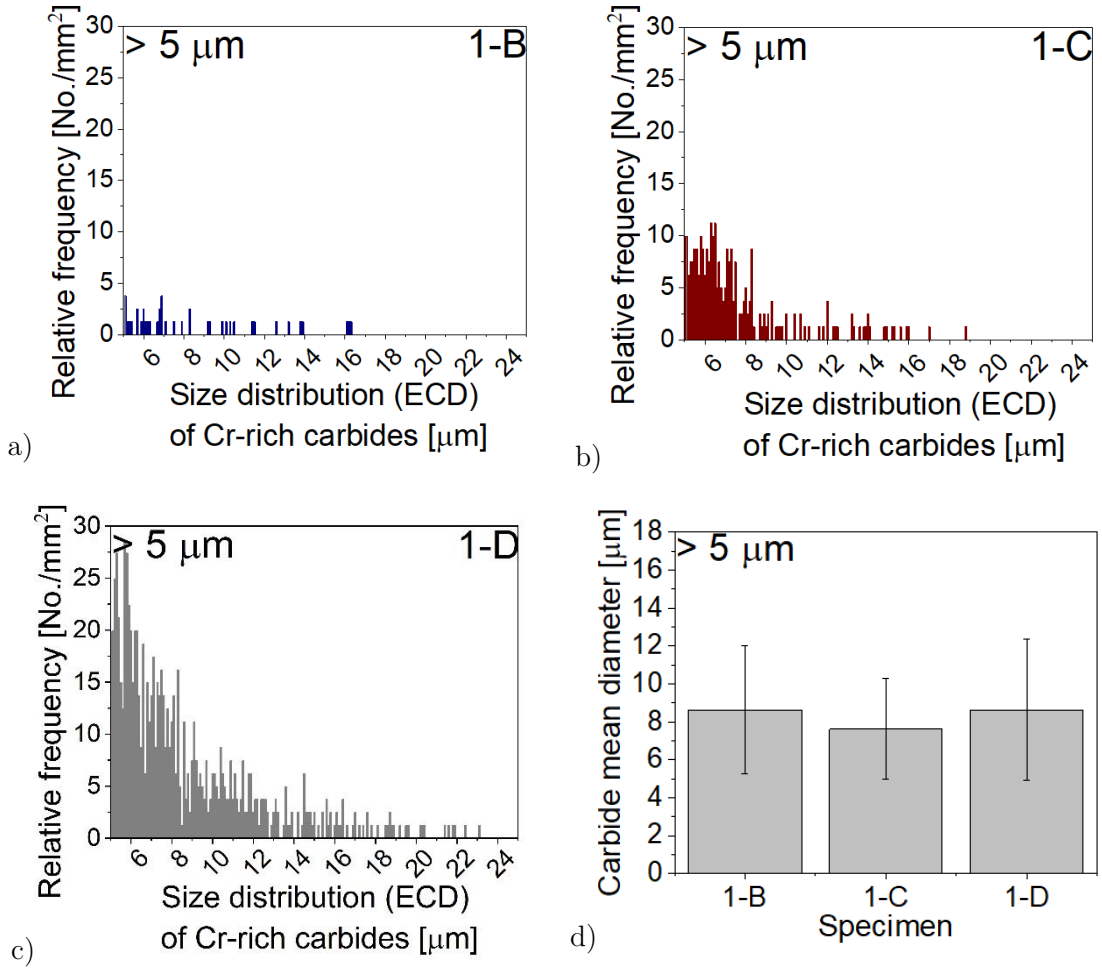

Figure 51: Size distribution of Cr-rich carbides larger than 5 µm for hardness group 1; specimens a) 1-B, b) 1-C, c) 1-D and d) carbides mean diameter.

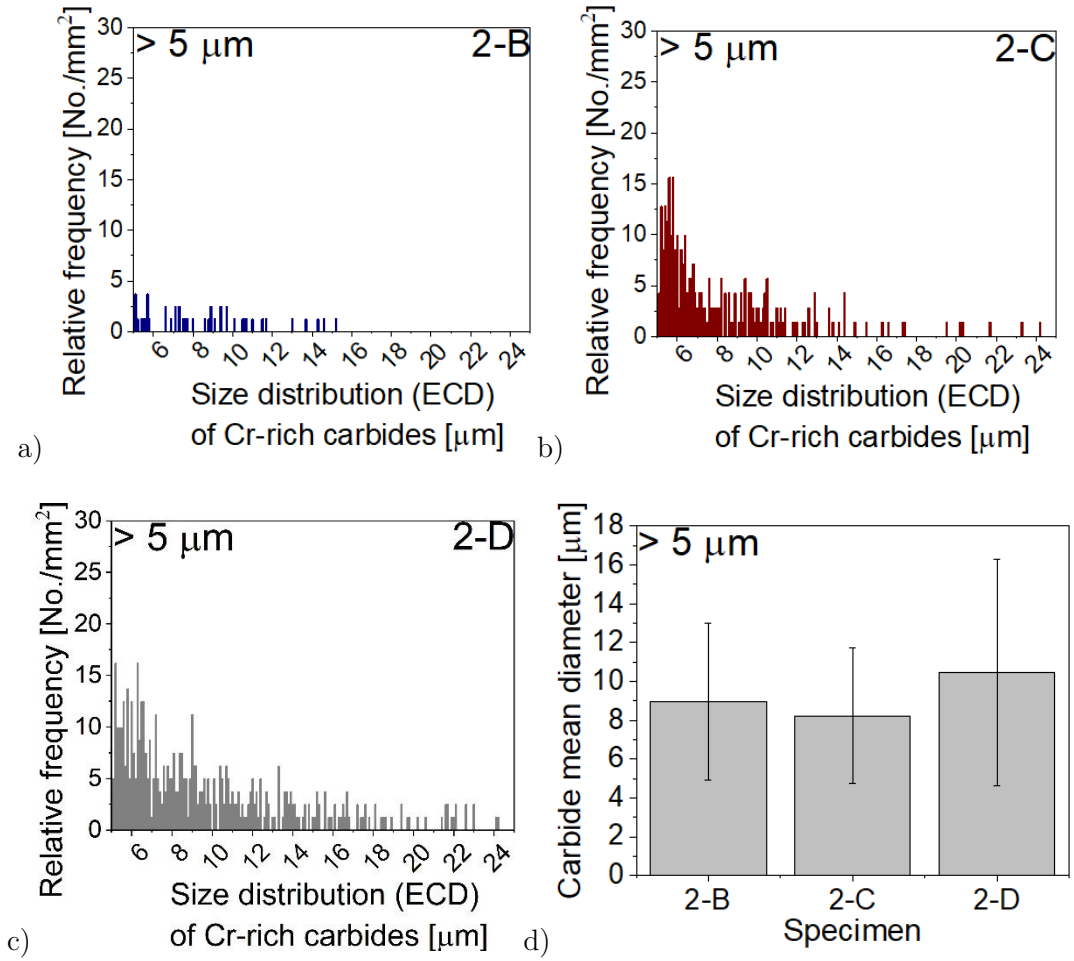

Figure 52: Size distribution of Cr-rich carbides larger than 5 µm for hardness group 2; specimens a) 2-B, b) 2-C and c) 2-D and d) carbides mean diameter.

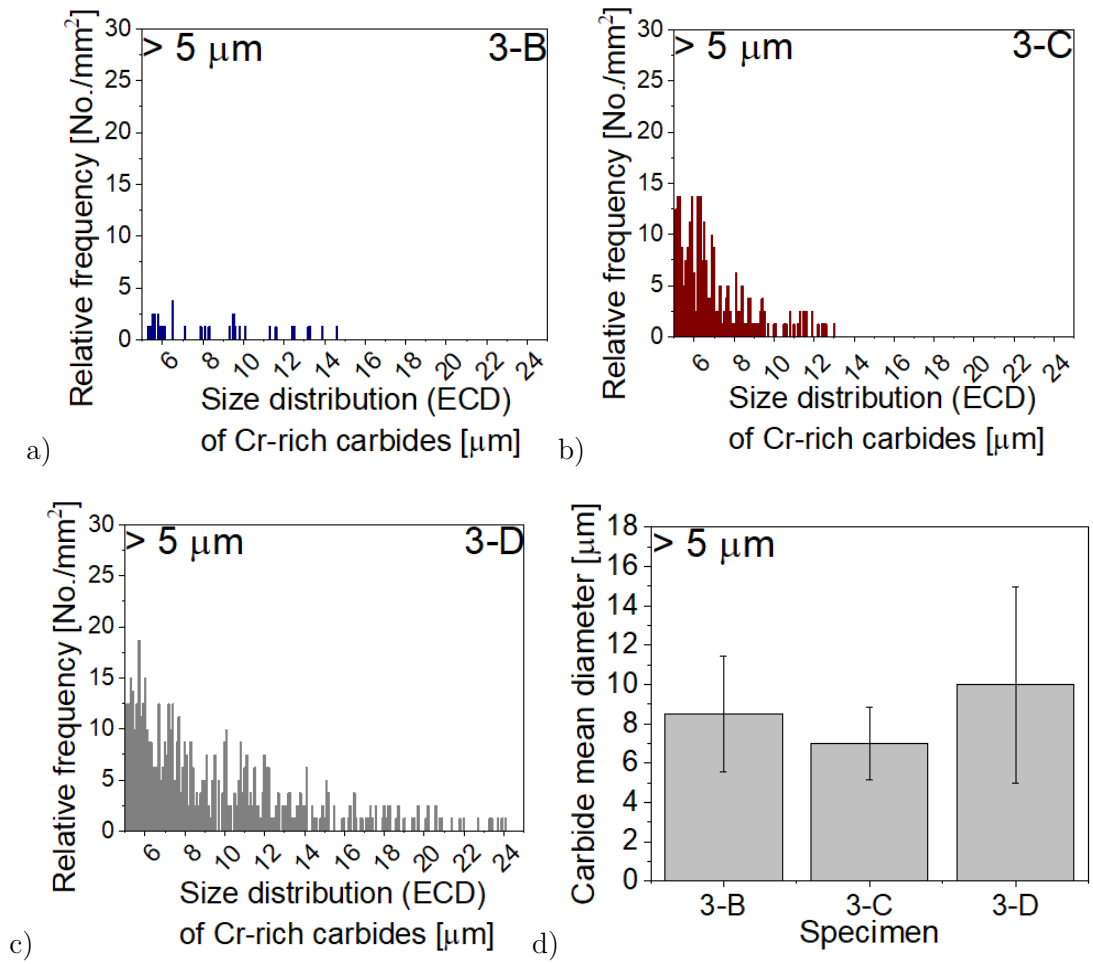

Figure 53: Size distribution of Cr-rich carbides larger than 5 µm for hardness group 3; specimens a) 3-B, b) 3-C and c) 3-D and d) carbides mean diameter.

Analysing the group of large secondary carbides (size between 1 µm and 5 µm) a steep decrease in the carbides' density with sizes above 1 µm is present for cold-work tool steels B and D in all the hardness groups (Figure 54, Figure 55 and Figure 56). Material B also shows the highest density of secondary Cr-rich carbides in the 1-µm size range (≈1700 carbides/mm^2). Material C, on the other hand, displays a more uniform distribution of carbides between 1 µm and 5 µm, indicated by slower flattening of the size-distribution curve (Figure 54b, Figure 55b, and Figure 56b). For steel B the larger Cr-rich secondary carbides are mainly in the 1–1.5 µm range, with about 3600 particles/mm^2. In the case of steel C, larger secondary carbides are up to 2.5 µm, in total averaging at about 6500 particles/mm^2. For steel D the larger Cr-rich secondary carbides stretch even above 3.5 µm, resulting in over 7500 particles/mm^2, the highest density of larger secondary carbides/mm^2 among the tool steels investigated. Looking at the secondary carbides mean diameter for the 1–5 µm size group, the largest of about 2 µm is displayed by steel D, followed by steel C (1.65 µm) and steel B (1.25 µm), being more or less independent of the hardness group (Figure 54d, Figure 55d and Figure 56d).

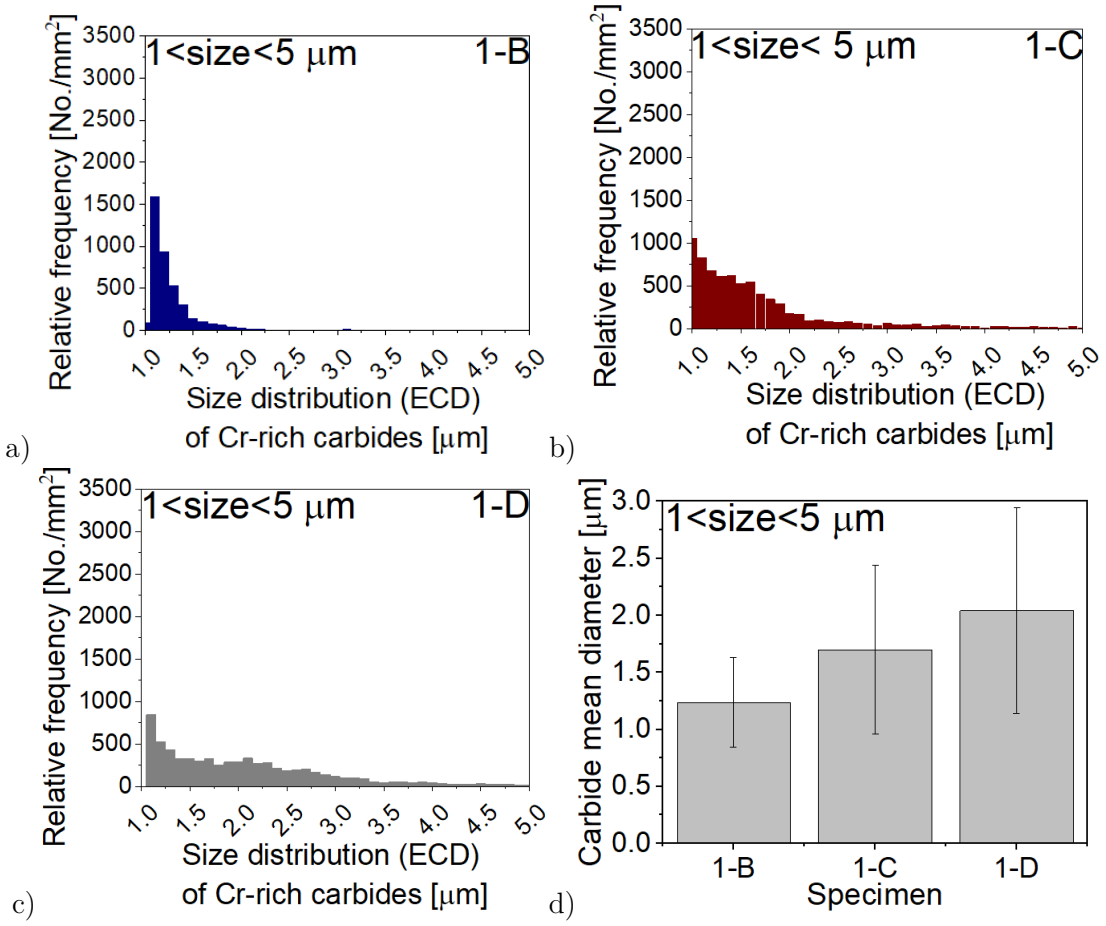

Figure 54: Size distribution of larger Cr-rich secondary carbides ranging between 1 and 5 µm for hardness group 1; specimens a) 1-B, b) 1-C and c) 1-D and d) carbides mean diameter.

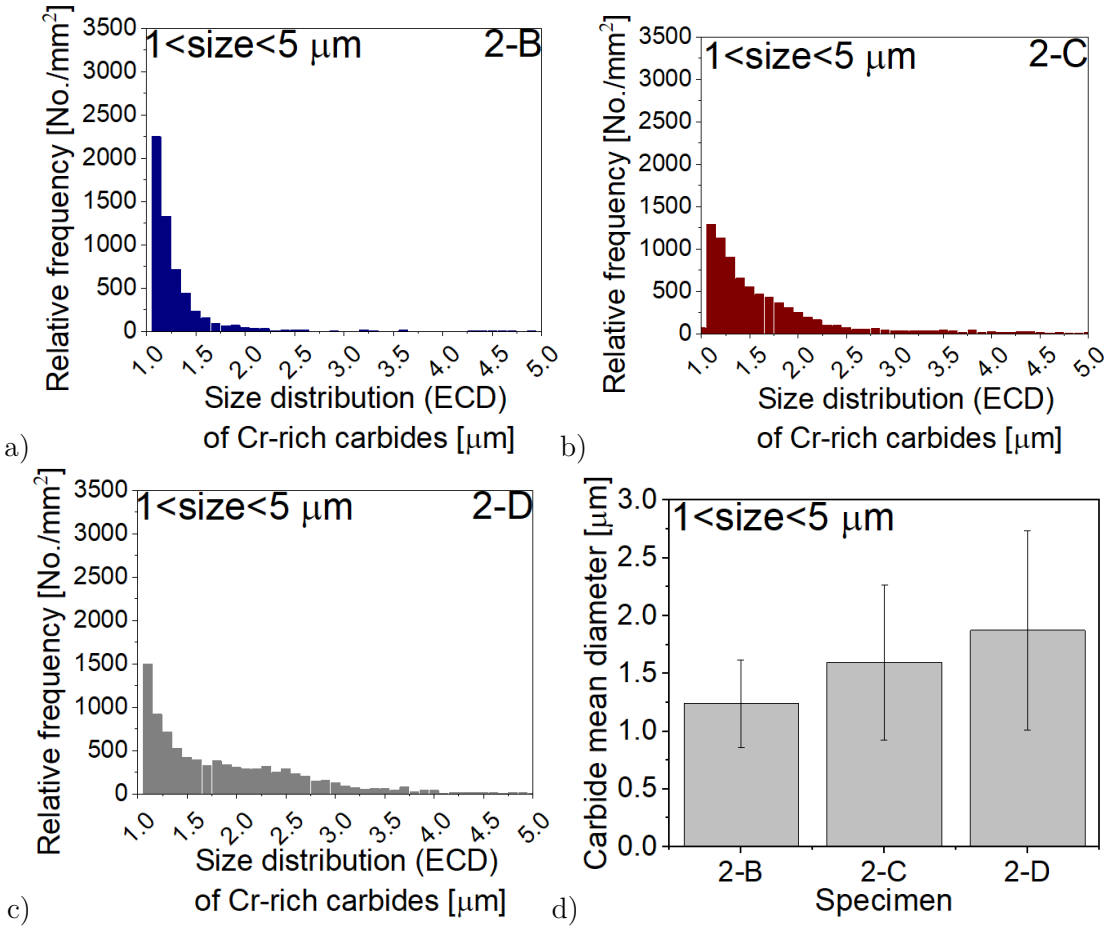

Figure 55: Size distribution of larger Cr-rich secondary carbides ranging between 1 and 5 µm for hardness group 2; specimens a) 2-B, b) 2-C and c) 2-D and d) carbides mean diameter.

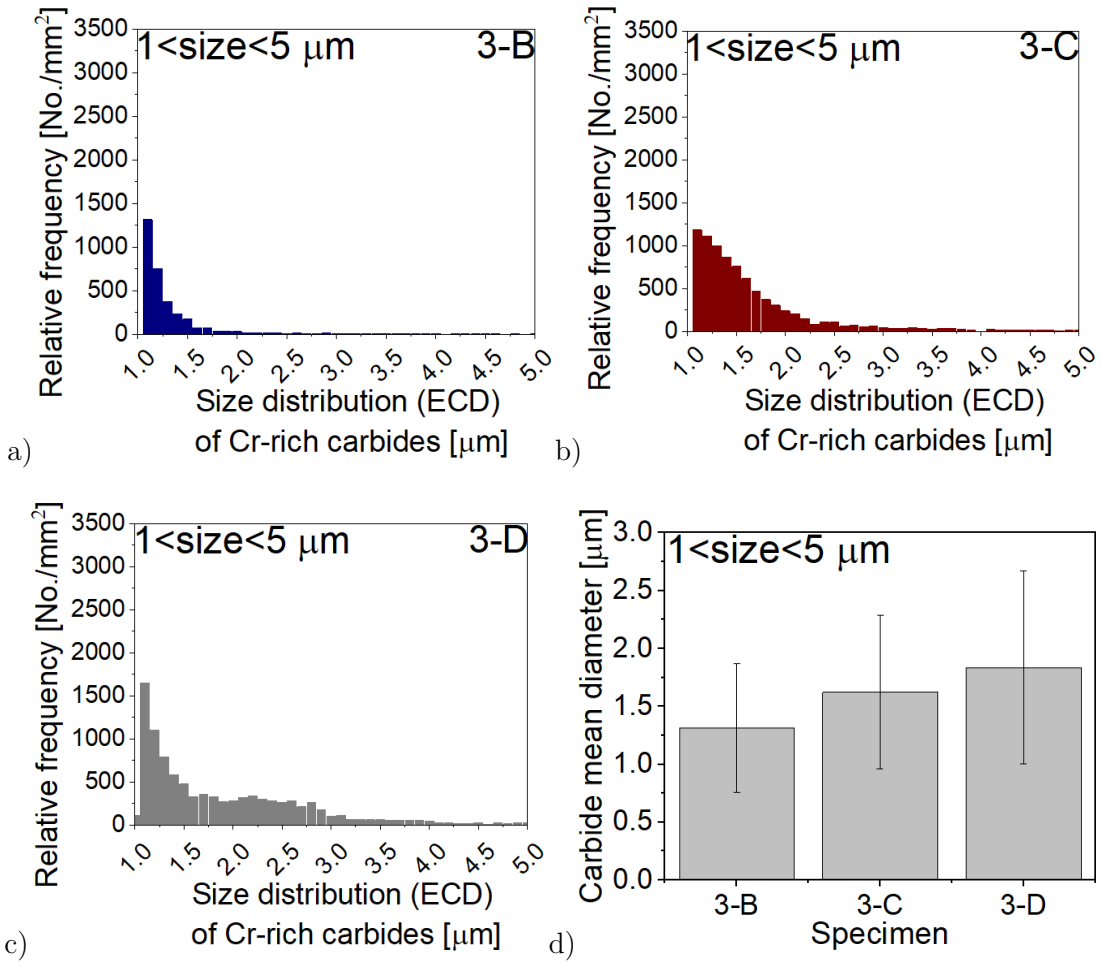

Figure 56: Size distribution of larger Cr-rich secondary carbides ranging between 1 and 5 µm for hardness group 3; specimens a) 3-B, b) 3-C and c) 3-D and d) carbides mean diameter.

Finally, for the submicron sized Cr-rich secondary carbides, the carbide-density results are presented in Figure 57, Figure 58 and Figure 59. For the investigated cold-work tool steels the smaller Cr-rich secondary carbides are mainly in 0.1–0.5 µm range with a much higher density compared to the large carbides (>1 µm). However, their areal coverage contribution is considerably smaller. In the case of steel B the peak number of carbides of about 12000 particles/mm^2 is observed for carbides ≤ 0.1 µm, followed by a step decrease towards larger carbides (Figure 57a and Figure 59a). For steel C, smaller Cr-rich secondary carbides are mainly in 0.1–0.2 µm range, with up to about 5000 carbides/mm^2 in certain size class. In the case of steel D, however, smaller Cr-rich secondary carbides are more evenly distributed in a larger size range, even up to 0.5 µm, with their number increasing with a higher tempering temperature (Figure 57c, Figure 58c and Figure 59c). On average, in the size range from 0.1 to 0.3 µm the total number of Cr-rich secondary carbides ranges from 150,000 to 180,000 carbides/mm^2. For the SSC group of carbides, all three cold-work tool steels show a very similar mean diameter of about 0.6 µm, as shown in Figure 57d, Figure 58d and Figure 59d.

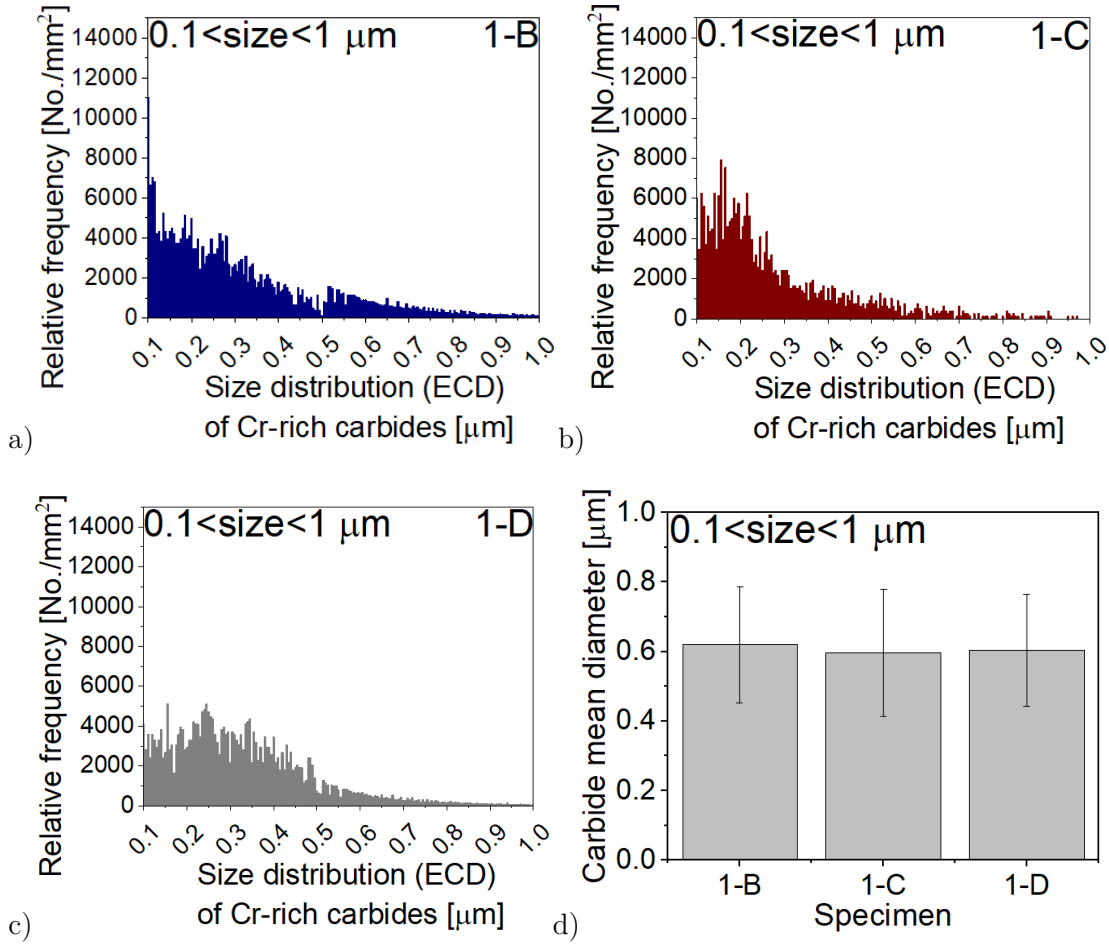

Figure 57: Size distribution of small Cr-rich carbides for hardness group 1; specimens a) 1-B, b) and 1-C c) 1-D and d) carbides mean diameter.

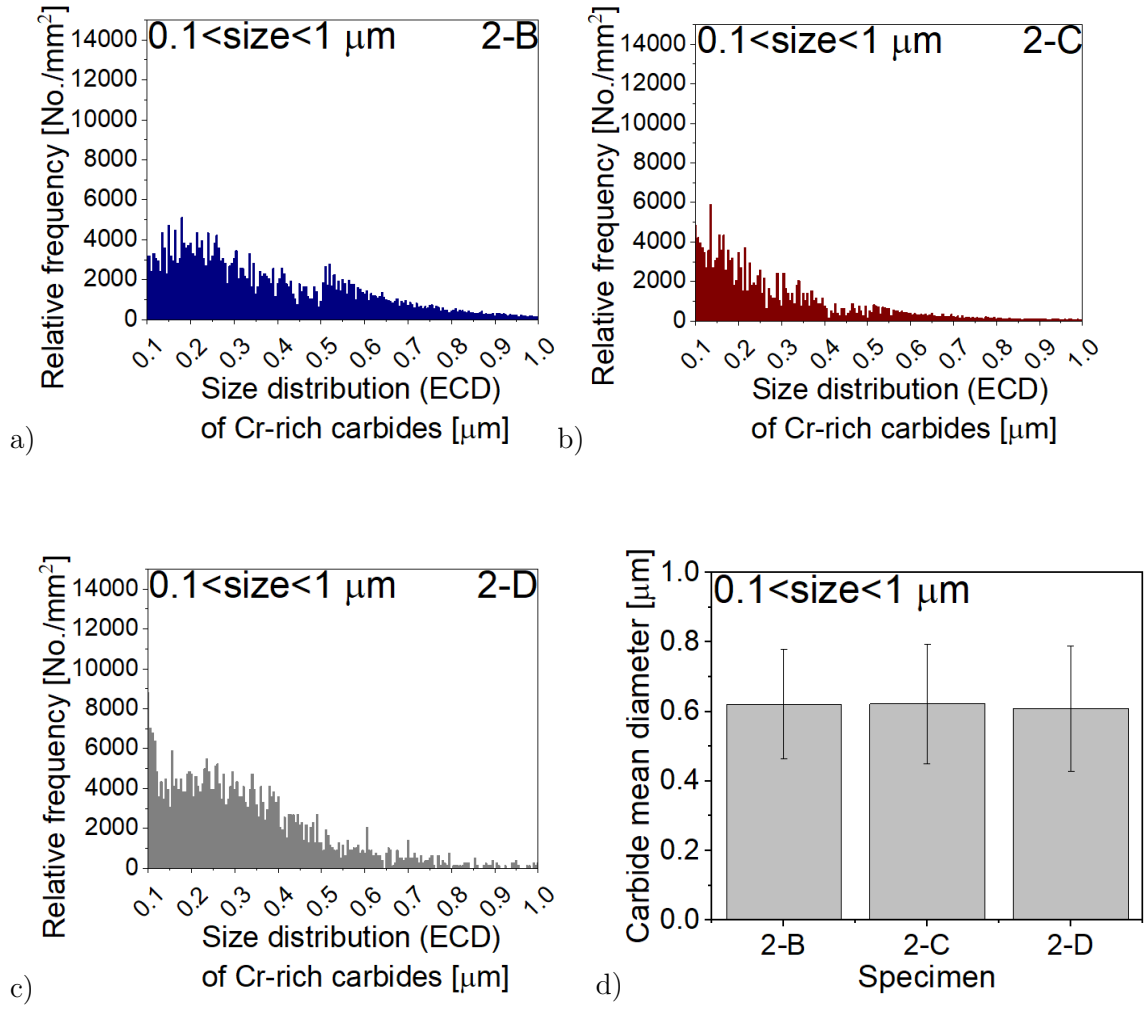

Figure 58: Size distribution of small Cr-rich carbides for hardness group 2; specimens a) 2-B, b) 2-C and c) 2-D and d) carbides mean diameter.

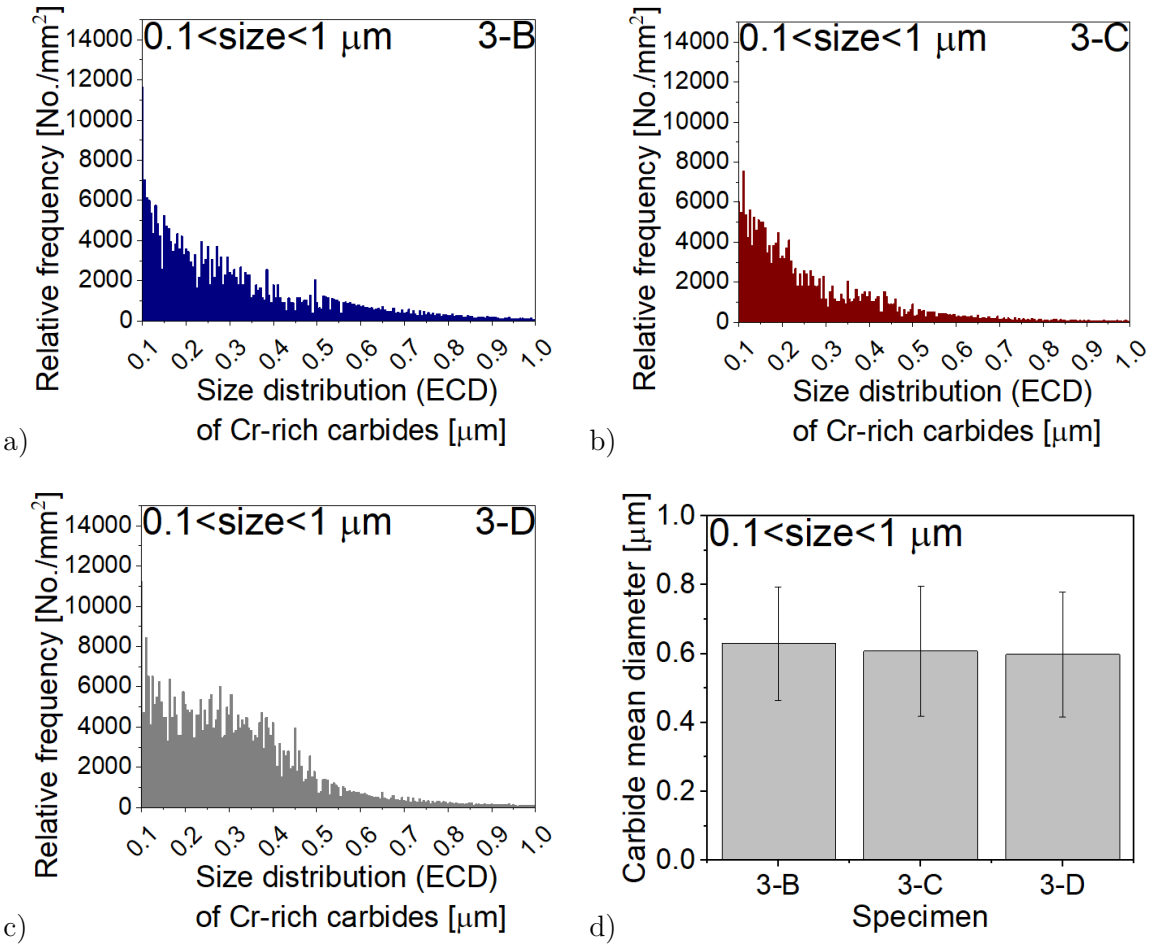

Figure 59: Size distribution of small Cr-rich carbides for hardness group 3; specimens a) 3-B, b) 3-C and c) 3-D and d) carbides mean diameter.

Besides small Cr-rich carbides, cold-work tool steel C (Mat. No. 1.2990) also includes a large amount of fine V-rich MC-type carbides, a significantly larger fraction compared to the other tool steels in this study (Figure 60 and Figure 61). The highest density of V-rich carbides was found for the smallest carbides, ranging below 0.5 µm, but mainly being smaller than 0.3 µm (Figure 60b, d, f). However, also V-rich carbides larger than 1 µm and up to 8 µm can be found in steel C, albeit in a relatively small number, as shown in Figure 61. The average size of small V-rich carbides is 0.3 µm and for large ones, about 4 µm (Figure 60g and Figure 61d).

In the case of hot-work tool steel A (Mat. No. 1.2367 mod.) only fine V-rich carbides were detected, with an average of 138,000 particles per mm^2. For all three hardness groups, the majority of carbides is in the 0.2-µm range (Figure 60g). The particles' density starts to significantly decrease as the carbides become larger, as shown in Figure 60a, c and e. Furthermore, this steel does not contain any type of wear-resistant carbides larger than 1 µm.

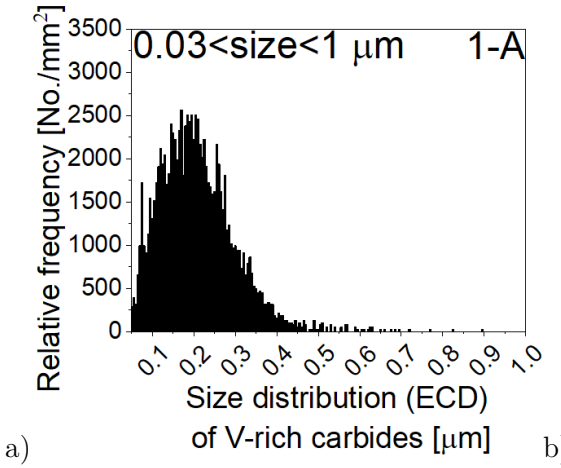
0.03<size<1 μm
1-A
Relative frequency [No./mm²]
Size distribution (ECD)
of V-rich carbides [μm]

a)

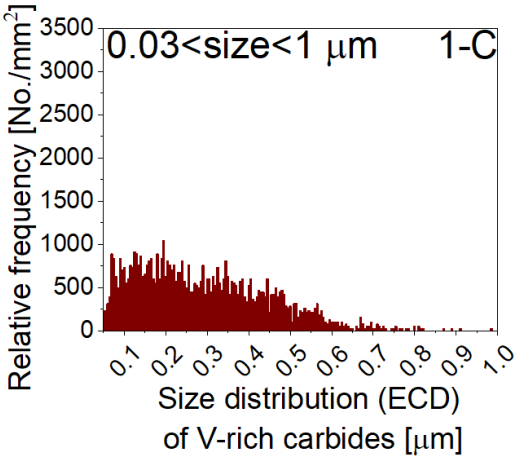
0.03<size<1 μm
1-C
Relative frequency [No./mm²]
Size distribution (ECD)
of V-rich carbides [μm]

b)

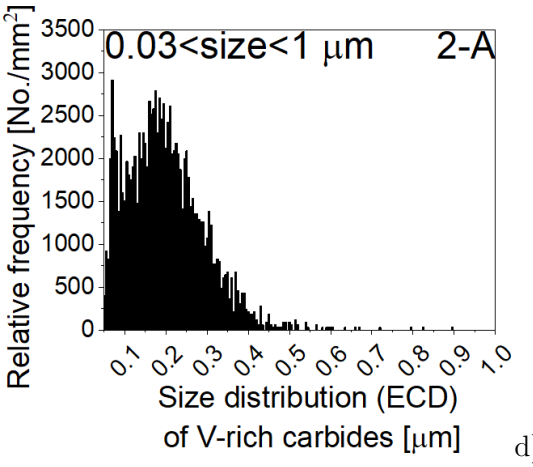
0.03<size<1 μm
2-A
Relative frequency [No./mm²]
Size distribution (ECD)
of V-rich carbides [μm]

c)

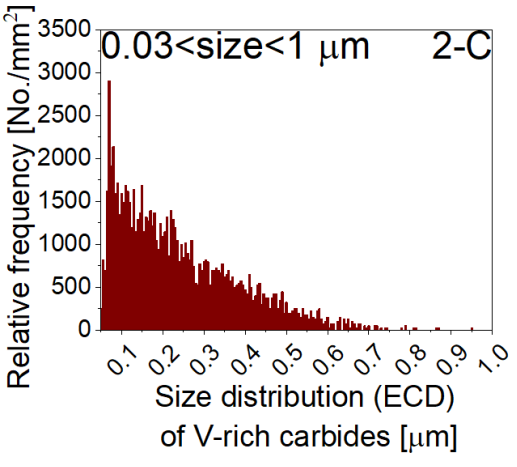
0.03<size<1 μm
2-C
Relative frequency [No./mm²]
Size distribution (ECD)
of V-rich carbides [μm]

d)

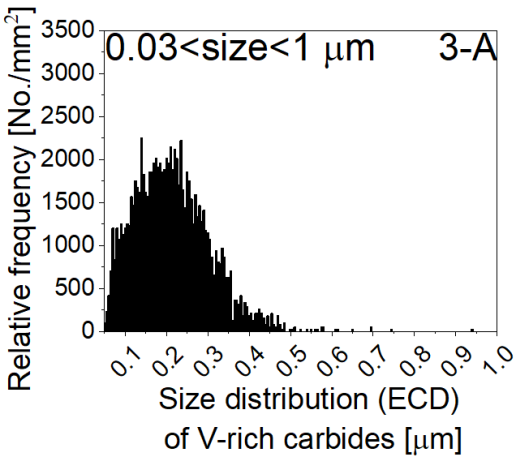
0.03<size<1 μm
3-A
Relative frequency [No./mm²]
Size distribution (ECD)
of V-rich carbides [μm]

e)

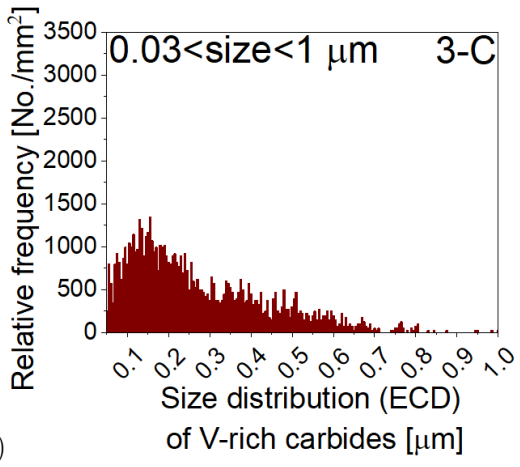
0.03<size<1 μm
3-C
Relative frequency [No./mm²]
Size distribution (ECD)
of V-rich carbides [μm]

f)

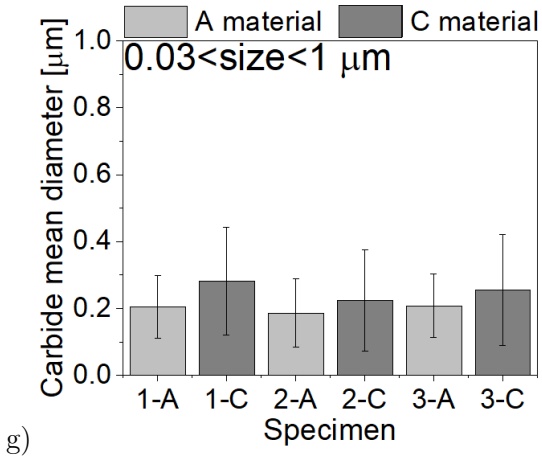

g)

Figure 60: Size distribution of fine V-rich carbides for tool steels A and C and hardness groups 1, 2 and 3; specimens a) 1-A, c) 2-A ,e) 3-A and b) 1-C, d) 2-C and f) 3-C g) carbides mean diameter.

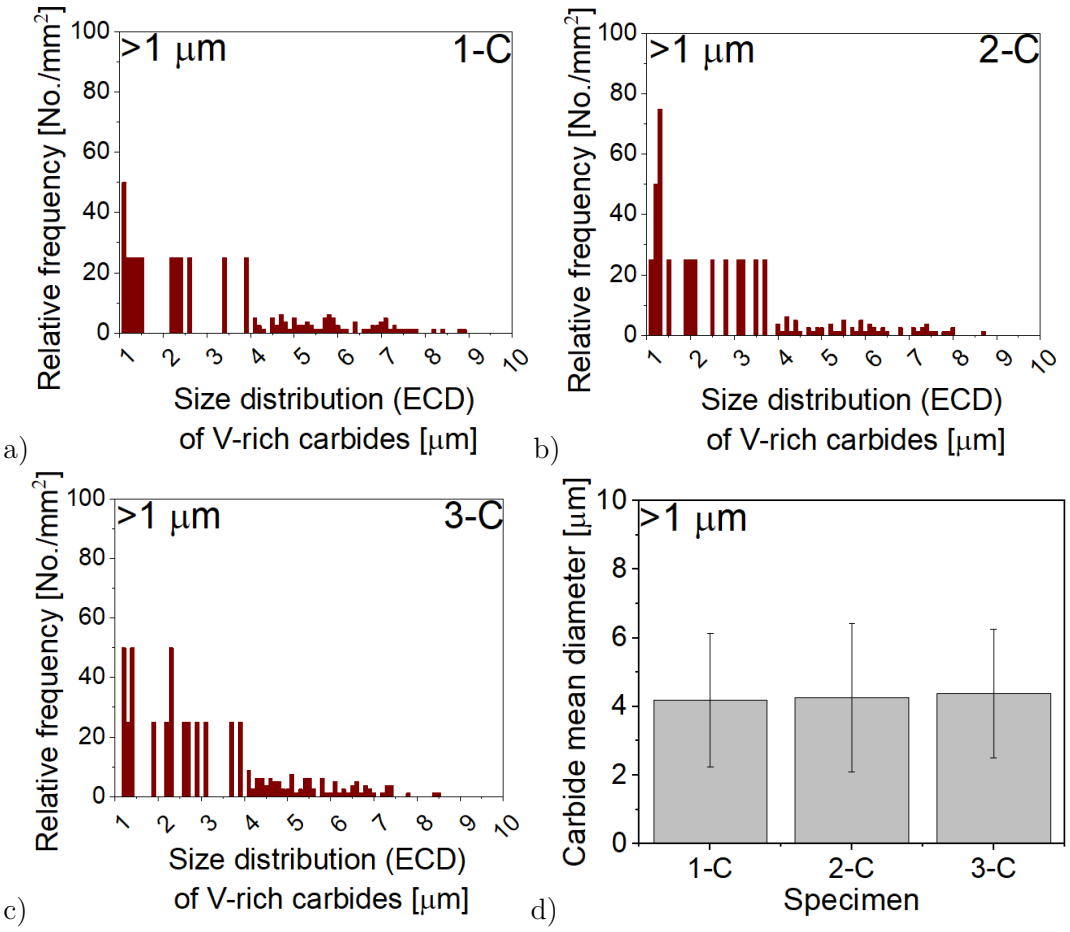

Figure 61: Size distribution of larger V-rich carbides in tool steel C and hardness groups 1, 2 and 3; specimens a) 1-C, b) 2-C and c) 3-C and d) carbides mean diameter.

Table 16 roughly summarizes size distribution graphs from Figures 51-61 and number of detected particles (carbides) per mm^2 for individual tool steel used, as was discussed above.

Table 16: Summarized data of the carbide size distribution per mm^2 as detected in the tool steels used.

	Number of carbide particles detected per mm²				
Specimen	**Cr-rich C**			**V-rich C**	
	(EC) >5 µm	**(LSC) 1-5 µm**	**(SSC) 0.3-1 µm**	**0.3-1 µm**	**>1 µm**
A material	/			138000	/
B material	40-55	3500-5500	250000-300000	60000-90000	400-500
C material	250-350	7500-8500	170000-250000	/	/
D material	550-650	7000-9500	280000-370000	/	/

Automatic particle analysis and size distribution as a function of the rolling direction for the hot-rolled cold-work tool steel D hardened to 60 HRC (w-D) is presented in Figure 62 and Table 17. In the case of the perpendicular direction (T_1) there is a high density of eutectic carbides in the 5–8 µm range (Figure 62a). On the other hand, for the microstructure in the longitudinal direction (L) (Figure 62b) a much smaller amount of carbides in this size range is observed, although carbides larger than 12 µm can also be found in this case. From Figure 62c it is also evident that the carbides' mean diameter in the cross-sectional plane and the longitudinal direction is almost identical ($\approx$ 8 µm), while the average length of the carbides in the longitudinal direction is larger: 15 µm as compared to 12 µm in the shorter cross-sectional plane.

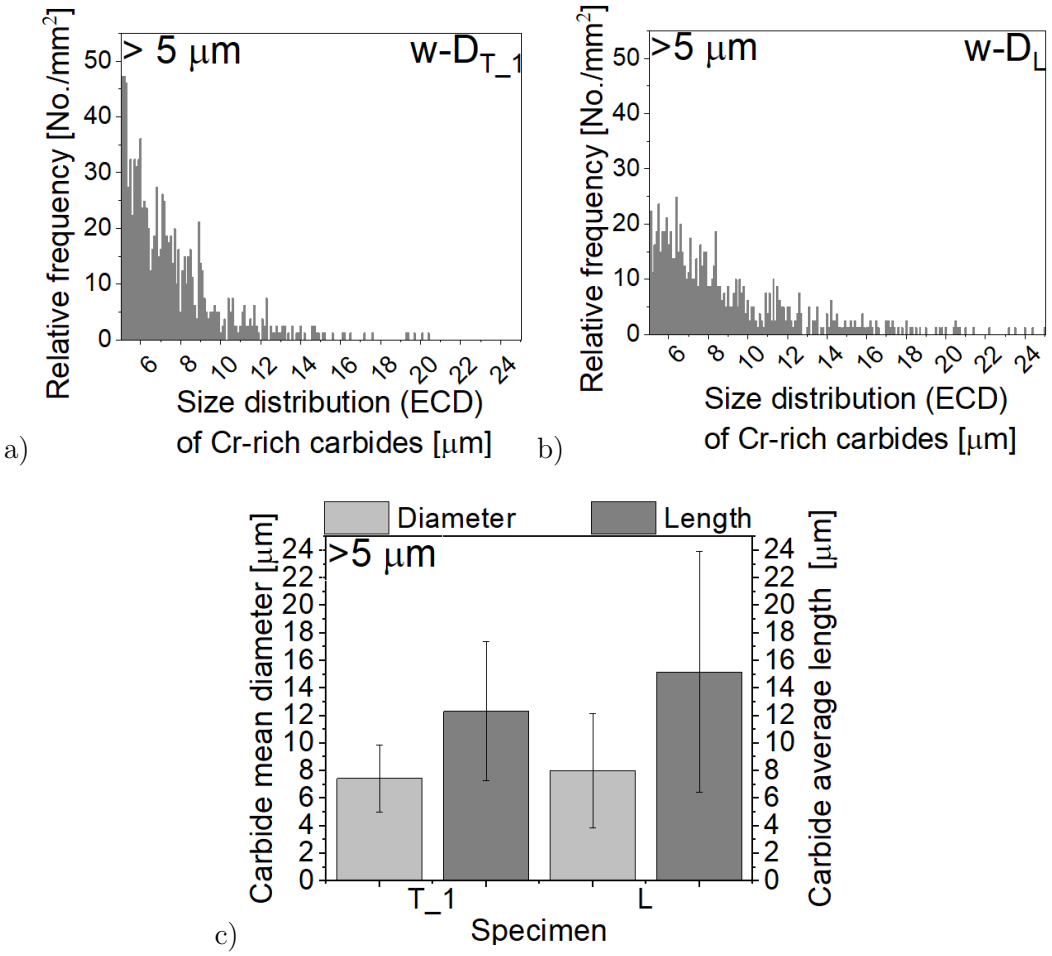

Figure 62: Size distribution of eutectic Cr-rich carbides in w-D specimen in a) perpendicular (T_1) direction and b) transverse (L) direction, and c) carbides mean diameter and length in considered directions (T_1 and L).

Table 17: Summarized data of the eutectic carbides size distribution per mm^2 in a perpendicular (T_1) and transverse (L) direction in tool steel Mat. No. 1.2379 (D material)

	Number of carbide particles detected per mm^2		
Specimen	**Cr-rich C**		
	(EC) >5 µm	**(EC) 5-8 µm**	**(EC) >12 µm**
w-D$_L$	860-1000	463	151
w-D$_{T_1}$		723	62

6.2 Mechanical Properties

6.2.1 Effect of heat treatment

The effect of austenitizing temperature on the as-quenched hardness of hot-work tool steel A (Mat. No. 1.2367 mod.) was determined by the dilatometry tests, performed at different austenitizing temperatures, ranging from 950 °C to 1150 °C. As shown in Figure 63, increasing the austenitization temperature increases the as-quenched hardness of hot-work tool steel A. At 950 °C the hardness of the investigated tool steel was approx. 590 HV10 (55 HRC) and increased to 675 HV10 (59 HRC) as the austenitizing temperature reached 1150 °C. This is due to the larger amount of carbon being dissolved in the matrix, contributing to the increase of the martensitic hardness.

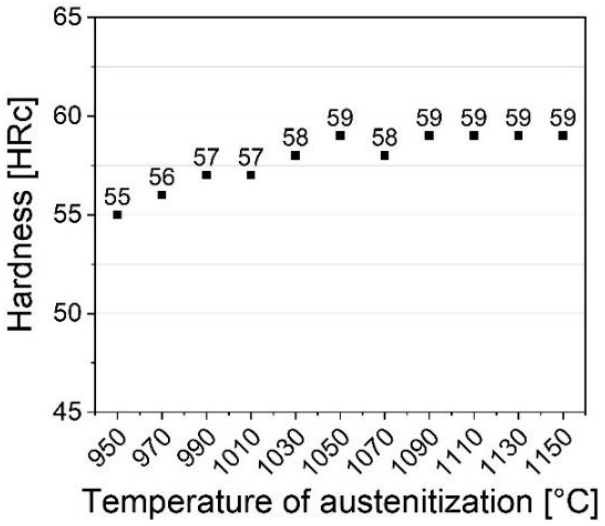

Figure 63: Hardness of as-quenched hot-work tool steel A specimens; hardening heat-treatment conducted in the dilatometer DIL805A/D.

Mechanical properties for hot-work tool steel A subjected to three different austenitizing temperatures (950 °C, 1030 °C and 1150 °C) and subsequent double tempering are presented in Figure 64. The tempering diagram obtained (Figure 64a) depicts a hardness drop with increasing tempering temperature. The highest hardness obtained was 59 HRC, shown by the as-quenched specimens austenitized from 1150 °C (Figure 64a). For the recommended austenitization temperature of 1030 °C 2 Rockwell's lower hardness of 57 HRC is obtained after quenching. On the other hand, the insufficient hardening temperature of 950°C resulted in as-quenched hardness of only slightly above 51 HRC. As expected, the hardness drop and increase in the impact toughness with increasing tempering temperature is observed, however only for austenitization at temperatures below 1150°C (Figure 64a). The highest hardness through all tempering steps showed material subjected to the highest austenitization temperature and the lowest material austenitized at 950 °C. Due to the secondary hardening effect, being typical for tool steels, a low hardness drop occurs at tempering temperatures above 520 °C [1]. A hardness drop from 57 to 55 HRC took place for the upper austenitization temperature, from 54 HRC to 52 HRC for the recommended temperature of 1030 °C and from 51 HRC to 48 HRC for the lowest austenitization temperature of 950 °C. The reduced hardness observed during tempering and the corresponding softening resistance of the investigated hot-work tool steel is correlated with the changes in the microstructure and alloy-carbide type as well as with

the martensitic structure recovery [8]. Looking at the impact toughness, the best results are shown by specimens austenitized from the recommended temperature of 1030 °C. Furthermore, tempering above 580 °C results in a significant increase in the impact toughness, observed for lower austenitization temperatures. However, this is not the case for the austenitization at very high temperatures (1150 °C). A significant increase of the prior austenite grains affects the toughness, which cannot be altered with the tempering procedure.

A similar trend as for the hardness is shown by the ultimate tensile strength (UTS) of the material. With increased tempering temperature, also a decrease in the tensile strength from ≈ 2180 MPa for specimens tempered at the lowest temperature (520 °C) to ≈ 1300 MPa for specimens tempered at the upper tempering temperature of 640 °C is observed (Figure 64b) when the material is subjected to austenitization at 1030 °C. Higher values for UTS are obtained at high austenitization temperatures (1150 °C). On the other hand, a drop in the UTS takes place when using low austenitization temperature (950 °C). Looking at the yield strength (YS), it first slightly increases with tempering, reaching a maximum at a tempering temperature of about 580°C, followed by a steep decrease, which is true for all three austenitization temperatures applied (Figure 64b). The lowest YS (≈ 850 MPa) is reached at the lowest austenitization temperature (950 °C) and the highest tempering temperature of 640 °C.

In terms of elastic properties and ductility (Figure 64c), similar properties are exhibited by the specimens subjected to low and intermediate austenitization temperatures (950 °C and 1030 °C), especially for the tempering temperatures below 600 °C. However, the hardness difference in those cases varies significantly. For example, for tempering at 580 °C the elongation is about 10.5 %, although specimens austenitized at 950 °C show hardness of 48 HRC, and specimens austenitized at 1030 °C above 52 HRC. Even for the hardest specimens, elongation does not drop below 9 % and increases up to 15 % for the highest tempering temperature. However, for the highest austenitization temperature the elongation remains low, between 3 % and 5.5 % across the whole tempering range (Figure 64c). The dissolution of the residual vanadium-rich MC carbides responsible for preventing the grains from growing has a negative effect on the toughness and ductility of the material [21].

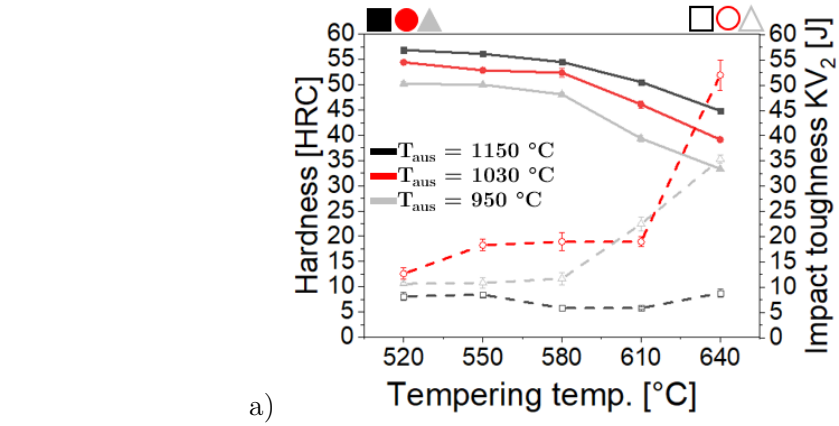

a)

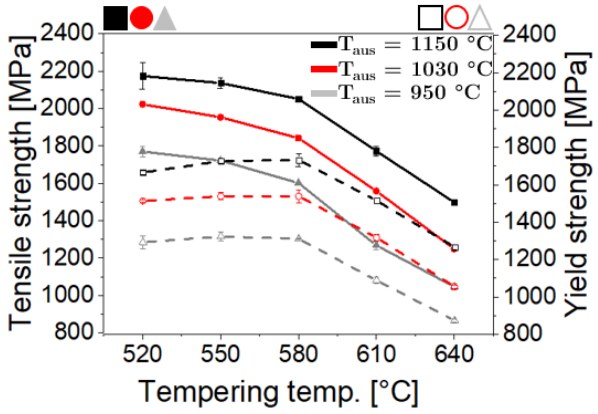

b)

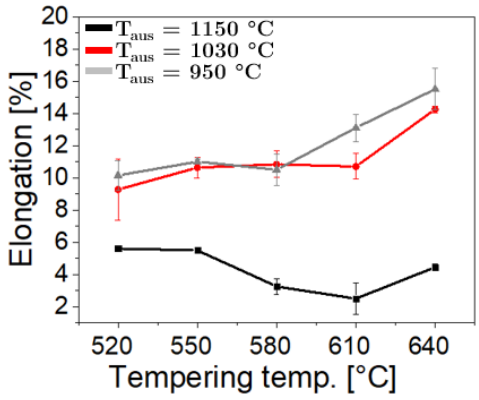

c)

Figure 64: Hot-work tool steel A mechanical properties; a) hardness and impact toughness b) ultimate tensile strength (UTS) and yield strength (YS), and c) elongation.

In the case of the P1–P3 hot-work tool-steel specimens subjected to different austenitization and tempering temperatures, aimed at obtaining a hardness of about 52 HRC, a hardness of between 50 and 52 HRC was obtained.

Table 18: Hardness of hot-work tool-steel specimens subjected to different heat-treatment parameters, aimed at obtaining the same hardness level.

Specimen	Heat-treatment condition	Hardness [HRC]
P1	T_A = 1150 °C / $T_{sec.temp.}$ = 610 °C	51±0.3
P2	T_A = 1030 °C / $T_{sec.temp.}$ = 580 °C	52±0.9
P3	T_A = 950 °C / $T_{sec.temp.}$= 520 °C	51±1.0

A comparison of the mechanical properties for the specimens with similar hardness values obtained at different austenitization and tempering temperatures is presented in Figure 65. All specimens, regardless of the austenitization temperature used, show similar ultimate tensile strengths of about 1800 MPa, but different yield strengths and elongations (Figure 65b). Greatly reduced elastic properties (elongation of just 3 %) are shown by the specimens austenitized at the highest austenitization temperature (P1), accompanied by the lowest impact toughness of just 6 J (Figure 65a). The highest toughness of 19 J and the best tensile properties (UTS = 1800 MPa, YS = 1500 MPa, A = 12 %) are achieved at the recommended austenitization temperature (P2 specimens). Too low austenitization

temperature (P3 specimens) results in intermediate toughness (10 J) and elastic properties (A = 10%), but in the lowest yield strength, being more than 200 MPa lower compared to the recommended austenitization temperature (Figure 65b).

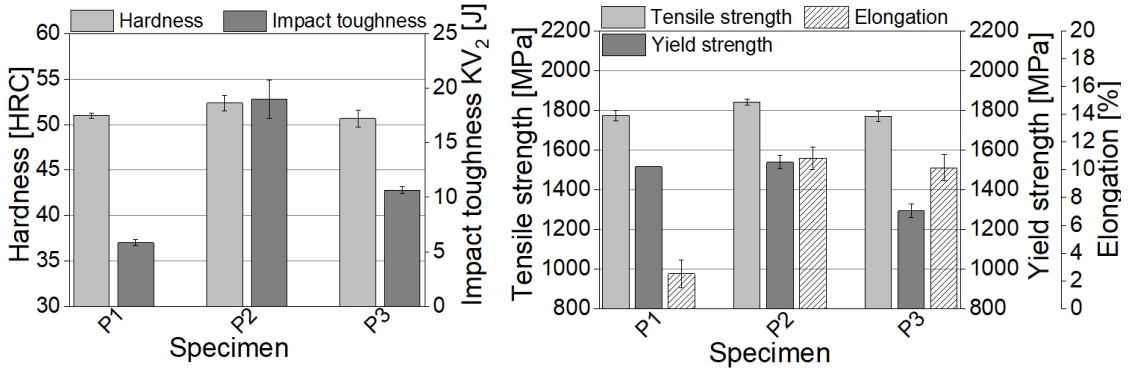

a) b)

Figure 65: Mechanical properties of the hot-work tool steel A with a similar hardness obtained at different austenitization temperatures; a) hardness and impact toughness and b) ultimate tensile strength (UTS), yield strength (YS) and elongation.

6.2.2 Hardness of tool steel after recommended heat treatment

Targeted hardness values (55, 50 and 45 HRC) set prior to the heat treatment were in general achieved. However, exact hardness levels were very hard to obtain. Therefore, hardness groups of 53–55 HRC, 48–50 HRC and 44–46 HRC were considered, since small differences in hardness usually do not have a significant effect on the wear performance of the tool steel [119]. Bulk hardnesses achieved after the recommended hardening heat treatment are shown in Table 19. In general, the slightly lower hardness of the specimens was achieved as compared to the targeted hardness level for a specific hardness group (1, 2, 3 or w). This is due to the fact that many factors, like heat-treatment stability as well as chemical composition variations from batch to batch, influence the outcome of the heat treatment. Manufacturers emphasise that the listed recommendations for steel heat treatment are only approximate and do not guarantee maximum or minimum hardness values. Therefore, in some cases several trials had to be made to obtain specimens of the desired hardness level.

Table 19: Achieved hardness levels of the test specimens.

Label	Target [HRC]	Achieved hardness [HRC]
	Mat. No. 1.2367 mod. (material A)	
1-A	55	54±0.5
2-A	50	49±0.2
3-A	45	45±0.1
	Mat. No. 1.2363 (material B)	
w-B	60	59±0.2
1-B	55	55±1.4
2-B	50	49±0.3
3-B	45	45±0.6
	Mat. No. 1.2990 (material C)	
1-C	55	54±0.4
2-C	50	49±0.3
3-C	45	46±0.6
	Mat. No. 1.2379 (material D)	
w-D	60	59±0.2
1-D	55	54±1.6
2-D	50	49±1.1
3-D	45	45±0.8

The matrix hardness for all the hardness groups was determined using the Vickers indentation technique and a load of 5 g. In this way the indents were restrained to the matrix phase with secondary carbides, avoiding the influence of coarse eutectic carbides. The results are presented in Figure 66a. It can be seen that for the highest hardness group (55 HRC; Figure 66a), the highest matrix hardness of 660 HV0.05 is shown by cold-work tool steel B (1-B), followed by hot-work tool steel A and cold-work tool steel C (645 HV0.05), while the lowest matrix hardness of 625 HV0.05 is displayed by cold-work tool steel D. The matrix hardness is more comparable between the different tool steels at lower hardness levels, being at about 570 HV0.05 for hardness group 2 and around 490 HV0.05 for hardness group 3. Again, tool steels A and C show very comparable values. Nevertheless, the matrix hardness for the different tool steels within the same hardness group is, in general, within the range of a standard deviation. The relatively low standard deviation associated with the microhardness is indicative of microstructural homogeneity and the uniform distribution of secondary carbides [89].

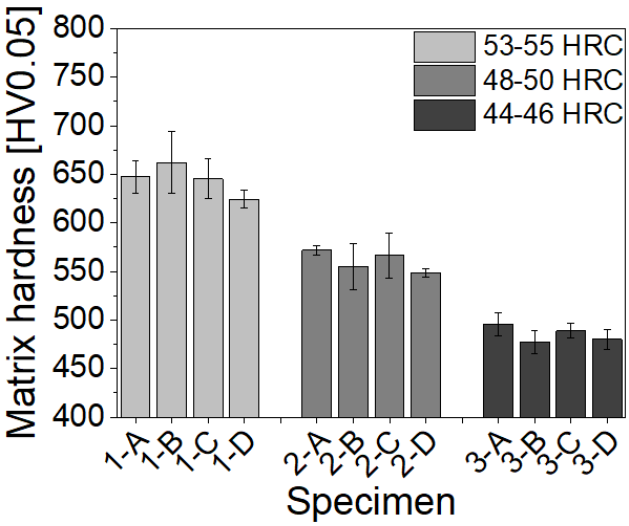

Figure 66: Matrix hardness of the investigated tool steels at different bulk-hardness levels (1, 2 and 3).

To further present the hardness variations among the different phases that co-exist in the microstructure, two specimens belonging to the hardness group 2 were analysed using nano-indentation hardness measurements. The specimens taken into consideration (2-A and 2-D) exhibited the largest differences in microstructure in terms of large eutectic carbides. Hot-work tool steel A (specimen 2-A) showed the lowest fraction of any carbides without large eutectic carbides and the cold-work tool steel D (specimen 2-D) the largest carbide fraction among the investigated tool steels in this study. The bulk hardness for both specimens was ≈ 49 HRC. Figure 67a and Figure 68a present optical micrographs of the nano-indentation sites (red rectangle) with marked areas (black rectangle) of magnified SEM/SEI images showing specific indents (Figure 67b and Figure 68b). The resulting hardness-distribution maps are then shown in Figure 67c and Figure 68c. In the case of cold-work tool steel D (specimen 2-D) with the highest density of large eutectic Cr-rich carbides distributed in the tempered martensite matrix, the hardness variation throughout the microstructure ranges from 5.5 GPa for the matrix and up to 19 GPa when the indent is made in the carbide. As shown, cold-work tool steel D exhibits a highly non-uniform hardness distribution, with the hardness of the large eutectic Cr-rich M_7C_3 carbides ranging between 16 GPa and 19 GPa (orange regions in Figure 67c and Figure 67d). The green regions represent the hardness of the matrix/carbide interface and blue region of the matrix (Figure 67c and Figure 67d). Even within the matrix a deviation in hardness values is present, which can be attributed to the presence of small secondary carbides.

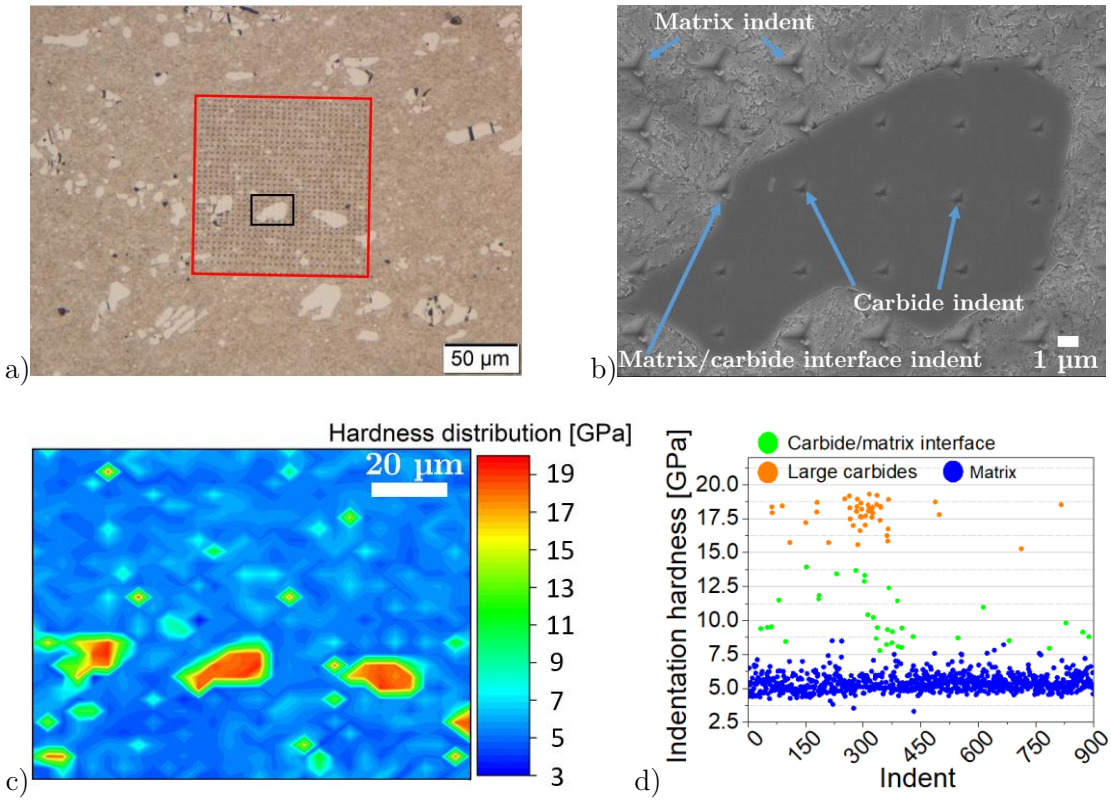

Figure 67: Nano-indentation of specimen 2-D; a) optical and b) SEI micrograph of nano-indentation site and c) hardness map and d) hardness distribution.

On the other hand, the hardness distribution map is very different for hot-work tool steel specimen (2-A), the microstructure without large eutectic carbides as well as a much lower fraction of fine secondary carbides (Figure 68). In this case no abrupt hardness increase throughout the microstructure can be observed (Figure 68c). The whole area analysed shows a hardness of about 5.5 GPa (blue region), indicating a prevailing tempered martensite matrix, which is similar to the matrix hardness of the 2-D specimen. The results of the nano-indentation tests for the matrix and carbides analysed are summarized in Table 20.

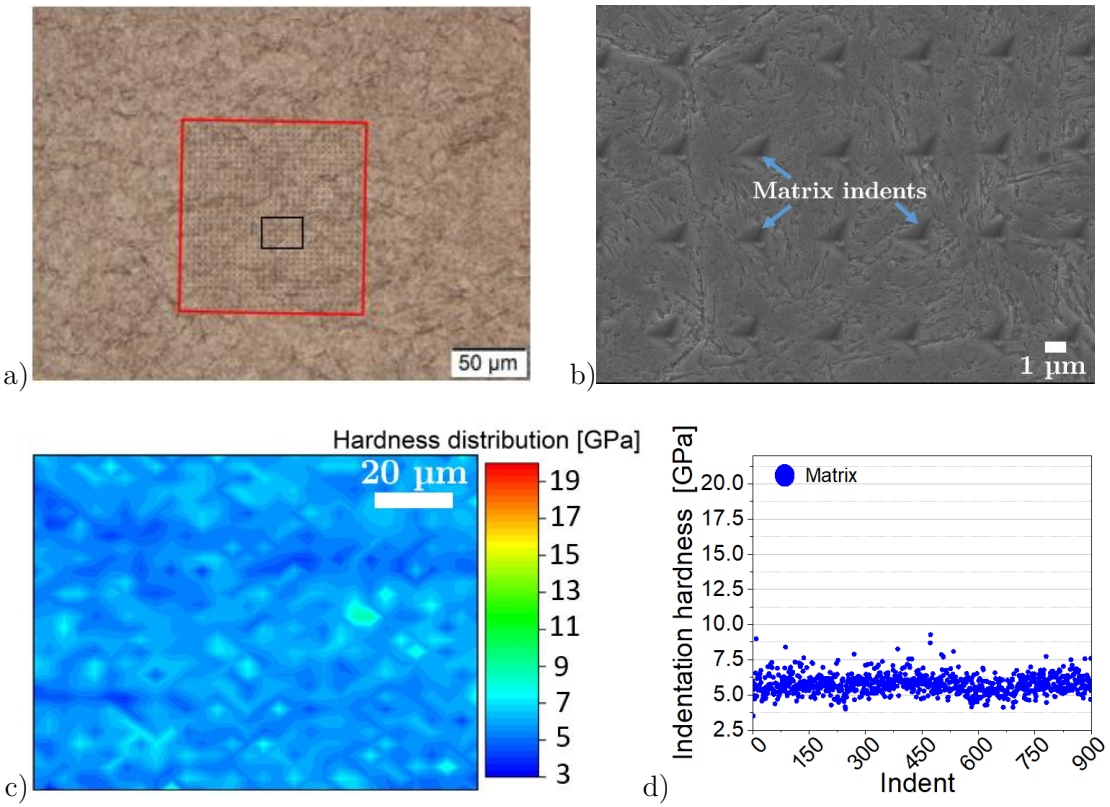

Figure 68: Nano-indentation of specimen 2-A; a) optical and b) SEI micrograph of nano-indentation site and c) hardness map and d) hardness distribution.

Table 20: Nano-indentation hardness results for matrix and M_7C_3 carbides.

Specimen	**IIM* [GPa]**		**IIM* [HV]**		**Rockwell [HRC] - bulk**
2-A	5.8±0.7		533±62		49±0.2
2-D	**Matrix**	**Carbide (M_7C_3)**	**Matrix**	**Carbide (M_7C_3)**	49±1.1
	5.4±0.6	18.0±0.8	498±54	1672±74	

*IIM – Instrumented Indentation method

The results of the nano-indentation tests show that large eutectic carbides significantly influence the hardness distribution throughout the material microstructure. We can assume that the degree of hardness non-uniformity is directly correlated to the fraction and type of carbides present in the steel matrix. Besides large eutectic carbides of M_7C_3 type, also harder carbide types (i.e., MC) can be present, which results in an even higher difference between the matrix and the carbides. MC-type carbides are present in some of the tool steels investigated in this study (A and C), but were difficult to evaluate due to their small size and low volume fraction.

6.2.3 Fracture toughness after recommended heat treatment

The average values of the fracture toughness for the four investigated tool steels at a given hardness level are presented in Figure 69. The highest fracture toughness at all hardness levels is displayed by hot-work tool steel A. Its fracture toughness is about twice as high

as the cold-work tool steel types. As can be seen, the fracture toughness is decreasing with an increase in hardness, with the lowest values obtained for hardness group 1 (53–55 HRC). In this case, hot-work tool steel (1-A) has fracture toughness of 39 MPa√m, followed by cold-work tool steels C and D (1-C and 1-D) having almost similar fracture toughness's of 24 MPa√m, while the lowest resistance to crack propagation is displayed by cold-work tool steel B (17 MPa√m). Similar results are also shown by the lower hardness groups (Figure 69). In the case of hardness group 2 (48-50 HRC), hot-work tool steel A reaches fracture toughness slightly above 70 MPa√m, while cold-work tool steels show significantly lower values. Cold-work tool steel C of about 38 MPa√m, followed by steel D (34 MPa√m) and steel B (29 MPa√m). The highest toughness values are reached in hardness group 3 (44–46 HRC). Hot-work tool steel A, as the toughest material among the investigated tool steels, reaches a fracture toughness of almost 81 MPa√m. Also, the fracture toughness of cold-work tool steels increases with a reduced hardness, albeit remaining about 3-times lower than hot-work tool steel A. In the third hardness group, cold-work tool steel C displays a toughness of 54 MPa√m and tool steels B and D of about 39 MPa√m.

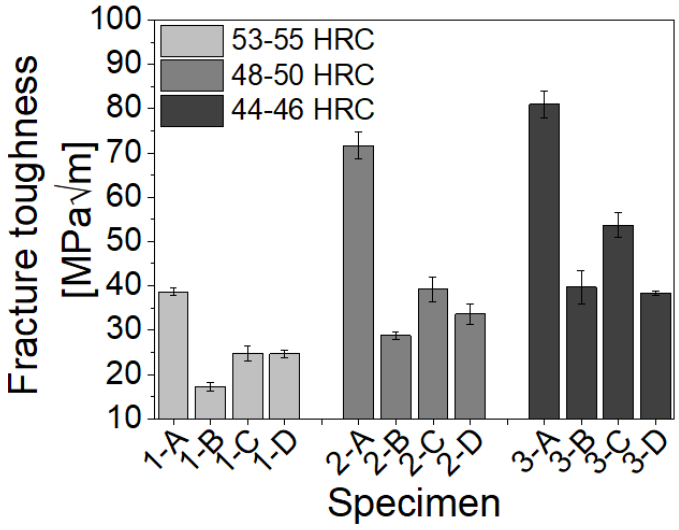

Figure 69: Fracture toughness of investigated tool steels at different hardness levels.

6.2.4 High-temperature properties of hot-work tool steel

For hot-work tool steel A (Mat. No. 1.2367 mod.) high temperature testing of impact toughness, ultimate tensile strength and yield strength was also performed and correlated with the high-temperature abrasive wear resistance (Chapter 6.4).

The results for impact toughness as a function of material hardness level and testing temperature are shown in Figure 70a. As shown, the impact toughness is increased with the drop in hardness as well as the increase in the temperature. The investigated hot-work tool steel exhibits the lowest impact toughness of only 13 J at room temperature and the highest hardness level (54 HRC), which at 500 °C increases above 30 J. Similar trends but at higher increase level are found for the other two hardness groups, with the impact toughness increase with temperature being in the range of 3–4 times. On the other hand, a drop in the values at elevated temperatures is observed for the ultimate tensile strength (UTS) and yield strength (YS), as shown in Figure 70b. The UTS drops by about 20% (≈ 400 MPa) and the TS by about 30% (≈ 350 MPa), even below 1000 MPa when the material is exposed to a temperature of 500 °C.

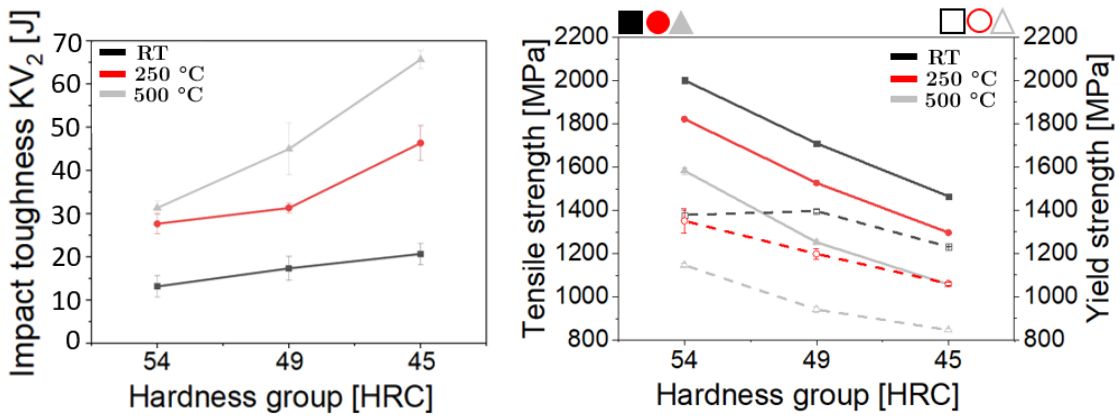

a) b)

Figure 70: Hot-work tool steel's mechanical properties at elevated temperatures; a) impact toughness and b) ultimate tensile strength (UTS) and yield strength (YS).

6.3 Tribological Properties at Room Temperature

6.3.1 Friction at the micro level

Figure 71a shows the topography of the area with a large eutectic carbide, indicating that during the preparation large eutectic carbides significantly protrude from the matrix surface. This effect is significantly smaller for the fine secondary carbides. In Figure 71b the friction results are shown using the lateral force measurement method (subtracted image of trace and retrace) and a silicon-based cantilever tip. As such, the results are not fully representative for a steel-steel contact. However, metallic tips are not available to perform such kinds of measurements. Nevertheless, the results shown in Figure 71b provide a microscale comparison of the friction behaviour between the carbides and the metallic matrix.

The level of friction was found to be independent of the scanning direction and more importantly, lower on the protruding carbide surface (lower/darker signal) as compared to the metal matrix. On the other hand, the protruding carbide has an effect on the friction as the needle hits the carbide edge, resulting in a friction spike visible as a bright line surrounding the carbide.

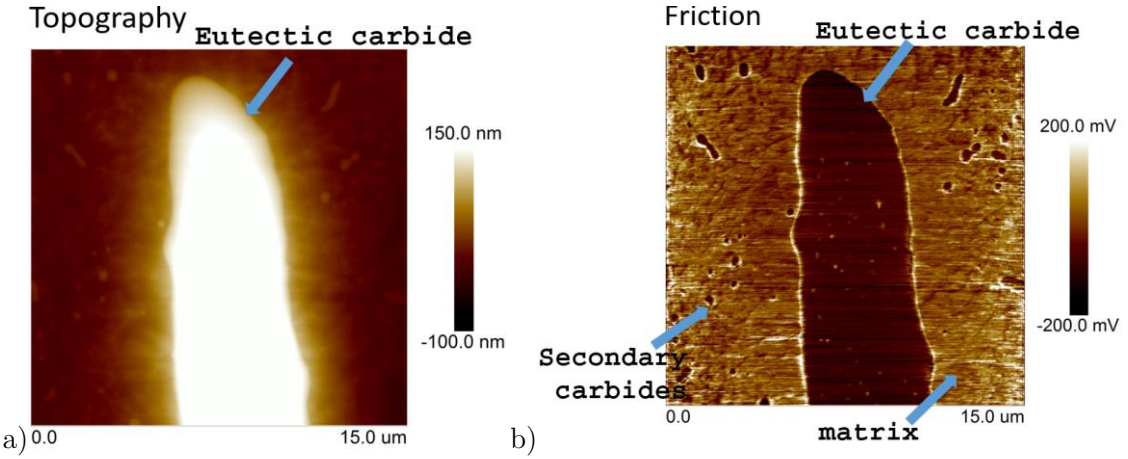

Figure 71: AFM-LFM study of hot-work tool steel D; protruding carbides a) height and b) microscale friction.

Looking at the coefficient of friction (COF) in the initial stages of sliding (Figure 72), obtained at the macro level with the unidirectional sliding test (0.12 m/s, 30 N) and ceramic counter-ball, a lower initial friction is again displayed by material D having the largest fraction and density of carbides, especially the large eutectic carbides. On the other hand, hot-work tool steel A with the predominating metal matrix shows a significantly higher initial friction. Similar results were observed during running-in in the high-stress abrasion-wear-resistance test (Chapter 6.3.2) using standard polished samples (Figure 73). Both results support the findings of the AFM measurements, indicating lower friction of carbides as compared to the metal matrix. However, this has no influence on steady-state friction, as different wear mechanisms lead to topography changes, material transfer and masking of the carbides, thus resulting in a similar overall friction.

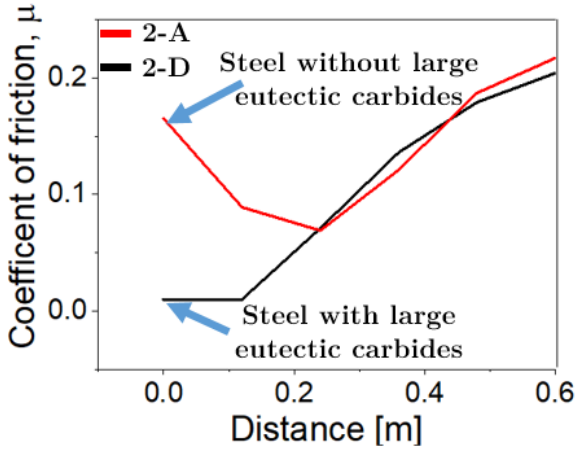

Figure 72: Development of COF during the initial stages of unidirectional sliding against Al_2O_3 counter ball.

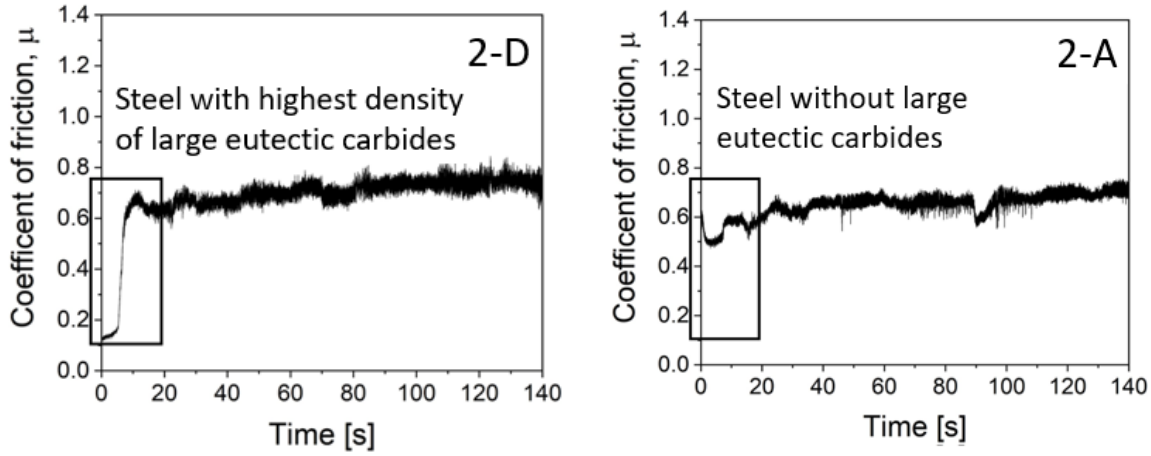

a) b)

Figure 73: COF during running-in in the high-stress abrasion-wear test of a) cold-work tool steel D (2-D; highest carbide fraction) and b) hot-work tool steel A (2-A; lowest carbide fraction).

6.3.2 Abrasive wear

6.3.2.1 Effect of austenitization temperature – hot-work tool steel

Tribological behaviour under reciprocating sliding conditions and dominating abrasive wear for hot-work tool steel subjected to different austenitizing temperatures and hardened to ≈ 51 HRC with the dominating tempered martensite microstructure is presented in Figure 74 and Figure 75. In Figure 74, for the high-load/stress conditions and in Figure 75 for low-load/stress conditions. Regardless of the sliding speed used, the highest abrasive wear rates for the high load case (102 N, p_H = 1600 MPa) were observed for specimen P3, subjected to a low austenitization temperature (Figure 74a). For the low sliding speed (0.01 m/s) the wear rate was of the order of $2.5 \cdot 10^{-5}$ mm^3/Nm and for the high sliding speed (0.12 m/s) of the order of $1.0 \cdot 10^{-5}$ mm^3/Nm. By increasing the austenitization temperature and with a more effective eutectic carbides' dissolution the high-stress abrasive wear resistance increases by up to 20%. For a low sliding speed the best resistance and the lowest abrasive wear rate is displayed by specimen P2 austenitized at the intermediate austenitization temperature of 1030 °C and for a high sliding speed by specimen P1 austenitized at high austenitization temperature(Figure 74a). The highest wear rate observed for the low austenitization temperature (P3), although giving the same level of hardness as the other two austenitization temperatures, can be related to the substantially lower yield strength (≈ 15% lower), presumably caused by a high degree of undissolved residual carbides, with the high-stress wear tests being performed at a level more than 20 % above the material's yield strength. Another thing is that for the P3 specimens, the tempering temperature does not exceed the secondary hardening peak, where strengthening occurs due to very small precipitated carbides (nano-sized) [7, 116, 117, 120], which are difficult to detect just by SEM. For the other two austenitization temperatures the yield strength is exceeded by only about 5 %. In terms of the coefficient of friction (COF), more or less identical steady-state values are obtained, regardless of the austenitization temperature used. In the case of a high load and a high sliding speed the steady-state COF was at the level of 0.5 and for low sliding speed at about 0.7 (Figure 74b).

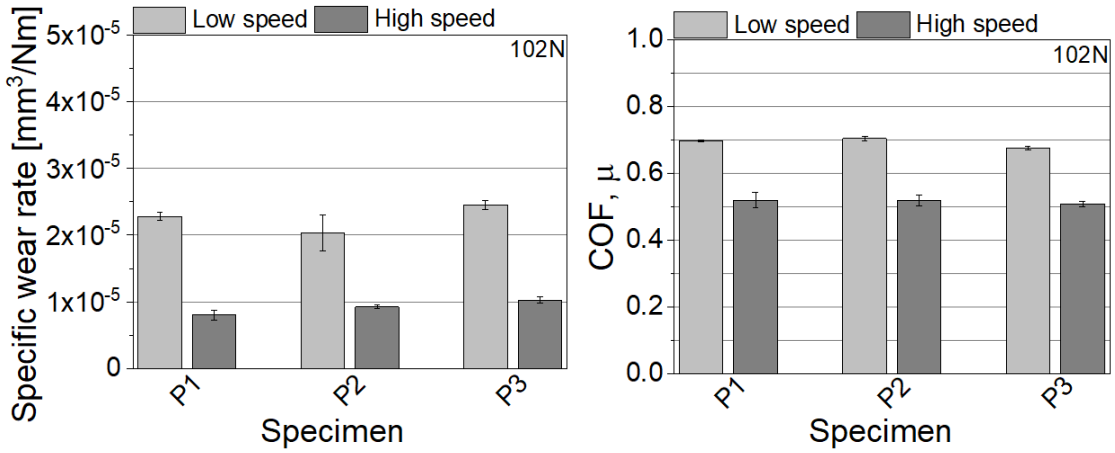

a) b)

Figure 74: Results of reciprocating sliding abrasive wear resistance tests at nominal load of 102 N; a) wear rates, b) corresponding steady-state coefficient of friction (COF).

In the case of low load (30 N, p_H = 1000 MPa) the wear rate for the high sliding speed follows the same trend as in the case of the high load, with the high austenitization temperature (P1) resulting in the lowest wear rate of about $1.2 \cdot 10^{-5}$ mm³/Nm and then increasing with a reduced austenitization temperature and the eutectic carbides' dissolution (Figure 75a). Again, the lowest wear rate at low sliding speed is shown by the hot-work tool steel specimen austenitized at the recommended austenitization temperature of 1030 °C (P2; k = $2.3 \cdot 10^{-5}$ mm³/Nm). However, the highest wear rate at low-load/low-sliding-speed conditions is found for a high austenitization temperature (P1), being in the range of $4.3 \cdot 10^{-5}$ mm³/Nm. In the case of the P1 specimens, also the largest difference between the low and high sliding-speed conditions is observed (4-times), while almost no difference regarding the sliding speed conditions is shown by the specimens' austenitized at 950 °C (P3). This may be because in the case of low load the contact stress is below the material's yield stress and a significant role in the wear behaviour is taken by the carbides, which are almost completely dissolved for the P1 specimen. However, under the high-speed conditions, high contact temperatures and heating of the surface and subsurface layer might lower its yield stress, thus the prevailing effect on the wear mode is taken by the yield stress , which is the lowest for the P3 specimen. As shown in Figure 75b, a similar steady-state coefficient of friction is observed for all the specimens (0.7–0.8), although slightly higher values are found for the intermediate austenitization temperature (P2).

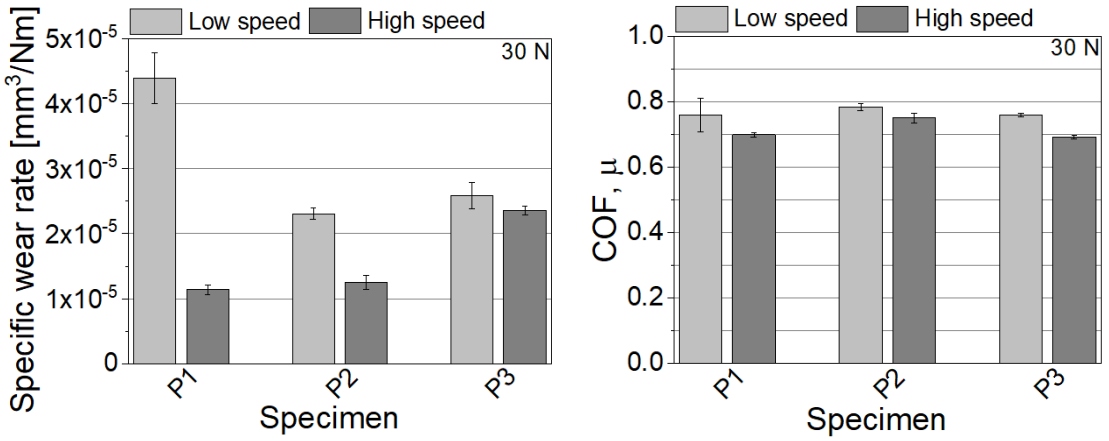

a) b)

Figure 75: Results of reciprocating sliding abrasive wear resistance tests at a nominal load of 30 N; a) wear rates, b) corresponding steady-state coefficient of friction (COF).

6.3.2.2 Different tool steels at the same hardness level – hardness group 1 (53–55 HRC)

The results from abrasive wear tests on tool steels having similar bulk hardnesses of 54 HRC (hardness group 1) but different fractions and types of carbides are shown in Figure 76 and Figure 77. For high-load and low-load conditions higher wear rates were in general obtained when performing reciprocating sliding tests at lower sliding speeds. In the case of high-load/low-speed conditions the lowest wear resistance and high wear rate of about $2.10 \cdot 10^{-5}$ mm^3/Nm was shown by hot-work tool steel A (1-A) and cold-work tool steel D (1-D);) although they have very different microstructures. Those are followed by cold-work tool steel B (1-B; $1.86 \cdot 10^{-5}$ mm^3/Nm), while the best wear resistance at high-load/low-sliding-speed conditions is shown by cold-work tool steel C (1-C), having a wear rate of approximately $1.68 \cdot 10^{-5}$ mm^3/Nm (Figure 76a). Two-to-four times lower wear rates were obtained under high-sliding-speed conditions. Again, the lowest wear rate of $4.97 \cdot 10^{-6}$ mm^3/Nm was displayed by cold-work tool steel C, followed by hot-work tool steel A and cold-work tool steel D, having 20–30% lower wear resistance. The lowest abrasive wear resistance under high-load/high-sliding-speed conditions showed cold-work tool steel B with its wear rate being doubled ($10.5 \cdot 10^{-6}$ mm^3/Nm) compared to cold-work tool steel C. Cold-work tool steel B has the worst fracture toughness and the lowest amount of large eutectic carbides among the cold-work tool steels investigated. On the other hand, the best fracture toughness values (39 MPa√m @54 HRC) are displayed by hot-work tool steel A, which also exhibits good abrasive wear resistance under high-sliding-speed conditions. On the other hand, the fracture toughness for cold-work tool steel D (1-D specimen) with the highest fraction of carbides, reaches only about half the value of specimen 1-A (24 MPa√m @54 HRC). Nevertheless, their wear resistance is very similar. Again, when we compare fracture toughness of cold-work tool steels C and D at 54 HRC, they show very similar values; however, their wear rates are quite different, with steel C showing about 20% lower wear. Even for steel B having the worst fracture toughness (17 MPa√m @54 HRC) the wear rates are not necessarily the highest ones. Therefore, these results clearly indicate that under sliding better fracture toughness does not necessarily contribute to better wear resistance. It is also very contact-conditions dependent.

In terms of the coefficient of friction (COF) similar steady-state values are displayed by all tool steels hardened to 54 HRC, being at about 0.7 for low-sliding-speed and 0.55 for high-sliding-speed conditions (Figure 76b). Hot-work tool steel A shows a slightly lower friction under high speed conditions, which can be related to the reduced matrix strength and ploughing resistance.

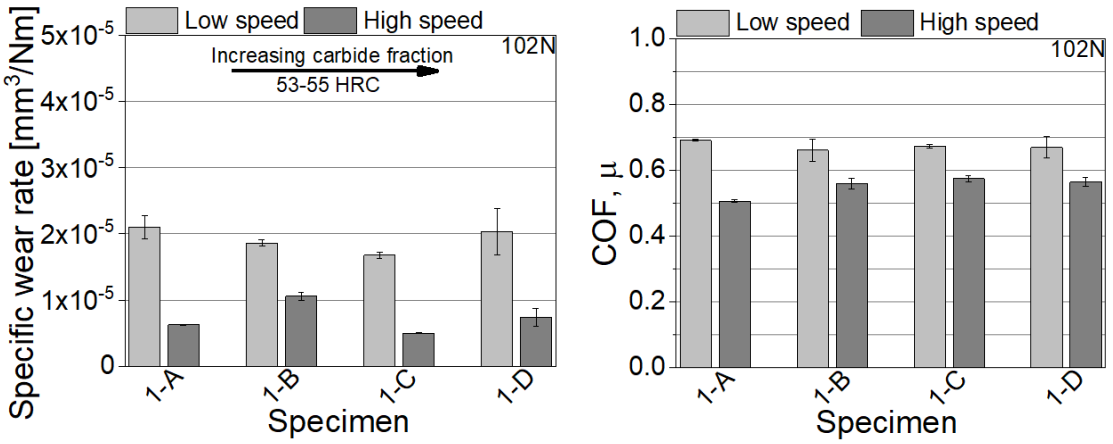

a) b)

Figure 76: Results of reciprocating abrasive wear resistance tests at nominal load of 102 N; a) wear rates of tool steels for hardness group 1, b) corresponding steady-state coefficient of friction (COF).

Performing tests at lower loads (30 N), the wear resistance trends were slightly changed (Figure 77a). Bigger differences between tool steels under investigation started to show, especially for low-speed conditions. Low-speed conditions were again the most detrimental for steel A and D. Regardless of its low fracture toughness tool steel B (1-B specimen) had the best wear resistance under low-load/low-sliding-speed conditions (wear rate below $1.7 \cdot 10^{-5}$ mm^3/Nm), being even lower than for the high-speed conditions (Figure 77a). It seems fracture toughness also here does not play any role when it comes to wear. On the other hand, in terms of the microstructure this steel has a significantly lower density of massive eutectic carbides in the steel matrix (Figure 51), and a slightly lower content of more evenly distributed smaller spherical carbides (Table 15) as compared to the other two cold-work tool steels. A significantly higher wear rate ($3.30 \cdot 10^{-5}$ mm^3/Nm) was displayed by the cold-work tool steel D (1-D) with the highest fraction of massive eutectic carbides present in the matrix. However, at higher sliding speeds, material with the lowest content of carbides, hot-work tool steel A (1-A), has a higher wear rate ($2.37 \cdot 10^{-5}$ mm^3/Nm) as compared to the cold-work tool steels. Among those, the best one in terms of wear resistance under low-load/high-sliding-speed conditions is cold-work tool steel C (1-C), with a high density of large Cr-carbides (Figure 54) as well as the presence of V-rich carbides with a size of up to several microns.

A lower contact stress (p_H = 1000 MPa) did not result in any significant change in the coefficient of friction when testing was performed under low-sliding-speed conditions (Figure 77b). It remained at a value of 0.7, similar to the high load case (Figure 76b). The only exception was cold-work tool steel B, with a drop in COF to ≈ 0.6 and a higher deviation being observed. Similar friction was displayed by all the specimens for low-load, high-speed testing conditions (~0.7), which slightly increased in the case of steel D.

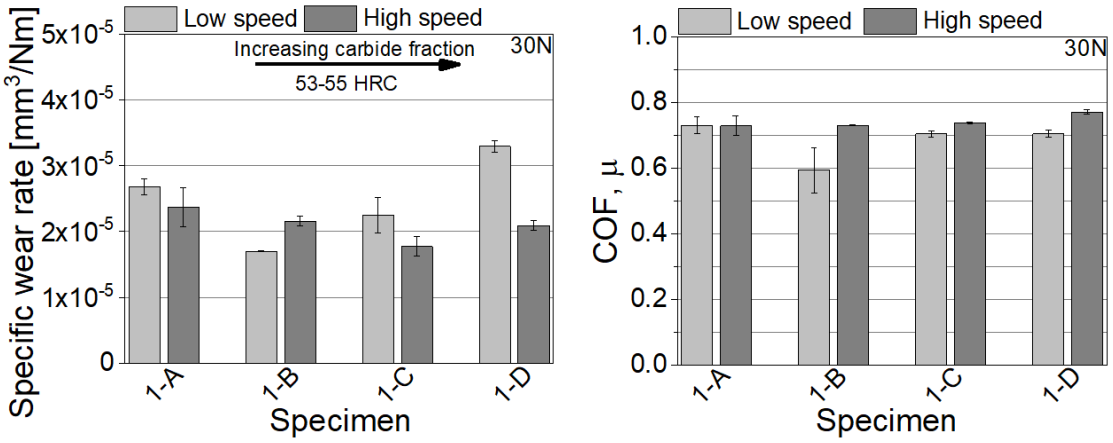

a) b)

Figure 77: Results of reciprocating abrasive wear resistance tests at nominal load of 30 N; a) wear rates of tool steels for hardness group 1, b) corresponding steady-state coefficient of friction (COF).

6.3.2.3 Different tool steels at the same hardness level – hardness group 2 (48–50 HRC)

Figure 78 shows the abrasive wear behaviour and resistance for tool-steel specimens with the hardness decreased to about 49 HRC. The same wear testing conditions were applied as for the previous hardness group (group 1) and the results are presented in the same manner. When tests were performed at a load of 102 N (high-load conditions; p_H = 1600 MPa) and sliding speed of 0.01 m/s (low-speed conditions), again all hardness group 2 specimens showed a higher wear rate than the high-speed testing conditions. In this case far worse wear resistance ($k = 3.87\times10^{-5}$ mm^3/Nm) was shown by the cold-work tool steel D (2-D), with the highest fraction of large carbides. At this hardness level the material exhibits the second-lowest fracture toughness, only slightly higher than tool steel B (2-B). For low-speed conditions tool steel D is followed by cold-work tool steel C (2-C; $k = 2.37\times10^{-5}$ mm^3/Nm), also displaying a high fraction of carbides larger than 5 µm (Figure 52 and Table 15), and steels A and B ($k = 2.11\times10^{-5}$ mm^3/Nm). However, at an increased sliding speed, the material response to abrasive wear is changed. Testing conditions are again the most detrimental for cold-work tool steel D (2-D); however, in this hardness group similar wear rates are also shown by the other two cold-work tool steels (2-B and 2-C). Looking at the fracture toughness for a given hardness level, it is favourable to cold-work tool steel C (2-C) and especially to hot-work tool steel A (2-A), with the lowest carbide fraction and the best wear resistance ($k = 5.71\times10^{-6}$ mm^3/Nm), as shown in Figure 78a.

The COF is in this case is again higher for low speed conditions ranging from 0.59 for the 2-B specimen to about 0.65 for the other ones. At a higher sliding speed the lowest COF is shown by hot-work tool steel (2-A; ≈ 0.48), which increases for cold-work tool steel specimens, ranging between 0.5 and 0.57 (Figure 78b).

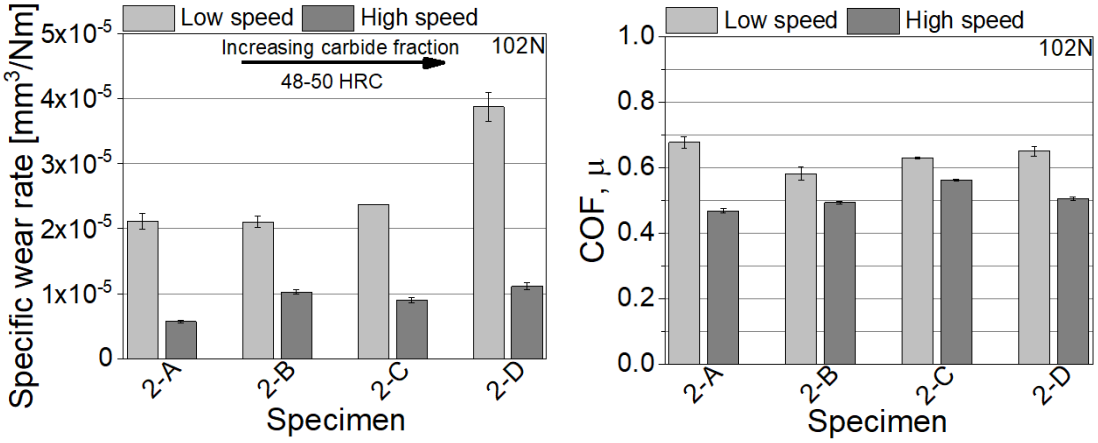

a) b)

Figure 78: Results of reciprocating abrasive wear resistance tests at nominal load of 102 N; a) wear rates of tool steels for hardness group 2, b) corresponding steady-state coefficient of friction (COF).

Figure 79 presents abrasive wear resistance results under low-load conditions (30 N) for tool-steel specimens in hardness group 2. As for the high-load conditions, cold-work tool steel D displays the lowest wear resistance at both sliding speeds used (2-D; $k_{0.01} = 4.36\times10^{-5}$ mm^3/Nm and $k_{0.12} = 2.90\times10^{-5}$ mm^3/Nm), and is again followed by cold-work tool steel C.. However, under low-load, low-speed conditions the best results were obtained for cold-work tool steel B, with a low amount of eutectic but a high fraction of secondary carbides and a wear rate of 1.84×10^{-5} mm^3/Nm. In this hardness group large eutectic carbides seem to play the most important role with the hot-work tool steel A (2-A) without any large carbides displaying the most beneficial wear resistance under high-speed conditions ($k = 2.31\times10^{-5}$ mm^3/Nm).

Regarding the COF, the highest values for low-load conditions of about 0.75 are displayed by hot-work tool steel A with a predominantly martensitic-matrix microstructure and the lowest (≈ 0.6) for cold-work tool steel B, almost without large eutectic carbides but still a high fraction of fine secondary carbides.

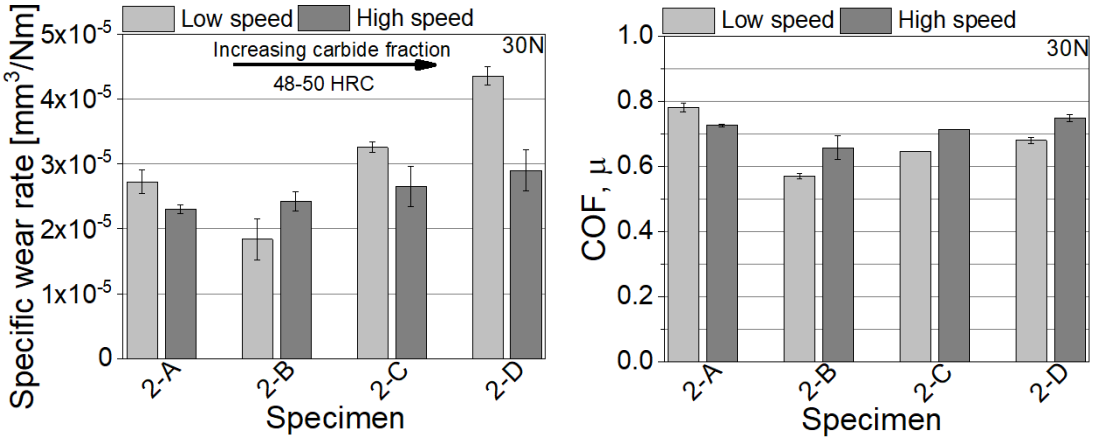

a) b)

Figure 79: Results of reciprocating abrasive wear resistance tests at nominal load of 30 N; a) wear rates of tool steels for hardness group 2, b) corresponding steady-state coefficient of friction (COF).

6.3.2.4 Different tool steels at the same hardness level – hardness group 3 (44–46 HRC)

With a further hardness drop to a level of 45 HRC, the wear trend for tool steels containing a high fraction of carbides is not changed (Figure 80). At high-load (102 N) and low-sliding-speed conditions cold-work tool steels C and D again show the highest wear rate ($k_{3\text{-}D}$ = 3.64×10^{-5} mm^3/Nm and $k_{3\text{-}C}$ = 3.02×10^{-5} mm^3/Nm). The fracture toughness of C steel (54 MPa√m @45 HRC) in this case is higher than the fracture toughness of steel D (39 MPa√m @45 HRC). Lower wear rates are obtained for hot-work tool steel A ($k_{3\text{-}A}$ = 2.49×10^{-5} mm^3/Nm) with the highest fracture toughness; however, cold-work tool steel B (3-B) is exhibiting the lowest abrasive wear rate of 1.67×10^{-5} mm^3/Nm, regardless of the fact that it has the lowest fracture toughness. Smaller differences are present at high-speed conditions. Nevertheless, tool steels A and B again show better abrasive wear resistance than the tool steels containing a high fraction of large eutectic carbides.

In Figure 80b the results for the COF of hardness group 3 and high-load conditions are presented. In the case of high-speed conditions the COF is in the range of 0.5, showing an increased trend with an increased carbides fraction, while for low-speed conditions it ranges from 0.7 to 0.5 and drops with a reduced fracture toughness.

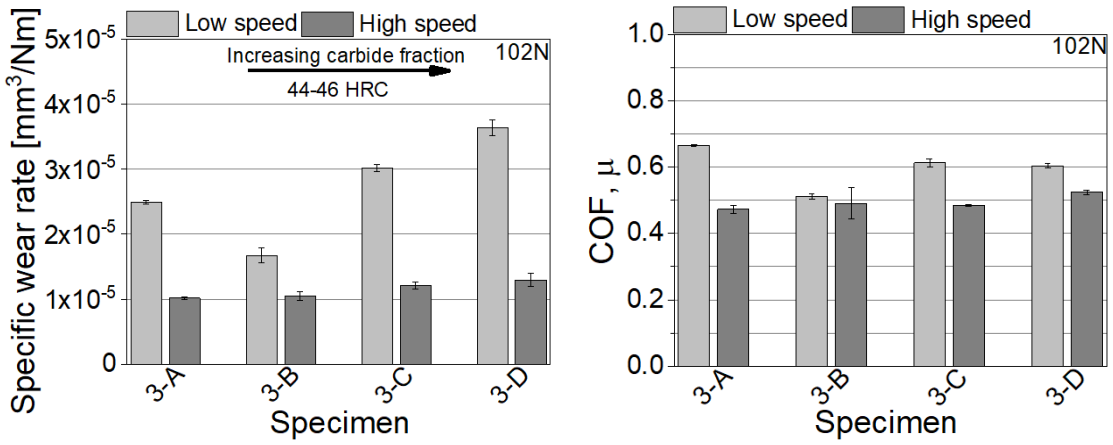

a) b)

Figure 80: Results of reciprocating abrasive wear resistance tests at nominal load of 102 N; a) wear rates of tool steels for hardness group 3, b) corresponding steady-state coefficient of friction (COF).

Wear-test results for specimens in hardness group 3 (45 HRC) tested under low-load conditions are shown in Figure 81. In this case, very similar results and wear rates were obtained for low- and high-sliding-speed conditions. In both cases high wear rates of about $3.5\cdot10^{-5}$ mm^3/Nm are displayed by the cold-work tool steels (3-D and 3-C) with a high fraction of carbides, especially large eutectic carbides and low wear rates ($\approx2.5\cdot10^{-5}$ mm^3/Nm) by hot-work tool steel A with the lowest fraction of carbides and high fracture toughness.

In terms of COF, for all materials it is higher under high-sliding-speed conditions, with cold-work tool steel B displaying the lowest values of about 0.5 and hot-work tool steel A

among the highest of about 0.7. Nevertheless, also cold-work tool steels with a high fraction of large eutectic carbides (C and D) show a higher friction.

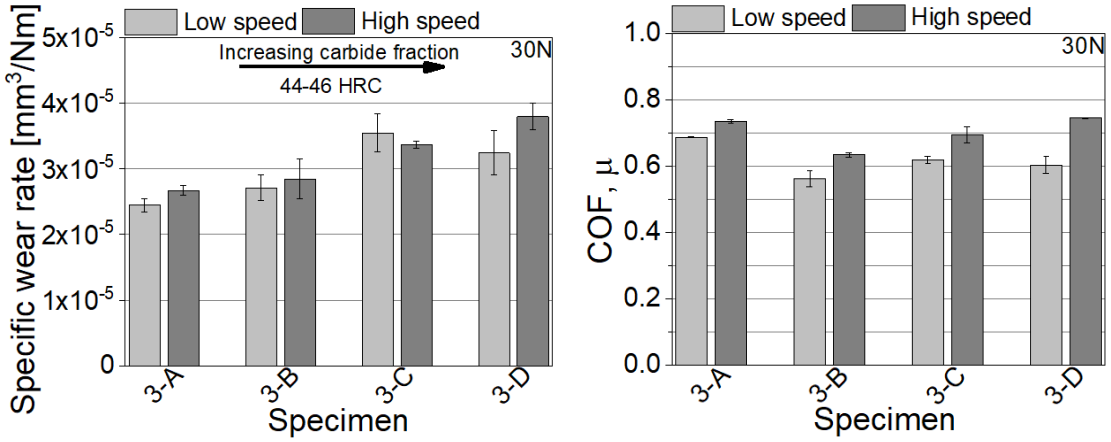

a) b)

Figure 81: Results of reciprocating abrasive wear resistance tests at nominal load of 30 N; a) wear rates of tool steels for hardness group 3, b) corresponding steady-state coefficient of friction (COF).

6.3.2.5 Different tool steels at the same hardness level – hardness group w (58–60 HRC)

Since the working hardness for cold-work tool steels is typically around 60 HRC, an additional group (w) of two cold-work tool steels, one with a high fraction of large eutectic and fine secondary carbides (D) and one with a reduced fraction of carbides (B), especially large ones, was prepared. For all the testing conditions tool steel D (w-D) with a high fraction of carbides shows substantially better (20–40 %) abrasive wear resistance but a higher friction (Figure 82 and Figure 83). On the other hand, at lower hardness values (55 HRC, 50 HRC and 45 HRC) cold-work tool steel D with a lower carbide fraction in general shows better wear resistance, with the difference diminishing with the increased hardness level and sliding speed. This indicates the importance of matrix hardness. In the case of tool steels with high fraction and density of large carbides, insufficient matrix hardness will result in increased wear due to carbide fracture and pull-out and their enrolment in the wear process, acting as hard third-body particles.

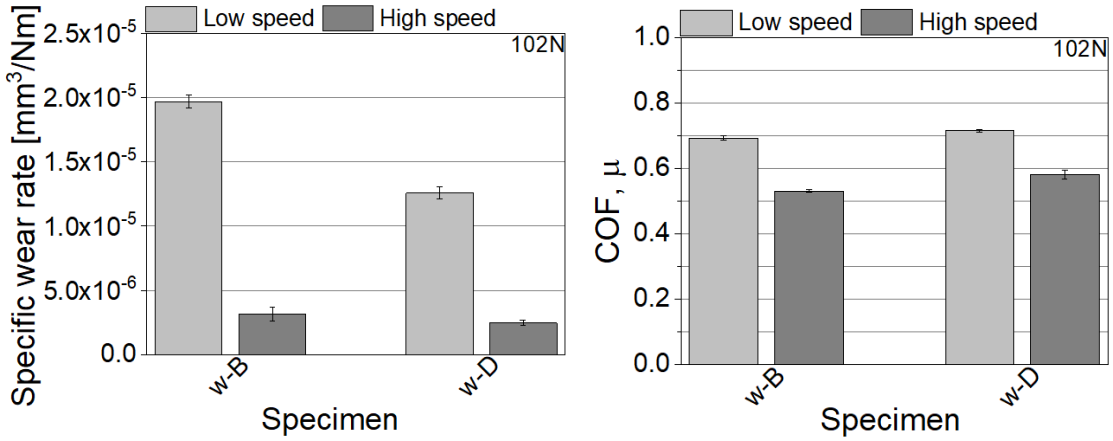

a) b)

Figure 82: Results of reciprocating abrasive wear resistance tests at nominal load of 102 N; a) wear rates of tool steels for hardness group w, b) corresponding steady-state coefficient of friction (COF).

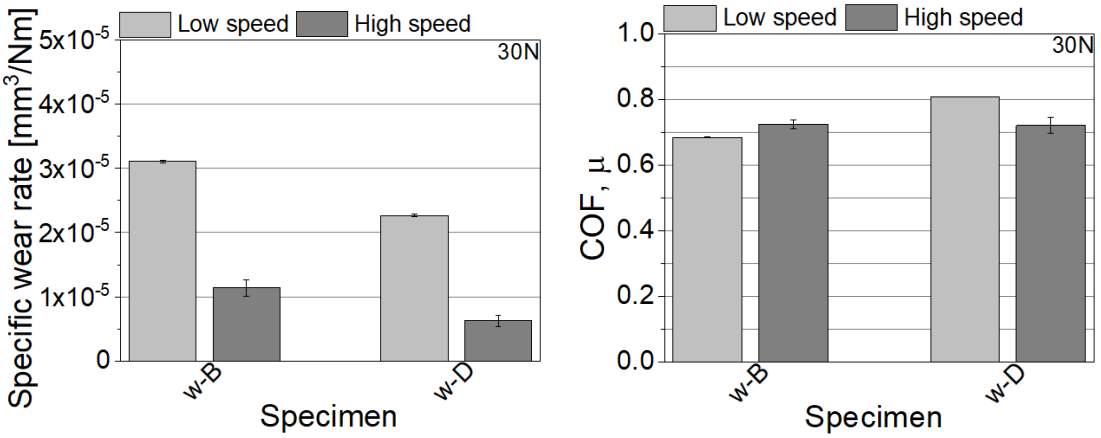

a) b)

Figure 83: Results of reciprocating abrasive wear resistance tests at nominal load of 30 N; a) wear rates of tool steels for hardness group w, b) corresponding steady-state coefficient of friction (COF).

6.3.3 Adhesive wear

In order to investigate how different microstructures influence the adhesive wear component, wear tests at a load of 40 N (p_H = 1000 MPa) were performed on tool steels in hardness group 1 using steel counter-balls. Two types of steel counter-balls were used, bearing steel ball (100Cr6; 58 HRC) simulating abrasive-adhesive wear and stainless steel ball (304L; <30 HRC) being much softer than the investigated tool steels and simulating pure adhesive wear. The main focus was on the adhesive wear component (i.e., transferred layer); therefore, only the volume of the adhered material above the reference surface of the polished tool steel sample was taken for the wear-rate calculation.

The initial adhesion of metals to the tool steel occurs locally on the metallic matrix of the tool steel due to the high affinity between pure metals [88]. However, by further sliding and growth of the transfer layer, tool wear is also influenced by the detachment of the transfer layer and its abrasive action, especially when using harder counter-materials (i.e.

100Cr6 steel). During prolonged reciprocating sliding and high loads, events of instant joining and fracturing take place, influencing the development and detachment of the transferred layer on the tool surface (Figure 86). Furthermore, high sliding speeds also create more severe wear conditions and intensified counter-material wear and removal. As shown in Figure 86, a lot of material has been removed from the softer 304L steel counter-ball on each side of the wear track. Accumulation of this material in the contact results in more turbulent and unpredictable contact behaviour, not being representative for the initial wear behaviour. In order to overcome this, adhesion tests were performed at two different sliding conditions. At a high sliding speed (0.12 m/s) with a prolonged sliding distance, and at a low sliding speed of 0.01 m/s for a very short sliding distance of just 4 m.

The results for the 100Cr6 steel ball are presented in Figure 84 and for 304L steel ball in Figure 85. For all four tool steels very similar adhesive wear rates and friction values were obtained against the 100Cr6 ball; ~3.1 $\cdot 10^{-5}$ mm^3/Nm and ≈0.55 at low sliding speed, and ≈0.15 $\cdot 10^{-5}$ mm^3/Nm and ~0.6 at high sliding speed, respectively. Only cold-work tool steel C displays 15–20% higher wear rates, with the difference diminishing with the increased severity of the contact conditions (i.e., a higher sliding speed and a longer time/distance). In the case of softer 304L steel counter-ball the adhesive wear component is much larger, being in the range of 6.5–8.5 $\cdot 10^{-5}$ mm^3/Nm for low sliding speed and 0.3–0.6 $\cdot 10^{-5}$ mm^3/Nm for high sliding speed. In both cases the COF is ≈0.45, as shown in Figure 85. However, in the initial phase (low speed, short sliding) the adhesive wear of the tool steels is increasing with the increased fraction of the carbides, while under more severe contact conditions (high sliding speed) and prolonged sliding, tool steel B, with a low fracture toughness, shows the lowest resistance towards adhesive wear. Wear tracks are shown and described in detail in subchapter 6.5.2, where the wear mechanism is described in detail.

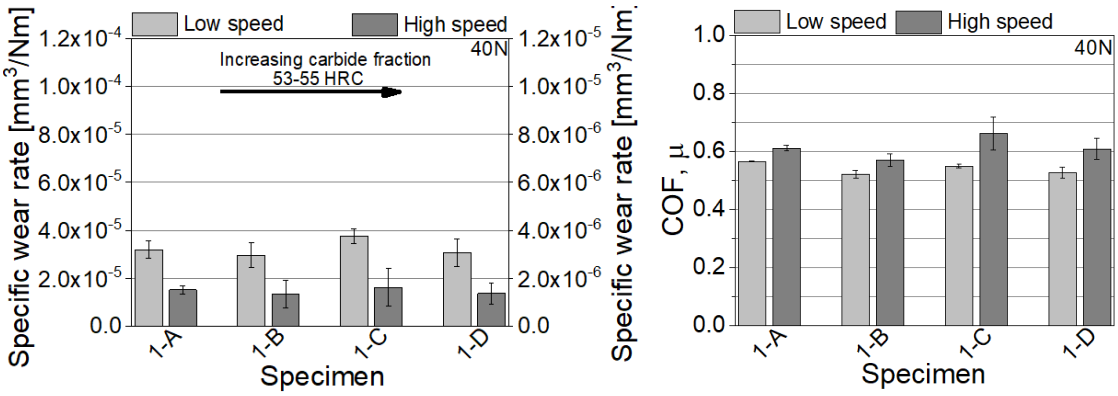

a) b)

Figure 84: Results of reciprocating adhesion promoted wear tests for hardness group 1 using 100Cr6 steel type counter ball; a) wear rates of tool steels and b) corresponding steady-state coefficient of friction (COF).

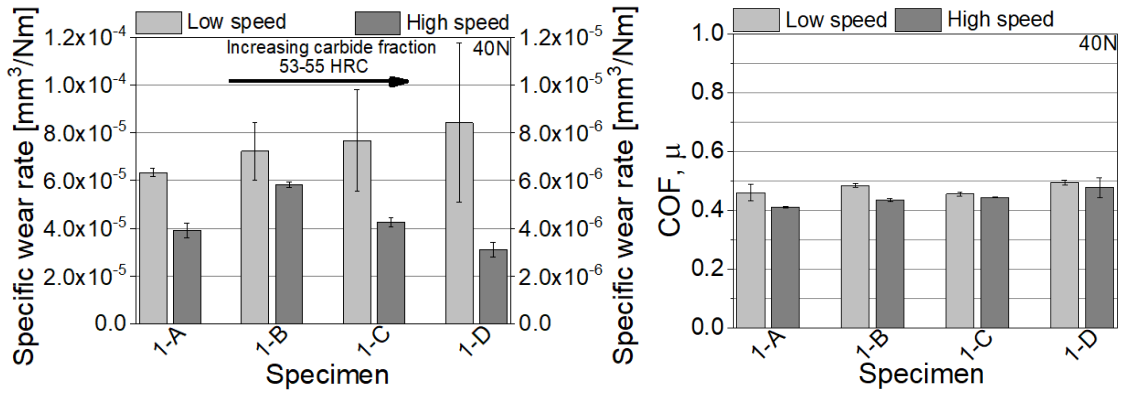

a) b)

Figure 85: Results of reciprocating adhesion promoted wear tests for hardness group 1 using 304L steel type counter ball; a) wear rates of tool steels and b) corresponding steady-state coefficient of friction (COF).

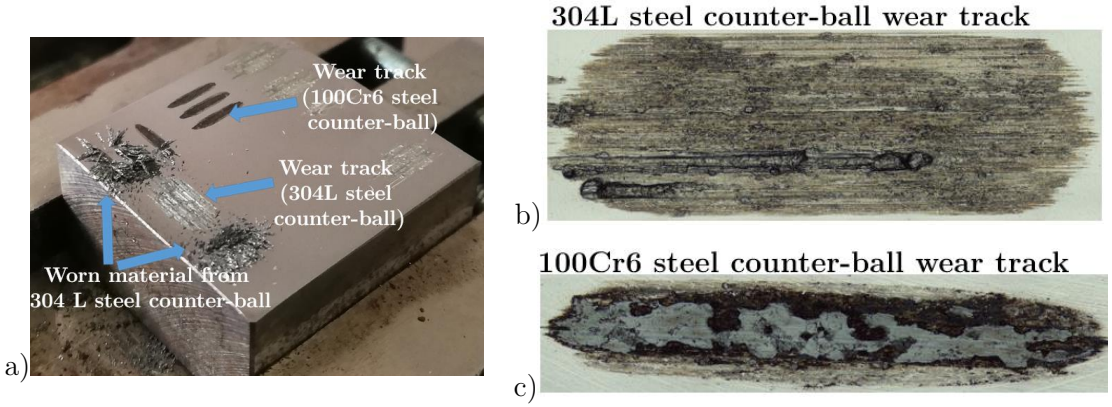

a) b) c)

Figure 86: Adhesion wear tracks on tool steel under low-speed conditions; a) OM macro image, b) wear track micrograph against 304L steel ball and c) wear track macrograph against 100Cr6 steel ball.

6.3.4 In situ wear debris removal

As mentioned in previous chapters, wear particles and detached carbides can have a significant impact on the wear. However, their role and how much they actively contribute to the overall wear during reciprocating sliding is not well known. Figure 87 shows how wear debris were successfully removed during the test using an air-blowing system (Figure 27). The wear test results for different tool steels in hardness group 1 (53–55 HRC) are shown in Figure 88. High-stress abrasion tests were performed under high sliding speed conditions (0.12 m/s) and a nominal load of 30 N (p_H = 1000 MPa) and compared to similar testing conditions without the in-situ wear-debris removal (Figure 77). Looking at the wear resistance graph in Figure 88a we can see that the difference between wear rates for hot-work tool steel containing a small fraction of fine secondary carbides is small. The wear rate without and with in-situ wear particles removal is not significantly different. There is some reduction in friction (Figure 88b), presumably due to a reduced ploughing effect in the metal matrix. However, when the same wear tests were performed on cold-work tool steels with higher fractions of large Cr-rich carbides and much lower fracture toughness the removal of wear particles proved to have a higher impact on the wear rates.

The highest difference was observed for cold-work tool steel B with the lowest fracture toughness, where the wear rate was reduced by ≈35 %. A significant improvement (≈25 %) was also achieved for the highest carbide fraction containing tool steel D, while for steel C reduction in the wear rate was of the order of 15 %. For cold-work tool steels the COF remained unaffected due to the specific microstructure containing large eutectic carbides.

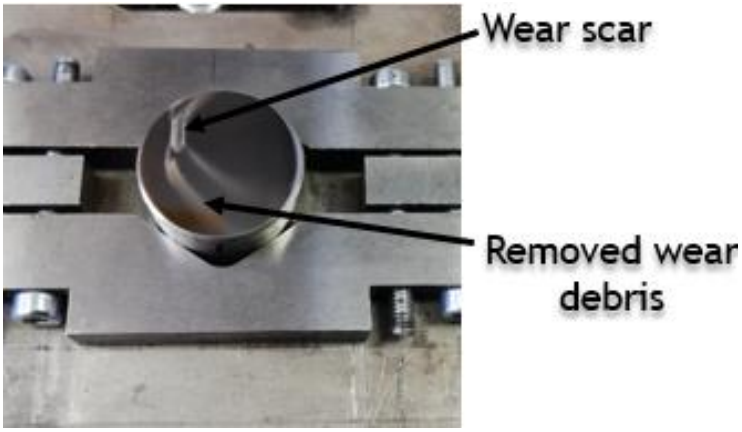

Figure 87: Indication of wear scar with removed wear debris.

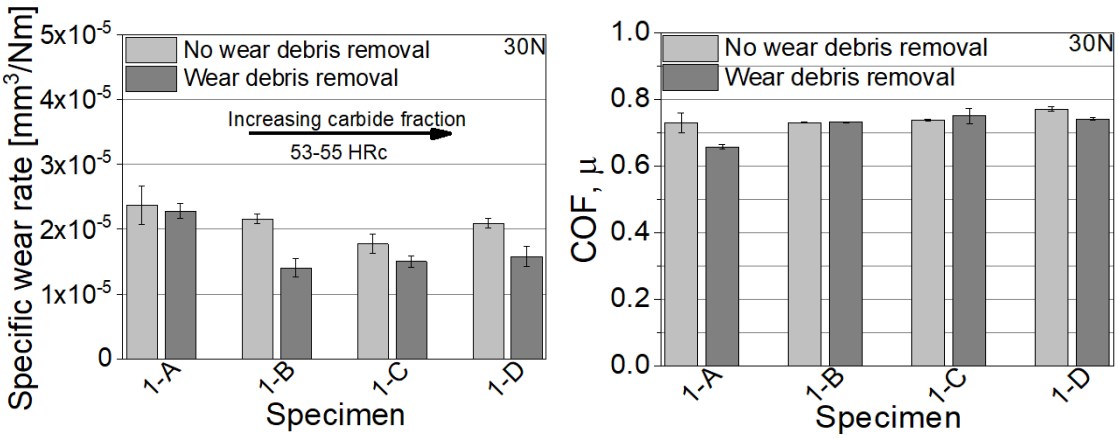

a) b)

Figure 88: Effect of wear particles' removal on abrasive wear test results; a) wear rates of tool steels for hardness group 1 and b) corresponding steady-state coefficient of friction (F_N = 30 N, v_s = 0.12 m/s; Al_2O_3 counter-ball).

6.3.5 Effect of eutectic carbides' orientation

To evaluate the effect of the carbides' orientation and the texturing of the microstructure on the wear resistance, hot-rolled and heat-treated cold-work tool steel D with the highest carbide fraction and density of large eutectic carbides was used and tested in the longitudinal and transverse directions under high-speed abrasive wear conditions (p_H = 1000 MPa, vs = 0.12 m/s, Al_2O_3 counter-ball). A low testing load (30 N) and a high tool-steel working hardness (58–60 HRC) were used to reduce the component of plastic deformation during sliding and focus purely on abrasion.

Figure 89 shows the wear rate of the specimens subjected to sliding in different directions. A wear rate of 6.24×10^{-6} mm³/Nm was obtained when the sliding was performed in the cross-section view with the microstructure corresponding to a more uniform distribution of carbides (direction T_1; Figure 28c). The wear rate in this case is 22 % lower than when

sliding perpendicular to the elongated eutectic carbides (direction T_2; Figure 28d) with a wear rate of 8.00×10^{-6} mm^3/Nm and 12 % lower as compared to sliding along the carbides (longitudinal direction; Figure 28d). The COF shows the same trend, as shown in Figure 89b.

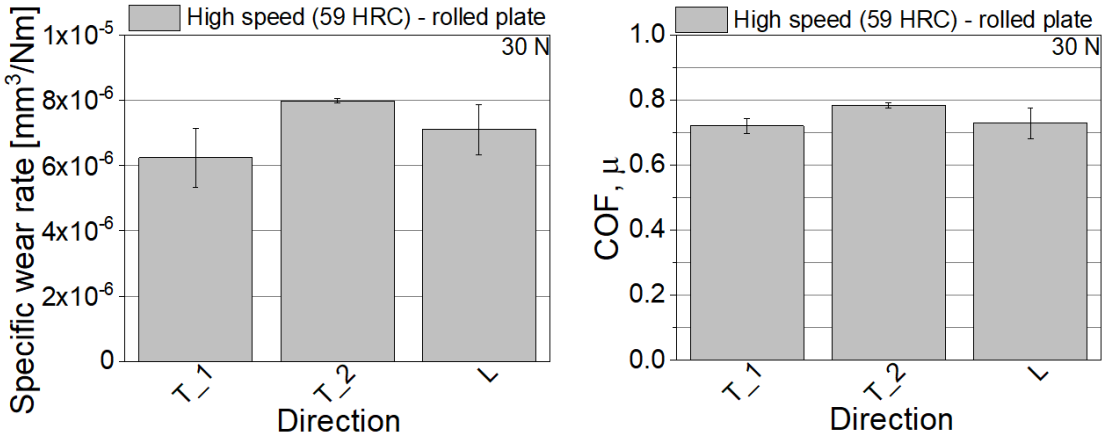

a) b)

Figure 89: Abrasive wear test results for hot-rolled and hardened (59 HRC) cold-work tool steel D depending on the eutectic carbides' orientation; a) wear rates b) corresponding steady-state coefficient of friction (COF).

6.4 Tribological Properties at Elevated Temperatures – Hot-Work Tool Steel

At elevated temperatures the wear properties of steels with coarse eutectic carbides (cold-work tool steels) deteriorate due to the drop in hardness. On the other hand, hot-work tools steel with microstructures consisting mainly of a martensitic matrix show greater matrix stability at elevated temperatures. Therefore, only hot-work tool steel A hardened to three different hardness levels was subjected to elevated-temperature sliding tests.

Abrasive wear resistance for hot-work tool steel A tested under reciprocating sliding conditions ($F_N = 30$ N, $v_s = 0.12$ m/s) at elevated temperatures of 250 °C and 500 °C and compared to RT is presented in Figure 90a. The corresponding steady-state COF is shown in Figure 90b.

The wear rates and wear mechanism at room temperature are very similar for hot-work tool steel A specimens in all three hardness groups, being in the range of 2.50×10^{-5} mm^3/Nm (Figure 90a). The COF at room temperature is ≈ 0.6 (Figure 90b). At increased testing temperature (250 °C) the wear rate increased by more than a factor of 2. However, it shows a decreasing trend with an increased tempering temperature and decreased sample hardness (1-A -> 2-A -> 3-A). On the other hand, the coefficient of friction decreased down to 0.3–0.4, with the softer surface displaying higher friction. (Figure 90b). With a further increase in the wear testing temperature to 500 °C the wear rate for all three hardness levels dropped significantly, again the hardest specimen (1-A) showing the highest wear rate (3.40×10^{-5} mm^3/Nm) and the softest one (3-A) the lowest wear rate (1.39×10^{-5} mm^3/Nm), as shown in Figure 90a. Similar to that, the COF also dropped, even below 0.2 (Figure 90b).

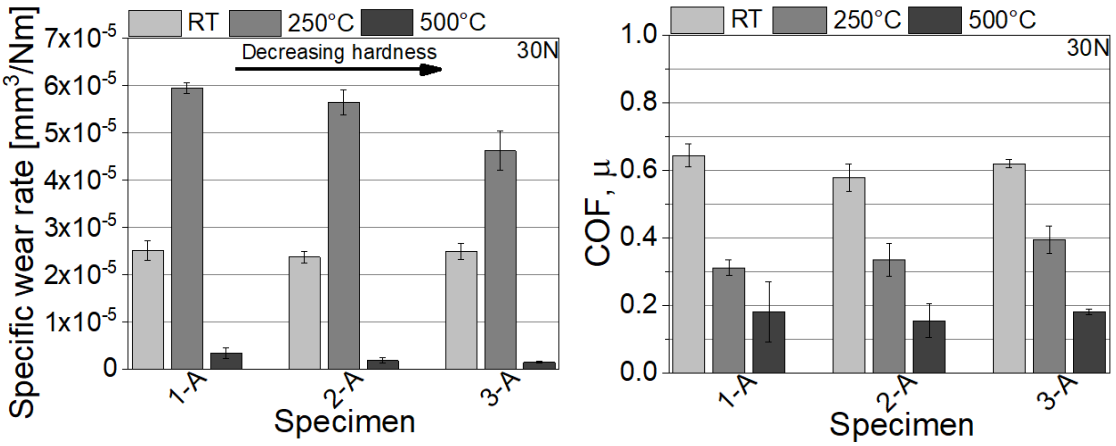

a) b)

Figure 90: Abrasive wear tests at elevated temperatures; a) wear rates, b) corresponding steady-state coefficient of friction (COF).

6.5 RT Wear-Related Microstructural Changes

6.5.1 Running-in stage of protruding carbides

Wear tracks for the short unidirectional sliding wear tests (10 cycles, p_H = 1000 MPa, v_s = 0.12 m/s, Al_2O_3 counter-ball) performed on the tool-steel specimens belonging to the hardness group 2 (2-A, 2-C and 2-D) and aimed at analysing the behaviour of protruding carbides during running-in are shown in Figure 91 and Figure 92. Cold-work tool steel B (2-B) was not considered as it contains similar Cr-rich carbides as found in the other two cold-work tool steels (C and D).

In the case of hot-work tool steel A the exposed carbides are small vanadium-rich carbides. Cold-work tool steel D shows a high fraction of chromium-rich carbides, large M_7C_3 type as well as smaller spherical ones of M_7C_3 or $M_{23}C_7$ type. However, for cold-work tool steel C both types, of fine V-rich and Cr-rich carbides are present, although Cr-rich carbides in a lower fraction and with a smaller average size of eutectic M_7C_3 carbides as compared to tool steel D. On the other hand, it shows a higher fraction of V-rich MC-type carbides, which can also be larger than 1 µm as compared to hot-work tool steel A.

The low fraction and small size of the hard carbide phase is not sufficient to bear the load in the case of hot-work tool steel A. Pro-eutectoid un-dissolved carbides are fractured, smoothened and glazed away already at the very beginning of the sliding contact (Figure 91a). Similar goes for the fine vanadium-rich secondary carbides present in the matrix of steel A and C, and displayed as white dots scattered in the dark-grey tempered martensite matrix (Figure 91a and b). The size and fraction of the carbides play an important role in the wear process. If they are too small, their direct role in improving wear resistance is negligible. The size level of the VC and fine secondary $(Cr, Mo)_{23}C_6$ carbides is too small to contribute to the direct wear resistance of the steel. However, looking at the large eutectic carbides present in a high fraction in tool steel D, no significant differences can be seen when comparing the worn and unworn surfaces (Figure 91b and c).

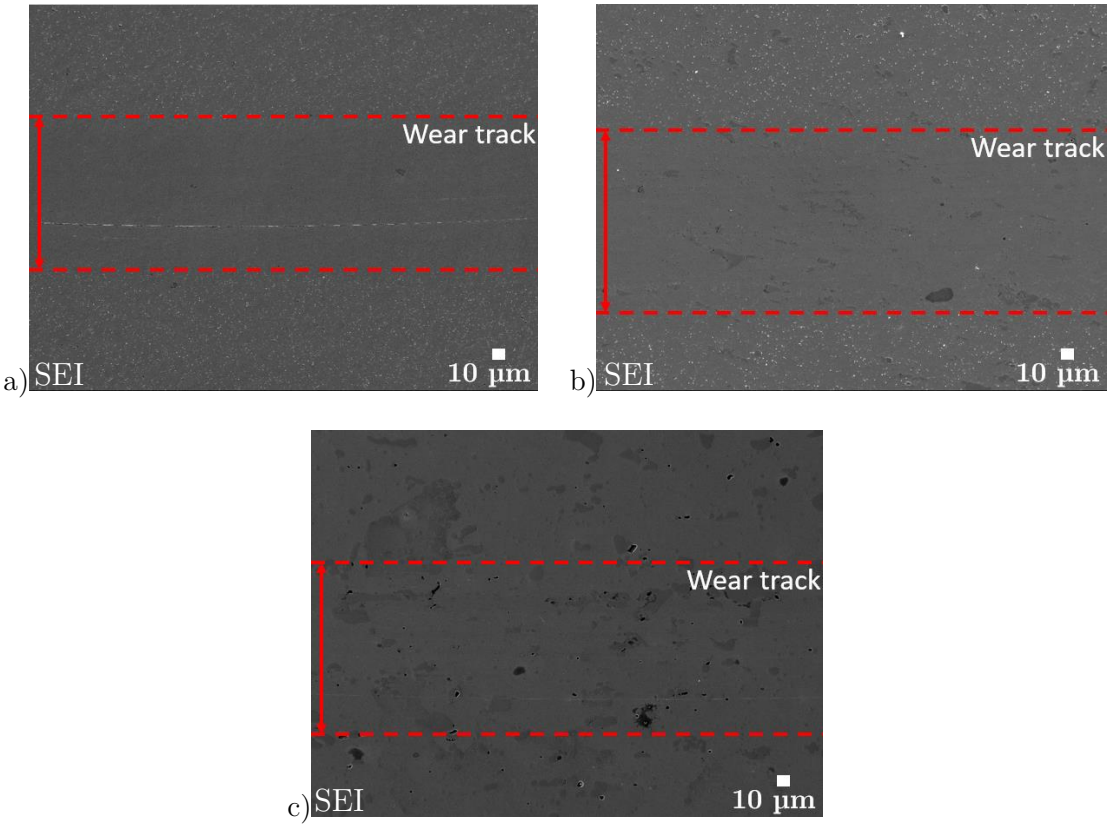

Figure 91: Wear track after initial unidirectional sliding for; a) 2-A, b) 2-C and c) 2-D specimens with different microstructure.

Magnified areas of the wear tracks (Figure 91) identifying different damage mechanisms occurring during the initial stages of sliding are shown in Figure 92. In Figure 92a small protruding secondary Cr-rich carbides of roughly 1 µm in diameter can be seen, that are exposed to micro cutting. Even very thin cuts/scratches can be seen. This is also true for the V-rich MC type carbides as seen in Figure 92b, although being considered to have significantly higher hardness than the Cr-rich carbides. Figure 92a and d show fine Cr-rich carbides that are smoothened with micro cuts going directly through them, continuing from the matrix. Smoothening of fine V-rich carbides is shown in Figure 92f, while Figure 92c displays a large eutectic carbide of M_7C_3 type being detached from the matrix. In general, four damage mechanism that are occurring during wear can be identified:

1. Carbide micro cutting (Figure 92a, b, d, e)
2. Matrix micro cutting (Figure 92a, b, d, e)
3. Carbide detachment from the matrix (Figure 92c)
4. Carbide smoothing (Figure 92c, f, e)

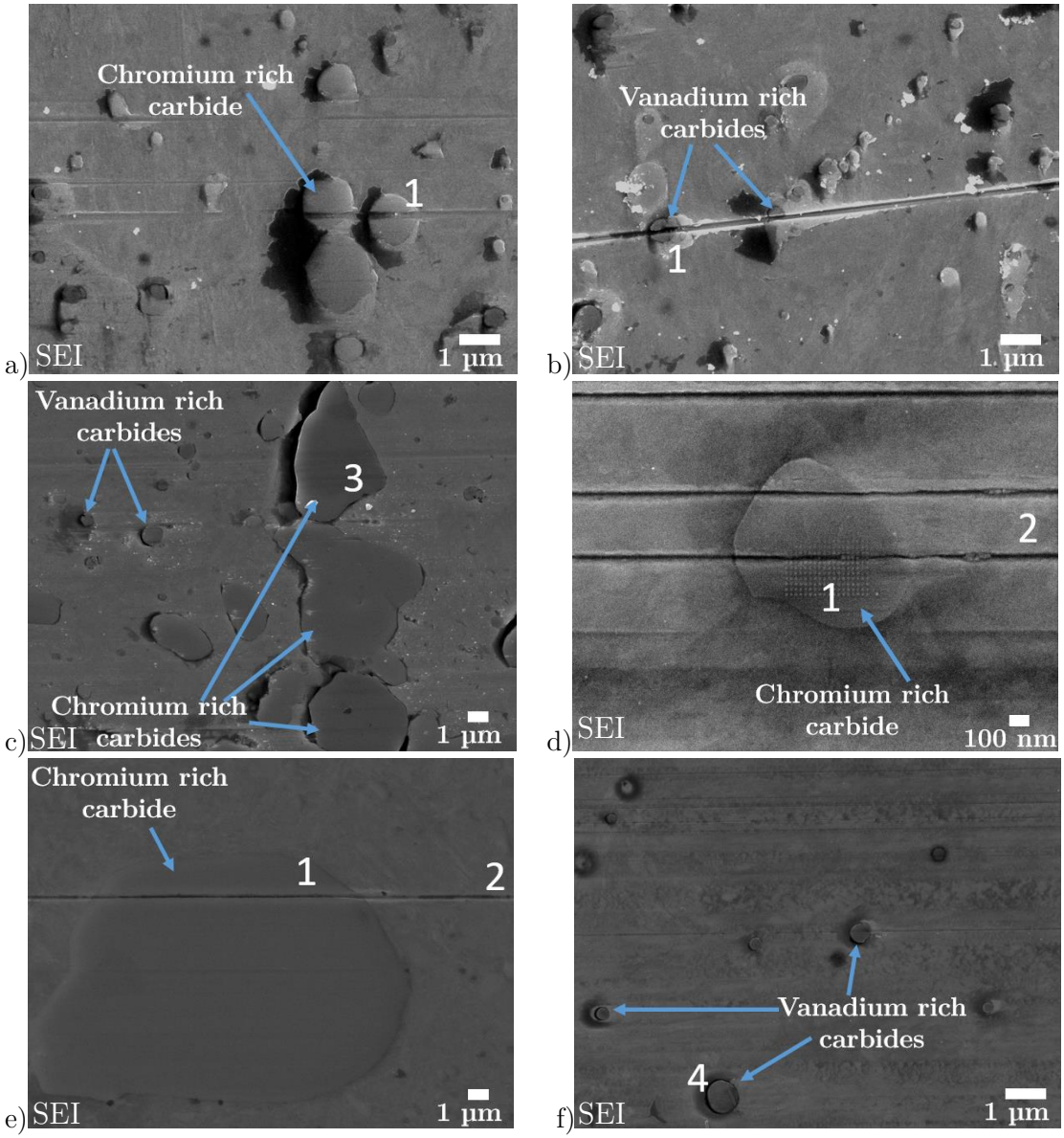

Figure 92: High-magnification micrographs of wear tracks after initial unidirectional sliding; a, b, c) 2-C specimen, e) 2-D and f) 2-A specimen.

A schematic representation of the carbides' behaviour during sliding against a hard counter-body is presented in Figure 93. Smaller carbides that do not bear the load are, when exposed to sliding, quickly fractured and smoothened. Larger ones also start to smoothen; however, it takes more cycles to be in the line with the matrix. Before that happens, they can also be detached and removed from the matrix, rather than completely smoothened out.

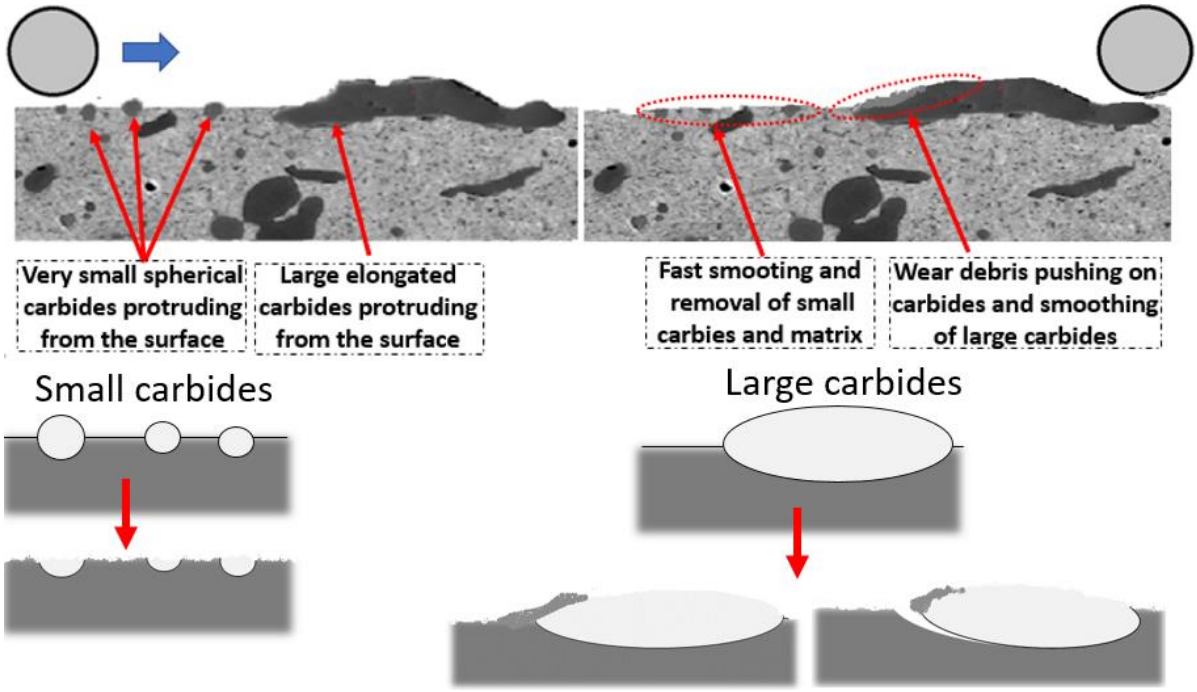

Figure 93: Schematic of carbides behaviour in the initial stage of abrasive-wear-promoted sliding.

6.5.2 Microstructural changes during prolonged sliding

Scanning electron micrographs of wear tracks after 100 m of reciprocating sliding under abrasive wear conditions for hardness group 1 specimens are shown in Figure 94. Wear tracks for cold-work tool steel D containing the highest fraction of Cr-rich carbides are shown in Figure 94a and for hot-work tool steel A with a very low fraction of fine V-rich carbides in Figure 94b. In the case of tool steel D areas of large carbides that are fractured and smoothened can be seen (Figure 94a). It has to be mentioned that when making tool steel (i.e., hot-rolling or hot-forging) coarse eutectic carbides can be already fractured and as can be seen in the unworn microstructure (Figure 49). However, additional sliding further provokes their cracking and fracturing, with the pre-existing cracks accelerating their removal from the matrix. Some patches of accumulated wear debris can also be seen in the wear-scar region. Similar destructive processes involving carbide fracturing, groove formation, smoothening of the worn surface (carbide and matrix) as well as plastic deformation of the matrix can be observed for all tool-steel specimens containing large eutectic carbides in the matrix, regardless of the severity of the contact (load and sliding speed). However, in the case of hot-work tool steel with the predominantly metal-matrix microstructure with only very fine carbides mainly carbides smoothening, grooving and plastic deformation of the matrix can be observed without areas of carbide fracturing (Figure 94b).

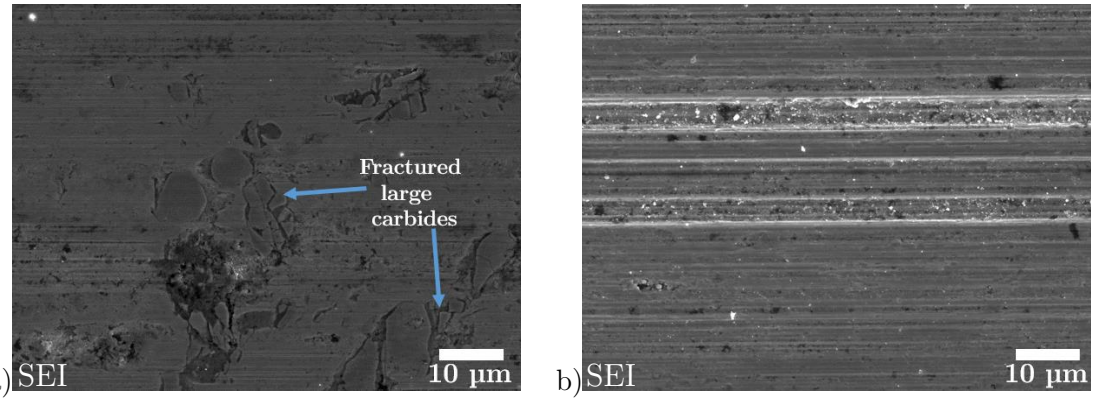

Figure 94: Top view of reciprocating abrasive wear track for a) 1-D specimen and b) 1-A specimen.

In the case of adhesive wear (Figure 95) a large amount of adhered counter-body material (more distinctive for softer materials, i.e., 304L stainless steel) is built up on the surface of the harder tool-steel specimen, regardless of the type and quantity of carbides in the martensite matrix. However, exposed carbides visible in the case of a high amount and large carbides containing cold-work tool steel D (Figure 95a) confirm the lower affinity and easier detachment of adhered material from the carbide region than from the matrix. On the other hand, even for low carbides containing hot-work tool steel, sharp edges of the adhered material are observed (Figure 95b), indicating its fracturing and delamination during sliding.

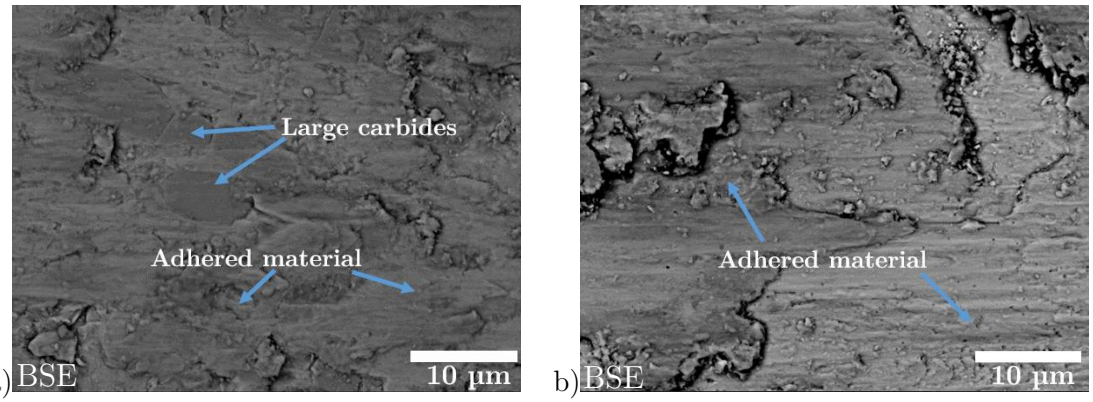

Figure 95: Top view of reciprocating adhesive wear track against 304L stainless steel counter-ball for a) 1-D specimen and b) 1-A specimen.

In the case of a harder counter-material (i.e., 100Cr6 steel ball) adhesive wear is accompanied by an abrasive wear component, being more vivid for hot-work tool steel with a significantly smaller volume and size of the hard carbide phase (Figure 96).

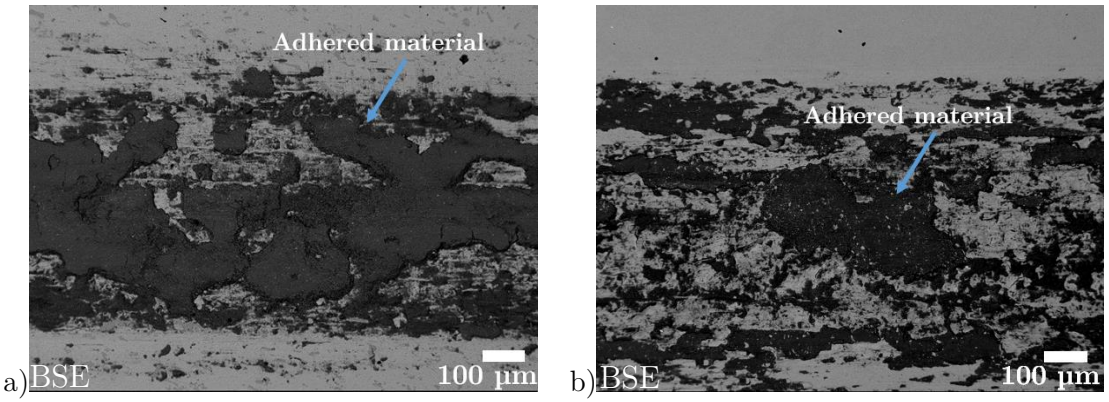

a) b)

Figure 96: Top view of reciprocating adhesive wear track against 100Cr6 steel counter-ball for a) 1-D specimen and b) 1-A specimen.

To better observe the microstructure's response to wear and especially the carbides' behaviour during wear, unidirectional sliding wear tests were also performed and analysed, focusing on hardness groups 2 (48–50 HRC) and 3 (44–46 HRC). The wear-track analysis for cold-work tool steel D, having the highest amount of large eutectic carbides is shown in Figure 97, and for hot-work tool steel A with the lowest carbide fraction in Figure 98. Both tool steels were hardened to the same bulk hardness of 49 HRC (2-D and 2-A). In the wear region, islands of generated wear debris, mainly originating from the investigated tool-steel material are visible in both cases. However, they are more abundant in the case of the tool steel with the higher fraction of carbides. Furthermore, wear debris are mainly built up in the matrix region, in front of the sites containing a high density of carbides. This indicates that larger protruding particles catch the wear debris, which then start building up at the carbides' leading edge (Figure 97b) on the matrix with a higher adhesion affinity, if the carbides are not plane parallel to the matrix and smoothened beforehand, as shown in Figure 97a. However, in the case of material A with a very small number and size of carbides, most of the wear particles are pushed out of the contact, thus taking longer to start accumulating in the contact zone.

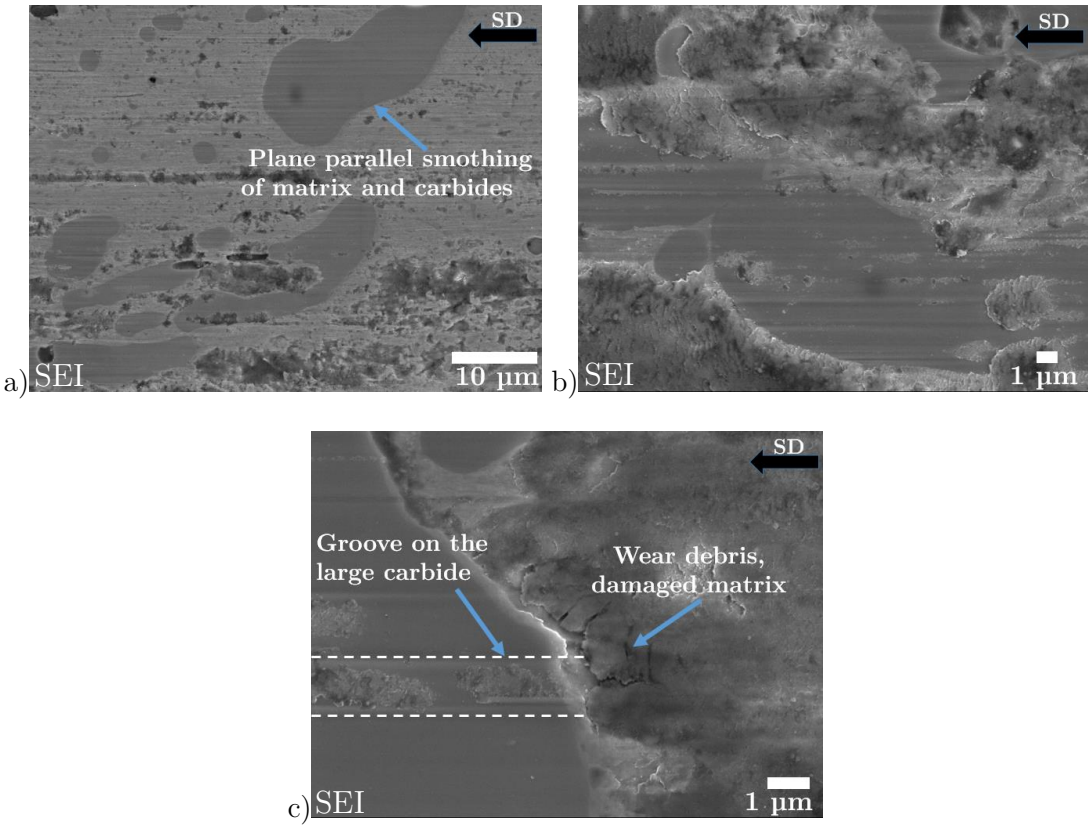

Figure 97: Top view of unidirectional abrasive wear track for cold-work tool steel D (2-D specimen); a) worn surface at lower magnification, b, c) detail of M_7C_3-type carbide/matrix interface; SD – sliding direction.

In the case of the hot-work tool steel with a very fine and low fraction of MC-type carbides (2-A specimen) wear-debris build up is considerably smaller (Figure 98a). Very fine hard carbide particles still act as traps for the wear-debris accumulation, but on a much smaller scale, as shown in Figure 98c. However, carbide exposure from the matrix is quickly achieved by removal of the embedding matrix, resulting in tearing the carbides from the matrix.

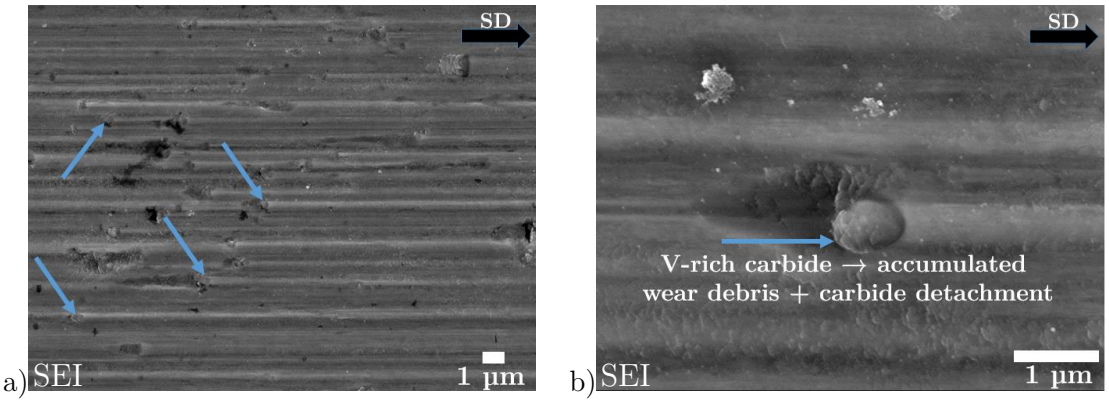

Figure 98: Top view of unidirectional abrasive wear track for hot-work tool steel A (2-A specimen)); a) worn surface at lower magnification, b) detail of small MC type carbide in the matrix; SD – sliding direction.

In order to investigate the wear provoked by sub-surface changes in the microstructure, hardness group 3 specimens were selected, where the highest degree of damage was expected. This also enabled an easier observation of the wear processes and the hard carbides' behaviour. Cross-section views of the unworn surface for hot-work tool steel A (3-A) and cold-work tool steel D (3-D) hardened to 45 HRC are shown in Figure 99. Corresponding cross-section views of the wear tracks are presented in Figure 100 to Figure 102. In the case of cold-work tool steel D, with the highest fraction of large eutectic and fine secondary carbides, the microstructure shows large undamaged M_7C_3 Cr-rich carbides as well smaller secondary Cr-rich $M_{23}C_6$-type carbides in the tempered martensite matrix (Figure 99b).

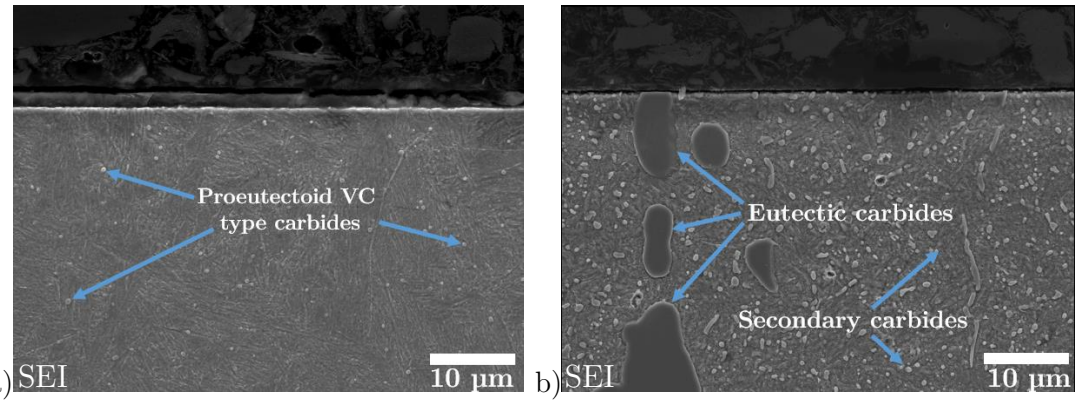

Figure 99: Cross-section view of the etched, unworn microstructure of (a) specimen 3-A and (b) specimen 3-D.

When such a material is exposed to sliding against a much harder counter material (Al_2O_3 ceramic ball) and high loads, a severely damaged subsurface region is observed, as shown in Figure 100. In Figure 100a the subsurface microstructure with a fragmented large eutectic carbide that has already been in contact with the counter-body can be seen. Crushed carbide is trapped between the hard counter body and the matrix (Figure 101a) or another hard carbide particle beneath (Figure 101c). As the martensite matrix starts to deform under the loading from the counter-body, carbides will start to crack, as their deformability is much lower than the matrix and plastic deformation of the matrix embedding large eutectic carbides occurring only in the area directly below the contact. The surrounding matrix is too far from the contact zone for the plastic deformation to take place. The large carbide is pinned from the bottom side and dynamically loaded by the sliding counter-body. Thus, the carbide is gradually removed from its position and crushed (Figure 100). Large pre-cracks formed in eutectic carbides (Figure 48) during the steel-making process and insufficient hardness of the matrix further accelerates the carbides exfoliation during sliding. Figure 100 and Figure 101b show areas with severe plastic deformation of the matrix, which pushes the large elongated eutectic carbide and their fragments in the sliding direction. Carbides' detachment and movement create voids even way below the worn surface (Figure 100 and Figure 101b). This further weakens the region exposed to the wear. Smaller carbides, on the other hand, are mainly moved along with the plastically deformed, surrounding, tempered martensite matrix. Cracks can also form in the matrix itself, especially in regions close to the worn surface (Figure 101c).

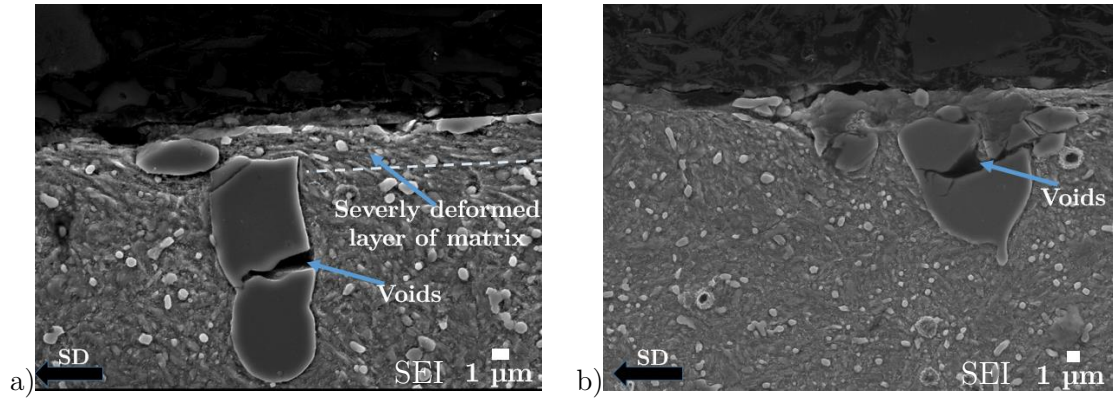

Figure 100: Unidirectional abrasive wear-induced microstructural changes in cold-work tool steel D (3-D specimen); a, b) eutectic carbide fracturing; SD sliding direction.

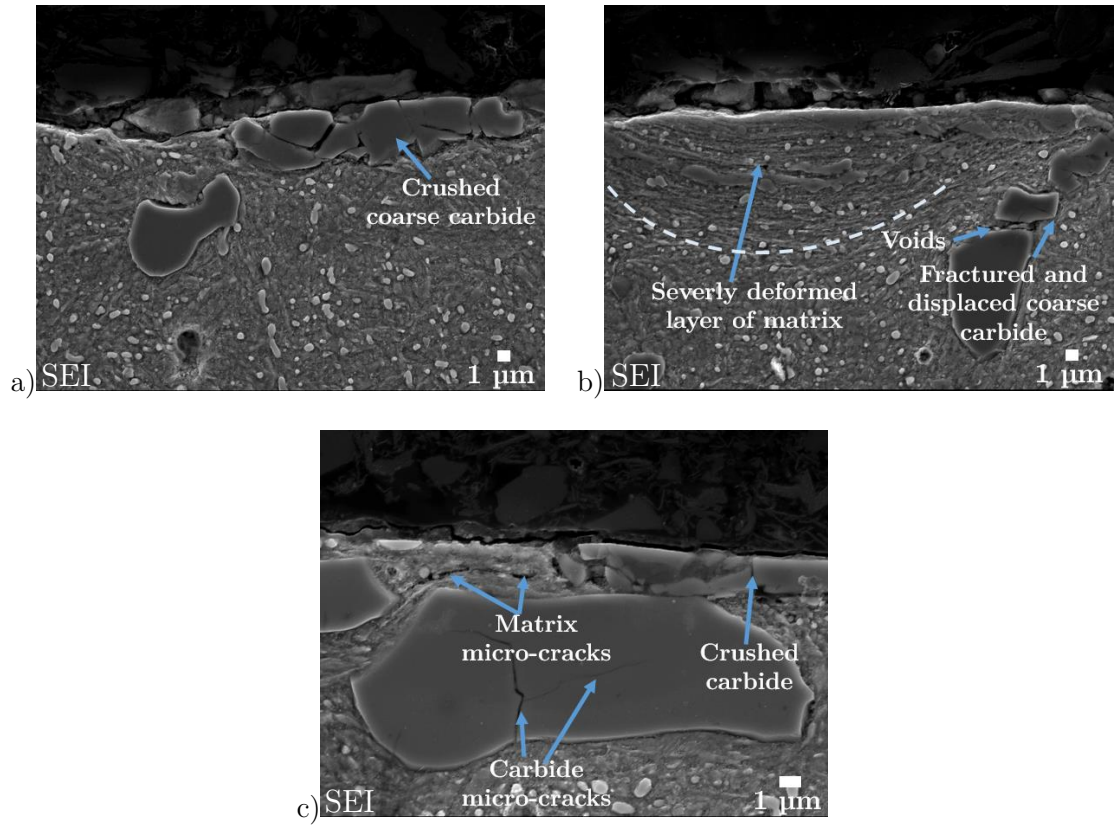

Figure 101: Reciprocating abrasive wear-induced microstructural changes in cold-work tool steel D (3-D specimen); a) crushed carbide ploughing the matrix, b) severe plastic deformation of subsurface and fracturing of carbide and c) matrix micro cracking and crushed carbide.

In the case of hot-work tool steel A (Figure 99a) the microstructure mainly consists of tempered martensite with a very small fraction of carbides. Only a few undissolved V-rich MC-type carbides are visible, scattered through the martensite matrix.

When material with a prevailing martensitic matrix microstructure is exposed to high-load abrasive wear, very distinct deformation of the subsurface layers occurs, as shown in Figure 102. Martensitic laths in the subsurface region are being compressed and bend in

the sliding direction, with only a few and very small carbides obstructing the martensite matrix's deformation.

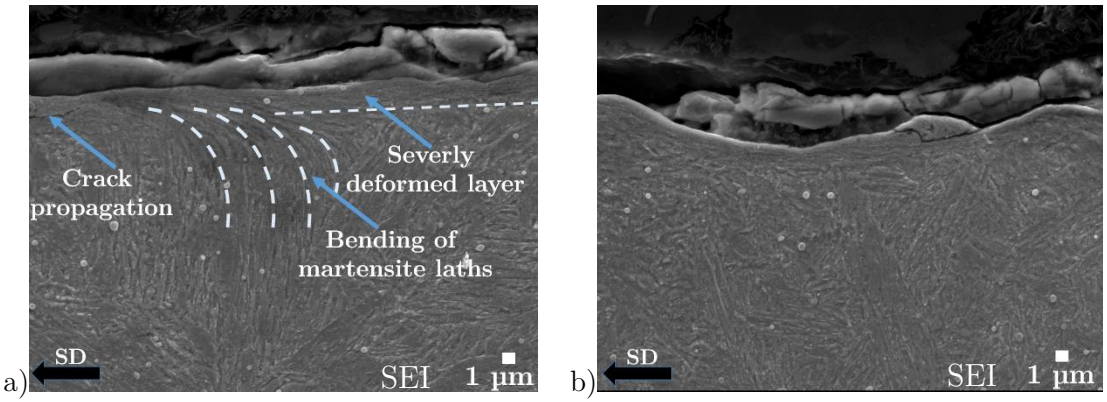

Figure 102: Unidirectional abrasive wear-induced microstructural changes in hot-work tool steel A (3-A specimen).

6.6 HT Wear-Related Microstructural Changes

Wear tracks for room and high-temperature reciprocating sliding tests of hot-work tool steel A are shown in Figure 103 and Figure 104. As was presented before, the wear rates and wear mechanism at room temperature were very similar for hot-work tool steel A specimens in all three hardness groups (Figure 90a). From the microstructure point of view, the difference in the wear resistance between the specimens in different hardness group is due to the higher degree of decomposition of the martensite structure and the loss of tetragonality, which results in a hardness drop. The decomposition of martensite, on the other hand, leads to the precipitation of carbides. Typical for hot-work tool steels are facetted M_7C_3-type carbides, large globular carbides of $M_{23}C_6$ type, elongated M_3C carbides and small globular carbides (MC type), as shown by Mebarki et al. [117]. However, in the current case only MC-type carbides were identified for all tempering conditions and being significantly smaller than 1 µm, thus not directly contributing to the abrasive wear resistance. At elevated temperatures, material loss is governed by a detrimental combination of thermal loading, wear processes and oxidation, called tribo-oxidation. In this case metallic debris created in the contact region are oxidised during sliding [21].

During RT tests a large amount of oxidized wear debris was found in the contact zone (Figure 104a). On the other hand, for tests performed at 250 °C, deeper wear tracks were observed, with only sporadic, oxidized wear particles present within the central part of the wear track (Figure 104b). However, some larger oxide particle patches do accumulate at the wear track outskirt, but do not form a protective glaze layer (Figure 103b, e). Such a protective oxide glaze layer, covering almost the complete wear track, can be seen for the tests performed at 500 °C (Figure 103c and f and Figure 104c). For the 250 °C and 500 °C tests the same type of oxide is formed (Table 21); however, due to the too low temperature, the particles are not compacted in a continuous protective glazed layer. In contrast, elevated temperature and oxide particle formation result in a significant increase in the abrasive wear component. However, as shown previously, the wear rate at 250 °C started to decrease with a lower material hardness. For the specimen with a lower hardness (3-A vs. 2-A and 1-A), a larger amount of oxide particles are formed, resulting in the formation of intensified oxide layer patches within the wear track (larger amount of grey phase in the

wear track seen in Figure 103e compared to Figure 103b) and reduced wear. As determined from the chemical analysis, the individual patches and compacted glaze layer contain large amounts of oxygen as well as elements from the tool steel and Al from the counter-body (Table 21). This confirms that the patches and glaze layer result from the agglomeration and compaction of the wear debris. It has been indicated that the tendency to form a glaze layer is readily influenced by the chemistry of the oxide generated and the temperature [121]. The formation of such layers is associated with the establishment of compacted layers of oxide and partially oxidized alloy particles on the sliding surfaces, determining the COF and wear rate [122].

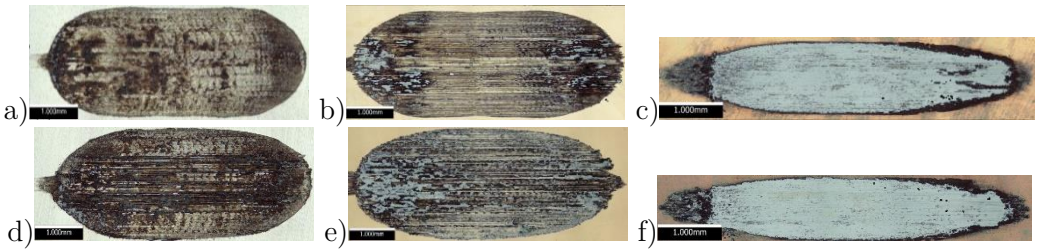

Figure 103: Top view of reciprocating abrasive wear tracks for hot-work tool steel A; a, b c) 1-A specimen and d, e, f) 3-A specimen tested at (a, d) room temperature (RT), (b, e) 250 °C and (c, f) 500 °C.

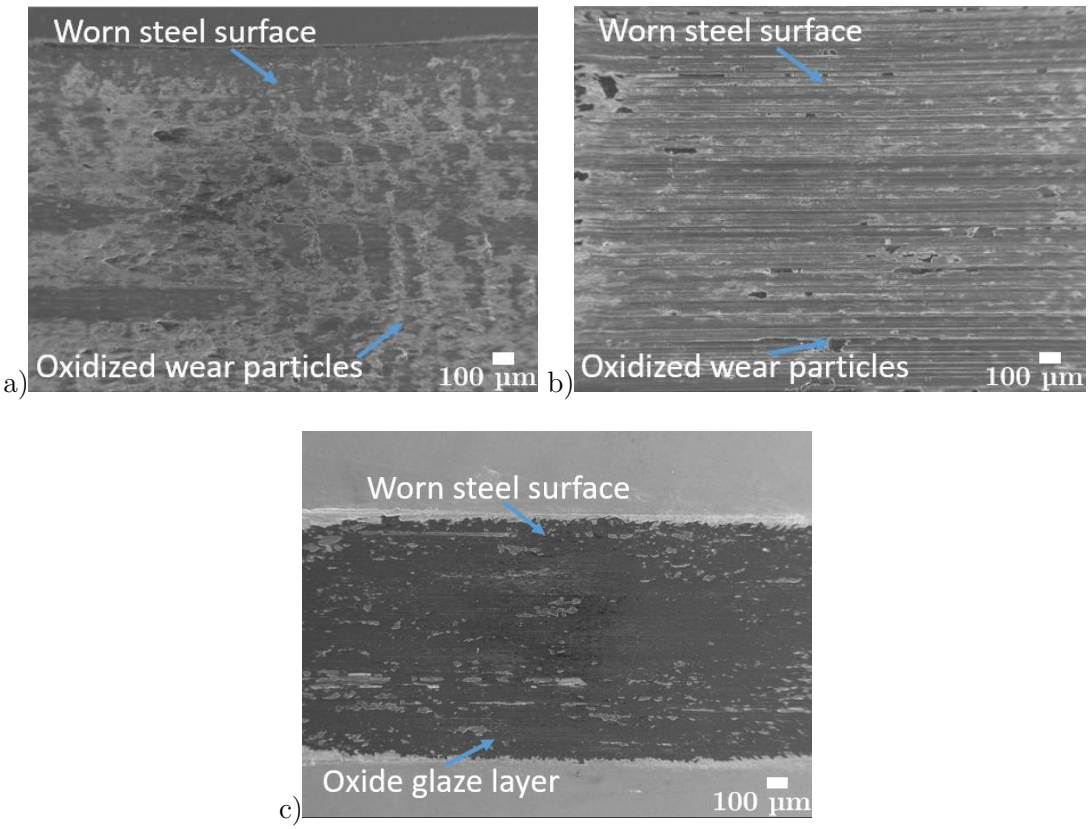

Figure 104: SEI images of top view of reciprocating abrasive wear tracks for hot-work tool steel A (1-A specimen) tested at (a) room temperature (RT), (b) 250 °C and (c) 500 °C.

Table 21: Comparison of EDS analyses for glazed layer and oxide particles created on the worn surface after wear tests at 250°C and 500 °C for softest (3-A) test specimen.

Element	EDS of	C	O	Al	V	Cr	Fe	Ni	Mo	Total
3-A 250 °C	glazed	1.8	33.2	0.4	0.4	3.5	57.4	1.6	0.9	100
3-A 500 °C	layer	1.5	36.9	1.9	0.4	2.9	54.2	1.3	1.0	100

Looking at the wear track cross-sections (Figure 105) severe plastic deformation of the martensitic laths can be seen, regardless of the testing temperature, even at room temperature. Although at room temperature the nominal contact stress is below the material's yield strength, local variations in the stress distribution and load spikes due to entrapped wear particles can lead to local plastic deformation. On the other hand, the formation of a thick oxide layer at the highest testing temperature of 500 °C provides a certain load-carrying effect, even though the contact stresses may exceed the material's yield strength for specimens in the lower hardness groups (<50 HRC). As shown in Figure 105c and f, a thick oxide glazed layer is present on all the hot-work tool steel specimens, the hardest (1-A; Figure 105c) and the softest (3-A; Figure 105f). However, for the harder specimen the interface between the glazed layer and the wear surface is continuous, with some micro-cracks visible deeper below the worn surface (Figure 105c), while for the softest specimen the layer seems to be detached from the tool-steel surface (Figure 105f). In the case of the wear tests performed at 250 °C (Figure 105c and d) the main wear mechanism is severe abrasion with the presence of plastic deformation, which is more pronounced for the softer test specimen. In this case, many valleys are filled with oxidized wear particles (Figure 105d).

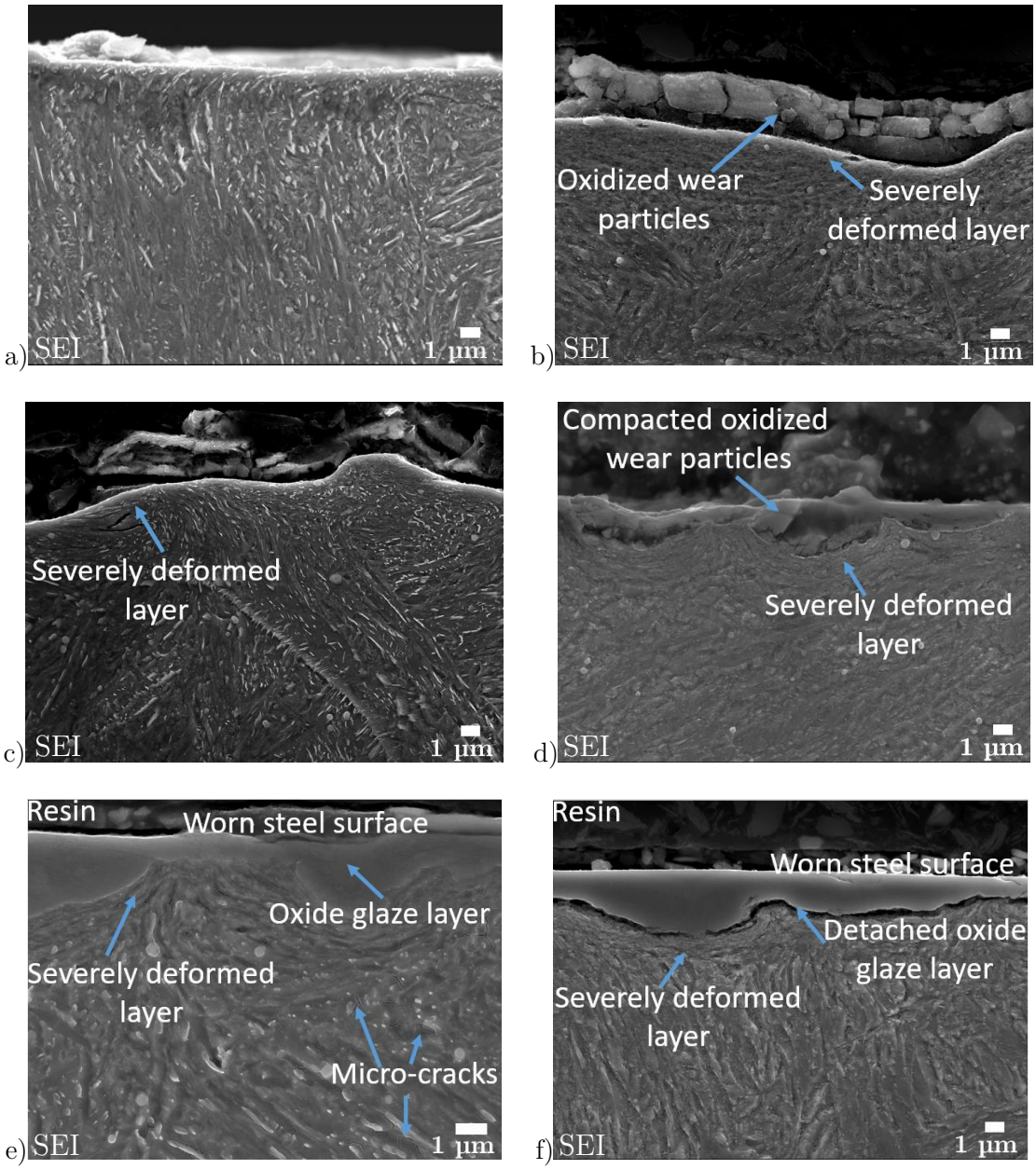

Figure 105: HT abrasive wear-induced microstructural changes in hot-work tool steel specimens 1-A (left) and 3-A (right), tested at (a, b) room temperature, (c, d) 250°C and (e, f) 500°C.

Chapter 7

Discussion

7.1 Microstructure

The tool steels included in the investigation were microstructurally characterized using different techniques. We started with the thermodynamic software calculations of phase stability. This served as a mere approximation and told us what carbide types are to be expected in the tool steels based on their chemical compositions. ThermoCalc simulations are limited to the equilibrium state and the extent of the thermodynamic data available in the database. Therefore, deviations from the microstructures achieved in practice were expected. In the case of hot-work tool steel Mat. No. 1.2367 mod. (material A), the most stable are vanadium-rich carbides, stable up to about 1140°C. The other carbides predicted to exist in the material A are $M_{23}C_6$ (chromium-rich carbides) and M_6C (molybdenum-rich carbides). For the recommended hardening temperature of 1030°C, only vanadium-rich carbides were found in this steel, as confirmed by SEM and EBSD. This is in the agreement with the literature, reporting mainly MC-type vanadium carbides to remain undissolved in the matrix [19, 111]. In terms of the austenitization temperature, being too low, at 950°C, results in retarded dissolution of the residual carbides, with two types of residual carbides present ($M_{23}C_6$ and MC) and a smaller grain size (36.9 µm; 6.9 ASTM). On the other hand, being too high (1150 °C), almost complete dissolution of the pro-eutectoid carbides takes place, being accompanied by a significant increase in the prior-austenite grain size (199.7 µm (2.0 ASTM). Small undissolved MC-type carbides are present at the austenite grain boundaries, pinning the grains and obstructing their growth.

For cold-work tool steel Mat. No. 1.2363 (material B) ThermoCalc software calculations predicted mainly M_7C_3- and MC-type carbides. The presence of large M_7C_3-type eutectic carbides, which can improve wear resistance [83], was confirmed in this steel. However, due to the lower amounts of carbon and chromium (1 % C, 5 % Cr) their volume fraction is low (0.5 ±0.1 %), the lowest among the cold-work tool steels investigated. Another carbide type present in tool steel B was $M_{23}C_6$, not the MC type, as predicted by the ThermoCalc calculations. Most of those Cr-rich carbides are smaller than 5 µm and were further size classified based on the method presented in [88, 89]. The group of small Cr-rich secondary carbides sums up to a volume fraction of about 4 %.

Three types of carbides were predicted in the case of the cold-work tool steel Mat. No. 1.2990 (material C). Those were M_7C_3, $M_{23}C_6$ and MC type, with the highest fraction of about 10 % predicted for $M_{23}C_6$-type carbides and their volume fraction slowly decreasing with the increased tempering temperature. The existence of all three carbide types was confirmed, although at lower fractions compared to the theoretical calculations. Compared to cold-work tool steel B, steel C shows a higher fraction of all carbides, eutectic and secondary, with a total carbide fraction of about 6.3 % in all the hardness groups. It

contains over 2 % of the eutectic carbides as well up to 1 % of the MC-type carbides rich in vanadium and in sizes over a few microns. A higher fraction of eutectic carbides is due to a higher amount of chromium (8 wt.%). This steel also has an increased amount of molybdenum and vanadium, resulting in a higher fraction and size of MC-type carbides as compared to other tool steels used. The aim of the larger MC-type carbides is to provide an enhanced wear resistance without compromising the material's toughness [83].

One of the most widely used cold-work tool steels is AISI D2 or Mat. No. 1.2379 (material D). As compared to other tool steels used in the current study, it contains the highest fraction of large eutectic Cr-rich carbides of M_7C_3 type. A mass fraction above 10 % in the high-tempering-temperature range was predicted with the ThermoCalc software, also indicating the presence of other chromium-rich $M_{23}C_6$-type and vanadium-rich MC-type carbides. However, only M_7C_3- and $M_{23}C_6$-type carbides were experimentally confirmed. This steel shows the highest fraction of carbides of up to 12 %. The fraction of large eutectic carbides is up to 7 % and smaller secondary carbides up to 3 %, which is in a good agreement with other studies [89]. Large amounts of carbide-forming elements such as carbon, chromium and molybdenum found in this steel result in the formation of massive, wear-resistant eutectic carbides that are not dissolved even during high-temperature austenitizing [1].

7.2 Influence of Grain Size on Mechanical Properties and Wear Resistance

Grain size and the dissolution of small residual carbides have an impact on the mechanical properties as well as the wear resistance of tool steels. To eliminate the hardness as a wear determining factor, hot-work tool-steel specimens displaying the same hardness (≈51 HRC) but having different microstructures as a result of the altered heat-treatment parameters (austenitizing and tempering temperature) were prepared and tested. Under low-speed conditions the best abrasive wear resistance was displayed by the specimens subjected to the recommended intermediate austenitization temperature. Under these hardening conditions, both the grain size and the fraction of residual carbides were not the most beneficial ones (small grain size and high fraction of carbides). This indicates that wear resistance is not only grain-size and carbides-fraction dependent, but indirectly influenced also by the mechanical properties (i.e., ductility, toughness and yield strength).

The wear rate of the material is greatly influenced by the load used, with high loads being in the material-yield-strength range leading to greater plastic deformation and wear, but with smaller differences in terms of wear resistance between the different microstructures. In the case of low austenitization temperatures the yield strength of the investigated steels can easily be exceeded. However, high austenitization temperatures resulting in a low wear resistance, also give a larger grain size and increased brittleness of the material, thus having a very detrimental effect on the wear. On the other hand, as the contact conditions become harsher (i.e., increased sliding speed) the effect of the material toughness on the wear resistance diminishes. This indicates that microstructures providing a good combination of a smaller grain size, high yield strength and sufficient toughness are beneficial.

7.3 Correlation of Fracture Toughness, Microstructure and Tribological Behaviour

The highest fracture toughness for all the hardness levels and materials investigated was shown by hot-work tool steel A (Mat. No. 1.2367 mod.), with the smallest fraction of carbides and no large eutectic carbides. Large eutectic carbides are known to have a detrimental effect on the material toughness and ductility [100]. Steel A had an about two-times better fracture toughness compared to the other cold-work tool-steel types. On the other hand, the differences between the cold-work tool steels were much smaller. Nevertheless, among the cold-work tool steels investigated, materials C (Mat. No. 1.2990). and D (Mat. No. 1.2379) show higher fracture toughnesses than steel B (Mat. No. 1.2363), although having a much higher fraction of large eutectic carbides. Material B (Mat. No. 1.2363) greatly contradicts the literature, which due to the lowest fraction of eutectic carbides should show better fracture resistance. It should be pointed out that in our work we were focused on obtaining specimens with similar hardness levels and therefore different tool steels were heat treated according to the steel producer's recommendations using different heat-treatment parameters (austenitizing and tempering temperatures) for each steel. Furthermore, hardness groups selected in this investigation are lower than typical cold-work tool-steel working hardness, thus having a direct influence on the secondary hardening and the degree of it. On the other hand, microhardness measurements showed a higher matrix hardness for material B (Mat. No. 1.2363) compared to material D (Mat. No. 1.2379), thus exhibiting a more brittle matrix structure. In line with that, work by J. R. Davis et al. [119] also indicates that the fracture toughness of steel D (Mat. No. 1.2379) can be up to two times higher than for material B (Mat. No. 1.2363).

In terms of tribological behaviour, the AFM measurements performed on the martensitic matrix and larger eutectic carbides clearly demonstrate that friction for the carbides is lower compared to tempered martensite matrix. The measurement is not fully representative for large scale steel-steel contact; however, it shows the difference in friction behaviour of different phases in the microstructure. Therefore, the high fraction and density of large eutectic carbides on the contact surface has an influence on the running-in behaviour of the tool steels, especially at higher sliding speeds. However, prolonged sliding of the harder ceramic counter-body over the steel surface quickly results in the abrasion of the softer metallic matrix and fracturing and breaking of the brittle carbide phases, creating wear debris which further influence the contact behaviour and the wear mechanisms. This is displayed as a quick increase in the coefficient of friction, switching from low values of about 0.2 to high steady-state values above 0.5 in a very short running-in period. Different microstructures also show very similar steady-state COF behaviours, with the materials with more carbides not necessarily showing lower or higher COFs. Therefore, lower friction provided by the larger carbides embedded in the steel matrix does not have a significant effect on the steady-state COF. It is mainly affected by the type of counter-material and contact conditions, i.e., sliding speed and loads used. Softer counter-bodies and low-load/high-sliding-speed conditions in general resulted in lower friction, while a drop in tool steel's bulk hardness gave a larger deviation.

Comparing the reciprocating abrasive-wear-test results for different microstructures at different hardness levels provided some interesting new insights. In the case of high material hardness (group 1; 55 HRC) the lowest wear resistance for low-sliding-speed conditions was displayed by hot-work tool steel A (1-A) and cold-work tool steel D (1-D), with very different microstructures, while the best was exhibited by cold-work tool steel C (1-C). Also, for high-speed conditions the best wear resistance was shown by material C, while with others the wear resistance was lower by more than 20 %. Among the investigated tool

steels, material A has the lowest amount of carbides and the highest fracture toughness, material D the highest fraction of carbides, including large eutectic carbides and an about-two-times-lower fracture toughness than material A, and material B the lowest fracture toughness, although having the lowest fraction of large eutectic carbides among the investigated cold-work tool steels. These results indicate that the better fracture toughness or the high fraction of large carbides do not necessarily contribute to a better wear resistance. However, comparing materials C, D and A, a significant difference in the carbide fractions and type can be observed. Material C contains large eutectic (M_7C_3) as well smaller secondary Cr-rich ($M_{23}C_6$) and V-rich (MC) carbides. Material D, on the other hand, contains no MC carbides, but an increased amount of large eutectic carbides, material B no MC carbides and very low fracture toughness, while material A has only fine V-rich MC carbides, although in smaller amounts and sizes than material C. The presence of fine V-rich MC carbides combined with a certain amount of coarse Cr-rich carbides turns out to be very effective in providing the improved wear resistance of tool steels at a high hardness level. However, as the contact conditions becomes milder (low load & low sliding speed) the matrix hardness and the carbide-distribution uniformity start to play a decisive role, with the cold-work tool steel B (1-B) showing the best results.

With a bulk hardness drop to 50 HRC (group 2), the worst wear resistance was shown by material D (2-D) and was followed by material C, both with high fraction of carbides, especially M_7C_3 carbides larger than 5 µm. The best abrasive wear resistance in this case was displayed by material A (2-A), with the lowest carbide fraction and an at least two-times better fracture toughness at a given hardness value. It is interesting to note that steel B again shows better wear resistance under milder contact conditions, which is in contrast to the trends of other tool steels under investigation. A lower density of massive eutectic carbides, but a more homogenous distribution of smaller ones, turns out to be beneficial under low-load, low-speed conditions. These results indicate that when the bulk hardness is too low (≤50 HRC) a high fraction of large eutectic carbides present in the tempered martensitic matrix, although not necessarily connected with a very low fracture toughness, will result in a reduced wear resistance. The carbides' hardness is very high, much higher than the matrix, as confirmed by the nano-indentation. However, at low bulk hardness levels the hardness of the matrix is too low to support and maintain large eutectic carbides in their position in the matrix. As a result, they are fractured and detached from the matrix, and together with abrasive wear particles, enrolled in a wear process. They act as third-body abrasive particles and provoke more severe abrasive wear of the matrix area. However, the lack of larger, wear-resistant carbides is also not the best solution, still providing a certain load-carrying capacity and scratching resistance, especially under low-sliding-speed conditions. Tests with in-situ wear debris removal confirmed the third-body abrasive action of the fractured and removed eutectic carbides, with the wear rates being reduced, especially for cold-work tool steels containing larger coarse carbides. However, the difference was still the highest in the case of cold-work tool steel B with the lowest fracture toughness, indicating the linked importance of the matrix hardness, the fraction of large carbides and the material's fracture toughness.

For the group of specimens having the lowest hardness (hardness group 3; 45 HRC), the lowest wear rates were obtained by cold-work tool steel B (3-B), regardless of the fact that it shows the lowest fracture toughness. In this case microstructures without or with a very small amount of large carbides and a uniform distribution of smaller ones in the tempered martensitic matrix (samples 3-A and 3-B) provide very good abrasive wear resistance, regardless of the contact conditions used.

For the running-in stage, very small spherically shaped carbides, which are too small to carry the load, are quickly fractured, smoothened and glazed away. The larger eutectic carbides, on the other hand, initially provide lower friction, load-carrying capability and scratching resistance. However, with further sliding, also large eutectic carbides start to fracture and are subjected to smoothening, while their absence can result in more pronounced ploughing damage to the metal matrix. Wear-track cross-section observations clearly show that for a reduced material hardness the large eutectic carbides are crushed, even before reaching the sliding surface. Under high loads, the metal matrix with reduced hardness will start to deform plastically, thus not providing sufficient support for coarse eutectic carbides. If those are pinned, a combination of normal and tangential loads will lead to carbide fracturing and gradual removal from its original position. In many cases large eutectic carbides already contain cracks, formed during steel production (i.e., hot forging or rolling). Such pre-existing cracks will accelerate their partial or complete exfoliation from the soft matrix and the formation of hard abrasive particles, which will accelerate the wear of the matrix. Smaller carbides, on the other hand, remain embedded in the metal matrix and more-or-less move together with the plastically deformed matrix region. In this case the tempered martensitic laths are mainly compressed and bend in the sliding direction, albeit with the deformation being extended deeper below the contact surface than for the microstructure containing large carbides. For low hardness groups the most pronounced abrasive wear was found for steels containing a high density of large, Cr-rich eutectic carbides. Similar results were observed in the study conducted by Garcia et al. on powder metallurgy (PM) and metal-injection-molding (MIM) steels [73]. The addition of large amounts of reinforcement VC carbides created large precipitates at the grain boundaries with a low adhesion level with respect to the matrix, thus being more susceptible to fracturing and creating third-body effects as well as resulting in higher wear rates.

The negative effect of large eutectic carbides on the abrasive wear resistance of tool steels in the lower hardness groups (mainly 50 HRC and 45 HRC) can also be related to low matrix-hardness levels, which in general are below the usual working hardness for cold-work tool steels. The typical working hardness for cold-work tool steels used in practice is in the range of 60 HRC [119]. However, this is much higher than the typical hardness for hot-work tool steels with less than 1 % of precipitates and not containing any large eutectic carbides. When hardened to typical working hardness levels (cold-work tool steel to 60 HRC and hot-work tool steel to 50 HRC) cold-work tool steels will show up to 4-times better abrasive wear resistance, provided by the eutectic carbides embedded in the strengthened metal matrix. This statement was verified with the tribological testing performed on two cold-work tool steels (material B and D) containing a considerably different amount of coarse eutectic carbides and both being hardened to a typical working hardness of 60 HRC. For all the testing conditions (load and sliding speed) the material with the higher fraction of large eutectic carbides (steel D; w-D) showed an up to 40 % better abrasive wear resistance. As can be seen, large Cr-eutectic carbides play an important role in providing abrasive wear resistance. However, if used in the matrix with insufficient hardness and exposed to an abrasive environment, at high loads they do more damage than good.

To further investigate the influence of the large eutectic carbides' orientation on the tool steel's wear performance, cold-work tool steel D hardened to a typical working hardness of 60 HRC and containing a large amount of M_7C_3 eutectic carbides was used. Furthermore, to minimize the plastic deformation of the matrix during sliding and focus purely on the abrasion, low-load conditions were applied. The results show that a microstructure with a more uniform distribution of large carbides, positioned in the transverse direction (T_1 direction; Figure 28a and c) provides the best abrasive wear

resistance. In this case large, elongated, eutectic carbides are more firmly anchored in the metal matrix, thus minimising their loading, cracking and pull-out (Figure 106a). Similar to cementite lamellas in hyper-eutectoid steels [25], they provide an improved load-carrying capability and act as rigid barriers to scratching and plastic deformation. On the other hand, when positioned in the longitudinal direction (Figure 28b and d) their cracking, fracturing and pull-out is intensified, especially if oriented perpendicular to the sliding direction (L direction; Figure 106c), thus resulting in a more than 20 % higher abrasive wear.

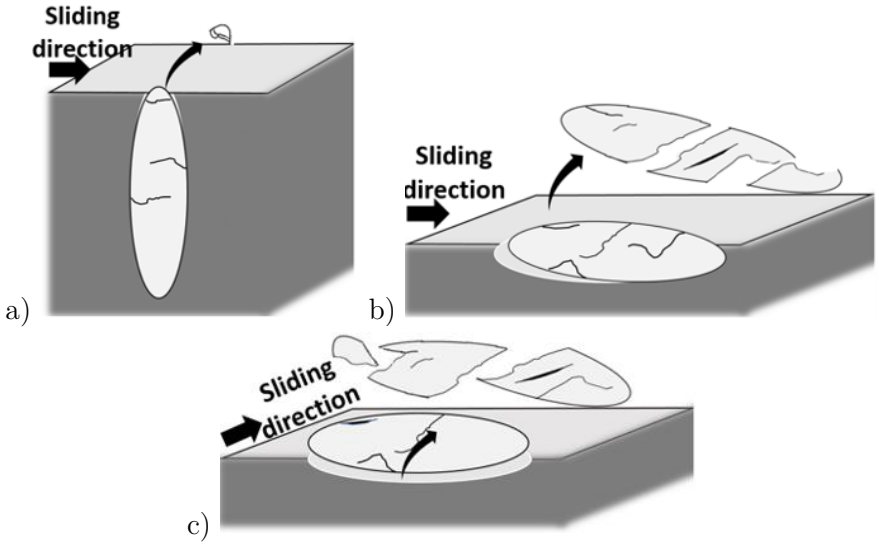

Figure 106: Schematic of elongated eutectic carbides removal during sliding; (a) transverse position (T_1), (b) longitudinal position parallel to sliding direction (L) and (c) longitudinal position perpendicular to sliding direction (T_2).

The influence of different microstructures on the adhesive wear component was simulated by using two steel balls as counter-material. A hardened 100Cr6 bearing steel ball with similar hardness as the investigated tool steels (58 HRC) to simulate the combination of adhesive-abrasive wear and much softer 304L austenitic stainless-steel ball (< 30 HRC) to simulate pure adhesive wear. In general, the initial metallic material adhesion to the tool steel surface will occur locally at the metallic matrix due to its higher affinity towards the matrix than the carbides present in the tool steel [88]. Therefore, the material with larger carbides and a higher carbide fraction should present lower adhesive wear component. However, other aspects also have to be taken into account.

The positive effect of the carbides content on the adhesive wear resistance has been confirmed, at least partially. For the soft 304L stainless-steel counter-ball and high-sliding-speed conditions, cold-work tool steel D with the largest carbides and their highest density displays the best adhesive wear resistance. Also, for the harder 100Cr6 bearing steel ball, the adhesive wear component seems to be reduced with the increased fraction of carbides, but increased with their size and matrix hardness drop. However, the differences are very small, with the abrasive component still being the dominant one. On the other hand, reciprocating sliding tests with a 304L stainless-steel ball performed under milder contact conditions (low sliding speed) show the opposite trend, with the adhesive wear rates being larger for higher carbide fractions, especially large eutectic ones. As mentioned previously, the initial adhesion and transfer of the steel counter-material to the tool-steel surface under severe contact conditions is localized at the matrix region [88]. However, the further formation and growth of the transfer layer is influenced by its flaking, work hardening,

detachment and re-attachment, as well as the wear particles' formation during prolonged sliding. Accumulation of the material in the contact, especially under reciprocating sliding, thus results in more turbulent and unpredictable behaviour as well as the appearance of an abrasive wear component. Milder contact conditions, on the other hand, provoke soft counter-material cutting rather than adhesion. Coarse eutectic carbides thus act as the cutting edges and traps for the wear debris and the transferred material's build-up, leading to high overall wear rates. This is in agreement with the study of Ko et al. [88], investigating the influence of cold-work tool-steel microstructures on the galling resistance. It was found that the size of the carbides has a greater influence on the galling resistance than their total amount. Materials with a large amount of small, spherical secondary carbides displayed the best galling resistance, much better than the ones with the large, coarse carbides.

7.4 Elevated-Temperature Wear Behaviour

In the case of high-speed and cold-work tool steels, a high concentration of large eutectic carbides provides good wear resistance at room and moderate temperatures. However, in the case of elevated temperatures, large eutectic carbides cause the formation of voids and cracks in the matrix due to its softening and large plastic deformations. This has a markedly negative effect on the wear, as indicated by high-load abrasion tests on the group 3 cold-work tool-steel specimens. Hot-work tool steels with a mainly martensitic microstructure, on the other hand, are designed to be resistant to softening at elevated temperatures. A higher degree of decomposition of martensite and fine carbides (<1 µm) precipitated during the secondary hardening, provide a reduced drop in strength at elevated temperatures with a gradual increase in the toughness. Therefore, only hot-work tool steel A (Mat. No. 1.2367 mod.) was investigated under elevated-temperature abrasive wear conditions and its wear response evaluated in terms of the temperature changes and the mechanical properties.

Recently, the work of Chengru Li et al. [123] shows that the wear mechanism changes from abrasion and fatigue to oxidative wear and plastic deformation as the temperature rises. In the current case, the room-temperature yield strength of the hot-work tool-steel specimens from all three hardness groups was always above the Hertzian contact pressure. And while higher tempering temperatures resulted in a reduced hardness and a drop in the UTS and YS, albeit with a slight increase in impact toughness (Figure 70), the wear rates and wear mechanism under room-temperature wear testing remained very similar (Figure 90). At an increased testing temperature (250 °C) a drop in the tensile properties was observed for the specimens from all the hardness groups (Figure 70b), although still maintaining a yield strength above the Hertzian contact pressure. However, specimens from the softest hardness group (3-A) possess a much higher impact toughness (almost 35 % higher) than the higher hardness group specimens. In accordance with the drop in the tensile strength and the properties, the wear rate at 250 °C increased significantly, but became impact toughness dependent, with the toughest sample showing the lowest wear (Figure 90a). With a further increase in the wear testing temperature to 500 °C, the wear rate for all three hardness groups dropped significantly (about one order of magnitude), again being the lowest for the material with the highest toughness (3-A). In this case the contact pressure was above the YS for group-2 and group-3 specimens and very close to the YS for group 1. Certainly, such a wear response cannot be attributed solely to the change in the mechanical properties.

At RT the best abrasive wear resistance is not shown by the hardest specimen (1-A), but the one having the best combination of hardness, high YS and good toughness (2-A). At moderate temperatures (i.e., 250 °C) and contact stresses still being below the material's

YS, wear rates will increase due to the drop in the material's strength and the formation of oxides, but the material toughness properties become the most dominant. On the other hand, the formation of oxides may lead to a reduced friction. However, at high temperatures (i.e., 500 °C) the wear response of metals is mainly connected to oxidation and other process that alter the chemistry of the tribo-contact [124]. At elevated temperatures metallic materials react with oxygen, which may result in oxidative wear [125] and a "glazed" layer formation [126]. Barrau et al. [21] demonstrated that the oxide layers play a role as a solid lubricant, reducing COF as a combined effect of a lower shear strength and reduced mechanical properties at elevated temperatures. This was also true for our wear tests performed at 500 °C, where the wear was mainly governed by the formation of a glazed oxide layer (Figure 104, Figure 105e and f), resulting in a decreased COF and significantly lower wear rates. Furthermore, better results were displayed by specimens having a lower strength and a YS below the contact stresses, but higher toughness, in line with the results of Barrau et al. [21].

7.5 Critical judgment and future work

The central point of this doctoral dissertation was determining the role of microstructure on wear mechanisms and wear resistance of tool steels. Due to a very broad range of tool steels, research work was focused solely on conventional chromium type tool-steels with microstructure of tempered martensite matrix, hardened to a similar hardness levels by selecting different heat treatments. It is known that for good wear resistance it is important to obtain proper microstructure with adequate matrix properties. Matrix microstructures that provide good combination of a small grain size, high yield strength and sufficient toughness are the most beneficial. However, in the presence of hard particles (carbides) matrix should first provide proper support for those particles, holding them firmly in the place. If matrix does not provide sufficient support, hard particles lose their wear resistance function, or even become detrimental by provoking and amplifying abrasive wear mechanism. As observed, certain correlations exist between maximum size and fraction of large carbides, and the hardness of the supporting matrix. Therefore, the heat treatment has to be primary planned to meet the requirements of the matrix. This is especially important in the case of tool steels with high fraction of large carbides subjected to repetitive abrasive loading. It is incorrect to assume that regardless of the matrix hardness level tool steels with high fraction of large eutectic carbides (i.e. Mat. No. 1.2379) will provide great abrasive wear resistance simply due to high content of hard wear resistant particles. Large carbides are extremely important wear protective constituent in the steel microstructure, but only when supported by proper matrix. At higher hardness levels high fraction of hard particles being larger than 5 microns and not necessarily of uniform spherical shape, provides the best abrasive wear resistance. On the other hand, for softer matrixes, smaller and more uniformly shaped (spherical) hard particles are more beneficial in resisting abrasive wear. However, there are also other factors influencing the final wear behavior like load level and type, speed, temperature and type of contact, which have to be taken into account.

This doctoral dissertation provides some new insights into the effect of microstructure and its constituents on the wear mechanisms and resistance of tool steels. However, understanding is still far from being complete. The future work should be expanded and proceeded in the direction of heat treatment regimes, mainly hardening phase, as well as tool steel selection. By changing austenitizing temperature and holding time the matrix grain size can be altered thus affecting matrix support and carbides interactions effect. On

the other hand, other tool steels should also be considered and investigated. Lately a lot of effort has been done in the field of advanced tool steel production, including powder metallurgy (P/M) and metal injection molding (MIM), which provide tool steels and tools with very fine and uniform microstructure and thus significantly improved performance. The conventional methods often result in coarse, non-uniform microstructure and problems with hardness uniformity after heat treatment process [6]. Last but not least, mechanical properties evolution through the whole hardness level range should be investigated and tool steel wear properties correlated to the set of material properties (hardness, tensile and yield strength, fracture and impact toughness) rather than a single one. It is clear that hardness alone is not the key parameter that determines tool wear.

Chapter 8

Conclusion

This study proposed several hypotheses regarding tool-steel wear behaviour and the material's response when subjected to wear. The investigation was focused on tool steels with different compositions, providing different microstructures especially in terms of carbides fraction, size and type. New insights were gained and a step forward was made in understanding the influence of microstructure and its constituents on the wear in terms of correlating the microstructure, mechanical properties and tribological behaviour. Experimental work consisted of some existing as well novel approaches in order to confirm or disprove the hypotheses. Based on the results, the following conclusions can be drawn:

- The microstructure of tool steels in general consists of tempered martensite with abrasion-resistant carbides of the M_7C_3, $M_{23}C_6$, and MC types, with their volume fraction and size varying, depending on the tool steel's composition and type. Thermodynamic calculations using Thermocalc software predicted the presence of those carbides for all the investigated tool steels. However, not all the carbides were found in every steel. The highest fraction of Cr-rich carbides and the density of the large M_7C_3 eutectic carbides (> 5 µm) had material Mat. No. 1.2379 with the highest Cr content, followed by material Mat. No. 1.2990 and Mat. No. 1.2363. Due to the high V content, small V-rich MC-type carbides were also found in material Mat. No. 1.2990, besides M_7C_3 and $M_{23}C_6$ Cr-rich carbides. However, the lowest fraction of carbides, being mainly small V-rich MC-type carbides (< 1 µm), were found in hot-work tool steel Mat. No. 1.2367 mod., also showing reduced tetragonality of the martensite.

- The wear test results indicated that hardness, better fracture toughness and a high fraction of large eutectic carbides do not necessarily contribute to a better abrasive wear resistance. This is mainly true when the hardness of tool steel is below its working hardness level. Better wear resistance is achieved when using a microstructure with the preferred type and volume fraction of carbides, as compared to the material with the same hardness, but different volume fraction of carbides, being more or less independent of the level of the fracture toughness. However, wear behaviour is still dominated by the wear conditions and bulk hardness of the material. At high hardness levels an increased fraction of large M_7C_3 eutectic carbides, albeit resulting in a low fracture toughness, greatly improves the abrasive wear resistance. Furthermore, a more uniform distribution of large carbides oriented in the transverse direction, provides the best results. On the other hand, as the bulk hardness drops below 54 HRC a high fraction of large eutectic carbides within the tempered martensitic matrix, although not necessarily

connected with very low fracture toughness, will result in a reduced wear resistance. In this case, a homogeneous distribution of small secondary carbides ($M_{23}C_6$ and/or MC type) combined with a low density of large eutectic ones (< 1 %) provides the best abrasive wear properties. At a low bulk hardness, coarse eutectic carbides are removed from the matrix and start acting as third-body abrasive wear particles, provoking more severe abrasive wear of the matrix, even at high fracture toughness levels. All that confirms the mutual effect of the matrix hardness, the fraction of large carbides and the material's fracture toughness. To obtain a good abrasive wear resistance, a high matrix hardness combined with a homogeneous distribution of some large, but predominantly small, secondary carbides is required, with an increased fracture toughness having a positive, although not decisive, effect.

- The positive effect of carbides and their content on the adhesive wear resistance has been confirmed, but only partially. For high-sliding-speed conditions, the adhesive wear component is reduced with an increased fraction of carbides. However, under milder contact conditions the trend of increasing adhesive wear was observed for higher carbides fractions, especially for large eutectic ones. Coarse eutectic carbides act as the cutting edges of softer counter-body and traps for wear debris and transferred material build-up, leading to high wear rates. Accumulation of the material in the contact region, especially under reciprocating sliding conditions, results in more turbulent and unpredictable tribological behaviour.

- Inappropriate heat treatment, mainly the austenitization temperature, results in a tool-steel microstructure with large grains or an increased number of undissolved carbides and consequently in deteriorated mechanical properties as well as reduced wear resistance. This is true for different hardness levels. However, wear resistance is not only grain-size and carbide-fraction dependent. It is also indirectly influenced by the mechanical properties (i.e., ductility, toughness and yield strength). The most beneficial tool-steel microstructure in terms of wear resistance is one that provides a good combination of small grain size, high yield strength and enhanced toughness.

- Under room-temperature, high-load abrasive wear conditions, the tempered martensitic microstructure of hot-work tool steel with a low fraction and mainly very small carbides, being smaller than 1 μm, shows a similar wear resistance for the different hardness levels. However, the hardest specimens do not provide the best wear resistance. The best results are provided by the hot-work tool steel at intermediate hardness (49 HRC) with the optimal combination of hardness, toughness and tensile properties. At elevated temperatures the material is exposed to thermal loading, which results in a significant decrease in the tensile and yield strengths, although providing an improvement in the impact toughness. However, wear at elevated temperatures is mainly governed by the softening of the tempered martensite matrix and a drop in the tensile properties. But in this case, also a lower initial hardness level of the matrix is beneficial, leading to the faster creation of oxidized wear debris and the formation of a protective oxide glazed layer on the contact surface. Patches of oxide glazed layer start to appear at 250 °C, which are then compacted in a protective layer at 500 °C, the most effectively for the softest material, also displaying the lowest wear rate at high temperatures.

References

[1] G. A. Roberts, R. Kennedy, and G. Krauss, *Tool steels*. Materials Park: ASM international, 1998.

[2] M. X. Wei, S. Q. Wang, L. Wang, X. H. Cui, and K. M. Chen, "Effect of tempering conditions on wear resistance in various wear mechanisms of H13 steel," *Tribol. Int.*, vol. 44, no. 7–8, pp. 898–905, 2011, doi: 10.1016/j.triboint.2011.03.005.

[3] A. S. Philip and A. Schweitzer, "Metallic Materials: Physical, Mechanical, and Corrosion Properties," *NY, Pensylvania, USA.2003.702 p*, 2003.

[4] A. S. M. Handbook, "Vol. 3: Alloy Phase Diagrams," *ASM Int.*, vol. 9, p. 2, 1992.

[5] A. S. M. Handbook, "Properties and selection: irons, steels, and high performance alloys," *ASM Int.*, vol. 1, pp. 140–194, 1990.

[6] G. E. Totten, *Steel heat treatment: metallurgy and technologies*. crc Press, 2006.

[7] C. Højerslev, *Tool steels*. Riso National Laboratory, Denmark, 2001.

[8] A. Medvedeva, J. Bergström, S. Gunnarsson, and J. Andersson, "High-temperature properties and microstructural stability of hot-work tool steels," *Mater. Sci. Eng. A*, vol. 523, no. 1, pp. 39–46, 2009.

[9] H. Bhadeshia and R. Honeycombe, *Steels: microstructure and properties*. Butterworth-Heinemann, 2011.

[10] K.-E. Thelning, *Steel and its heat treatment*. Butterworth-Heinemann, 2013.

[11] V. Marinković, "Fizikalna metalurgija II," *skripta, NTF, Ljubljana*, 1999.

[12] H. Brandis, E. Haberling, and H. H. Weigard, "Processing and Properties of High Speed Tool Steels," in *TMS_AIME*, 1980, pp. 1–18.

[13] D. Casellas, J. Caro, S. Molas, J. M. Prado, and I. Valls, "Fracture toughness of carbides in tool steels evaluated by nanoindentation," *Acta Mater.*, vol. 55, no. 13, pp. 4277–4286, 2007.

[14] R. A. Mesquita, *Tool Steels: Properties and Performance*. CRC press, 2016.

[15] H. F. Fischmeister, R. Riedl, and S. Karagöz, "Solidification of high-speed tool steels," *Metall. Trans. A*, vol. 20, no. 10, pp. 2133–2148, 1989.

[16] S. Karagöz and H. F. Fischmeister, "Cutting performance and microstructure of high speed steels: Contributions of matrix strengthening and undissolved carbides," *Metall. Mater. Trans. A*, vol. 29, no. 1, pp. 205–216, 1998.

[17] E. Pippel, J. Woltersdorf, G. Pöckl, and G. Lichtenegger, "Microstructure and nanochemistry of carbide precipitates in high-speed steel S 6-5-2-5," *Mater. Charact.*, vol. 43, no. 1, pp. 41–55, 1999.

[18] H. Torres, M. Varga, and M. R. Ripoll, "High temperature hardness of steels and iron-based alloys," *Mater. Sci. Eng. A*, vol. 671, pp. 170–181, 2016, doi: 10.1016/j.msea.2016.06.058.

[19] D. Delagnes, P. Lamesle, M. H. Mathon, N. Mebarki, and C. Levaillant, "Influence of silicon content on the precipitation of secondary carbides and fatigue properties of a 5% Cr tempered martensitic steel," *Mater. Sci. Eng. A*, vol. 394, no. 1, pp. 435–

444, 2005.

[20] S. Walter, H. Haferkamp, M. Niemeyer, F.-W. Bach, and A. Henze, "Material failure mechanisms of forging dies," Fifth International Conference on Tooling, F. Jeglitsch, ed., R. Ebner ed., H. Leitner ed., University of Leoben, Leoben, Austira, pp. 215–222, 1999.

[21] O. Barrau, C. Boher, R. Gras, and F. Rezai-Aria, "Analysis of the friction and wear behaviour of hot work tool steel for forging," *Wear*, vol. 255, no. 7, pp. 1444–1454, 2003.

[22] B. Miquel, S. Jean, S. Le Roux, P. Lamesle, and F. Rézai-Aria, "Heat-checking of hot work tool steels," *Eur. Struct. Integr. Soc.*, vol. 29, pp. 185–193, 2002.

[23] D. Delagnes, F. Rezai-Aria, C. Levaillant, and A. Grellier, "Influence of temperature and initial hardness on fatigue behaviour and life of a 5% Cr hot work tool steel," in *Proceedings of the Fifth International Conference on Tooling*, F. Jeglitsch, ed., R. Ebner ed., H. Leitner ed. University of Leoben, Leoben, Austira, pp. 195–204, 1999.

[24] F. T. Barwell, "Tribology in Metalworking, Developments in Perspective." Inst. of Mech. Engineers, Conference Publications, p. 51, 1980.

[25] and A. W. B. Stachowiak, Gwidon, *Engineering tribology*. Butterworth-Heinemann, 2013.

[26] A. Bahrami, S. H. M. Anijdan, M. A. Golozar, M. Shamanian, and N. Varahram, "Effects of conventional heat treatment on wear resistance of AISI H13 tool steel," *Wear*, vol. 258, no. 5–6, pp. 846–851, 2005, doi: 10.1016/j.wear.2004.09.008.

[27] B. Bhushan, *Modern tribology handbook, two volume set*. CRC press, 2000.

[28] P. Kivikytö-Reponen, "Correlation of material characteristics and wear of powder metallurgical metal matrix composites," Helsinki University of Technology, 2006.

[29] H. Torres, M. Varga, K. Adam, and M. R. Ripoll, "The role of load on wear mechanisms in high temperature sliding contacts," *Wear*, vol. 364, pp. 73–83, 2016.

[30] C. Vergne, C. Boher, R. Gras, and C. Levaillant, "Influence of oxides on friction in hot rolling: experimental investigations and tribological modelling," *Wear*, vol. 260, no. 9, pp. 957–975, 2006.

[31] M. Varga, H. Rojacz, H. Winkelmann, H. Mayer, and E. Badisch, "Wear reducing effects and temperature dependence of tribolayer formation in harsh environment," *Tribol. Int.*, vol. 65, pp. 190–199, 2013.

[32] R. Stock and R. Pippan, "RCF and wear in theory and practice—the influence of rail grade on wear and RCF," *Wear*, vol. 271, no. 1, pp. 125–133, 2011.

[33] C. Kammerhofer, A. Hohenwarter, and R. Pippan, "A novel laboratory test rig for probing the sensitivity of rail steels to RCF and wear--first experimental results," *Wear*, vol. 316, no. 1, pp. 101–108, 2014.

[34] M. Varga, H. Winkelmann, and E. Badisch, "Impact of microstructure on high temperature wear resistance," *Procedia Eng.*, vol. 10, pp. 1291–1296, 2011.

[35] C. M. Mate, *Tribology on the small scale: a bottom up approach to friction, lubrication, and wear*. Oxford University Press, 2008.

[36] A. Anderson, "ASM Metals Handbook Volume 18: Friction, Lubrication and Wear."

ASM International, USA, 1995.

[37] J. Perret, E. Boehm-Courjault, M. Cantoni, S.Mischler, A. Beaudouin, W. Chitty and J.P. Vernot, "EBSD, SEM and FIB characterisation of subsurface deformation during tribocorrosion of stainless steel in sulphuric acid," *Wear*, vol. 269, no. 5–6, pp. 383–393, 2010.

[38] X. Meng-Burany, T. A. Perry, A. K. Sachdev, and A. T. Alpas, "Subsurface sliding wear damage characterization in Al--Si alloys using focused ion beam and cross-sectional TEM techniques," *Wear*, vol. 270, no. 3–4, pp. 152–162, 2011.

[39] X. Y. Li and K. N. Tandon, "Mechanical mixing induced by sliding wear of an Al-Si alloy against M2 steel," *Wear*, vol. 225, pp. 640–648, 1999.

[40] R. Pan, R. Ren, C. Chen, and X. Zhao, "Formation of nanocrystalline structure in pearlitic steels by dry sliding wear," *Mater. Charact.*, vol. 132, pp. 397–404, 2017.

[41] W. Cai, J. Mabon, and P. Bellon, "Crystallographic textures and texture transitions induced by sliding wear in bronze and nickel," *Wear*, vol. 267, no. 1–4, pp. 485–494, 2009.

[42] S. Tekeli and A. Güral, "Dry sliding wear behaviour of heat treated iron based powder metallurgy steels with 0.3% Graphite+ 2% Ni additions," *Mater. Des.*, vol. 28, no. 6, pp. 1923–1927, 2007.

[43] S. G. Sapate, A. D. Chopde, P. M. Nimbalkar, and D. K. Chandrakar, "Effect of microstructure on slurry abrasion response of En-31 steel," *Mater. Des.*, vol. 29, no. 3, pp. 613–621, 2008.

[44] K. Singh, R. K. Khatirkar, and S. G. Sapate, "Microstructure evolution and abrasive wear behavior of D2 steel," *Wear*, vol. 328, pp. 206–216, 2015.

[45] V. Leskovšek, B. Šuštaršič, and G. Jutriša, "The influence of austenitizing and tempering temperature on the hardness and fracture toughness of hot-worked H11 tool steel," *J. Mater. Process. Technol.*, vol. 178, no. 1, pp. 328–334, 2006.

[46] I. M. Hutchings and P. Shipway, *Tribology: friction and wear of engineering materials*. Oxford: Butterworth-Heinemann, 2017.

[47] C. Mueller and I. Schruff, "Steel selection contributing to wear reduction of forging dies." Forgetech India, New Delhi, pp. 124–130, 2016.

[48] E. Zdravecká, J. Tkáčová, M. Ondáč, and others, "Effect of microstructure factors on abrasion resistance of high-strength steels," *Res. Agric. Eng.*, vol. 60, no. 3, pp. 115–120, 2014.

[49] A. Kasak and T. A. Neumeyer, "Observations on wear of high-hardness steels," *Wear*, vol. 14, no. 6, pp. 445–454, 1969.

[50] G. Telasang, J. D. Majumdar, G. Padmanabham, and I. Manna, "Wear and corrosion behavior of laser surface engineered AISI H13 hot working tool steel," *Surf. Coatings Technol.*, vol. 261, pp. 69–78, 2015.

[51] X. H. Cui, S. Q. Wang, M. X. Wei, and Z. R. Yang, "Wear characteristics and mechanisms of H13 steel with various tempered structures," *J. Mater. Eng. Perform.*, vol. 20, no. 6, pp. 1055–1062, 2011.

[52] S. Hernandez, J. Hardell, H. Winkelmann, M. R. Ripoll, and B. Prakash, "Influence of temperature on abrasive wear of boron steel and hot forming tool steels," *Wear*, vol. 338, pp. 27–35, 2015.

[53] V. Abouei, H. Saghafian, and S. Kheirandish, “Dry sliding oxidative wear in plain carbon dual phase steel,” *J. Iron Steel Res. Int.*, vol. 14, no. 4, pp. 43–48, 2007.

[54] A. Persson, “On tool failure in die casting,” PhD Thesis. Acta Universitatis Upsaliensis, 2003.

[55] B. Podgornik and V. Leskovšek, “Wear mechanisms and surface engineering of forming tools,” *Mater. Tehnol.*, vol. 49, no. 3, pp. 313–324, 2015.

[56] J. Guo, L. Ai, T. Wang, Y. Feng, D. Wan, and Q. Yang, “Microstructure evolution and micro-mechanical behavior of secondary carbides at grain boundary in a Fe-Cr-W-Mo-V-C alloy,” *Mater. Sci. Eng. A*, 2018.

[57] J. Heinrichs, M. Olsson, and S. Jacobson, “Mechanisms of material transfer studied in situ in the SEM:: Explanations to the success of DLC coated tools in aluminium forming,” *Wear*, vol. 292, pp. 49–60, 2012.

[58] H. Berns, “Microstructural properties of wear-resistant alloys,” *Wear*, vol. 181, pp. 271–279, 1995.

[59] K. Mori, P. F. Bariani, B. A. Behrens, A. Brosius, S. Bruschi, T. Maeno, M. Merklein and J. Yanagimoto, “Hot stamping of ultra-high strength steel parts,” *CIRP Ann.*, vol. 66, no. 2, pp. 755–777, 2017.

[60] P. Schwingenschlögl, P. Niederhofer, and M. Merklein, “Investigation on basic friction and wear mechanisms within hot stamping considering the influence of tool steel and hardness,” *Wear*, vol. 426, pp. 378–389, 2019.

[61] E. Meurisse, C. Ernst, and W. Bleck, “Improvement of thermal conductivity of hot-work tool steels by alloy design and heat treatment,” in TOOL 2012: Proceedings of the 9th International Tooling Conference, H. Leitner, ed., R. Kranz, ed., A. Tremmel, ed., Knittelfeld : Verlag "Gutenberghaus", Leoben, Austira, 2012, pp. 215–224.

[62] F. H. Stott and M. P. Jordan, “The effects of load and substrate hardness on the development and maintenance of wear-protective layers during sliding at elevated temperatures,” *Wear*, vol. 250, no. 1, pp. 391–400, 2001.

[63] S. C. Lim, “The relevance of wear-mechanism maps to mild-oxidational wear,” *Tribol. Int.*, vol. 35, no. 11, pp. 717–723, 2002.

[64] F. H. Stott, “The role of oxidation in the wear of alloys,” *Tribol. Int.*, vol. 31, no. 1, pp. 61–71, 1998.

[65] A. Gåård, N. Hallbäck, P. Krakhmalev, and J. Bergström, “Temperature effects on adhesive wear in dry sliding contacts,” *Wear*, vol. 268, no. 7–8, pp. 968–975, 2010.

[66] P. Karlsson, A. Gåård, and P. Krakhmalev, “Influence of tool steel microstructure on friction and initial material transfer,” *Wear*, vol. 319, no. 1–2, pp. 12–18, 2014.

[67] P. C. Okonkwo, G. Kelly, B. F. Rolfe, and M. P. Pereira, “The effect of temperature on sliding wear of steel-tool steel pairs,” *Wear*, vol. 282, pp. 22–30, 2012.

[68] P. C. Okonkwo, G. Kelly, B. F. Rolfe, and M. P. Pereira, “The effect of sliding speed on the wear of steel--tool steel pairs,” *Tribol. Int.*, no. 97, pp. 218–227, 2016.

[69] L. Kirkhorn, V. Bushlya, M. Andersson, and J.-E. Ståhl, “The influence of tool steel microstructure on friction in sheet metal forming,” *Wear*, vol. 302, no. 1–2, pp. 1268–1278, 2013.

[70] E. Badisch and C. Mitterer, "Abrasive wear of high speed steels: influence of abrasive particles and primary carbides on wear resistance," *Tribol. Int.*, vol. 36, no. 10, pp. 765–770, 2003.

[71] F. Bergman, P. Hedenqvist, and S. Hogmark, "The influence of primary carbides and test parameters on abrasive and erosive wear of selected PM high speed steels," *Tribol. Int.*, vol. 30, no. 3, pp. 183–191, 1997.

[72] G. A. Fontalvo, R. Humer, C. Mitterer, K. Sammt, and I. Schemmel, "Microstructural aspects determining the adhesive wear of tool steels," *Wear*, vol. 260, no. 9–10, pp. 1028–1034, 2006.

[73] C. Garcia, F. Martin, G. Herranz, C. Berges, and A. Romero, "Effect of adding carbides on dry sliding wear behaviour of steel matrix composites processed by metal injection moulding," *Wear*, vol. 414, pp. 182–193, 2018.

[74] C. Yin, Y. Liang, Y. Jiang, M. Yang, and S. Long, "Formation of nano-laminated structures in a dry sliding wear-induced layer under different wear mechanisms of 20CrNi2Mo steel," *Appl. Surf. Sci.*, vol. 423, pp. 305–313, 2017.

[75] R. C. Bill and D. Wisander, "Recrystallization as a controlling process in the wear of some fcc metals," *Wear*, vol. 41, no. 2, pp. 351–363, 1977.

[76] H. Kato, M. Sasase, and N. Suiya, "Friction-induced ultra-fine and nanocrystalline structures on metal surfaces in dry sliding," *Tribol. Int.*, vol. 43, no. 5–6, pp. 925–928, 2010.

[77] X. Chen, Z. Han, X. Li, and K. Lu, "Lowering coefficient of friction in Cu alloys with stable gradient nanostructures," *Sci. Adv.*, vol. 2, no. 12, p. e1601942, 2016.

[78] O. A. Zambrano, J. A. Gómez, J. J. Coronado, and S. A. Rodriguez, "The sliding wear behaviour of steels with the same hardness," *Wear*, vol. 418, pp. 201–207, 2019.

[79] F. A. M. Alwahdi, A. Kapoor, and F. J. Franklin, "Subsurface microstructural analysis and mechanical properties of pearlitic rail steels in service," *Wear*, vol. 302, no. 1–2, pp. 1453–1460, 2013.

[80] W. Cai and P. Bellon, "Effect of annealing treatment on the dry sliding wear behavior of copper," *Wear*, vol. 426, pp. 1187–1194, 2019.

[81] H. A. N. Zhong, Y. Zhang, and L. U. Ke, "Friction and wear behaviors of nanostructured metals," *J. Mater. Sci. Technol.*, vol. 24, no. 04, pp. 483–494, 2009.

[82] W. E. Bryson, *Heat treatment, selection, and application of tool steels*. München: Carl Hanser Verlag, 2005.

[83] D. Viale, J. Béguinot, F. Chenou, and G. Baron, "Optimizing microstructure for high toughness cold-work tool steels," in *6th International Tooling Conference*, J. Bergström, ed. Karlstad : Univ. , Karlstad, Sweden, 2002, pp. 299–318.

[84] "TA instruments: The broadest line of Horizontal, Vertical and Optical Dilatometers."[Online]. Available: https://www.tainstruments.com/products/dilatometers/.

[85] G. E. Totten and M. A. H. Howes, *Steel heat treatment handbook*. CRC Press, 1997.

[86] "Thermo-Calc Software: Thermo-Calc." [Online]. Available: http://www.thermocalc.com/products-services/software/thermo-calc/.

[87] J. Blaha, C. Krempaszky, E. Werner, and W. Liebfahrt, "Carbide distribution effect in cold work tool steels," in *6th International Tooling Conference*, J. Bergström, ed.,

Karlstad : Univ., Karlstad, Sweden, 2002, pp. 289–298

[88] D.-C. Ko, S.-G. Kim, and B.-M. Kim, "Influence of microstructure on galling resistance of cold-work tool steels with different chemical compositions when sliding against ultra-high-strength steel sheets under dry condition," *Wear*, vol. 338, pp. 362–371, 2015.

[89] D. Das, A. K. Dutta, and K. K. Ray, "Influence of varied cryotreatment on the wear behavior of AISI D2 steel," *Wear*, vol. 266, no. 1–2, pp. 297–309, 2009.

[90] T. Maitland and S. Sitzman, *Electron backscatter diffraction (EBSD) technique and materials characterization examples*, vol. 14. Springer Berlin, 2007.

[91] R. Álvarez-Asencio, J. Pan, E. Thormann, and M. W. Rutland, "Tribological properties mapping: local variation in friction coefficient and adhesion," *Tribol. Lett.*, vol. 50, no. 3, pp. 387–395, 2013.

[92] "nanoScience Instruments: Atomic Force Microscopy." [Online]. Available: https://www.nanoscience.com/techniques/atomic-force-microscopy/.

[93] D. F. Arias, D. M. Marulanda, A. M. Baena, and A. Devia, "Determination of friction coefficient on ZrN and TiN using lateral force microscopy (LFM)," *Wear*, vol. 261, no. 11–12, pp. 1232–1236, 2006.

[94] D. Martinez-Martinez, L. Kolodziejczyk, J. C. Sánchez-López, and A. Fernández, "Tribological carbon-based coatings: An AFM and LFM study," *Surf. Sci.*, vol. 603, no. 7, pp. 973–979, 2009.

[95] "Bruker Alicona." [Online]. Available: https://www.alicona.com/.

[96] "Metallic materials - Rockwell hardness test - Part 1: Test method," no. SIST EN 6508-1:2016, 2016.

[97] H. Kuhn and D. Medlin, "ASM Handbook. Volume 8: Mechanical Testing and Evaluation," *ASM Int. Member/Customer Serv. Center, Mater. Park. OH 44073-0002, USA, 2000. 998*, 2000.

[98] "Metallic materials - Vickers hardness test - Part 1: Test method," no. SIST EN ISO 6507-1:2018, 2018.

[99] "Metallic materials - Charpy pendulum impact test - Part 1: Test method," no. SIST EN ISO 148-1:2016, 2017.

[100] V. Leskovšek and B. Podgornik, "Tool steels: Fracture Toughness.," in *Encylopedia of Iron, Steel, and Their Alloys.*, R. Colás et al., Ed. Taylor and Francis: New York, 2016, pp. 3687–3719.

[101] B. Podgornik, B. Žužek, and V. Leskovšek, "Experimental evaluation of tool steel fracture toughness using circumferentially notched and precracked tension bar specimen," *Mater. Perform. Charact.*, vol. 3, no. 3, pp. 87–103, 2014.

[102] B. Podgornik, V. Leskovšek, F. Tehovnik, and J. Burja, "Vacuum heat treatment optimization for improved load carrying capacity and wear properties of surface engineered hot work tool steel," *Surf. Coatings Technol.*, vol. 261, pp. 253–261, 2015.

[103] V. Leskovšek, B. Ule, and B. Liščić, "Relations between fracture toughness, hardness and microstructure of vacuum heat-treated high-speed steel," *J. Mater. Process. Technol.*, vol. 127, no. 3, pp. 298–308, 2002.

[104] V. Leskovšek, "Modelling of high-speed steels fracture toughness," *Mater. Manuf.*

Process., vol. 24, no. 6, pp. 603–609, 2009.

[105] V. Leskovšek and B. Ule, "Improved vacuum heat-treatment for fine-blanking tools from high-speed steel M2," *J. Mater. Process. Technol.*, vol. 82, no. 1–3, pp. 89–94, 1998.

[106] V. Leskovšek, B. Ule, and B. Lišcic, "The influence of microstructure on the fracture toughness of AISI M2 high-speed steel," *Steel Res.*, vol. 71, no. 8, pp. 310–315, 2000.

[107] F. Jeglitsch, R. Ebne, and H. Leitner, Eds., "Testing of metallic materials - Tensile test pieces," 2009, no. DIN 50125: 2009-07.

[108] S. C. Lim and M. F. Ashby, "Overview no. 55 wear-mechanism maps," *Acta Metall.*, vol. 35, no. 1, pp. 1–24, 1987.

[109] J. Archard, "Contact and rubbing of flat surfaces," *J. Appl. Phys.*, vol. 24, no. 8, pp. 981–988, 1953.

[110] J. F. Archard, "The temperature of rubbing surfaces," *Wear*, vol. 2, no. 6, pp. 438–455, 1959.

[111] W. F. Smith, *Structure and properties of engineering alloys*. McGraw-Hill, 1993.

[112] J. Sjöström, "Chromium martensitic hot-work tool steels: damage, performance and microstructure," 2004.

[113] C. G. De Andres, M. J. Bartolomé, C. Capdevila, D. San Martin, F. G. Caballero, and V. López, "Metallographic techniques for the determination of the austenite grain size in medium-carbon microalloyed steels," *Mater. Charact.*, vol. 46, no. 5, pp. 389–398, 2001.

[114] G. F. Vander Voort *et al.*, "ASM handbook," *Metallogr. Microstruct.*, vol. 9, pp. 40002–44073, 2004.

[115] A. Arain, "Heat treatment and toughness behavior of tool steels (D2 and H13) for cutting blades," National Library of Canada= Bibliothèque nationale du Canada, 1999.

[116] R. A. Mesquita and H. J. Kestenbach, "M3C and M7C3 Carbide Precipitation in Modified H11 Tool Steel," *Solid State Phenom.*, vol. 172, pp. 414–419, 2011.

[117] N. Mebarki, D. Delagnes, P. Lamesle, F. Delmas, and C. Levaillant, "Relationship between microstructure and mechanical properties of a 5% Cr tempered martensitic tool steel," *Mater. Sci. Eng. A*, vol. 387, pp. 171–175, 2004.

[118] B. L. Averbach, "The Effect of Plastic Deformation on Solid Reactions," in *Cold Working of Metals*, American Society for Metals Cleveland, 1949, p. 262.

[119] J. R. Davis, *ASM specialty handbook: tool materials*. Materials Park: ASM international, 1995.

[120] N. Mebraki, P. Lamesle, D. Delanges, F. Delmas, and C. Levaillant, "Proceedings of the 6th International Tooling Conference, The Use of Tool Steels: Experience and Research," 2002, pp. 617–632.

[121] I. A. Inman, S. R. Rose, and P. K. Datta, "Studies of high temperature sliding wear of metallic dissimilar interfaces II: Incoloy MA956 versus Stellite 6," *Tribol. Int.*, vol. 39, no. 11, pp. 1361–1375, 2006.

[122] A. Pauschitz, M. Roy, and F. Franek, "Mechanisms of sliding wear of metals and alloys at elevated temperatures," *Tribol. Int.*, vol. 41, no. 7, pp. 584–602, 2008.

[123] C. Li, X. Deng, L. Huang, Y. Jia, and Z. Wang, "Effect of temperature on

microstructure, properties and sliding wear behavior of low alloy wear-resistant martensitic steel," *Wear*, vol. 442, p. 203125, 2020.

[124] P. J. Blau, "Elevated-temperature tribology of metallic materials," *Tribol. Int.*, vol. 43, no. 7, pp. 1203–1208, 2010.

[125] J. L. Sullivan, T. F. J. Quinn, and D. M. Rowson, "Developments in the oxidational theory of mild wear," *Tribol. Int.*, vol. 13, no. 4, pp. 153–158, 1980.

[126] J. E. Wilson, F. H. Stott, and G. C. Wood, "The development of wear-protective oxides and their influence on sliding friction," *Proc. R. Soc. London. A. Math. Phys. Sci.*, vol. 369, no. 1739, pp. 557–574, 1980.

Bibliography

Journal Articles

1.01 Original scientific article

B. Skela, M. Sedlaček, F. Kafexhiu, and B. Podgornik, “Influence of Microstructure and Mechanical Properties of Hot-work Tool Steel on Wear Resistance Subjected to High-stress Wear Conditions,” *Tribol. Lett.,* vol. 68, pp. 1–12, 2020.

B. Skela, M. Sedlaček, F. Kafexhiu, and B. Podgornik, “Wear behaviour and correlations to the microstructural characteristics of heat treated hot work tool steel,” *Wear*, vol. 426, pp. 1118–1128, 2019.

F. Burkhardt, B. Skela, N. Daneu, Z. Samardžija, S. Šturm, E. Gaudry, S. Kobe and J.M. Dubois, “A new complex ternary phase in the Al-Cr-Sc push-pull alloy,” *J. Alloys Compd.*, vol. 768, pp. 230–239, 2018.

I. Naglic, S. Ilić, B. Markoli, M. Dolenc, B. Leskovar, Ž. Filipič, M. Perhoč, J. Kraner, M.Bizjak, B. Skela, L. Kelhar, Š. Kozole, D. Gerčar and T. Ramšak, “Modifikacija zlitine AlSi7Mg lite v peščeno formo/Modification of AlSi7Mg alloy cast in to a sand mould,” *Livar. Vestn.*, vol. 63, no. 1, p. 37, 2016.

1.08 Published scientific conference contribution

B. Skela, M. Sedlaček, and B. Podgornik, “Microstructure and Heat Treatment of Hot Work Tool Steel: Influence on Mechanical Properties and Wear Behaviour,” in *Key Engineering Materials*, 2018, vol. 767, pp. 196–203.

Conference Papers

1.12 Published scientific conference contribution abstract

B. Skela, M. Sedlaček, F. Kafexhiu, and B. Podgornik, “Wear behaviour and correlations to the microstructural characteristics of heat treated hot work tool steel,” 22nd International Conference on Wear of Materials, part B, Miami, April 2019.

B. Skela, M. Sedlaček, F. Kafexhiu, and B. Podgornik, PODGORNIK, Bojan. “Correlations of microstructural characteristic of tool steels on mechanical properties and wear behaviour," Program and book of abstracts, 27th International Conference on Materials and Technology, Portorož, October 2019.

B. Skela, M. Sedlaček and B. Podgornik. “Influence of microstructure achieved by various heat-treatments on wear resistance of hot work tool steel,” Program and book of abstracts, 26th International Conference on Materials and Technology, Portorož, October 2018.

B. Skela, M. Sedlaček, J. Burja, and B. Podgornik, ”Influence of microstructure and heat-treatment on mechanical and wear properties of hot work tool steel,” Program and book of abstracts, 25th International Conference on Materials and Technology, Portorož, October 2017.

J. M. Dubois, L. Kelhar, B. Skela, F. Burkhardt, and S. Kobe, “Push-pull alloys: the nucleation of complexity in metallic alloys,” Program and book of abstracts, 25th International Conference on Materials and Technology, Portorož, October 2017.

B. Skela, J. Burja, M. Sedlaček, F. Tehovnik, and B. Podgornik, “Precipitation of harmful [σ]-phase in 1.4462 duplex stainless steel grade at high temperatures,” Proceedings, 9th Jožef Stefan International Postgraduate School Students' Conference and 11th Young researchers' Day, Ljubljana, April 2017.

Other Publications

2.12 Final research report

M. Sedlaček, B. Skela, “Evaluation of friction between polyamide Ixef FC-1022 BK01,” Ljubljana: IMT, 2019. 7 str., ilustr. [COBISS.SI-ID 1490602] financier: Naročnik: BSH Hišni aparati d.o.o., Nazarje

M. Sedlaček, B. Skela, D. Steiner Petrovič, “Wear resistance of different bearings materials in different working mediums,” Ljubljana: IMT, 2018. 19 str., ilustr. [COBISS.SI-ID 1387178] financier: Naročnik: Litostroj Power d.o.o., Ljubljana

2.13 Treatise, preliminary study, study

B. Podgornik, B. Skela, “Tribološko testiranje steklarskih zlitin,” Ljubljana: Inštitut za kovinske materiale in tehnologije (IMT), 2020. 4 str., ilustr. [COBISS.SI-ID 27258627] financer: Naročnik: OMCO METALS Slovenia d.o.o., Žalec

B. Podgornik, F. Kafexhiu, B. Skela, “Analiza debeline stene mehov iz nerjavnega jekla,” Ljubljana: IMT, 2018. 11 str., graf. prikazi, ilustr. [COBISS.SI-ID 1452458] financier: Naročnik: Le-Tehnika d.o.o., Kranj

B. Skela, M. Sedlaček, B. Podgornik, “Analiza obrabe oplaščenih kontaktnih površin elektromehanskega prožilnega releja,”. Ljubljana: IMT, 2017. 9 f., ilustr. [COBISS.SI-ID 1328042] financier: Naročnik: ET I- elektroelement d.d., Izlake

Biography

Božo Skela was born on 31th March in 1990 in Ljubljana. He comes from Slovenska Bistrica where he finished high school in 2009. After high school, he started with University study programme in Materials Engineering on the Faculty of Natural Sciences and Engineering (NTF) in Ljubljana. He graduated in 2013, with the bachelor topic of Microstructure of Al-Sc-Zr type alloys. In the same year he signed up for the second-cycle (master's) University study programme in Materials and Metallurgy on the same faculty. In December 2013 he started receiving the scholarship of the Jožef Stefan Institute. In July 2014, he started working as a student on the Jožef Stefan Institute on a CalGad-X project and later continued his work in the frame of LIA PAC2-C project with the topic on Push-Pull Alloys and Complex Compounds. In the frame of this bilateral project in 2016 he work visited CNRS (Nancy, France) where part of the research concerning Al-Cr-Sc ternary system, he was working on that time, was conducted. During the second-cycle (master's) study he was also enrolled in a project Optimization of microstructure of aluminium cast alloys, that was a part of projects called Following the creative path to practical knowledge. The title of his master's degree work was the Ternary system of Cu-Gd-Ca. In 2016 he successfully defended his master thesis and obtained the title of mag. inž. metal. mat. After that he started his Ph.D. studies at the Jožef Stefan International Postgraduate School, program Nanosciences and Nanotechnologies and started working on the Institute of metals and technology as a young researcher. The topic of his PhD was on the tool steel wear behaviour. During his Ph.D. work he was also involved in research activities and analyses for Slovenian industry. Furthermore, he attended several regional as well as international conferences. Božo also won an 'Award for the Second Best Oral Presentation' at the 25th International Conference on Materials and Technology, Portorož, Slovenia (2017).